MATERIALS CHARACTERIZATION SERIES
SERIES EDITORS: **C. Richard Brundle** and **Charles A. Evans, Jr.**

CHARACTERIZATION OF Ceramics

Ronald E. Loehman

MOMENTUM PRESS

CHARACTERIZATION OF CERAMICS

MATERIALS CHARACTERIZATION SERIES
Surfaces, Interfaces, Thin Films

Series Editors: C. Richard Brundle and Charles A. Evans, Jr.

Series Titles

Encyclopedia of Materials Characterization, C. Richard Brundle, Charles A. Evans, Jr., and Shaun Wilson

Characterization of Metals and Alloys, Paul H. Holloway and P. N. Vaidyanathan

Characterization of Ceramics, Ronald E. Loehman

Characterization of Polymers, Ned J. Chou, Stephen P. Kowalczyk, Ravi Saraf, and Ho-Ming Tong

Characterization in Silicon Processing, Yale Strausser

Characterization in Compound Semiconductor Processing, Yale Strausser

Characterization of Integrated Circuit Packaging Materials, Thomas M. Moore and Robert G. McKenna

Characterization of Catalytic Materials, Israel E. Wachs

Characterization of Composite Materials, Hatsuo Ishida

Characterization of Optical Materials, Gregory J. Exarhos

Characterization of Tribological Materials, William A. Glaeser

Characterization of Organic Thin Films, Abraham Ulman

CHARACTERIZATION OF CERAMICS

EDITOR

Ronald E. Loehman

SERIES EDITORS

Lee E. Fitzpatrick

MOMENTUM PRESS

MOMENTUM PRESS, LLC, NEW YORK

Reissued volume published in 2010 by
Momentum Press®, LLC
222 East 46th Street, New York, N.Y. 10017
www.momentumpress.net

ISBN-13: 978-1-60650-194-8 (hard back, case bound)
ISBN-10: 1-60650-194-1 (hard back, case bound)

ISBN-13: 978-1-60650-196-2 (e-book)
ISBN-10: 1-60650-196-8 (e-book)

DOI forthcoming

Interior Design by Scribe, Inc. (www.scribenet.com)

10 9 8 7 6 5 4 3 2 1

Printed in Taiwan ROC.

Contents

INORGANIC GLASSES AND GLASS-CERAMICS

CERAMIC MICROSTRUCTURES

CERAMIC REACTIONS AND PHASE BEHAVIOR

MECHANICAL PROPERTIES AND FRACTURE

CERAMIC COMPOSITES

GLASS AND CERAMIC JOINTS

ELECTRONIC AND MAGNETIC CERAMICS

NONDESTRUCTIVE EVALUATION

APPENDIX: TECHNIQUE SUMMARIES

Preface to the Reissue of the Materials Characterization Series

The 11 volumes in the Materials Characterization Series were originally published between 1993 and 1996. They were intended to be complemented by the *Encyclopedia of Materials Characterization*, which provided a description of the analytical techniques most widely referred to in the individual volumes of the series. The individual materials characterization volumes are no longer in print, so we are reissuing them under this new imprint.

The idea of approaching materials characterization from the material user's perspective rather than the analytical expert's perspective still has great value, and though there have been advances in the materials discussed inl each volume, the basic issues involved in their characterization have remained largely the same. The intent with this reissue is, first, to make the original information available once more, and then to gradually update each volume, releasing the changes as they occur by on-line subscription.

C. R. Brundle and C. A. Evans, October 2009

Preface to Series

This Materials Characterization Series attempts to address the needs of the practical materials user, with an emphasis on the newer areas of surface, interface, and thin film microcharacterization. The Series is composed of the leading volume, *Encyclopedia of Materials Characterization*, and a set of about 10 subsequent volumes concentrating on characterization of individual materials classes.

In the *Encyclopedia*, 50 brief articles (each 10 to 18 pages in length) are presented in a standard format designed for case of reader access, with straightforward technique descriptions and examples of their practical use. In addition to the articles, there are one-page summaries for every technique, introductory summaries to groupings of related techniques, a complete glossary of acronyms, and a tabular comparison of the major features of all 50 techniques.

The 10 volumes in the Series on characterization of particular materials classes include volumes on silicon processing, metals and alloys, catalytic materials, integrated circuit packaging, etc. Characterization is approached from the materials user's point of view. Thus, in general, the format is based on properties, processing steps, materials classification, etc., rather than on a technique. The emphasis of all volumes is on surfaces, interfaces, and thin films, but the emphasis varies depending on the relative importance of these areas for the materials class concerned. Appendixes in each volume reproduce the relevant one-page summaries from the *Encyclopedia* and provide longer summaries for any techniques referred to that are not covered in the *Encyclopedia*.

The concept for the Series came from discussion with Marjan Bace of Manning Publications Company. A gap exists between the way materials characterization is often presented and the needs of a large segment of the audience—the materials user, process engineer, manager, or student. In our experience, when, at the end of talks or courses on analytical techniques, a question is asked on how a particular material (or processing) characterization problem can be addressed the answer often is that the speaker is "an expert on the technique, not the materials aspects, and does not have experience with that particular situation." This Series is an attempt to bridge this gap by approaching characterization problems from the side of the materials user rather than from that of the analytical techniques expert.

We would like to thank Marjan Bace for putting forward the original concept, Shaun Wilson of Charles Evans and Associates and Yale Strausser of Surface Science Laboratories for help in further defining the Series, and the Editors of all the individual volumes for their efforts to produce practical, materials user based volumes.

C. R. Brundle C. A. Evans, Jr.

Preface to the Reissue of *Characterization of Ceramics*

Fifteen specialists (ten from Sandia National Laboratories) combined their efforts to produce this comprehensive volume. Between them, they addressed the concerns and recommendations for the ceramics area presented in the National Academy of Sciences study, "Materials Science in the 1990's: Maintaining Competitiveness in the Age of Materials." The first five chapters deal with synthesis and processing, and the remainder cover structure, reaction, mechanical properties, composites and joining, and electronic and magnetic ceramics, all with an emphasis on characterization. Of course, there have been advances since the original publication, particularly with micro aspects being pushed down to the nano region, but all the principles involved in the characterization approaches discussed here remain valid and pertinent. Following the reissue of this volume, in a form close to the original, it is our intention to release updates and new material, as on-line downloads, as they become available.

C. R. Brundle and C. A. Evans, December 2009

Preface

Most ceramics are ionically bonded compounds found in complex crystal structures that are strong, stiff, lightweight, hard, and corrosion-resistant. Typically, they maintain their properties to high temperatures. In a broad sense, a ceramic is any man-made, inorganic, nonmetallic, solid material. Glass, usually considered a subset of ceramics, is any solid that lacks crystalline order. Traditionally, ceramics have been considered polycrystalline, although most ceramists today do not accept that restriction. Also traditional is the idea that high temperatures are required for the synthesis or processing of ceramics and glasses; but that limitation is no longer valid—new materials such as aerogels and tin fluorophosphate glasses are synthesized at room temperature or at a few hundred degrees above ambient.

Raw materials for ceramic and glass manufacture traditionally are earthy, oxide materials that are mined in high volume at low cost and are subjected to relatively little processing. The products made from them are commodity items such as brick, tile, bottles, and windows. Modern technical or engineering ceramics are higher-value materials that have superior properties as a result of more sophisticated processing and tighter control over raw materials. These advanced ceramics are much more varied in composition than simple oxides and include, for example, carbides, nitrides, and borides. The development of ceramic composites that are heterogeneous on the micrometer or nanometer scale is a rapidly expanding area of materials science and engineering. The need for better control of final properties requires increased use of modern characterization techniques at all stages of ceramic synthesis and processing. This volume describes characterization techniques and how they can be used to obtain that greater control.

This book is written in a time of changing priorities in materials science and engineering. Responding to a perception that research results in the United States were not being reliably translated into marketable products, the U.S. National Academy of Sciences conducted an influential study—the results of which were reported in a widely read book, *Materials Science in the 1990s: Maintaining Competitiveness in the Age of Materials*, National Academy Press, Washington, D.C., 1989—that recommended increased emphasis on materials synthesis and processing. These recommendations include

- interactive research on new materials synthesis that is linked with characterization and analysis of the product
- basic research on synthetic solid-state inorganic chemistry to produce new compounds

- synthesis of ultra pure materials, for example, fibers with low oxygen or carbon impurity levels
- research on techniques for synthesis to net-shape; that is, learning how to do synthesis, processing, and forming in a single step
- research on methods for processing ceramic materials far from equilibrium
- research on processing artificially structured or, as they are sometimes called, functionally gradient materials.

Characterization of Ceramics addresses these concerns and recommendations in two ways. First, the book stresses advanced synthesis and processing. Second, the central theme of the book, the application of characterization techniques, is a specific recommendation of the NAS study. The 13 chapters of this volume present a broad overview of ceramics and glasses. Each of the topics provides enough information for the reader to make intelligent choices among the myriad available characterization and analysis techniques. Many of the chapters are organized as case studies taken from the authors' own research, which help to illustrate how different methods can be integrated to give a more complete picture of a given process or phenomenon.

The first part of the book deals with the techniques of ceramic synthesis. Increasingly, advanced ceramics are being produced from highly processed powders made by methods collectively known as chemical preparation. Some of the more promising routes to the production of advanced ceramic powders are sol–gel processing, precipitation from solution, gas-phase synthesis, and powder-surface modification. J. A. Voigt discusses recent trends in the use of near–room temperature solution techniques to make ceramic precursors. An example of this is the sol–gel method, in which organometallic reagents in solution are hydrolyzed and condensed to form an inorganic polymeric gel that, when dried and fired, gives the desired ceramic composition. These chemical methods can generate controlled-size distributions, extremely reactive precursors, unusually shaped particles, and gels. Solution methods permit the intimate mixing of components, easy dispersion of second phases, and surface modification of precursor particles. Liquid precursor solutions also can be used to make thin films by dipping or spinning; because of the high reactivity of the precursor particles, film consolidation occurs at moderate temperatures. The chapter by R. W. Schwartz on electronic ceramics shows how analytical methods such as NMR are used to guide the solution synthesis of electronic ceramic films such as PZT (lead zirconate-lead titanate). Voig's chapter illustrates the importance of thorough characterization in the development of better synthesis methods.

Ceramic powders and films made by gas-phase techniques and their characterization are discussed by C. L. J. Adkins and D. E. Peebles. Ultrafine ceramic particles with enhanced surface reactivity, such as SiO_2, can be synthesized through nucleation or condensation reactions in gas-phase aerosols. Ceramic films and

coatings, such as diamond and diamond-like materials, are synthesized by a variety of vapor deposition techniques.

Ceramic processing methods are extremely diverse, with new ones being constantly developed. The technique with widest application is sintering bulk ceramics, in which a powder preform is typically converted to a dense, consolidated object through solid or liquid-phase diffusion. The driving force for diffusion is the lowering of the Gibb's energy by minimizing surface area and, possibly, by reaction to more stable products. K. G. Ewsuk discusses the essential features of bulk sintering and the analytical methods used to characterize the process. By contrast, T. J. Garino's chapter is concerned with the densification of ceramic thick films and the phenomena distinctive to them. For example, ceramic films usually are deposited on substrates, and differential shrinkage in drying or firing leads to stresses and possibly warping. Garino's discussion emphasizes characterization methods applicable to those ceramic films.

Much current ceramic processing research for both bulk materials and films is directed toward eliminating flaws, thereby increasing strength and fracture toughness. L. Neergaard's chapter on nondestructive evaluation shows how to detect flaws that are frequently generated in a ceramic despite the best of processing efforts.

Other types of ceramic processing discussed in this volume are inorganic glasses and glass-ceramics by R. K. Brow, ceramic composites by S. J. Glass, and ceramic joining by A. P. Tomsia. This selection of processing methods is not exhaustive, but is broad enough for most of the applicable characterization techniques to be presented. These three chapters share a common concern with interfaces and how to characterize their reactivities, compositions, and microstructures.

Because ceramics are brittle, they are susceptible to catastrophic failure under mechanical load. The useful strength of a ceramic is determined by the flaw population: stresses are concentrated at flaws, which cause cracks to propagate to failure. The critical property for ceramics in load-bearing uses is not the strength, but the fracture toughness—the resistance of the ceramic to crack propagation. The fracture surface of a ceramic bears the evidence of its failure. One must read the features in a fracture surface to understand the origin and path of the fracture. The case study by E. K. Beauchamp shows how much practical information can be obtained from ceramic fracture analysis.

The other two chapters are basic to much of ceramics. In ceramics, microstructure determines properties; the study of that relationship has been a main theme for decades. A. H. Carim's chapter illustrates the range of microscopic and microanalytic techniques used to determine the structures and composition of ceramic microstructures. Another foundation of ceramics is reactivity and phase behavior. Knowledge of these topics is basic to understanding all forms of thermal processing of ceramics. P. K. Gallagher's chapter on reactivity and thermal analysis is an authoritative account by one of the experts of the field.

Ronald E. Loehman

Contributors

Carol L. Jones Adkins
Sandia National Laboratories
Albuquerque, NM

Powder Preparation by Gas-Phase Techniques

Edwin K. Beauchamp
Sandia National Laboratories
Albuquerque, NM

Mechanical Properties and Fracture

Richard K. Brow
Sandia National Laboratories
Albuquerque, NM

Inorganic Glasses and Glass-Ceramics

Altaf H. Carim
The Pennsylvania State University
University Park, PA

Ceramic Microstructures

Kevin G. Ewsuk
Sandia National Laboratories
Albuquerque, NM

Consolidation of Bulk Ceramics

Patrick K. Gallagher
The Ohio State University
Columbus, OH

Ceramic Reactions and Phase Behavior

Terry J. Garino
Sandia National Laboratories
Albuquerque, NM

Consolidation of Ceramic Thick Films

S. Jill Glass
Sandia National Laboratories
Albuquerque, NM

Ceramic Composites

Ronald E. Loehman
Sandia National Laboratories
Albuquerque, NM

Glass and Ceramic Joints

Lynn Neergaard
New Mexico Institute of Mining and Technology
Socorro, NM

Nondestructive Evaluation

Diane E. Peebles
Sandia National Laboratories
Albuquerque, NM

Formation of Ceramic Films and Coatings

Robert W. Schwartz
Sandia National Laboratories
Albuquerque, NM

Electronic and Magnetic Ceramics

Rajan Tandon
University of California
Santa Barbara, CA

Ceramic Composites

Antoni P. Tomsia
Lawrence Berkeley Laboratory
Berkeley, CA

Glass and Ceramic Joints

James A. Voigt
Sandia National Laboratories
Albuquerque, NM

Powder and Precursor Preparation by Solution Techniques

1

Powder and Precursor Preparation by Solution Techniques

JAMES A. VOIGT

Contents

1.1 Introduction

The traditional scheme for fabricating ceramics involves preparing a powder, forming the powder into a green compact, and heating the compact to densify it to its final form.[1, 2] The driving force for densification, or sintering as it is more commonly called, is a reduction in the surface free energy of the powder compact. At elevated temperatures the surface tension of the particles gives rise to chemical potential gradients, which in turn produce a flow of matter in a direction that decreases the chemical potential. As a result of these differences in chemical potential gradients, the total free energy of the system decreases. The mass fluxes that arise during sintering may occur in the vapor phase, along the solid surface, in the bulk of the particles, or along grain boundaries.[3] The driving force for sintering illustrates why powder properties, such as particle size and surface area, are of importance in the preparation of ceramic materials. For example, to achieve equivalent densification, a highly active powder (i.e., fine particle size, high surface area) may be sintered at a lower temperature and for a shorter period of time than a poorly prepared powder of the same material. This usually produces a smaller grain size and a more uniform microstructure in the dense body, both of which improve mechanical and optical properties.

Mixed Oxide Processing

Applications of high-performance ceramics often require either new ceramic materials or ceramic materials with improved properties. To meet these demands, ceramics need to be prepared using optimally processed powders. Most traditional ceramic products, such as whiteware and brick, are manufactured using powders prepared by comminution and blending of naturally occurring ores and clays. In contrast, most engineering ceramics such as those used in electronics and structural applications require starting powders with compositions and phase assemblages that must be synthesized. Conventional powder synthesis, frequently referred to as mixed-oxide processing, involves mechanically mixing and milling different powders (most often oxides) that contain components of the phase to be prepared. When heated (or calcined), the powder mixture reacts to form the product powder. For example, to make $BaTiO_3$ powders for use in ceramic capacitors, $BaCO_3$ and TiO_2 are typically the component starting powders. One of the drawbacks of mechanical mixing of powders is the long diffusion distances between reacting components. These long diffusion distances necessitate the use of relatively high calcination temperatures that can lead to unwanted grain growth and the formation of hard agglomerates, both of which deleteriously affect ceramic properties. The mixing and milling operations also can introduce unwanted impurities that, at levels as low as a few tens of parts per million, can drastically alter the processability and final properties of many ceramic materials. The mixed-oxide processing approach, however, often is not capable of homogeneous incorporation of low-level additives when they are required.

Chemical Synthesis of Powders

Chemical synthesis techniques have been developed to overcome the limitations of conventional powder preparation methods. In chemical processing, powder components are intimately mixed as solutions or vapors. A state of supersaturation is created in the vapor or solution through chemical reaction, changes in temperature or pressure, solvent substitution, or solvent removal. The supersaturation is relieved and the free energy of the system reduced through spontaneous formation of a particulate solid phase. Because of the high degree of mixing, precursor powders prepared by these methods have short component diffusion distances; as a result, the precursors often can be calcined to final form at significantly lower temperatures than mixed-oxide processed powders. The milder calcination conditions, coupled with controlled precursor synthesis, lead to the formation of fine, controlled-morphology powders. Current trends in chemical synthesis involve developing methods that form the desired phase directly, thus avoiding the calcination operation completely. Also, homogeneous incorporation of low-level additives is facilitated by the chemical mixing process.

Types of chemical synthesis techniques can be distinguished by the medium in which solid particles form. Particle formation in solution is the topic of this chapter,

whereas gas-phase synthetic routes are described in Chapter 2. Many solution methods have been developed, such as solution freeze-drying, emulsion precipitation, hydrothermal processing, sol–gel processing, and precipitation of sparingly soluble salts (see References 4–8). This chapter is limited to two of the most widely studied synthesis routes—sol–gel processing and the precipitation of sparingly soluble salts, since the characterization techniques for the different solution methods are similar. Emphasis is placed on the different processes involved in particle formation and how these processes are characterized. An introduction to the general topic of ceramic powder characterization is first given in the form of a brief discussion of commonly used powder characterization methods (for more detailed information see References 1, 2, and 9).

1.2 Powder Characterization

It is convenient to classify particles into two types based on the mechanism of particle nucleation and growth. Primary particles are discrete units formed by nucleation from solution or by aggregation of much smaller clusters or nuclei. They can be crystalline or amorphous, do not break down during further processing, and generally are relatively dense. The other class of particles, named secondary particles, form by the agglomeration of primary particles. Depending on the strength of primary particle–primary particle contact points, secondary particles may or may not be broken during subsequent processing. The agglomerated particles are less dense than primary particles. It should be noted that these are rather broad definitions useful for visualizing particle formation.

Physical Characteristics

The most important physical properties of a ceramic powder are its particle size distribution, particle morphology, surface area, and state of agglomeration. These properties determine how well a powder can be packed during green body formation. For example, powders with a distribution of sizes can be formed into higher density compacts than those with an unimodal, narrow size distribution. This is because smaller particles can fit into the interstices of consolidated larger particles. Powders with fine particle sizes (<1 μm) and high surface areas are generally desired because of their high sinterability. Powders containing hard agglomerates (those that do not break down during green body formation) are undesirable because they can lead to differential sintering that results in nonuniform microstructures and reduced densities.

There are numerous commercial instruments available for determining powder particle size distributions. The instruments use sizing techniques that are based on a variety of principles, including sedimentation, light scattering, electrical sensing, image analysis of electron photomicrographs, hydrodynamic chromatography, and sieving.[9, 10] X-ray diffraction line broadening is often used to determine a powder's

average crystallite size and is applicable when crystallite sizes are less than 1000 Å. Particle morphology is characterized by image analysis of photomicrographs obtained using scanning electron microscopy (SEM) or transmission electron microscopy (TEM). The most widely used method to determine the specific surface area of a powders is by application of the Brunauer-Emmett-Teller (BET) model to gas adsorption data.[1, 9]

The characterization of powder agglomerate properties is much less standardized. Agglomerate pore size distributions in the range of 15–1000 Å can be obtained by analysis of gas adsorption-desorption isotherms. Mercury intrusion porosimetry is also used in pore size determination (applicable for pores ranging from 20 Å to larger than 1000 μm). This technique is based on application of the Washburn equation which relates the radius of a cylindrical pore to the pressure required to intrude a nonwetting liquid, such a mercury.[1, 9] Mercury porosimetry is only applicable to powders that contain agglomerates that can withstand maximum intrusion pressures of about 400 Pa. Agglomerate strength can be inferred from powder compaction data. Plots of the log of applied pressure versus compact density normally will have an inflection point at the point where agglomerates collapse. A technique developed by Ciftcioglu and co-workers[11] combines particle size distribution analysis with ultrasonic disruption to determine agglomerate strength. In this method, powder suspensions are subjected to ultrasonic irradiation with an intensity that has been calibrated in terms of a disruptive pressure. Particle size distribution data are measured after fixed times at progressively higher power inputs. The change in particle size distribution as a function of sonication intensity and time is related to agglomerate strength. Figure 1.1 gives an example of the application of this technique to continuously precipitated yttrium hydroxynitrate powders. The figure illustrates the influence of the precipitate dewatering method on powder particle size and agglomerate strength. In this example the precipitates were dewatered either by a series of organic washes or by suspension freeze-drying. The size distributions are compared before and after sonication (1 MPa sonication pressure for 10 min) and also to the size distribution of the precipitate before drying. The figure shows that the organic washed powder contains much weaker agglomerates than the freeze-dried sample, as evidenced by the shift of its particle size distribution to much finer sizes after sonication.

Chemical Properties

Thermal analysis is often used to characterize the decomposition and crystallization behavior of ceramic precursor powders.[12] The information gained from these analyses is used to determine appropriate calcination schedules. The two most common thermal analysis techniques are thermogravimetric analysis (TGA), in which weight loss is monitored during heating, and differential thermal analysis (DTA), in which the changes in sample temperature relative to a standard are monitored during heating (see Chapter 8 by Gallagher). Figure 1.2 shows typical TGA/DTA data for

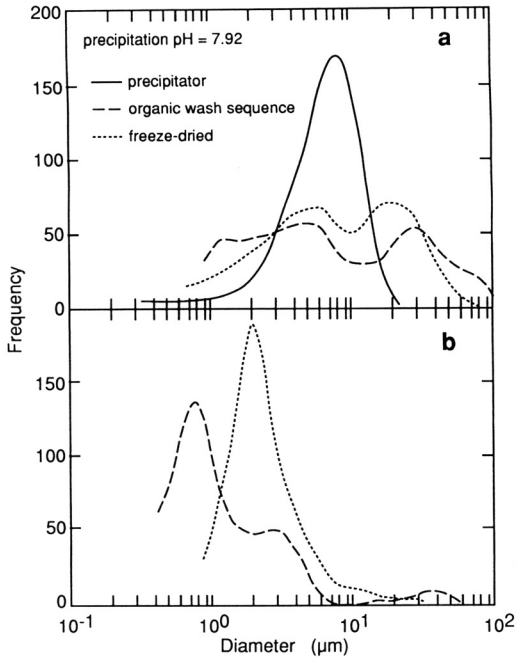

Figure 1.1 **Particle size distributions of yttrium hydroxynitrate precipitates dewatered by a sequence of organic washes (acetone, toluene, and acetone) and by freeze-drying (*a*) as suspended after drying and (*b*) after 10 min of 1 MPa ultrasonic irradiation. Also shown is the in situ precipitator-size distribution.**

the decomposition of yttrium hydroxynitrate precipitates formed under different pH conditions. The TGA data show that, regardless of pH, precipitate weight loss is complete by about 600 °C. At this temperature, X-ray powder diffraction results show that the hydroxynitrate is completely converted to the oxide (Y_2O_3). The plateaus in the TGA curves indicate formation of intermediate phases (phases are indicated on the figure) as the powder decomposes. The formation of these phases is endothermic, as shown by the thermal events in the DTA curves. As the precipitation pH is increased, the TGA plateaus are less distinct and the DTA thermal event spikes broaden. These trends indicate that the precipitate is less ordered when higher pH conditions are used.

The characterization of the surface properties of powders suspended in liquids is important in a number of areas of ceramic processing. Stable aqueous and nonaqueous suspensions (controlled by particle surface properties) are used in green body formation processes, such as tape casting, injection molding, and screen printing.[1, 2] Also, particle surface properties can control particle growth and agglomeration during solution synthesis. Fine particles (<1 μm) in suspension are subject to electrostatic forces, London–van der Waals forces, osmotic forces, gravitational

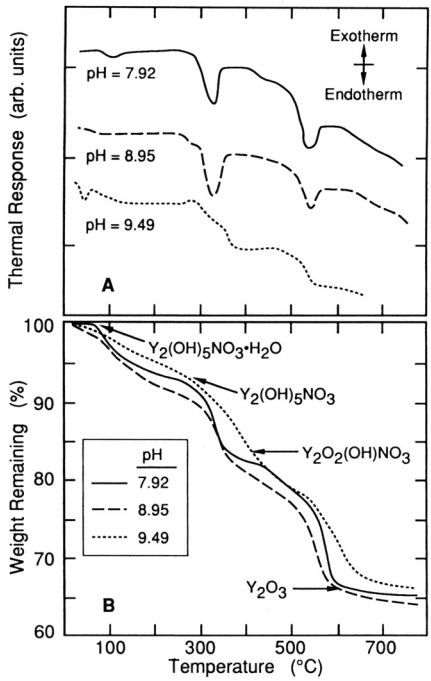

Figure 1.2 **(*a*) Differential thermal analysis, DTA, and (*b*) thermogravimetric analysis, TGA, of continuously precipitated yttrium hydroxynitrate powders as a function of precipitation pH. Stoichiometries at TGA plateaus were determined based on the analysis of Holcombe et al.[13]**

forces, and forces due to solvent structure. These forces, together with the effects of Brownian motion and suspension hydrodynamics, determine the stability of a dispersion.[14] Colloidal dispersions are often stabilized by addition of polymeric compounds that are preferentially adsorbed on particle surfaces.[1, 15] The repulsion of polymer chains attached to different particles sterically stabilizes the suspension.

Electrostatic stabilization is of importance in solution synthesis as another way to stabilize dispersions.[14, 16] Colloidal particles almost always have charged surfaces that tend to repel each other. One of the most common charging processes is the adsorption of charged species on the surface of the particle. To maintain electroneutrality, a diffuse cloud of counter ions forms in the fluid around the suspended particle. This phenomenon is described by the diffuse double-layer theory. When the diffuse ion clouds of particles interpenetrate, the particles tend to repel each other electrostatically. The electrostatic repulsive forces are opposed by attractive van der Waals forces that are always present between particles in suspension. The description of the potentials created by these two opposing forces is known as the Derjaguin–Landau–Verwey–Overbeek (DLVO) theory. The DLVO theory predicts

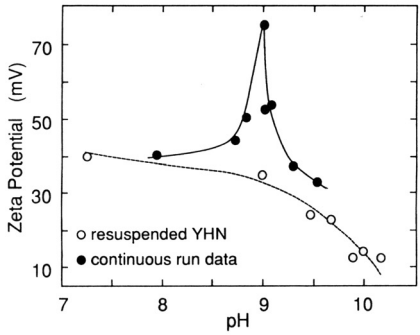

Figure 1.3 **Zeta-potential (ζ) data of aged yttrium hydroxynitrate, YHN, suspensions (prepared by resuspending dried, continuously precipitated YHN powder in 0.01 M $NaNO_3$ solutions) as a function of pH (adjusted with NaOH solution). Also shown are YHN zeta-potential data taken at steady-state continuous precipitation conditions.**

that a potential barrier to particle-particle contact will exist that is a function of suspension characteristics, including particle surface charge, the ionic strength of the dispersing medium, the properties of the suspended material, and the properties of the dispersing liquid. The magnitude of this barrier is often experimentally related to a quantity known as the zeta potential. The zeta potential is the electrical potential measured at the particle surface of shear and is most often determined electrophoretically.[16] In general, the higher the zeta potential, the higher the potential barrier for particle-particle contact and the more stable the suspension.

Let us refer again to the continuous precipitation yttrium hydroxynitrate: Figure 1.3 shows how the zeta potential of the precipitate varies with pH both during precipitation and when the powder has been resuspended after drying. The decrease in zeta potential with increasing pH for the resuspended sample is typical of the behavior of oxides and hydroxides. The surfaces of these solids possess a large number of amphoteric hydroxyl groups that can undergo reaction with either hydrogen ions or hydroxide ions, depending on the relative concentration of the ions or the pH of the system. In acidic conditions, the surface hydroxyls react with hydrogen ions to produce a positive surface charge or zeta potential, whereas under basic conditions the hydroxyls react with hydroxide ions to produce a negative surface charge or zeta potential. If the pH of the aged yttrium hydroxynitrate suspensions were adjusted to greater than 10 (Figure 1.3), the zeta potential would be negative. Surface properties of precipitates during formation can be inferred by comparing zeta potential measurements of growing precipitates with aged suspensions of the same material. As shown in Figure 1.3, the zeta potential of yttrium hydroxynitrate is significantly higher during precipitation than when it is aged in suspension and goes through a maximum at a precipitation pH of 9. This result

indicates that during precipitation the yttrium hydroxynitrate particle surfaces preferentially adsorb excess positive complexes from solution, which increase the zeta potential. This behavior helps explain a change in nucleation and growth kinetics that occur at a pH of 9.

Virtually all of the chemical characterization techniques described in the first volume of this series have been applied to ceramic powders.[5–9] The only limitation is in the difficulty of dealing with the small size of the particles. For example, when using surface analysis techniques it is not always possible to characterize individual particles; instead, groups of particles are simultaneously analyzed. It would be redundant to discuss the application of these techniques to ceramic powders here.

1.3 Precursor Powder Synthesis

The formation of particles in solution can be viewed as the result of a series of competing kinetic processes. First, metal cation-containing species must be formed and the chemistry or environment of these species altered to create a state of supersaturation. If the degree of supersaturation is high enough, particle nuclei form and either redisperse or grow to become primary particles. Those particles then can continue to grow either by addition of dissolved species or by agglomeration to form secondary particles. The nucleation and growth kinetics depend on the chemistry of the system and the processing conditions.

Speciation and Supersaturation

When creating supersaturation levels sufficient to induce particle formation, precipitation of sparingly soluble salts and sol–gel processes are viewed differently. Precipitation normally involves mixing a cation solution with a precipitant solution. For example, consider preparation of an oxalate precursor to a CoO- and MnO-doped ZnO powder. In this process, the Zn, Mn, and Co are coprecipitated with controlled stoichiometry and the precipitate is calcined to the oxide. To form the oxalate, a state of supersaturation is created by mixing an aqueous solution of the metal nitrates or chlorides with an oxalate precipitant solution. The system is supersaturated with respect to the different metal oxalate phases and a crystalline coprecipitate forms. Depending on precipitation conditions (pH, concentrations, temperature, etc.), different metal complexes are present in solution. The form and concentration of these complexes determine the phase, morphology, and particle size distribution of the resulting precipitate.

The sol–gel process is normally defined as the formation of a sol, gelation of the sol, and removal of the solvent to produce ceramic powders or monoliths.[5] The sol is formed by hydrolysis and condensation reactions of soluble metal salts (e.g., aluminum chloride or nitrate) or metalorganics such as alkoxides (e.g., $Al(OR)_3$ where R = $-CH_3$, $-C(CH_3)_3$, etc.). Examples of hydrolysis and condensation reactions for metal (M) alkoxides are

Hydrolysis: $M(OR)_4 + H_2O \longrightarrow HO-(OR)_3 + ROH$

Condensation:

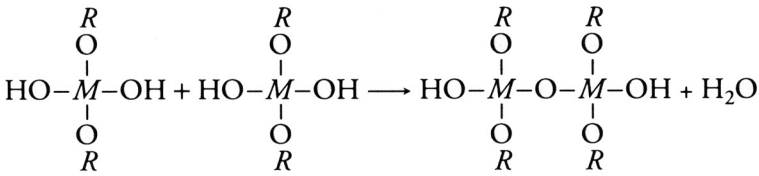

The kinetics of the two competing reactions are controlled by the precursors used (*M* and *R*) and the reaction conditions. For example, rapid addition of excess water to an alcoholic alkoxide solution generally leads to complete hydrolysis with little condensation. Because a hydroxide or hydrous oxide precipitate usually forms, this process resembles the sparingly soluble salt case. Polymeric species form when conditions are adjusted such that condensation occurs. It is the type and distribution of species in solution and how they react with water (hydrolysis) or among themselves (condensation) that determine the form and structure of the particulate or gel product. The ability to form large polymeric species is one of the primary differences between the sol–gel and salt precipitation processes.

The list of techniques used in characterizing speciation and the formation of complexes in solution is extensive and includes potentiometry, infrared and Raman spectroscopies, colorimetry, ultracentrifugation, light, X-ray and neutron scattering, electron spin resonance, inductively coupled plasma atomic emission spectroscopy, and nuclear magnetic resonance (NMR). The hydrolysis of aluminum is a good of example of a well-characterized system.[5, 17, 18] An aluminum salt dissolved in water exists below pH 3 as a hydrated monomer, $[Al(OH_2)_6]^{3+}$, and above pH 11 as the anionic hydrolysis product, $[Al(OH)_4]^-$. At intermediate pH and in the absence of any coordinating anions, oligomeric species form, for example $[AlO_4Al_{12}(OH)_{24}(OH_2)_{12}]^{7+}$, in which a central Al atom (tetrahedrally coordinated to 4 oxygens) is surrounded by 12 octahedrally coordinated Al atoms. The structure of this oligimer, referred to as Al_{13}, was determined by X-ray diffraction studies[19] and is shown in Figure 1.4. Figure 1.4 also illustrates the use of ^{27} Al NMR in following the conversion of the $[Al(OH_2)_6]^{3+}$ monomer to the Al_{13} ion as base is added to a 0.25 M Al^{3+} solution. In the figure (where m = moles base/mole Al), the resonance at 63 ppm relative to $[Al(OH_2)_6]^{3+}$ is attributed to the central Al atom of the Al_{13} oligimer. As more base is added, the monomeric species is consumed to form the oligimer. Using species formation constants that are determined experimentally by application of the techniques listed above, the distribution of species as a function of solution conditions can be calculated. Figure 1.5 shows an example of such calculations for the hydrolysis of aluminum.

If, in the previous example, the amount of added base is increased (m > 2.5), the aluminum solubility limit is exceeded and a precipitate spontaneously forms. The driving force for this process is a function of the supersaturation, *S*, which is the

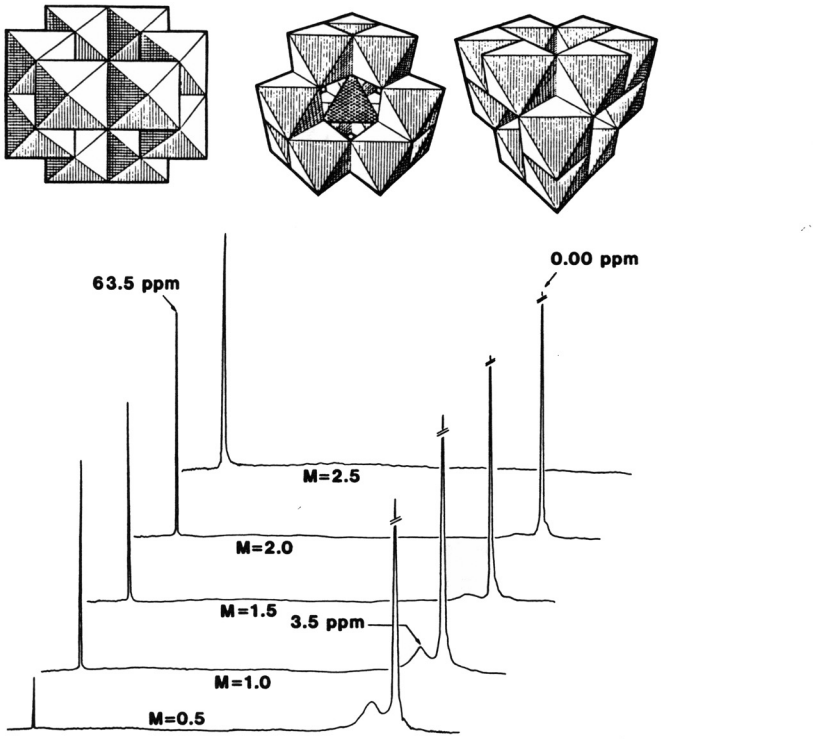

Figure 1.4 **The upper part of this figure shows three different views of the $[AlO_4Al_{12}(OH)_{24}(OH_2)_{12}]^{7+}$ ion. (From Johansson.[19]) The lower part is a plot of the ^{27}Al NMR spectra of 0.25 M Al^{3+} solutions hydrolyzed by the drop-wise addition of aqueous bicarbonate (where m = moles base/mole Al^{3+}). (From Wood et al.[17])**

ratio of the bulk concentration of the species (C) that are incorporated into the growing particle to the concentration of these species at equilibrium (C_e), or $S = C/C_e$. For the case of a sparingly soluble salt, M_aX_b, $S = [(A_M)^a(A_X)^b/K_{s0}]^{1/(a+b)}$, where A_M and A_X are the activities (concentrations) of species M and X, respectively, and K_{s0} is the solubility product of M_aX_b. Supersaturation levels are estimated using species formation constants.

Growth

Particle nucleation and growth are intimately related. Growth can occur in the absence of nucleation, as in the case of seeded crystal growth; however, the formation of stable nuclei can occur only through growth. Since the development of expressions for the kinetics of nucleation require consideration of growth mechanisms, growth will be discussed first. Primary particle growth can occur by deposition of ions or molecules on a particle surface, normally leading to a crystalline product. Growth can also occur by aggregation of microscopic clusters (polymers)

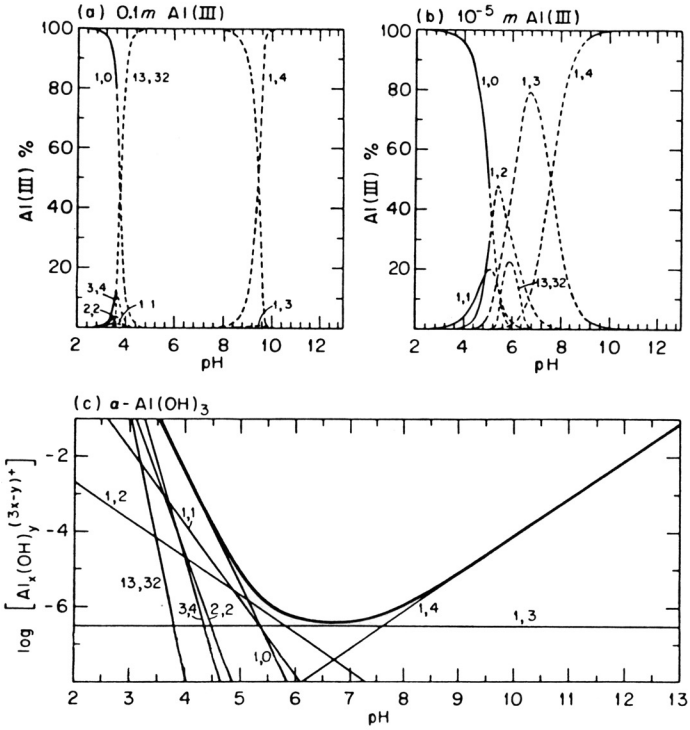

Figure 1.5 **Distribution of aluminum hydrolysis products (*x*,*y*) at ionic strength = 1 M and 25 °C in (*a*) 0.1 M Al(III), (*b*) 10^{-5} M Al(III), and (*c*) solutions saturated with respect to α-$Al(OH)_3$; the heavy curve in *c* is the total concentration of Al(III). (From Baes and Mesmer.[18])**

with sizes on the order of tens of angstroms to a few microns. Growth of a crystalline phase may be visualized as a series of successive steps[20]:

1 Diffusion of lattice ion-containing species to the crystal surface
2 Adsorption of species on the crystal surface
3 Possible surface reactions between species to form two-dimensional nuclei
4 Complete or partial dehydration of adsorbed species
5 Surface diffusion of growth units to energetically favorable lattice sites
6 Incorporation of growth units into crystal lattice (may or may not include chemical reaction)
7 Similar steps involving dissolution of growth units back into solution.

In order to explain experimental results, crystal growth theories have been developed that consider different steps in the growth process as rate limiting. The step that is rate limiting is dependent on the substance being precipitated and the experimental conditions. Most sparingly soluble salts at moderate supersaturation levels ($S < 20$) have been found to have a parabolic dependence of growth on

supersaturation. At low levels of supersaturation ($S < 2$), this dependence is consistent with the rate-limiting process being the incorporation of growth units into spiral growth steps, as described by the theory developed by Burton et al.[21] The fact that the rate of crystallization remains parabolic for $S > 2$ indicates that another step is rate limiting. Numerous theories have been developed to explain this dependence, including the incorporation of charged interfaces due to double-layer formation, surface reaction control, or the dehydration of cationic species as being rate limiting.[20, 22] High supersaturation conditions ($S > 20$) are normally used for the synthesis of ceramic powders since, as discussed in the next section, nucleation rates increase faster with increasing supersaturation than do growth rates. High supersaturation conditions tend to produce the greatest number of fine particles (assuming agglomeration can be controlled), which is desired for ceramic applications. Although important in the controlled synthesis of ceramic powders, little work has been done in understanding growth kinetics under these conditions.

Growth processes are normally characterized by monitoring the change in particle size as a function of time for fixed supersaturation levels. Characterization of particle size is done in situ by visually monitoring growing crystals by optical microscopy, by using image analysis of photomicrographs, or by using a suitable commercial particle size analyzer. The precipitation of lead chromate is a system where particle growth at high supersaturation levels has been characterized.[23] Results of this study are shown in Figure 1.6, where growth rate as a function of relative supersaturation, S-1, is plotted. The data are fit[22] to a growth expression based on a surface-reaction/molecule integration mechanism ($G = K([A^+]_0^2[A^+]_e^2)$, where $[A^+]_0$ and $[A^+]_e$ are the bulk and equilibrium concentrations of lead, respectively) which reduces to the simple parabolic rate law ($G = K(S\text{-}1)^2$) at high supersaturation levels.

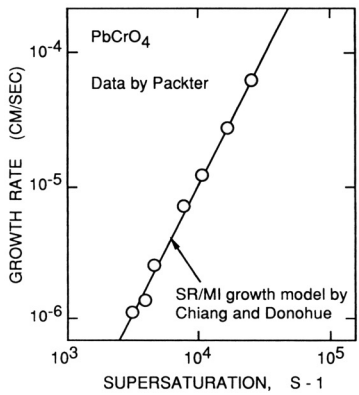

Figure 1.6 **Dependence of the rate of crystal growth upon relative supersaturation for lead chromate. The line is the fit of the data to a growth expression based on a surface-reaction/molecule integration mechanism. (From Chiang and Donohue.[22] Data is from Packter.[23])**

The structure and morphology of precipitates are generally characterized by X-ray diffraction and, depending on particle size, by optical microscopy, SEM, or TEM. Figure 1.7 illustrates the use of SEM in showing how the morphology of continuously precipitated zinc oxalate precipitates changes as a function of pH and the oxalate precipitant. Figure 1.8 shows X-ray diffraction results indicating that as pH increases, the phase assemblage in the precipitate progressively changes from a zinc oxalate dihydrate to a mixture of the dihydrate and a hydroxy oxalate, and finally to mainly zinc oxide. The changes in phase assemblages result from differences in the solubility of the various phases with pH. In general, according to Stranski's rule (also called the Ostwald rule of stages), the most soluble phase precipitates first when particle formation is dominated by homogeneous nucleation (see next section, "Nucleation") because the energetics of nucleation favor the formation of the least stable phase (most soluble).

The species present in solution can have a dramatic effect on the morphology of the phase formed. This is illustrated in Figure 1.7 by SEM photomicrographs comparing $ZnC_2O_4{\cdot}2H_2O$ formed by reacting a Zn nitrate solution with either

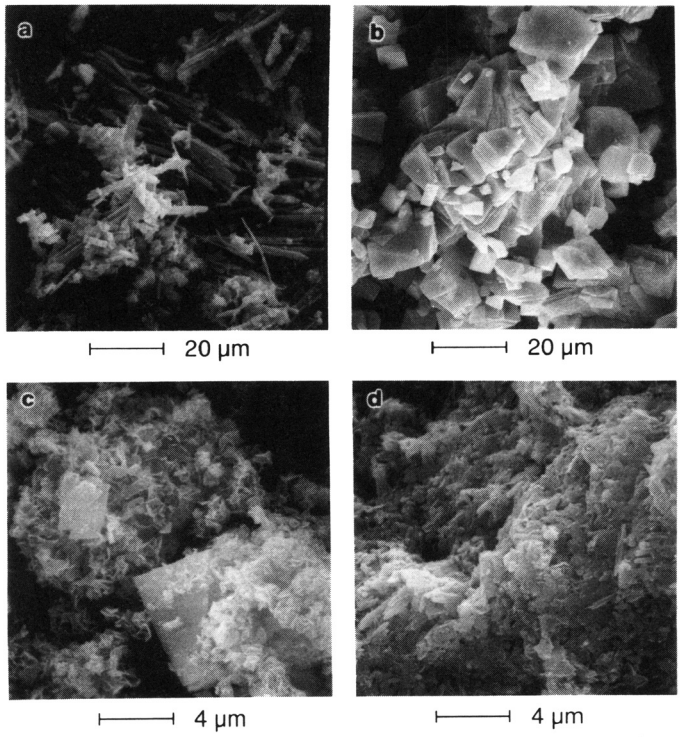

Figure 1.7 **SEM photomicrographs of continuously precipitated zinc salts as function of pH and precipitant: (*a*) pH = 5.5, $(NH_4)_2C_2O_4$ precipitant; (*b*) pH = 5.1, $Na_2C_2O_4$ precipitant; (*c*) pH = 8.5, $Na_2C_2O_4$ precipitant; and (*d*) pH = 10.4, $Na_2C_2O_4$. (From Thomas et al.[24])**

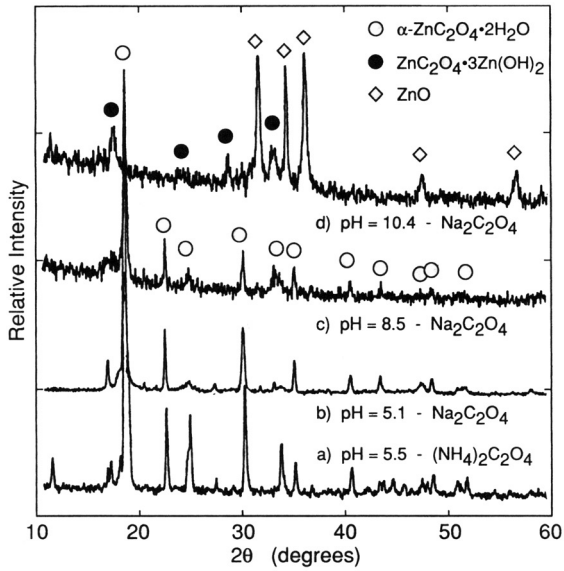

Figure 1.8 **X-ray powder diffraction patterns of continuously precipitated zinc salts as function of pH and precipitant: (*a*) pH = 5.5, $(NH_4)_2C_2O_4$ precipitant; (*b*) pH = 5.1, $Na_2C_2O_4$ precipitant; (*c*) pH = 8.5, $Na_2C_2O_4$ precipitant; and (*d*) pH = 10.4, $Na_2C_2O_4$. (From Thomas et al.[24])**

ammonium oxalate or sodium oxalate. Under the precipitation conditions, used Zn forms ammonium complexes. The presence of these complexes inhibits crystal growth on certain crystallographic faces, resulting in needle-shaped particles. Addition of growth inhibitors is one way to control particle size. An example of this control is the precipitation of zinc oxalate in the presence of parts-per-million levels of poly(acrylic) acid (PAA). Figure 1.9 shows particle size data for zinc oxalate

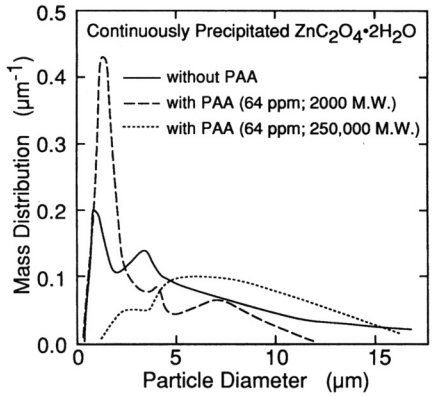

Figure 1.9 **Effect of poly(acrylic) acid (PAA) additions on the particle size of continuously precipitated zinc oxalate. (From Mydlarz et al.[25])**

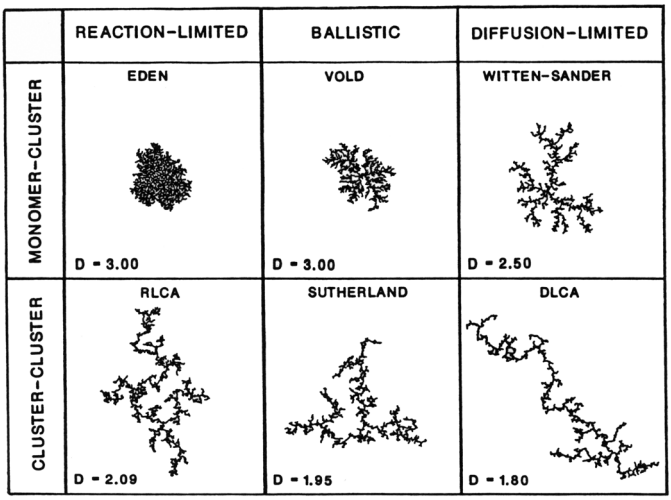

Figure 1.10 Structures resulting from simulations using various kinetic growth models.[27] Fractal dimensions are listed for 3-d clusters even though their 2-d analogs are shown. Each cluster contains 1000 primary particles. (Simulations by Meakin.[26])

precipitated under otherwise identical conditions with and without PAA additions. In the presence of 64 ppm low molecular weight PAA (2000 mol wt), the particle size distribution is narrow, with the majority of particles below 2 μm.

The growth of particles by hydrolysis and condensation reactions can lead to precursors with seemingly random structures. Such kinetic growth processes have been simulated using growth laws based on interaction type (i.e., monomer–cluster, cluster–cluster) and growth limiting mechanism, such as diffusion, reaction, or ballistic.[26] Figure 1.10 shows simulated precursor structures that result when the different combinations of interaction types and growth limiting steps are modeled. Such simulations can be applied to real systems by coupling them with fractal geometry concepts and experimental scattering data.[27]

Fractal geometry provides a means of quantifying the structures of objects such as those shown in Figure 1.10. Mass fractals are objects in which the object mass (m) and radius (r) are related according to $m \propto r^{d_m}$, where d_m is called the mass fractal dimension and is less than 3. Physically, this means that the density of a mass fractal decreases with increasing radius, since density, ρ, is related to r and m by the relation, $\rho \propto m/r^3$. The complex structures shown in Figure 1.10 are characterized by a single fractal dimension (shown as D in the figure). The surface roughness of an object can be quantified by what is called the surface fractal dimension, d_s. Surface fractals are defined by the relation $S \propto r^{d_s}$, where S is the surface area. For example, a smooth object will have a surface fractal dimension of two, as is the case for a smooth sphere. Fractally rough objects have surface fractal dimensions that range between 2 and 3.

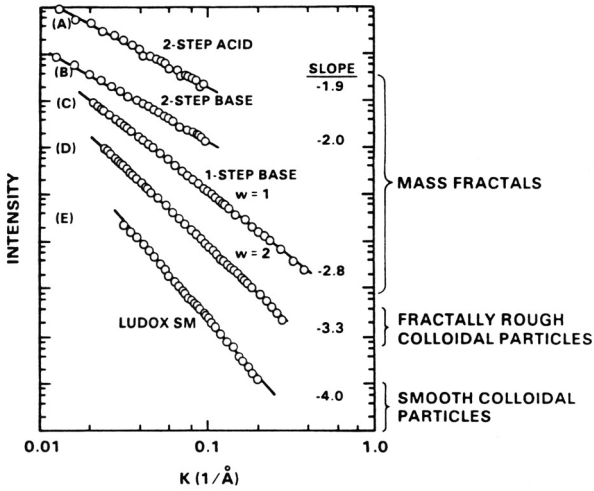

Figure 1.11 **Porod plots of scattering data of silicates polymerized under a variety of conditions (from a study by Schaefer and Keefer[28]): (*a*) two-step acid-catalyzed tetraethoxysilane (TEOS) system; (*b*) two-step acid- and base-catalyzed TEOS system; (*c*) one-step base-catalyzed system TEOS system ($W = 1$); (*d*) one-step base-catalyzed system TEOS system ($W = 2$); (*e*) aqueous silicate system, LUDOX®. *W* is the water/silica ratio.**

The scattering at small angles of various forms of incident radiation provides a means of obtaining the fractal properties of real systems. Small-angle scattering of X-rays (SAXS), neutrons (SANS), and visible light (either static or quasi-elastic [QELS]) gives structural information on length scales from 1 Å to 1 μm.[5, 27] An investigation by Schaefer and Keefer[28] of the hydrolysis and condensation of silicates is representative of the application of SAXS to ceramic precursor systems. Results from their study are shown in Figure 1.11 and illustrate the expected power-law dependence of scattering intensity versus the wave vector, *K*, for the Porod region of scattering space. In the Porod region, fractal properties are related to the slope of a plot of the log(Scattering Intensity) versus log *K* (as shown in Figure 1.11).[27] The hydrolysis and condensation of silicates is a good example of the importance of synthesis conditions in controlling precursor structure in sol–gel processing.

Through the appropriate aging of hydrolysis products, monodisperse particles with a wide variety of morphologies can be formed as shown by the examples given in Figure 1.12. The processes involved in the growth of such particles are not well understood and are a complicated function of system solution chemistry and processing conditions. The complexities are discussed in excellent reviews of the hydrolysis of iron(III) salts[30] and phase transformations of iron oxides, oxyhyhroxides, and hydrous oxides in aqueous media.[31] Along with the techniques already discussed, a method known as cryo-TEM has been used to study particle growth. In

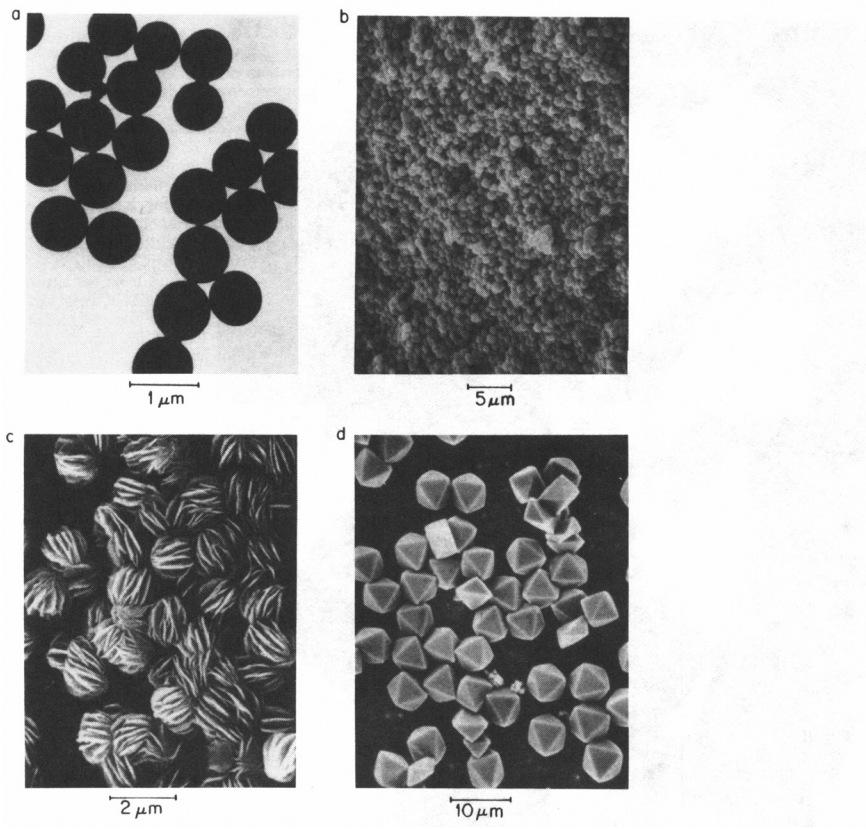

Figure 1.12 **TEM and SEM photomicrographs of homogeneously precipitated metal oxides and hydroxides: (*a*) aluminum hydroxide particles obtained by aging a 0.002 M solution of $Al(SO_4)_3$ at 97 °C for 48 h (TEM); (*b*) hematite, α-Fe_2O_3, particles formed by aging a solution 0.032 M $FeCl_3$ + 0.005 M HCl at 200 °C for 2 weeks (SEM). (*c*) boehmite, α-AlOOH, particles formed by aging a 0.0030 M solution of $Al(ClO_4)_3$ at 125 °C for 12 h (SEM). (*d*) alunite, $Fe_3(SO_4)_2(OH)_5{\cdot}2H_2O$, particles formed by aging a 0.18 M $Fe(NO_3)_3$ + 0.27 M $(NH_4)_2SO_4$ solution at 80 °C for 1.5 h (SEM). (From Matijevic.[29])**

cryo-TEM, samples are prepared by placing a droplet of solution on a holey carbon grid suspended in a controlled environmental chamber. The grid is blotted to produce thin liquid films in the grid holes. The grid is then plunged into liquid ethane (at about –180 °C) to vitrify the solvent. The fast-frozen structures are directly imaged by TEM using a cold-stage sample holder. A study by Bailey and co-workers[32] on the growth mechanisms of iron oxide particles from the forced hydrolysis of ferric chloride solutions is an example of the application of this technique. Cryo-TEM (Figure 1.13) results from their study show how rod-like

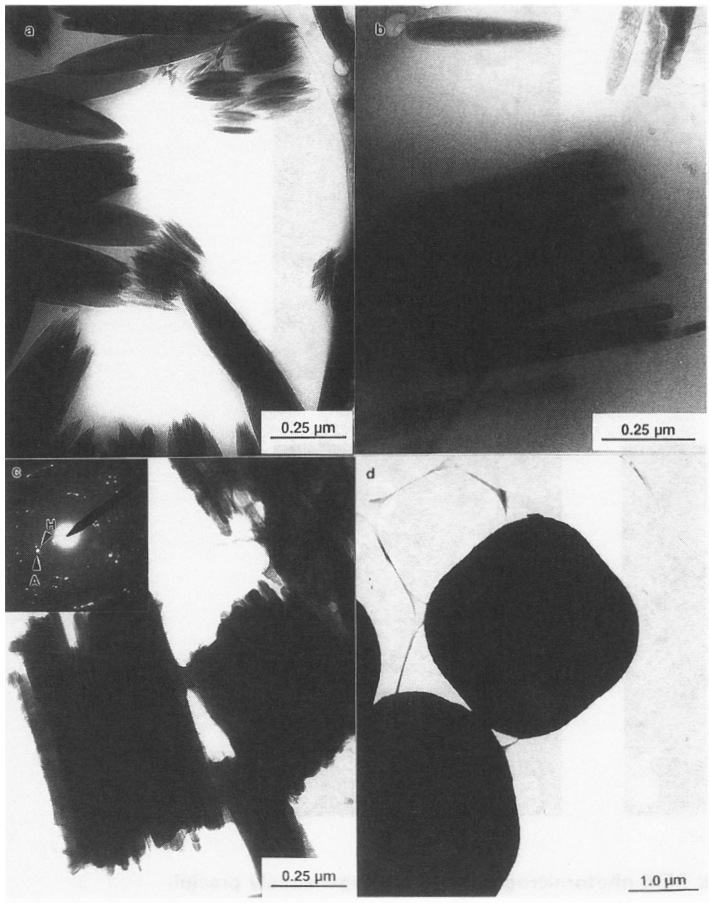

Figure 1.13 **Cryo-TEM and dried TEM photomicrographs illustrating the growth of hematite (α-Fe_2O_3) cubes by the aggregation and conversion of akaganeite (β-FeOOH) rods: (*a*) cryo-TEM of akaganeite particles formed after heating a 0.45 M $FeCl_3$ and 0.01 M HCl solution at 150 °C for 13 min; (*b*) cryo-TEM of akaganeite particles aggregated into rafts after 1 h of aging; (*c*) dried TEM sample after 3 h of aging (inset electron diffraction pattern of a single raft shows crystallographic alignment of the akaganeite rods [marked A] and the presence of hematite [marked H]); (*d*) dried TEM sample showing fully converted hematite cubes formed after 24 h of aging. (From Bailey et al.[32])**

particles of akaganeite (β-FeOOH) that form initially aggregate into rafts of rods with aging. Upon further aging, the more stable hematite phase (α-Fe_2O_3) nucleates within the rafts and eventually the akaganeite is completely converted to hematite. This example illustrates how crystalline primary particles can be formed by a controlled aggregation process.

Nucleation

Homogeneous nucleation is the formation of new particles from a solution as a result of supersaturation alone. For the process to be spontaneous, there must be a net reduction in free energy. In a supersaturated system, clusters of molecules are continuously forming and redispersing. Their free energy is made up of two parts—a volume free energy resulting from bond formation and a surface free energy resulting from the formation of a new surface. The surface free energy is always positive. For nucleation to occur, the volume free energy must be sufficiently negative to overcome the positive surface free energy so that the cluster will not decompose spontaneously. As the cluster size increases, the net free energy goes through a maximum value called the critical free energy of nucleation. In a sufficiently supersaturated solution, this barrier to nucleation can be overcome and stable nuclei are produced. Subsequent growth of these nuclei can further reduce the free energy of the system. Classical nucleation theory is derived based on these free energy considerations. The kinetics of nucleation can be described by combining the classical theory with expressions for particle growth kinetics (described in the previous section) that account for depletion of supersaturation.[33, 34]

Homogeneous nucleation dominates at high levels of supersaturation. New particles may be created in less supersaturated solutions by heterogeneous nucleation, secondary nucleation, and attrition. Heterogeneous nucleation, the formation of crystals on submicroscopic insoluble materials (preexisting surfaces), occurs in systems of moderate supersaturations; growth on substrate materials is energetically more favorable since it reduces the energy barrier by having to create less new surface. At lower levels of supersaturation, secondary nucleation can take place. It is induced by the presence of other crystals. The creation of new particles by attrition results from the mechanical breakage of larger crystals. Because ceramic applications require fine powders, solution processes are normally operated so that homogeneous nucleation dominates since it produces the highest nucleation rates (i.e., the greatest number of particles).

Characterization of the nucleation process is difficult because of experimental problems in accurately measuring supersaturation, in differentiating between nuclei and clusters in solution, and in measuring nuclei densities. The most common technique used to characterize nucleation is to mix solutions rapidly to induce precipitation (assuming that mixing time is much shorter than the induction time for nucleation). After allowing the nuclei to grow with no agglomeration, the particles are counted using various particle-sizing techniques, including image analysis of TEM, SEM, or optical photomicrographs, light scattering, and zone sensing. Figure 1.14 shows typical nuclei densities (N) as a function of initial supersaturation for the formation of crystalline $Ca(OH)_2$ and $Mg(OH)_2$.[35] The nuclei concentrations were determined by analysis of optical and TEM photomicrographs. The relationship between $\log N$ and $[\log S]^{-2}$ supports the occurrence of homogeneous nucleation.

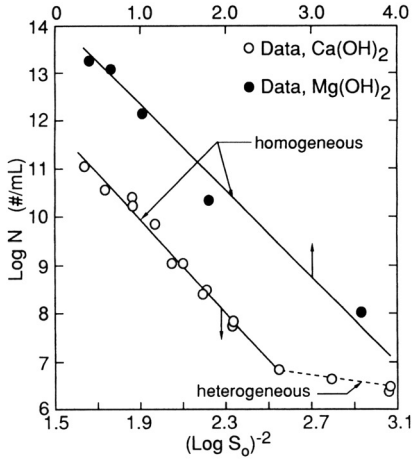

Figure 1.14 **Particle number density data as a function of initial supersaturations for the $Ca(OH)_2$ and $Mg(OH)_2$ systems. Regions indicative of homogeneous and heterogeneous nucleation are shown on the graph. (From Bandarkar et al.[35])**

The nucleation of particles leading to the formation of sols for the case in which polymerization reactions dominate (sol–gel) is shown schematically in Figure 1.15 for aqueous silicates. The figure shows how monomeric species react to form particles or gels, depending on the reaction conditions used. These processes are studied as a function of time using the same techniques described in the section on speciation. For example, the hydrolysis of zirconyl chloride has been followed by small-angle X-ray scattering to obtain information on cluster sizes in solution.[37]

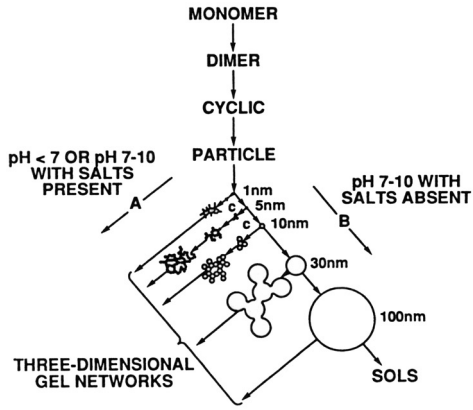

Figure 1.15 **Polymerization pathways for the formation of (*a*) sols and (*b*) three-dimensional gel networks in the aqueous silica system. (From Iler.[36])**

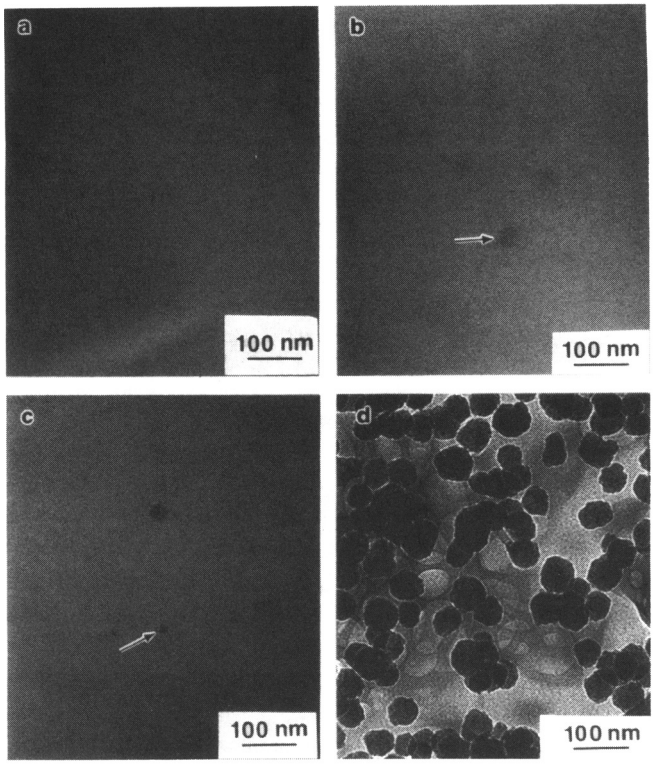

Figure 1.16 **Growth sequence observed by cryo-TEM for particles prepared from a solution of 0.17 M tetraethoxysilane (TEOS), 1.0 M H_2O, and 1.0 M NH_3 in *n*-propanol: (*a*) sample frozen 6 min into reaction, no particles visible; (*b*) sample frozen 16 min into reaction (arrow indicates low-density particle), average particle size 26 nm; (*c*) sample frozen 24 min into reaction (arrow indicates high-density particle), average particle size 20 nm; and (*d*) sample frozen 66 min into the reaction, average particle size 48 nm. (From Bailey and Mecartney.[38])**

Analysis of the scattering data showed that the expected tetramer with a radius of gyration of 4 Å polymerizes to form either spherical or rod-shaped particles, depending on $ZrOCl_2$ concentration.

Bailey and Mecartney[38] used cryo-TEM to determine the formation mechanism of colloidal silica particles from alkoxides. Figure 1.16 shows the nucleation and growth sequence of silica particles observed by cryo-TEM. At 6 min into the reaction there are no visible particles. Low-density, 26-nm-sized particles form after 16 min. These particles collapse into high-density, 20-nm particles after 24 min. Finally, the figure shows the particles have grown to an average size of 66 nm after 66 min. This information along with NMR results led to the nucleation and growth mechanism shown schematically in Figure 1.17.

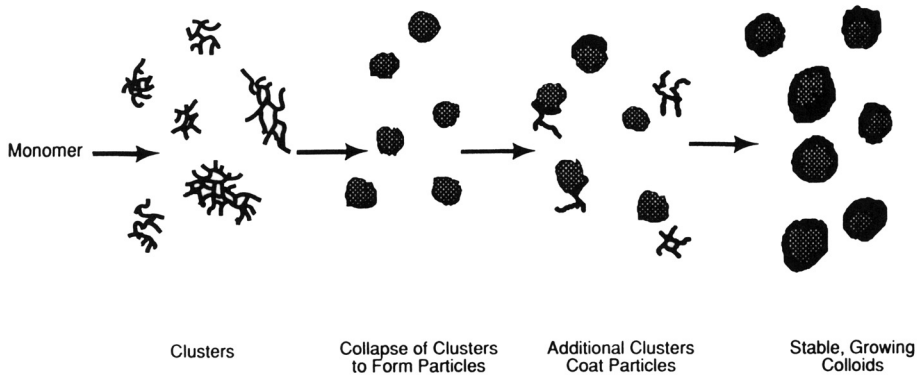

Figure 1.17 Growth mechanism for the formation of monodisperse colloidal silica particles from alkoxides. (From Bailey and Mecartney.[38])

Particle nucleation rate (B) is often related to crystal growth rates by the empirical expression, $B = KG^i$, where i is the order of the nucleation process and K is a constant.[39] At low to moderate supersaturation levels, the order of nucleation parameter is commonly about 2. Higher values of i have been found for systems operated under high supersaturation conditions, as shown in Figure 1.18 for continuously precipitated yttrium hydroxynitrate. The hydroxynitrate nucleation and growth rates values were obtained from analysis of particle size data measured by image analysis of TEM photomicrographs. In the figure, the hydroxynitrate results compare favorably to the power law expression found by Wey et al. for AgBr.[40] The values of i of 5.1 (yttrium hydroxynitrate) and 4 (AgBr) can be explained theoretically by assuming (1) the growth rates of large crystals follow a second-order dependence (i.e., $G = K(S\text{-}1)^2$); (2) nucleation is controlled by surface reaction of lattice ion-containing species; and (3) the dissolution of nuclei is controlled at the molecule integration step.[34] The results shown in Figure 1.18 illustrate the similarity in nucleation and growth of a simple sparingly soluble salt (AgBr) and a crystalline hydroxide in which hydrolysis reactions dominate.

Agglomeration

Agglomerates, or secondary particles (as they have been defined) nucleate from collisions between primary particles. They grow by further collisions with other primary particles or agglomerates. The kinetics of the aggregation process have been extensively studied and are described by incorporation of particle number density, particle size and morphology with system hydrodynamics, and interparticle forces (see the section "Chemical Synthesis of Powders").[41, 42] Agglomeration is studied using techniques already described to characterize particle surface properties and particle size distributions. For example, a study by Zukoski and co-workers[43] illustrates how particle surface charge can be used to inhibit agglomeration during particle growth. In their work, acid additions were used to control the surface

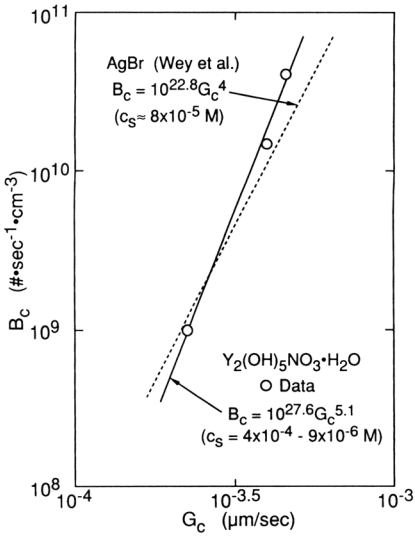

Figure 1.18 **Particle nucleation rate (B_c) as a function of particle growth rate (G_c) for the precipitation of yttrium hydroxynitrate at a pH between 7.8 and 8.8. Also plotted are the results of Wey et al.[40] for the precipitation of AgBr. The c_s values given in the figure are the approximate values of the concentration of metal ions at equilibrium for the two systems.**

charge of growing hydrous titanate particles formed by the hydrolysis of tetraethyl-ortho titanate in ethanol. Figure 1.19 shows TEM results for titanate particles formed with and without electrostatic stabilization. Without the addition of HCl, electrophoretic mobility measurements showed that the particles were very weakly charged, which allowed agglomerates to form (left side of Figure 1.19). Those agglomerates were relatively strong due to neck growth by solute deposition at primary particle contact points. When agglomeration was prevented through electrostatic stabilization (acidic conditions), monodisperse, spherical particles formed as shown in the right side of Figure 1.19.

1.4 Summary

The techniques used to characterize ceramic powders have been briefly reviewed. Powder physical characteristics such as particle size distribution, particle morphology, surface area, and state of agglomeration are of critical importance in establishing a powder's processability and activity toward sintering (see Chapter 5 by Ewsuk). Of equal importance is the characterization of a powder's chemical properties (i.e., stoichiometry, phase assemblage, impurity levels, etc.). The processes involved in particle formation by solution methods have been discussed by comparing the precipitation of sparingly soluble salts powder preparation approach with

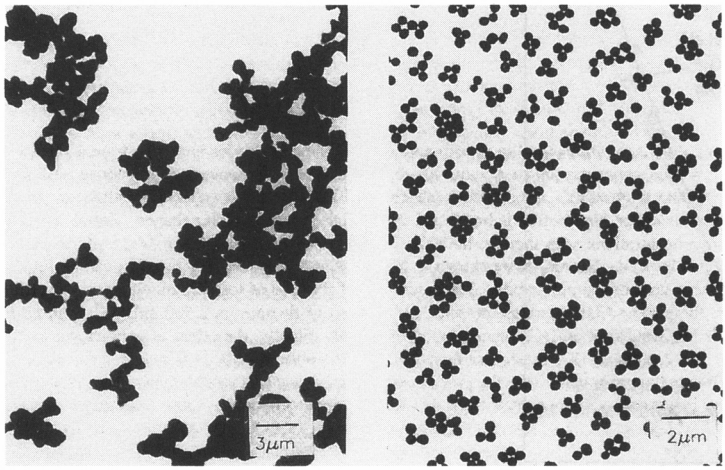

Figure 1.19 Particles precipitated from 0.05 M tetraethylortho titanate in ethanol containing (*left*) 0.4 M H_2O and (*right*) 0.25 M H_2O and 10^{-4} M HCl to electrostatically stabilize the suspension. (From Zukoski et al.[43])

the sol–gel synthesis method. As shown by the examples used in this chapter, a wide range of techniques are required to characterize both the solution chemistry that occurs during particle synthesis and the processes involved in particle nucleation, growth, and agglomeration.

References

1 J. S. Reed. *Introduction to the Principles of Ceramic Processing*. John Wiley & Sons, New York, 1988.

2 D. W. Richardson. *Modern Ceramic Engineering*. 2nd ed., Marcel Dekker, New York, 1992.

3 D. L. Johnson. In *Processing of Crystalline Ceramics*. (H. Palmour III, R. F. Davis, and T. M. Hare, Eds.) Materials Science Research, Vol. 11. Plenum Press, New York, 1978, pp. 137–139.

4 D. W. Johnson, Jr. *Am. Ceram. Soc. Bull.* **60** (2), 221–224, 243, 1981.

5 C. J. Brinker and G. W. Scherer. *Sol-Gel Science, the Physics and Chemistry of Sol-Gel Processing*. Academic Press, New York, 1990.

6 Ceramic Powder Processing Science series: *Ceramic Powder Science*, Advances in Ceramics, Vol. 21, (G. L. Messing, K. S. Mazdiyasni, J. W. McCauley, and R. A. Haber, Eds.) The American Ceramic Society, Columbus, OH, 1987; *Ceramic Powder Science II*, Ceramic Transactions, Vol. 1, Parts A & B, (G. L. Messing, E. R. Fuller, Jr., and H. Hausner, Eds.) The American

Ceramic Society, Columbus, OH, 1988; *Ceramic Powder Processing Science*, (H. Hausner, G. L. Messing, and S. Hirano, Eds.) Deutsche Keramische Gesellschaft, Cologne, Germany, 1989; *Ceramic Powder Science IV*, Ceramic Transactions, Vol. 22, (S. Hirano, G. L. Messing, and H. Hausner, Eds.) The American Ceramic Society, Columbus, OH, 1992.

7 Better Ceramics Through Chemistry series: *I, II*, and *III*, Vols. 32, 73, and 121, (C. J. Brinker, D. E. Clark, and D. R. Ulrich, Eds.) Materials Research Society, Pittsburgh, 1984, 1986, and 1988; *IV*, Vol. 180, (B. J. J. Zelinski, C. J. Brinker, D. E. Clark, and D. R. Ulrich, Eds.) Materials Research Society, Pittsburgh, 1990.

8 P. K. Gallagher. In *Ceramics and Glasses*. Engineering Materials Handbook, Vol. 4. ASM International, Materials Park, OH, 1991, pp. 52–64.

9 S. G. Malghan and A. L. Dragoo. In *Ceramics and Glasses*. Engineering Materials Handbook, Vol. 4. ASM International, Materials Park, OH, 1991, pp. 65–74.

10 T. Allen. *Particle Size Measurement*. 4th ed., Chapman and Hall, New York, 1990.

11 M. Ciftcioglu, M. Akinc, and L. E. Burkhart. *J. Am. Ceram. Bul*. **65** (12), 1591–1596, 1986.

12 C. A. Sorrell. In *Ceramics and Glasses*. Engineering Materials Handbook, Vol. 4. ASM International, Materials Park, OH, 1991, pp. 557–563.

13 C. E. Holcombe, C. C. Edwards, and D. A. Carpenter. "New Yttria Plasters." Y-2104. Report for the Dept. of Energy, Oak Ridge Y-12 Plant, Oak Ridge, TN, 1978.

14 P. Hiemenz. *Principles of Colloid and Surface Chemistry*. Marcel Dekker, New York, 1977.

15 D. H. Napper. *Polymeric Stabilization of Colloidal Dispersions*. Academic Press, New York, 1983.

16 R. J. Hunter. *Zeta Potential in Colloid Science*. Academic Press, London, 1981.

17 T. E. Wood, A. R. Siedle, J. R. Hill, R. P. Skarjune, and C. J. Goodbrake. In *Better Ceramics Through Chemistry IV*. Mater. Res. Soc. Vol. 180. (B. J. J. Zelinski, C. J. Brinker, D. E. Clark, and D. R. Ulrich, Eds.) Mater. Res. Soc., Pittsburgh, 1990, pp. 97–116.

18 C. F. Baes, Jr., and R. E. Mesmer. *The Hydrolysis of Cations*. John Wiley & Sons, New York, 1976, pp. 112–123.

19 G. Johansson. *Acta Chem. Scand*. **14**, 771, 1960.

20 G. H. Nancollas. In *Ceramic Powder Science II (Part A)*. Ceramic Transactions, Vol. 1. (G. L. Messing, E. R. Fuller, Jr., and H. Hausner, Eds.) The American Ceramic Society, Columbus, OH, 1988, pp. 8–22.

21 W. K. Burton, N. Cabrera, and N. C. Frank. *Phil. Trans. Roy. Soc. Lond. A*. **243**, 299, 1951.

22 P. Chiang and M. C. Donohue. *J. Colloid Interface Sci*. **122**, 230–250, 1988.

23 A. Packter. *J. Chem. Soc. A*. 859, 1968.

24 E. Thomas, D. Briedis, and J. A. Voigt. Presented at Annual Mtg. of AIChE. San Francisco, 5–10 Nov., 1989.

25 J. Mydlarz, J. Reber, D. Briedis, and J. A. Voigt. In *Particle Design via Crystallization*. AIChE Symposium Series, No. 284, Vol. 87. (R. Ramanarayanan, W. Kern, M. Larson, and S. Sikdar, Eds.) American Institute of Chemical Engineers, New York, 1991, pp. 158–169.

26 P. Meakin. In *On Growth and Form*. (E. Stanley and N. Ostrowsky, Eds.) Martinus-Nijhoff, Dordrocht, The Netherlands, 1986, p. 111.

27 D. W. Schaefer. *MRS Bull*. **8** (2), 22–27, 1988.

28 D. W. Schaefer and K. D. Keefer. In *Fractals in Physics*. (L. Pietronero and E. Tosatti, Eds.) North-Holland, Amsterdam, 1986, pp. 39–45.

29 E. Matijevic. *Acc. Chem. Res*. **14**, 22–29, 1981.

30 C. M. Flynn, Jr. *Chem. Rev*. **84**, 31–41, 1984.

31 M. A. Blesa and E. Matijevic. *Advances in Colloid and Interface Science*. **29**, 173–221, 1989.

32 J. K. Bailey, M. L. Mecartney, and C. J. Brinker. *J. Colloid Interface Sci*., in press.

33 R. Mohanty, S. Bhandarkar, and J. Estrin. *AIChE J*. **36**, 1536–1544, 1990.

34 P. Chiang, M. C. Donohue, and J. Katz. *J. Colloid Interface Sci*. **122**, 251–265, 1988.

35 S. Bhandarkar, R. Brown, and J. Estrin. *J. of Crystal Growth*. **97**, 406–414, 1989.

36 R. K. Iler. *The Chemistry of Silica*. Wiley, New York, 1979.

37 J. A. Jutson, R. M. Richardson, S. L. Jones, and C. Norman. In *Better Ceramics Through Chemistry IV*. Mater. Res. Soc. Vol. 180. (B. J. J. Zelinski, C. J. Brinker, D. E. Clark, and D. R. Ulrich, Eds.) Mater. Res. Soc., Pittsburgh, 1990, pp. 123–128.

38 J. K. Bailey and M. L. Mecartney. *Colloid and Surfaces*. **63**, 151–161, 1992.

39 A. D. Randolph and M. A. Larson. *Theory of Particulate Processes*. Academic Press, New York, 1971.

40 J. S. Wey, J. P. Terwilliger, and A. D. Gingello. *AIChE Symp. Ser. No. 193*. **76**, 34, 1980.

41 R. J. Hunter. *Foundations of Colloidal Science*, Vol. 1. Clarendon Press, Oxford, 1987.

42 W. B. Russel, D. A. Saville, and W. R. Schowalter. *Colloidal Dispersions*. Oxford University Press, Oxford, 1989.

43 C. F. Zukoski, M. K. Chow, G. H. Bogush, and J.-L. Look. In *Better Ceramics Through Chemistry IV*. Mater. Res. Soc. Vol. 180. (B. J. J. Zelinski, C. J. Brinker, D. E. Clark, and D. R. Ulrich, Eds.) Mater. Res. Soc., Pittsburgh, 1990, pp. 131–140.

2

Powder Preparation by Gas-Phase Techniques

CAROL L. JONES ADKINS

Contents

2.1 Introduction

Today, gas-phase processing plays an important role in the commercial production of a number of ceramic powders.[1] These include titanium dioxide, carbon black, zinc oxide, and silicon dioxide. The total annual output of these materials is on the order of 2 million tons.[1] The physical processes involved in gas-phase synthesis are typical of those involved in solution-phase synthesis—chemical reaction kinetics, mass transfer, nucleation, coagulation, and condensation.

Since the phenomena associated with ceramic processing begin with preparation of the starting powder, new techniques and methods for synthesizing high-purity, non-agglomerated, well-characterized, submicron powders having a narrow size distribution are constantly being sought. Gas-phase synthesis methods offer a number of benefits in the production of ceramic powders. These are: (1) direct formation of the particulate—calcining is not generally required as a separate step; (2) complex oxide formation is possible; (3) intimate mixing of the components; (4) high purity; (5) size distribution control; and (6) waste minimization. Perhaps the greatest disadvantages to gas-phase synthesis are the difficulty of the processes and their control, and lack of a full understanding of the relationship between the physical processes involved and their impact on the resulting product powder morphology.

Gas-phase powder synthesis techniques include aerosol precursor thermal decomposition, vapor precursor thermal decomposition, thermal plasma processing, glow discharge processing, rapid expansion of supercritical fluid solutions, laser-heating, and electron-beam evaporation methods. The scope of this chapter will be limited to the two thermal decomposition techniques, plasma processing, and the new, but exciting, powder synthesis technique using supercritical fluid solutions.

2.2 Powder Production by Thermal Decomposition Techniques

The term "thermal decomposition" describes those processes in which powder production results from the thermally driven decomposition or reaction of a precursor material. That precursor material may be delivered to the reactor either as an aerosol or a vapor. The two processes differ in that the formation of the powder is initiated by drying and reaction in the former, and nucleation and coagulation in the latter. Consequently, although the two processes and the associated apparatus appear quite similar at first glance, further inspection reveals that the physical phenomena driving them differ significantly.

Aerosol Precursor Processes

Processes characterized by the use of an aerosol precursor source are known by a variety of terms—spray pyrolysis, spray roasting, evaporative decomposition, and aerosol decomposition, to name a few. A schematic of a generic thermal decomposition apparatus is presented in Figure 2.1 and the aerosol precursor source is

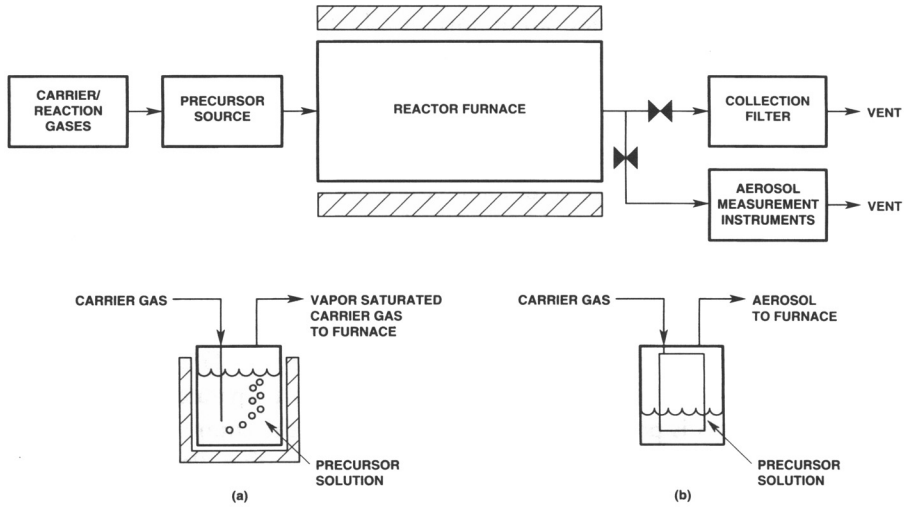

Figure 2.1 **Schematic of a generic thermal decomposition aerosol reactor: (*a*) vapor-feed precursor source and (*b*) aerosol-feed precursor source.**

represented in Figure 2.1*b*. A carrier gas flows through an aerosol generator, carrying the precursor material into the furnace reactor. Choice of the carrier gas depends on whether or not it is involved in the decomposition reaction of the precursor material. The aerosol generator used could be an atomizer, an ultrasonic generator, a nebulizer, or a spray gun. The only requirement is that the precursor material must be formed into an aerosol that can be carried into the reactor. However, the technique chosen affects the ultimate size distribution and number concentration of the product powder. The product aerosol is collected at the reactor outlet. For laboratory equipment, filtration is often an adequate collection method. If high aerosol throughput is generated, alternate methods may have to be explored.[2]

Solutions of precursor materials, be they ionic species, molecular species, or a suspension of a precursor powder, are converted to the desired ceramic powder product through the following steps: (1) formation of the initial precursor aerosol; (2) solvent evaporation and solute precipitation; and (3) thermal decomposition of the solute to a ceramic powder in the reactor (see Figure 2.2). As mentioned above, the nature of the initial precursor aerosol—both size distribution and number concentration—is determined by the aerosol generator chosen and affects the output aerosol. The concentration of the precursor solution also affects the size of the output aerosol since the "dry," unreacted particle can be no smaller than the size determined by the solution concentration. Advantages of the spray pyrolysis technique include precise control of the product stoichiometry and formation of loosely or un-agglomerated powders. Depending on the technique chosen for the initial precursor aerosol generation, high throughput is also possible. The primary disadvantage of this method is poor control of the particle morphology. Hollow or porous particles are often formed and can result in low green-body densities and subsequent densification problems.

A considerable amount of effort has gone into trying to understand the requirements for formation of solid particles,[3–6] since this incomplete understanding is one of the major impediments to widespread commercial use of spray pyrolysis processing. Typically, these studies have focused on control of the solvent evaporation

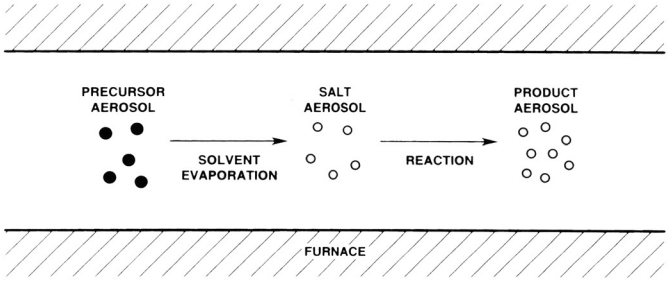

Figure 2.2 Schematic representation of product formation in a spray pyrolysis process.

process. As might be expected, evaporation behavior is highly dependent on the chemical system chosen. Leong[3, 4] determined that a nuclei-free solution, a solute having high solubility, and low drying rates favored the formation of solid particles. Zhang and Messing[5] studied the formation of zirconium oxide particles using a spray pyrolysis approach. A variety of precursor materials (e.g., zirconium acetate, zirconyl chloride, zirconyl nitrate, zirconyl hydroxychloride) having a range of solubilities in water was studied. An atomizer was used that had been characterized with respect to droplet size as a function of solution properties. The morphology of the powders produced was found to depend strongly on the relative saturation (the ratio of the initial solution concentration to the saturated concentration, C_i/C_s) of the solution. Those precursors having high relative saturations reached their solubility limit at the surface very quickly upon exposure to the furnace temperatures and formed a crust. The internal liquid volume then continued to evaporate, building up pressure, until the salt-encrusted droplet exploded. Precursors having a low relative saturation lost solvent and shrunk to smaller sizes before saturation levels were reached. Concentration gradients are more likely to be uniform in smaller particles since the diffusion distance is minimized. Lowering the initial solution concentration for a given precursor also was more likely to result in solid particles. The final oxide powder diameter, D_p, was predicted by the equation

$$\log D_p = \tfrac{1}{3}\log(C_i/C_s) + \log D_i + \tfrac{1}{3}\log A$$

where D_i is the initial aerosol diameter out of the atomizer and A is a constant that depends on the oxide yield of the precursor, the oxide and salt densities, and the particle porosity. Summarizing the results, high-solubility precursors, low-concentration solutions, and small initial particles have the greatest likelihood of producing solid particles. Clearly, optimization must occur for individual precursors because merely following these guidelines could lead to unacceptably low powder throughputs. An alternate approach was used by Ortega et al.[6] in the production of dense barium calcium titanate ($Ba_{0.86}Ca_{0.14}TiO_3$) powders. Hollow and porous particles were formed, but at sufficiently high reactor temperatures they were densified to solid spheres in the aerosol phase.

The work of Cesarano et al.[7] is another variation of the spray pyrolysis technique. Powders in the size range 0.1–1 μm were desired for use in forming mullite ($3Al_2O_3{\cdot}2SiO_2$) compacts. The starting precursors, boehmite platelets 70 × 40 nm and silica spheres of 30 nm, were too small for optimal processing. A boehmite/silica water suspension was nebulized into an air furnace at 700 to 1300 °C. The resulting particles (see Figure 2.3) were a composite of silica and alumina having the correct ratios for mullite and in the appropriate size range. This powder was then formed into a green body and fired to formed dense mullite by reaction.

The gas-phase spray pyrolysis technique is not limited to the production of oxide ceramic powders. Lindquist et al.[8] used this method to generate boron nitride powders by the decomposition of poly(borazinylamine) solutions. The process was

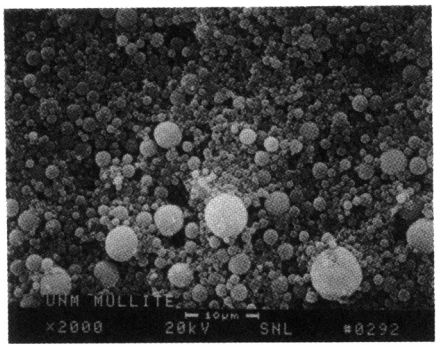

Figure 2.3 **SEM of mullite precursor, alumina–silica composite powders produced in an aerosol reactor at 1000 °C.[7]**

conducted under anhydrous and oxygen-free conditions at 1000 °C. Hollow, porous, amorphous boron nitride powders were produced. On heating to 1600 °C, dense, spherical, hexagonal boron nitride resulted.

Vapor Precursor Processes

The generic apparatus used in a vapor precursor process is very similar to that used in spray pyrolysis, except that the precursor material is introduced to the reactor as a vapor (see Figure 2.1, 2.1*a*). If the precursor is a liquid, carrier gas is typically bubbled through it. If the precursor is a solid, then the carrier gas is often passed through a heated, packed bed of the material. The vapor-laden carrier gas then flows to a furnace reactor, where thermal decomposition of the precursor occurs and particle formation results. Product powder is collected or measured at the reactor outlet. Flame processes also fall into the vapor precursor/thermal decomposition category of gas-phase powder synthesis. The only difference is that the thermal energy is provided by combustion as opposed to an external source.

The physical processes involved in the formation of a powder from a vapor precursor (see Figure 2.4) are (1) reaction of the gaseous precursor molecules to form product vapor, (2) supersaturation of the product vapor resulting in ultrafine clusters formed by homogeneous nucleation, (3) coagulation of the clusters, and (4) vapor condensation onto the clusters. The relative importance of these various processes determines the number concentration and size distribution of the product aerosol. Many researchers have modeled the powder formation process in order to better understand the interplay among these various steps.[9–13] For ceramic species, the critical stable nuclei, as defined by classical nucleation theory, typically are monomers, or single-product molecules. Nucleation and chemical reaction are therefore indistinguishable, and coagulation and condensation become the driving forces for particle growth.[10] High source or fast reaction-rate systems dominated by coagulation typically result in broad particle size distributions. On the other hand, runaway nucleation can be suppressed by controlling the reaction rate such that the initially formed particles act as "seeds" and scavenge the new molecules as they are formed. Narrower size distributions result since coagulation of clusters is

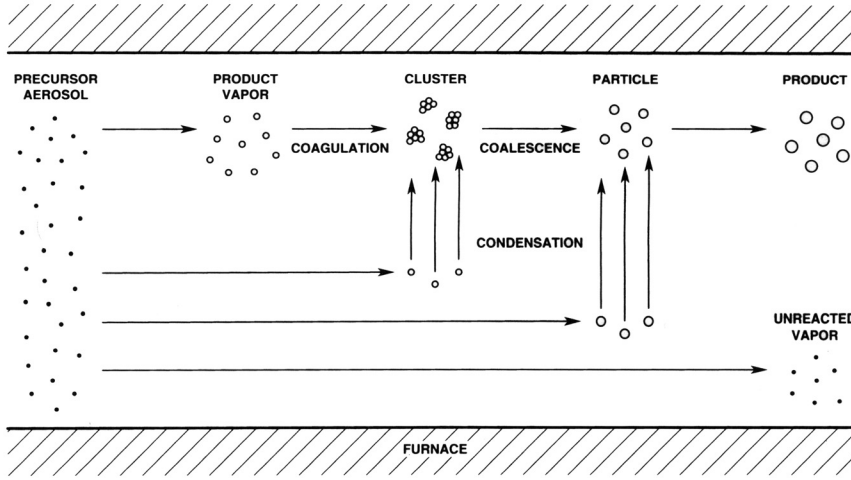

Figure 2.4 **Schematic representation of product formation in a vapor precursor process.**

no longer the primary mechanism of growth.[9] Whereas the number concentration of the product aerosol depends on the initial aerosol generation technique in the aerosol precursor method discussed in the previous section, for vapor precursor synthesis product number concentration is controlled by both the reaction/nucleation and coagulation rates. Clearly, powder production from vapor-fed thermal decomposition follows a very complicated mechanism. Only recently have design correlations based on the modeling results been developed to aid engineers in determining the relationship between process variables and powder characteristics.[11–13]

The commercial production of titania pigment is accomplished using titanium tetrachloride ($TiCl_4$) as the precursor. Upon reaction with oxygen, titania (TiO_2) and chlorine gas (Cl_2) are formed. This reaction is typically run at temperatures on the order of 1000 °C and can be performed either in an externally heated reactor or a combustion flame. Seed particles are used and the reaction is quenched to prevent excessive growth.[14] Note that these processing conditions are typical of those used when coagulation is to be minimized. Alternatively, the hydrolysis or pyrolysis reactions of titanium alkoxides to titania can be carried out at lower temperatures.[15–18] Okuyama et al.[18] studied the thermal decomposition of titanium isopropoxide ($Ti(OC_3H_7)_4$) and the subsequent formation of titania. The precursor alkoxide was vaporized and carried into the reactor furnace by an inert carrier gas. The carrier gas was carefully dried to avoid hydrolysis reactions. A variety of aerosol instrumentation was used to measure the resulting titania powder size distribution characteristics. Particle size distributions having a mean on the order of 0.01–0.06 μm and a total number concentration on the order of 10^8 particles/cm^3 were generated. The distribution shifted to larger sizes as the mean reactor temperature was increased from 400 to 600 °C. A broadening of the distribution

was also observed. This behavior is consistent with model predictions that as the source, or reaction, rate is increased, coagulation of clusters dominates particle growth. Particles produced at temperatures greater than 400 °C were found to be anatase titania. Amorphous particles were produced at temperatures less than 400 °C. Similar results were also found for the thermal decomposition of silicon tetraethoxide ($Si(OC_2H_5)_4$) and aluminum tri-sec-butoxide ($Al(OC_4H_9)_3$) into amorphous silica and amorphous alumina, respectively.

2.3 Powder Production by Plasma Techniques

Both thermal (equilibrium, high temperature) and glow discharge (nonequilibrium, low temperature) plasmas have been used in ceramic synthesis. Thermal plasmas are characterized by extremely high temperatures of both the gas and electrons. At these high temperatures, chemical reaction rates are much faster than those found in conventional processing.[19] Glow discharge plasmas are characterized by high electron temperatures, but only slightly elevated gas temperatures. Chemical reaction is driven by the interaction of electrons with the gas-phase species.[20]

A schematic of a generic, thermal rf-plasma reactor is shown in Figure 2.5. The precursor material is fed to the tail flame of the plasma through a water-cooled probe. The exact location of the injection depends on the nature of the precursor material. A solid precursor may be fed upstream of the plasma so that it can experience the high temperatures necessary for vaporization.[21] Indeed, the precursor may be gaseous, liquid, or solid. The hot gases are then quenched. Quench rates can be on the order of 10^3–10^8 K/s.[21] Powder formation begins as the gases cool and the quench rate affects the nature of the powder produced. The physical processes are similar to those involved in the vapor precursor/thermal decomposition process (see Figure 2.6). A gaseous precursor source is generated by the plasma. No particle formation occurs because the saturation ratio is low and the evaporation rate is high. Upon quenching, supersaturation of the product vapor results and nucleation occurs. Particle growth then proceeds as a result of coagulation and condensation. There is a transition region in which both evaporation and coagulation are important and modeling of the process has shown that this strongly affects the resulting particle size.[22]

Nitrides, carbides, and oxides have all been synthesized using thermal plasmas. Vogt et al.[23] used a thermal rf-plasma reactor to synthesize silicon carbide (SiC) powders. A pure argon plasma at roughly atmospheric pressure was used. The gaseous precursors, silane premixed with methane, were injected into the tail flame. Pure β-phase crystalline silicon carbide powders were formed. The primary particle diameter ranged from 10–60 nm, although agglomeration resulted in an apparent particle size of greater than 0.1 μm. By varying the precursor injection location within the tail flame, Vogt et al. altered the powder surface area. Reactant feed rates and quench gas properties also affected the mean particle size.

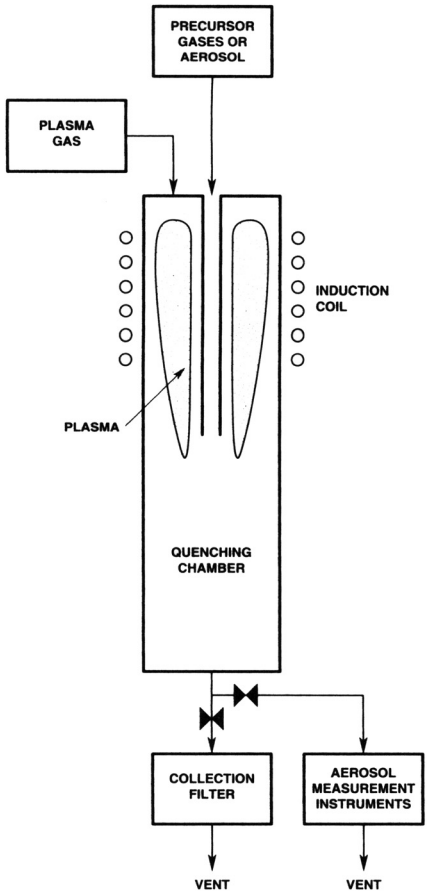

Figure 2.5 **Schematic of a generic thermal rf-plasma aerosol reactor.**

A slightly different approach was used by Suzuki et al.[24] to generate various metal titanate powders in a thermal rf-plasma reactor. Solutions of the appropriate metal salts were ultrasonically atomized and transported into the plasma using an argon carrier gas. For instance, a mixed solution of strontium nitrate ($Sr(NO_3)_2$) and titanium tetrachloride ($TiCl_4$) was used to form 10–50 nm strontium titanate ($SrTiO_3$) powders. In order to produce barium titanate ($BaTiO_3$) powders, solutions of barium nitrate ($Ba(NO_3)_2$) and $(NH_4)_2TiO(C_2O_4)_2$ were atomized and introduced into the reactor separately.

The powder formation process in a glow discharge plasma—chemical reaction, supersaturation, nucleation, growth by condensation and coagulation—is similar to that in a thermal plasma. However, as was mentioned earlier, the driving force for chemical reaction differs, and the processes of coagulation and condensation can be considered to occur under isothermal conditions. Ho et al.[20] used an rf glow discharge plasma to synthesize silicon nitride (Si_3N_4) precursor powders from silane (SiH_4) and ammonia (NH_3). The reactor pressure was maintained at approximately

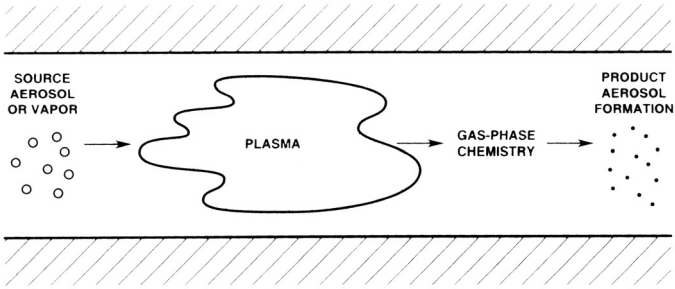

Figure 2.6 Schematic representation of product formation in a plasma process.

1 torr. A filter was used to trap the powder an the vacuum pump inlet port. It was found that the silicon to nitrogen ratio in the product powders could be varied by changing the silane to ammonia ratio in the feed gas. As synthesized, the powders contained a lot of hydrogen. The primary particles ranged from 10 to 200 nm in diameter and were highly agglomerated. No trends in the particle size with respect to processing parameters were observed. Heat treatment at 1600 °C for 8 h transformed the powders into crystalline silicon nitride.

2.4 Powder Production by Supercritical Fluid Techniques

A supercritical fluid is defined as a material above its critical temperature and critical pressure (see Table 2.1). These fluids are characterized by "gas-like" transport properties and "liquid-like" densities. They also offer a greatly enhanced solvating capability in comparison with gases. Recently, the use of supercritical fluids has been applied to the generation of ceramic powders.[26–28] The rapid expansion of a supercritical fluid solution results in the formation of a powder.[26, 27] As the pressure is reduced, the solubility of the solute decreases and supersaturation occurs. Stable

Solvent	Critical Temperature, °C	Critical Pressure, atm
Carbon dioxide	31	72.9
Ammonia	132.5	112.5
Water	374.1	218.3
Nitrous Oxide	36.5	71.7
Isopropanol	235	47
Ethanol	243	63

Table 2.1 Critical properties of common fluids.[25]

nuclei are formed and coagulation and condensation result in particle growth. The process is much like that which occurs in the vapor precursor/thermal decomposition process. The advantages of this process include (1) waste minimization since the process fluid is recyclable, (2) submicron powder formation, and (3) "nonequilibrium" products as a result of the rapid particle formation. Disadvantages include (1) the high-pressure operation and (2) a general lack of information and understanding about the behavior of supercritical fluids.

A schematic of a generic rapid expansion of supercritical fluid solutions (RESS) process is shown in Figure 2.7. The working fluid is compressed to a supercritical condition and flows to a vessel containing the bulk material that is to be dissolved. Solute-rich fluid flows to a collection chamber where it is allowed to expand through a nozzle. The gaseous working fluid passes out of the chamber. In the laboratory the gas is typically vented, although it could easily be recycled.

Matson et al.[27] have used the RESS process to produce silica powders from supercritical water. The solubility of silica in water at 500 °C and 1000 atm is 2600 ppm.[26] It was found that the size of the product depended strongly on the silica concentration in the supercritical fluid prior to expansion. Particle sizes ranged from 0.1 to 0.5 μm in diameter. The morphology of the particles was found to depend on the nature of the expansion nozzle—an orifice nozzle produced elongated particles, while a capillary nozzle produced spheres.

Pommier et al.[28] produced spinel, $MgAl_2O_4$, powders in supercritical ethanol. In this case, the supercritical fluid served as a reactive medium as opposed to merely a carrier fluid. A 0.1 M solution of the precursor material, $Mg(Al(OR)_4)_2$ where R is a sec-butyl group, was charged into a high-pressure reactor. The reactor was pressurized and heated. The vessel was then depressurized and the powders collected and dried. Primary particle sizes ranged from 0.04 to 0.2 μm, although due to agglomeration the light scattering measurements indicated particle sizes on the order of several microns. Low levels of residual organic were detected after drying and the particles were approximately 10–30% crystalline. After annealing at 1000 °C for an hour, complete crystallization was obtained.

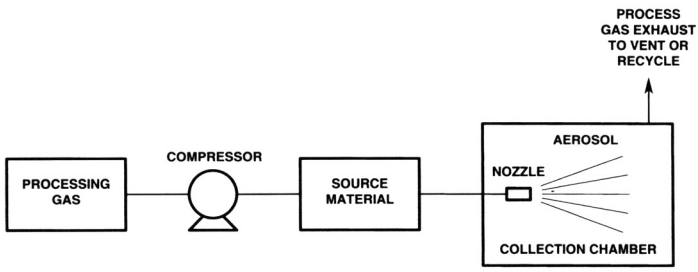

Figure 2.7 **Schematic of a supercritical fluid rapid expansion powder production apparatus.**

2.5 Powder Characterization

As with powders prepared using solution techniques, the most important physical properties of gas-phase generated ceramic powders are the size distribution, particle morphology, surface area, and degree of agglomeration. These properties can either be measured after the powder is collected, or while the powder is being generated using in situ techniques or traditional aerosol measurement instruments. The chemical properties of the powder can be determined using the techniques described in the previous chapter on solution techniques and need not be repeated here.

Gas-phase measurement techniques can be divided into two categories—in situ and extractive. Light-scattering techniques fall into the former category while traditional aerosol measurement instruments fall into the latter. Extractive techniques require that a sample of the aerosol-laden gas be removed from its environment and transferred to the location where the measurement is made. The transfer must be made without biasing the sample, which is often difficult to accomplish. In situ techniques can often overcome these limitations.

Instrument	Type	Property Measured	Approximate Size Range, μm	Approximate Concentration Range, particles/cm^3
Electrical aerosol analyzer	extractive	electrical mobility	0.003–1.0	10–10^7
Condensation nuclei counter	extractive	number	0.003–1.0	10^{-2}–10^7
Optical/laser particle counter	extractive	scattered light	≥0.3	$\leq 10^5$
Differential mobility analyzer	extractive	electrical mobility	0.005–1.0	$\leq 10^8$
Diffusion battery	extractive	Brownian diffusion	0.005–0.2	$\leq 10^8$
Phase doppler particle analyzer	in situ	frequency of Doppler-shifted scattered light	1–8000	$\leq 10^6$
Ensemble diffraction instruments	in situ	ensemble diffraction pattern	1–300	~10^4–10^9
Dynamic light scattering	in situ	degree of spectral broadening by Brownian motion	0.01–1	~10^4–10^9

Table 2.2 Selected on-line particle measurement instruments.

There have been many good reviews published on in situ[29, 30] and extractive[31–33] gas-phase measurement techniques and sampling and transport issues.[34] Listed in Table 2.2 is basic information about a number of on-line particle measurement instruments. It should be noted that specific instruments within a general class may or may not cover the whole diameter or number concentration ranges given. Manufacturer specifications should be sought. New measurement techniques (e.g., in situ Raman scattering[35]) are constantly being developed. Some of the issues important to ceramic powder synthesis include high particle concentrations (many of the extractive instruments cover only a limited concentration range), ultrafine particles, and fractal agglomeration (new techniques are being developed that allow traditional techniques to address the fractal issue[36]). The use of either extractive or in situ on-line particle measurement allows for greater process control as a function of time and the optimized production of a ceramic powder.

2.6 Summary

Many unique gas-phase powder synthesis techniques have been developed in the laboratory—aerosol precursor thermal decomposition, vapor precursor thermal decomposition, thermal plasma processing, glow discharge processing, rapid expansion of supercritical fluid solutions, laser-heating, and electron beam evaporation methods. All offer the advantages of clean processing, intimately mixed components, waste minimization, and a controllable particle size distribution. Those techniques that involve the nucleation process also offer the added benefit of high number concentrations. The commercialization of these technologies will depend on the added value these benefits bring to the ceramic powder product. Clearly, additional work is needed to understand these processes fully at a fundamental level and transfer these technologies to industry.

References

1 P. Stamatakis, C. A. Natalie, B. R. Palmer, and W. A. Yuill. *Aerosol Sci. and Technol*. **14** (3), 316–321.

2 R. C. Flagan. *Fundamentals of Air Pollution Engineering*. Prentice Hall, Englewood Cliffs, NJ, 1988, Chapt. 7.

3 K. H. Leong. *J. Aerosol Sci*. **18**, 511–524, 1987.

4 K. H. Leong. *J. Aerosol Sci*. **18**, 525–552, 1987.

5 S. Zhang and G. L. Messing. *J. Am. Ceramic Soc*. **73** (1), 61–67, 1990.

6 J. Ortega, T. T. Kodas, S. Chadda, D. M. Smith, M. Ciftcioglu, and J. E. Brennan. *Chem. Matls*. **3**, 746–751, 1991.

7 J. Cesarano III, R. Slilaty, and D. M. Smith. "Nanophase Processing of Mullite from Aerosol Generated Powders." Presented at the 94th Annual

Meeting of the American Ceramic Society, Minneapolis, Minnesota, 12–16 April 1992.

8 D. A. Lindquist, T. T. Kodas, D. M. Smith, X. Xiu, S. L. Hietala, and R. T. Paine. *J. Am. Ceramic Soc*. **74** (12), 3126–3128, 1991.

9 J. J. Wu, H. V. Nguyen, R. C. Flagan, K. Okuyama, and Y. Kousaka. *AIChE J*. **34** (8), 1249–1256, 1988.

10 G. D. Ulrich. *Comb. Sci. and Technol*. **4**, 47–57, 1971.

11 S. E. Pratsinis, J. D. Landgrebe, and S. V. R. Mastrangelo. *J. Aerosol Sci*. **20** (8), 1457–1460, 1989.

12 J. D. Landgrebe and S. E. Pratsinis. *Ind. Engr. Chem. Res*. **28**, 1474–1481, 1989.

13 J. D. Landgrebe, S. E. Pratsinis, and S. V. R. Mastrangelo. *Chem. Engr. Sci*. **45** (9), 2931–2941, 1990.

14 R. E. Kirk, D. F. Othmer, M. Grayson, and D. Eckroth. "Titanium Compounds (Inorganic)." In *Kirk-Othmer Encyclopedia of Chemical Technology*, Vol. 23, 3rd ed., John Wiley & Sons, New York, 1983, pp. 145–148.

15 F. Kirkbar and H. Komiyama. *Adv. Ceramic Matls*. **3** (5), 511–515, 1988.

16 F. Kirkbar and H. Komiyama. *Can. J. Chem. Engr*. **65**, 759–766, 1987.

17 H. Komiyama, T. Kanai, and H. Inoue. *Chem. Letters*. **8**, 1283–1286, 1984.

18 K. Okuyama, Y. Kousaka, N. Tohge, S. Yamamoto, J. J. Wu, R. C. Flagan, and J. H. Seinfeld. *AIChE J*. **32** (12), 2010–2019, 1986.

19 E. Pfender. *Pure & Appl. Chem*. **60** (5), 591–606, 1988.

20 P. Ho, R. J. Buss, and R. E. Loehman. *J. Matl. Res*. **4** (4), 873–881, 1989.

21 G. J. Vogt and L. R. Newkirk. "Thermal Plasma Chemical Synthesis of Powders." In *Proc. of the Symp. on High Temperature Matls-III*, (Z. A. Munir and D. Cubicciotti, Eds.) The Electrochemical Society, Pennington, NJ, 1985, p. 164.

22 S. L. Girshick and C. P. Chiu. *Plasma Chem. and Plasma Processing*. **9** (3), 355–369, 1989.

23 G. J. Vogt, R. S. Vigil, L. R. Newkirk, and M. Trkula. "Synthesis of Ultrafine Ceramic and Metallic Powders." In *Proc. of the 7th Intl. Symp. on Plasma Chem*. 1985, pp. 668–673.

24 M. Suzuki, M. Kagawa, T. B. Williams, Y. Syono, and T. Hirai. "Ultra-fine Particles and Thin Films of Oxides Formed by the Spray-ICP Technique." In *Ceramic Developments, Matls. Sci Forum*, Vol. 34–36. (C. C. Sorrell and B. Ben-Nissan, Eds.), Trans Tech Publ. Ltd., Switzerland, 1988, pp. 791–795.

25 *CRC Handbook of Chemistry and Physics*. 56th ed. (R. C. Weast, Ed.) CRC Press, Cleveland, 1975, pp. F85–F86.

26 D. W. Matson and R. D. Smith. *J. Am. Ceramic Soc*. **72** (6), 871–881, 1989.

27 D. W. Matson, J. L. Fulton, R. C. Petersen, and R. D. Smith. *Ind. Engr. Chem. Res*. **26**, 2298–2306, 1987.

28 C. Pommier, K. Chhor, J. F. Bocquet, and M. Barj. *Matl. Res. Bull*. **25**, 213–221, 1990.

29 D. J. Rader and T. J. O'Hern. "Optical Direct Reading Techniques: In Situ Sensing." In *Aerosol Measurement: Principles, Techniques, and Applications*. (K. Willeke and P. Baron, Eds.), Van Nostrand Reinhold, in press.

30 J. E. Martin and A. J. Hurd. *J. Appl. Cryst*. **20**, 61–78, 1987.

31 S. V. Hering. *Air Sampling Instruments for Evaluation of Atmospheric Contaminants*. 7th ed., American Conference of Governmental Industrial Hygienists, 1989.

32 S. K. Friedlander. *Smoke, Dust and Haze*. John Wiley & Sons, New York, 1977, Chapt. 6.

33 D. A. Lundgren, F. S. Harris, Jr., W. H. Marlow, M. Lippmann, W. E. Clark, and M. D. Durham, Eds. *Aerosol Measurement*. University Presses of Florida, Gainesville, FL, 1979.

34 J. E. Brockmann. "Sampling and Transport of Aerosols." In *Aerosol Measurement: Principles, Techniques, and Applications*. (K. Willeke and P. Baron, Eds.) Van Nostrand Reinhold, in press.

35 G. Schweiger. *J. Aerosol Sci*. **21** (4), 483–509, 1990.

3

Formation of Ceramic Films and Coatings

DIANE E. PEEBLES

Contents

3.1 Introduction

Ceramic films and coatings are used for a wide variety of purposes, all of which take advantage of the special properties of ceramic materials. The insulating nature of most ceramic films and coatings makes them a natural choice for electrical isolation in systems ranging from the microscopic, as in microelectronic circuits, to the massive, as in wires and heater elements. The refractory nature of ceramic coatings gives added protection to coated materials in high–temperature environments. The chemical inertness exhibited by many ceramic materials means that ceramic films and coatings may be used to protect materials from reaction and corrosion in hostile environments. The extreme hardness of many ceramic coatings provides excellent mechanical protection against wear and deformation, while the natural lubricity of ceramic surfaces often allows elimination of additional lubricants for surfaces in moving contact. In fact, the combination of these properties, and others specific to particular ceramic materials, produces protective coatings of exceptional performance in a wide variety of applications. To date, the major limitation of applications of ceramic coatings is the inability to produce adherent coatings with the desired properties.

In this chapter, some of the approaches for ceramic film deposition and analysis are discussed. Section 3.2 discusses the most common methods of depositing ceramic films and coatings: physical vapor deposition (PVD), chemical vapor deposition (CVD), solution and sol–gel techniques, and thermal spray processing. Formation of hard carbon coatings (primarily diamond and diamond-like films) are discussed as a special topic. The remaining three sections of the chapter cover general characterization and analysis of ceramic films and coatings, broadly categorized into physical, chemical, and mechanical characterization. Since ceramic coatings are utilized for such a wide range of applications, numerous other types of analyses may be appropriate, including electrical resistivity, thermal conductivity, chemical reactivity, and optical and magnetic properties. However, due to the space limitations of this chapter, the discussion is limited to properties that are important to almost every ceramic film and coating. References 1 and 2 are excellent books for general film and coatings information, especially for details of the basics of PVD and CVD film deposition processes. References 2 and 3 are also good sources for information of PVD and CVD deposition processes, with ceramic film example applications, including hard carbon coatings.

3.2 Film Deposition and Coating Processes

Physical Vapor Deposition

Physical vapor deposition (PVD) processes use vapor transport (usually in a vacuum) of a material from a solid or liquid source onto a substrate to form a coating. The most common PVD methods used to produce ceramic coatings include sputtering and ion-plating techniques and plasma processes utilizing compound ceramic source targets. Laser ablation and evaporation techniques may also be used to produce ceramic coatings. However, PVD methods yield primarily line-of-sight coverage and may have difficulties coating substrates with complex shapes. In addition, because many ceramic materials do not vaporize or sputter congruently, the product film often will not have the same stoichiometry as the starting target material. Such films will typically be deficient in the anodic species (for example, in oxide films, the oxygen concentration may end up being less than stoichiometric in the coated product). Often this problem may be corrected by backfilling the deposition chamber with a small amount of the deficient species (oxygen gas, for oxide films), relying on chemical reactions to return the coating composition to stoichiometric values. The major advantages of PVD processes are the very wide range of deposition rates that are obtainable, as well as the ability to form dense films at relatively low substrate temperatures. In addition, coatings may be formed with nonequilibrium compositions, since the coating composition is generally a function of the target makeup and the ambient background gas during deposition.

Chemical Vapor Deposition

Chemical vapor deposition (CVD) processes, on the other hand, rely on chemical reactions to produce the desired film composition. The starting materials in a CVD reaction are often reactive organometallic gases. These gases react on or near the substrate surface to produce the desired film composition. The CVD process may be very simple, relying only on thermal reaction of the starting materials, or it may be activated by any of the methods utilized for PVD processing, such as hot filaments, ion sputtering, and plasma processing. Because CVD processes do not require line-of-sight vapor transport, complex substrates may often be coated, especially if no activating processes are utilized. However, since the film deposition processes rely on chemical reactions to form the desired coating composition, it is more difficult to produce coating compositions that vary from equilibrium values. Although this may restrict the choice of coating compositions, it allows reproducible film composition, even if some of the deposition parameters vary slightly from specified values. The major disadvantage of CVD processes is the high substrate temperature required for film deposition. Although the substrate temperature can be lowered if activating processes are used, the rate of film deposition and the ability to coat complex shapes are enhanced if the substrate temperature is raised.

Solution and Sol–Gel Techniques

Some ceramic coatings may be prepared by solution or sol–gel deposition techniques. In the simplest case, the film precursors are dissolved or suspended in a fluid solution. The solution can be sprayed or brushed onto the substrate or the substrate can be dipped into the solution. The solvent is then evaporated and the ceramic coating is condensed to its final structure. Postdeposition processing may include further chemical treatments designed to change the bonding or structure of the coating. The film precursors may be soluble or may be very fine insoluble particles colloidially dispersed in the fluid mixture to give film deposition by solution techniques. For deposition by sol–gel techniques, the film precursors are inorganic polymers where specific condensation reactions may be tailored to produce the desired coating properties. These methods provide a very inexpensive and relatively rapid way to coat materials; large or complex substrates may be coated with ease. The thickness of the coating is controlled by the concentration of the coating precursors in the solution and by the method of supplying the solution to the substrate. For sol–gel techniques in particular, variation in the structure of the deposited film is controlled by precursor variables, including molecular weight (or particle size), structure (branched versus straight), reactivity, surface tension of the solvent, and the rate of evaporation of the solvent. Although only limited types of coatings may currently be deposited, the variety of available coating types is rapidly increasing as new techniques are developed. The reproducibility of the deposition process relies on careful preparation of the precursors and solutions and on the

ability to apply the fluid solution consistently to the substrate. A short review of the basics of sol–gel deposition is given in Reference 4.

Thermal Spray Processing

Thermal spray processing techniques are of great interest for the rapid deposition of coatings to large substrates in industrial applications. Thermal spray processes include flame, arc, detonation, and plasma spray techniques. The main difference between these techniques is the method of generating heat in the spray head—combustion or chemical reaction, electric arc, controlled explosion, and gas plasma, respectively. In each case, powder precursors are fed into the spray head where the local temperature is in excess of 3000 °C. The heated precursor material is then accelerated onto the substrate at particle velocities of 90 m/s (flame spraying) to over 700 m/s (detonation spraying). The high temperatures and high kinetic energies of the arriving particles allow formation of adherent, dense coatings. The coating properties are directly related to the type of spray technique used, and adjustment of spray parameters allows some modification of coating properties, including density, strength, adhesion, composition, and surface finish. These techniques may produce coatings rapidly; their real value lies in the ability to coat very large substrates. In addition, quite thick coatings may be readily applied. Coating composition is limited primarily by the availability of powdered precursor materials. However, the substrates must be able to survive the physically agressive deposition conditions, including the very high temperatures and high kinetic energies of the incident particles. Thermal- or shock–sensitive coatings and substrates cannot be deposited or used, respectively, with these techniques. Additionally, fine–tuning of the composition and structure of the coating is difficult. A brief review of thermal spray techniques is given in Reference 5.

Hard Carbon Coatings

Deposition of hard carbon coatings is treated here as a special topic because of the enormous interest in these coatings today. Ideally, these films contain only carbon and varying amounts of hydrogen; the only difference between the forms of hard carbon coatings is how the carbon is chemically bonded in the film. This difference in bonding presents special problems in the analysis of these films, since elemental analysis can detect only impurities in the films, and chemical bonding analysis must be used to properly identify the particular phases in the coating. Several major forms of hard carbon coatings are recognized today, ranging from amorphous carbon film, which is predominantly an sp^2-bonded material with no long-range order, through diamond–like carbon, to diamond coatings with long-range sp^3 bonding. The hydrogen content of these films can vary dramatically, from near 30% (atomic) in diamond-like carbon to less than 1% in diamond films. These changes in bonding give rise to some very dramatic differences in properties of the coatings. For example, amorphous and diamond-like carbon coatings are typically very fine-grained,

with very smooth surface finishes possible. On the other hand, diamond coatings are typically composed of very large, well-defined crystal grains, with many well-developed facets. This extreme crystallinity produces a coating that is very rough, with many sharp cutting edges where the facets come together. Hard carbon coatings have historically been produced by activated CVD processes, using gas phase mixtures of hydrocarbons (typically methane) and hydrogen for starting materials. The process activation is typically by a hot filament or a plasma, depending on the type of hard carbon coating to be obtained. However, many novel deposition methods have also been applied with limited success, including the full technological spectrum from laser activation to deposition from an oxy-acetylene flame torch. Reference 6 reviews the deposition and analysis of diamond and diamond-like carbon films.

3.3 Physical Characterization

Density, Porosity and Voids

Since ceramic films and coatings are most often used for protective overcoats or optical applications, it is usually important to be able to deposit films with a minimum of porosity and voids. If the voids and pores are large, they can easily be seen with scanning electron microscopy (SEM). Transmission electron microscopy (TEM) is commonly used to evaluate voids and pores on a smaller scale. This is illustrated in Figure 3.1, which shows TEM plan and cross-sectional views for a

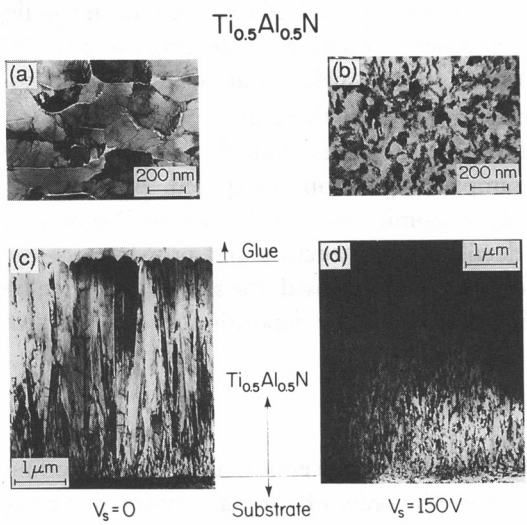

Figure 3.1 **Transmission electron microscope images in plan view (*a* and *b*) and cross-sectional view (*c* and *d*) of a $Ti_{0.5}Al_{0.5}$ N film prepared with no substrate bias (*a* and *c*) and with a 150 V substrate bias (*b* and *d*) during deposition.[7]**

$Ti_{0.5}Al_{0.5}N$ coating deposited with and without a substrate voltage bias during deposition by a PVD sputtering process.[7] The substrate bias caused the microstructure to change from columnar to equiaxed, with a corresponding decrease in grain size and void volume. Coating density is somewhat harder to measure. If the coating can be removed from the substrate, conventional density measuring techniques (like sink or float measurements) can be used. If the density is to be measured with the coating in place, more indirect methods must be used. If the weight gain attributed to the coating can be measured, then a determination of the area and thickness of the coating (see the section on Thickness) will allow the density of the coating to be calculated. If the weight gain cannot be readily measured, then a technique such as Rutherford backscattering spectroscopy (RBS) may be used to determine the total mass density per unit area (grams per square centimeter) of the coating. If this measurement is combined with an evaluation of the coating thickness, then an estimate of the volume density may be obtained.

Morphology

The most common tool for examining surface morphology of the deposited coatings is SEM. Because of the very large depth of field and the ability to examine the surface at a very large range of magnifications, SEM enables the analyst to examine in detail the morphology of all but the most fine-grained of films. Examination by SEM often allows determination of the growth mode, grain size, and structure, and other details relating to the physical appearance and topography of the surface. As an illustration, Figure 3.2 shows the evolution of the surface morphology of hard carbon coatings as a function of the composition of the feed gas mixture.[8] It should be noted that most ceramic coatings will need to have a conducting overcoat deposited before SEM analysis to prevent problems of surface charging during analysis.

If films with smaller grain sizes are to be examined, there are a couple of common alternative techniques for analysis. TEM can measure there are fine details of the surface morphology, but extensive sample preparation is required. Alternatively, scanning tunneling microscopy (STM) or atomic force microscopy (AFM) maybe used, depending on the particular details of the structure and properties of the surface to be examined. Depending on the technique used, the surface can often be examined directly with these techniques, without the deposition of a conductive overcoat.

Thickness

The desired thicknesses of ceramic coatings can cover an enormous range, depending on the application. Although thicknesses on the order of 1 μm are common, a coating as thin as 10 nm or as thick as 0.1 mm may be desired. The thicker coatings may be measured using standard high-precision manufacturing metrology tools. The more conventional film thicknesses of several hundred nanometers to about 100 μm are most commonly measured through a variety of stylus instruments (surface

profilometry) or microscopy techniques (SEM, TEM, STM, and AFM are the most common). The film thicknesses at the lowest end are most easily measured by optical methods, including primarily interferometry and elipsometry techniques. Two recent papers review the various methods of measuring surface thickness, roughness and topography and discuss the application of non-optical techniques[9] and optical techniques.[10] Reference 1 also gives basic descriptions of optical and specialty (magnetic and electrical) techniques for coating thickness determinations.

Surface Finish

Three major aspects of surface finish are important to ceramic films and coatings. The first aspect is that of surface roughness of the deposited coating. For some applications, the roughness of the coating is not an issue and the user can accept

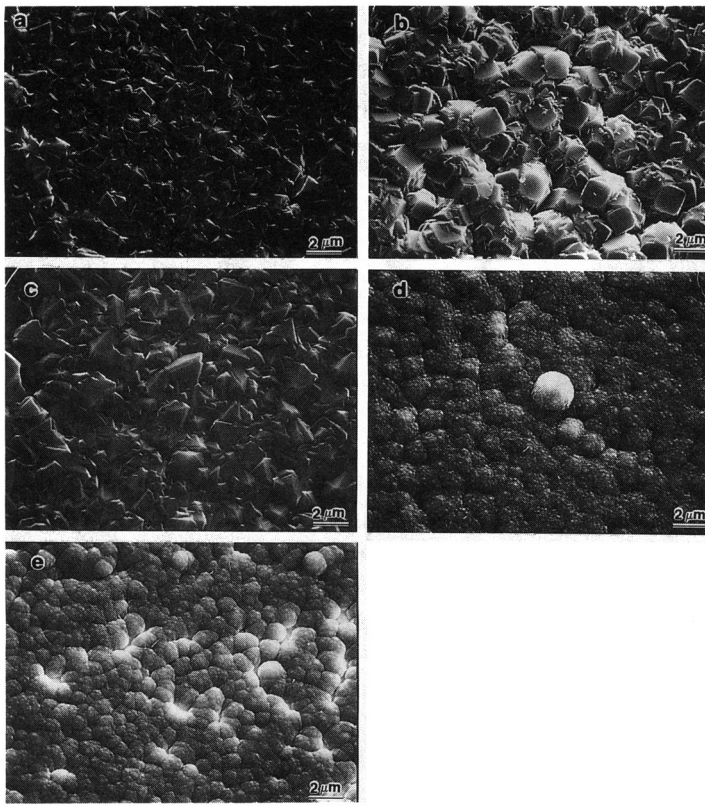

Figure 3.2 **SEM images of hard carbon coatings as a function of the composition of the feed gas. Each of the images shows the surface of the coating resulting from a feed gas composition consisting of (*a*) 0.1%, (*b*) 0.5%, (*c*) 1.0%, (*d*) 1.5%, and (*e*) 2.0% methane by volume in hydrogen.[8]**

whatever the deposition technique provides. However, for some film applications the surface roughness of the coating is of primary importance, especially for coatings used in electronics, optical, tribological, or decorative applications. Surface roughness is closely related to the coating morphology, and may be quantitatively measured by the techniques used to measure coating thickness. Surface roughness may often be controlled by variations in the deposition method. A second aspect of surface finish potentially important to ceramic coatings is color, especially if the coating is to be used for optical or decorative purposes. Color is primarily affected by the coating composition and may often be modified by adjusting the film composition or adding small amounts of color-affecting dopants to the coating. Color may also be affected by the coating thickness and roughness, especially for very thin coatings. The final major aspect of surface finish is that of conformality of the coating. Many applications (especially electronics, optical, and tribological) often require very controlled coating thicknesses, even around corners and on complex substrate shapes. Deposition techniques vary widely in their ability to coat complex-shaped substrates to produce a uniform, conformal coating. Modification of the deposition method or the fixturing used to hold the substrates during deposition may be required to produce a conformal coating.

3.4 Chemical Characterization

Elemental Analysis

Elemental analysis plays a very important role in characterizing ceramic coatings because the properties obtained for these coatings can often vary dramatically with composition. Elemental analysis is used to determine the composition of the coating, to judge the levels of dopants or modifiers added to ceramic films or coatings, and to determine the concentration and types of chemical impurities. This is especially important since the presence of even low levels of impurities may drastically change the properties of the coating (consider the very dramatic effects of adding only very small amounts of dopants to silicon). Impurities can result from contamination before or during film deposition, from improper handling after deposition, from exposure of the coating to reactive environments, or from processes used to modify the material or finish the surface after deposition (for instance, sintering, polishing, or drying). All of the usual surface and thin film analytical techniques are applicable to ceramic coatings. Many thin film analytical techniques provide information about elemental distribution as a function of depth into the coating, and similar types of information may be obtained from surface analytical techniques combined with depth profiling.

Auger electron spectroscopy (AES) provides qualitative elemental information relatively quickly. That it also allows fine spatial resolution and elemental mapping of the surface (known as scanning Auger microscopy, or SAM) enhances the information gained. However, quantitative elemental analysis can be complicated by

overlapping spectral lines and sensitivity factors that are dependent upon the chemical matrix present. In addition, some films or coatings may be susceptible to degradation or modification upon exposure to the electron beam necessary for analysis. Films containing halide ions are notorious for loss of the halide upon electron-beam irradiation, for example. Finally, because most ceramic films and coatings are electrically insulating, electrical charging caused by the incident electron beam can cause the peaks to broaden to the point that the spectrum literally disappears. A conductive overcoat on the film can alleviate the charging problems, if it can be tolerated, although it will modify the observed composition.

X-ray photoelectron spectroscopy (XPS), also known as electron spectroscopy for chemical analysis (ESCA), is much less sensitive to sample charging problems since the incident X-ray beam contributes no charge accumulation and the low-photon absorption cross section results in greatly reduced numbers of electrons emitted from the sample. Charging can still be a problem on highly insulating samples, but can often be compensated for or nullified with relative ease. Since the X-ray absorption cross section is much less than that for electrons, sample damage attributable to the incident radiation is also greatly reduced relative to AES analysis. However, some samples, primarily metastable or unstable oxides, are susceptible to reduction under X-ray bombardment. Quantitative elemental analysis is more straightforward with XPS relative to AES, because of the reduction in changes of sensitivity factors with the chemical matrix. However, the same factors that benefit the above factors also produce a much slower data acquisition time and spatial information is virtually impossible in most XPS systems. Even the new small-spot-size imaging XPS systems have only very limited spatial resolution relative to AES, and the time to produce an image with good signal to noise statistics can be orders of magnitude above that required for AES.

Secondary ion mass spectrometry (SIMS) can have similar speed and spatial resolution to those obtained with AES, including the ability to provide elemental mapping information. The strength of SIMS lies in its abilities to detect elements at extremely low concentration limits (orders of magnitude below AES and XPS) and—the only general utility surface analytical technique able to do so—to detect hydrogen directly. However, quantitative elemental analysis is extremely difficult with SIMS because of a strong dependence of elemental sensitivity factors on the chemical matrix. In addition, because of the very high flux of incident ions, SIMS is usually considered a destructive analysis technique. Problems may occur with sample charging for insulating films or coatings, but can often be eliminated by adjusting the ion current density or by adding supplementary coincidental electron bombardment. Sample modification under ion-beam bombardment can—and readily does—occur, but does not generally affect the detected elemental distribution other than modifying the relative elemental sensitivity factors.

Electron probe microanalysis (EPMA), X-ray analysis (energy dispersive, EDX, or wavelength dispersive, WDX), and X-ray fluorescence spectroscopy (XRF) are

all thin film techniques that may be used to gain elemental information. These techniques use electron or X-ray bombardment of the sample to produce X-rays that are analyzed to yield elemental composition of the coating. The energies of the incident electrons or X-rays are quite high, with well-known absorption cross sections enabling accurate quantitative elemental analysis. Sample damage under bombardment is often reduced because of the reduced absorption of the high incident energies. Sample charging is not a problem with XRF, but must be eliminated for EPMA, EDX, or WDX by the application of a conductive overcoat on the sample. These techniques analyze quite deeply into the sample (up to several micrometers), relative to surface analytical techniques because of their high incident energies. Spatial resolution is limited by the spread of electrons through scattering in the film or coating for EPMA, EDX, and WDX, and by the inability to focus X-rays for XRF. Elemental mapping may be obtained, but at lower spatial resolution than is available for SAM or SIMS. All of the X-ray detection techniques are limited in elemental detection, since elements with atomic numbers below 8 (oxygen) can be detected only with special equipment like windowless detectors.

Rutherford backscattering spectrometry (RBS) is another thin film technique that often provides useful elemental analysis information of a sample by detecting the number and energy of elastically scattered high-energy ions (usually alpha particles, $^4He^+$). The energy of the detected ions is determined by the element the ion was scattered from, with modifications for the depth of that atom. The number of detected ions as a function of energy is determined by the number of scattering atoms of a particular element as a function of depth. Since the interaction of very high-energy ions with materials is well understood, RBS produces good quantitative elemental analysis as a function of depth within the sample. Since the interactions of the high-energy ions with the material are small, RBS is usually considered to be nondestructive, although some ion-induced damage may occur for particularly sensitive materials. However, the technique has trouble detecting light elements (similar to the limit discussed in the previous paragraph) and may have difficulty discriminating elements of similar mass as a function of depth. In addition, the technique requires an accelerator to produce the incident high-energy ions.

Directly related to RBS, elastic recoil detection (ERD) provides equivalent information for hydrogen in materials. In this case, experimental conditions are adjusted so that hydrogen atoms scattered by the incident high-energy $^4He^+$ particles are detected. This technique provides good quantitative analysis of hydrogen concentrations directly as a function of depth in the film. While the amount of hydrogen contained in most ceramic films is not large, the amount of hydrogen contained in hard carbon coatings is critical to the performance and properties of the coatings. Figure 3.3 illustrates the distribution of hydrogen in a variety of hard carbon films.[11] The ERD technique is not only able to show up small differences in hydrogen concentration in the various films, it is also able to show that the hydrogen concentration is always higher on the surface for these films, a result of hard carbon deposition techniques that cap dangling carbon bonds with hydrogen atoms.

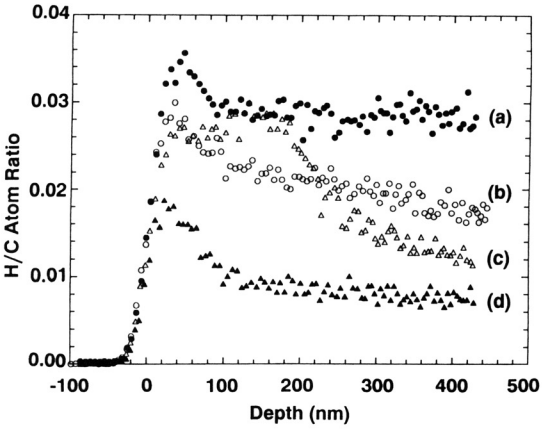

Figure 3.3 **Hydrogen/carbon atom ratio in hard carbon coatings as a function of depth into the film, as measured by elastic recoil detection. The different curves are for different film samples.[11]**

Chemical State Analysis

The previous section discussed the importance of elemental analysis in determining film properties. However, ceramic films and coatings may exhibit a range of chemical bonding structures for identical elemental compositions. The specific type of chemical bonding within the coating may dramatically affect the properties of the film. An extreme, but common, example is hard carbon coatings, where the type of chemical bonding fully determines the properties of the film and the elemental composition does not vary over the entire range of possible film structures. In addition, films with different chemical bonding states may present very different behavior in terms of the protective qualities so often desired of ceramic coatings. Consequently, a very important step in the analysis of deposited coatings can be the determination of the chemical bonding states present.

Most ceramic films involve compounds of light elements. This is a great advantage with most surface analytical techniques, because information from the valence bonding levels is readily available and spectral changes with chemical state are often quite pronounced. This enables the use of the usual surface analytical techniques to obtain chemical bonding information. One of the best techniques for obtaining chemical bonding information is XPS because of the great amount of information that can be obtained from chemical shifts and peak lineshapes. However, the reader is referred to the detailed technique descriptions in the lead volume of this series, the *Encyclopedia of Materials Characterization*, or to any of the many good literature reviews available for information on the chemical bonding applications of XPS, so that the limited space available here may be used to address alternative techniques.

Although AES is usually considered only as an elemental analysis technique, Auger spectra may show significant changes in lineshape with chemical bonding. Since the AES lineshapes arise from transitions involving three separate energy

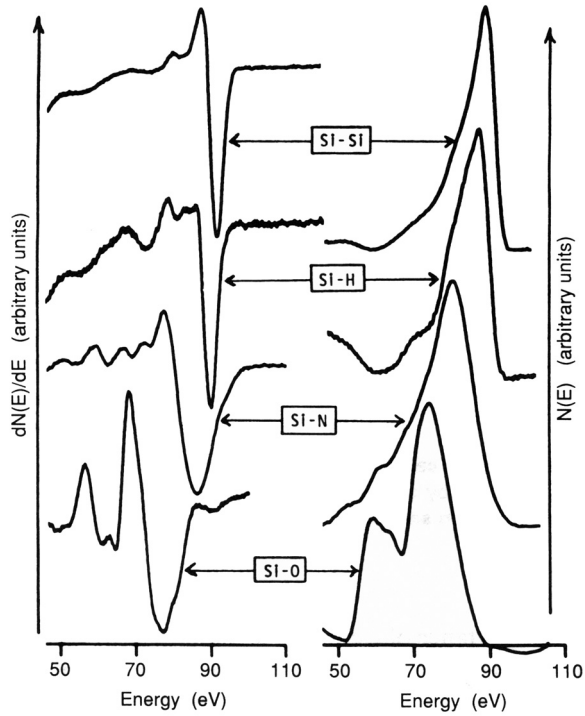

Figure 3.4 **Auger lineshapes for the Si LVV region for elemental silicon (Si–Si), chemisorbed hydrogen on silicon(100) (Si–H), a CVD silicon nitride film (Si–N), and a silicon dioxide film (Si–O). The left side of the figure gives uncorrected, first-derivative signals, while the corresponding, background corrected and loss deconvoluted integral signals are shown on the right side.[12]**

levels, some of the Auger lines involving valence levels (especially if two of the levels involved are valence levels) can show very dramatic changes as the local chemical environment is changed. This effect is illustrated in Figure 3.4 for the LVV silicon line in a variety of Si compounds.[12] The different silicon species can be easily identified by the peak lineshape, including the presence of Si–H bonds, even though the Auger process cannot directly detect hydrogen. These changes in lineshape may be used to identify directly the species present, if the bonding in the coating is predominantly of one type. However, even if the coating contains a mixture of species, peak fitting routines may be used to separate the individual chemical components, especially if individual reference spectra are available for the bonding types of interest, as demonstrated in Reference 12.

The ability to resolve individual chemical bonding states through the use of changes in lineshape, combined with the high spatial resolution and the ability to scan the surface to produce elemental maps, gives AES a unique ability to do chemical bonding maps of the surface. This is illustrated in Figure 3.5, where the

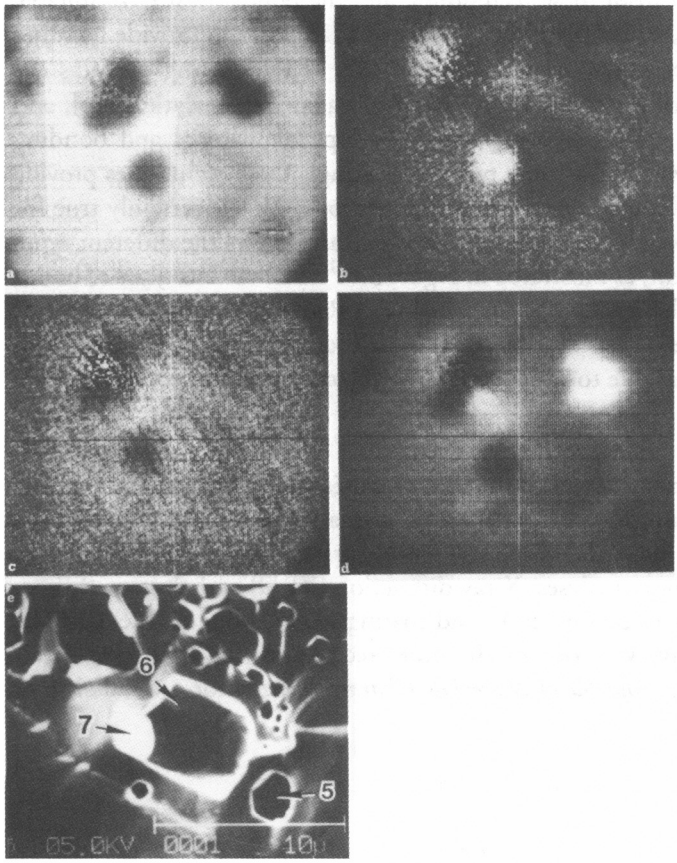

Figure 3.5 **Scanning Auger images from a boron carbide fracture surface. Image (*a*) is from the B KVV line representative of B_4C, whereas image (*b*) is from the B KVV line representative of BN. Image (*c*) is from the C KVV line representative of B_4C, whereas image (*d*) is from the C KVV line representative of graphite. Image (*e*) is the secondary electron image from the same region of the surface. The numbers in image (*e*) show locations of point spectra taken for the original work and have no particular meaning to the figure as shown.[13]**

differences in lineshape for the B KVV and C KVV lines are used to produce a chemical map of a boron nitride fracture surface, showing the relative distributions of B_4C, BN, and graphite.[13] Where the differences in lineshape allow this technique to be used with selectivity and high enough sensitivity, it is an extremely effective tool for correlating grain structure and surface inhomogeneities with the local chemical bonding states.

For some ceramic coatings, vibrational spectroscopies such as infrared (IR) and Raman spectroscopy can also yield chemical bonding information. No elemental

information is obtained from these techniques, and the bonds must have suitable frequencies, transitions, and absorption cross sections in order to provide bonding information. These techniques are usually applicable if the coating contains covalent bonds. Neither of these techniques is strictly a surface analytical tool, and the depth of material probed will vary with the type of material and bonding structures present. However, for some types of coatings, these techniques provide information that is difficult to obtain by other methods. This is certainly true for hard carbon coatings, where Raman spectroscopy clearly shows the different types of chemical bonds present, as illustrated in Figure 3.6.[14] The various types of bonding environments may be readily distinguished with Raman spectroscopy, even for coatings with multiple types of bonds, although quantitation of the relative amounts may be difficult due to variations in the absorption cross-sectional values.

Microstructure

Examination of the microstructure of the film or coating yields information on the crystallographic structure, including degree of crystallinity, phase identification, interatomic spacings, structural defects, and texture orientation of the coating. The two primary tools for these analyses, X-ray diffraction (XRD) and electron diffraction, are both applicable to ceramic films and coatings. Depending on the materials and film thicknesses involved, one or the other technique will often give better results (consult the *Encyclopedia of Materials Characterization* for a discussion of

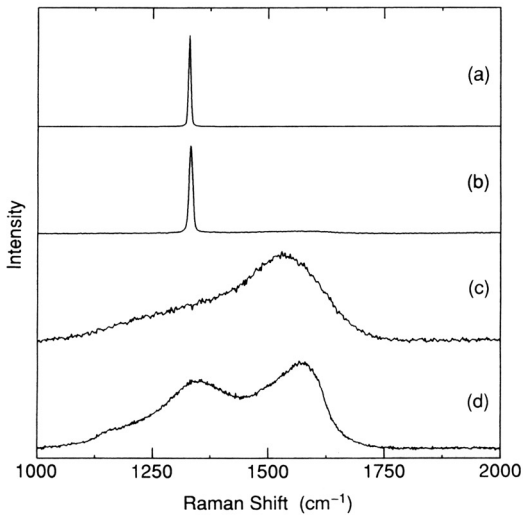

Figure 3.6 **Raman spectra of carbon coatings. Spectrum (*a*) is from a natural gem-quality diamond. Spectrum (*b*) is from a high-quality diamond film. Spectrum (*c*) is from a diamond-like (amorphous) carbon coating. Spectrum (*d*) is from a glassy carbon film.[14]**

each of these techniques); for the thinnest films, specific thin film accessories and methods may be required.

Although the film microstructure may sometimes be of only passing importance, for some applications—thermal management and optical coatings, for example—the microstructure may be one of the most important materials variables. For some types of film or coating applications, it may be desirable to tailor the film to a specific single-phase structure, to adjust lattice parameters to achieve specific film properties, or to adjust the structural orientation of the film to expose a particular crystal face at the surface. In the most extreme cases, growth of epitaxial single-crystal films may be desired. All of these constraints require extensive evaluation of the film microstructure as a function of deposition parameters in order to achieve the goals set for the coatings. A good summary of X-ray diffraction techniques is given by A. Segmuller and M. Murakami in Chapter 8 of Reference 3. S. Mader gives a good review of both X-ray and electron diffraction techniques in Reference 1, Chapter 9.

3.5 Mechanical Characterization

Adhesion

In order for ceramic films and coatings to perform as desired, the coating must adhere to the substrate sufficiently to endure throughout the desired activities and lifetime. Adhesive failures can cause particulate generation, film spallation, and even catastrophic delamination of the entire coating. The requirement for good adhesive strength varies with the application, with protective coatings often requiring the greatest adhesion in order to withstand continued mechanical wear of the coated material. However, adhesion is one of the more difficult properties to achieve and also to measure. Qualitative measurements of adhesion have historically consisted of tests where removal of the coating with adhesive tape constitutes failure and where clean removal of the adhesive tape while leaving the coating behind is regarded as acceptable. Functional qualitative tests of adhesion have also been devised for particular applications—such as whether or not the coating is removed from the substrate when the coated material is ultrasonically cleaned. For applications which do not require strong adhesion of the coating, such qualitative tests are often sufficient. Reference 2, Chapter 12, provides a discussion of some of the qualitative adhesion tests that have been developed. For applications that require better, more predictable, or more consistent coating adhesion, a quantitative adhesion measurement is required. However, quantitation of film adhesion is a complex question that is made even more difficult by the high hardness often exhibited by ceramic coatings.

Scratch testing is one method that has been developed for quantitatively measuring coating adhesion. For this test, a diamond-tipped stylus is used to scratch the surface at an increasing loading force until the coating is removed. Examination of

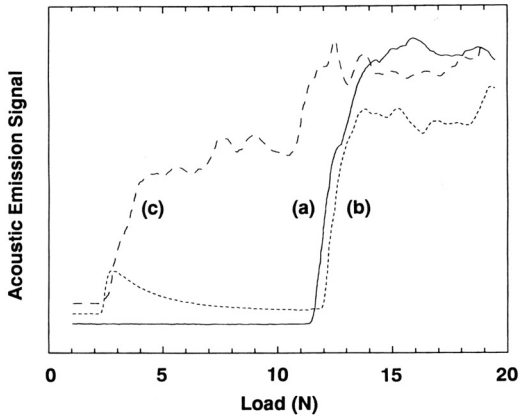

Figure 3.7 **Representative curves for acoustic emission signal versus load for diamond-like carbon coatings on silicon. The solid line (*a*) illustrates the case with no local adhesion failure. The short-dashed line (*b*) illustrates the case with limited local adhesion failure. The long-dashed line (*c*) illustrates the case with "continuous" local adhesion failure. The spectra are offset vertically for clarity.[11]**

the scratch shows the force required for failure (the critical load) and where the failure occurred (in the film or substrate, or at the interface). This technique may be supplemented with detection of acoustic emission from the surface during scratching to help identify the critical load required for failure. Figure 3.7 shows the detected acoustic emission from a diamond-like carbon-coated silicon wafer during scratch adhesion testing where the adhesion testing demonstrates several modes of failure.[11] The resulting scratches are illustrated in the SEM micrographs of Figure 3.8.[11] Although this method is widely used, especially for examining hard coatings, there are a number of inherent problems with the technique. First, if the coating is very hard, the diamond stylus may wear, crack, or fracture instead of, or in addition to, the coating failing. Second, there is no known quantitative relationship between the measured critical load and adhesive strength. Finally, the measured critical load may be strongly affected by many coating properties that include but are not limited to thickness, hardness, microstructure, composition, and internal stress. Reference 15 reviews briefly the scratch adhesion testing method.

Another group of popular adhesion testing methods includes various ways of pulling the film from the substrate. In these tests a mandrel is attached to the film by an epoxy. After the epoxy is cured, the mandrel is removed by pulling it straight up or pushing it over. In either case, the force required to separate the coating from the substrate is measured and related to the adhesive force between the film and the substrate. While easily performed, these methods require a good bond between the epoxy and the film surface, which may require cleaning or modification of the surface before bonding. In addition, this technique is not applicable to films with very high adhesive strengths, because the adhesive strengths that may be examined

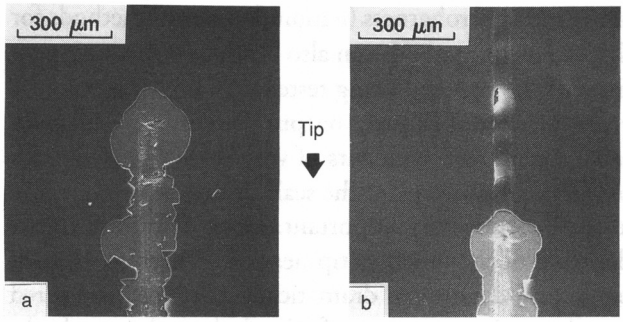

Figure 3.8 **Typical scanning electron micrographs of the scratches resulting from adhesion testing, in the region of the application of the critical load (region of the onset of adhesion failure). An example of a scratch with no local adhesion failure (*a*) and an example of a scratch with limited local adhesion failure (*b*). The direction of travel of the tip across the sample is also shown.[11]**

are limited by the ultimate cohesive strength of the bonding epoxy itself. If the interfacial adhesion exceeds the cohesive strength of the epoxy, the joint will fail within the epoxy and no quantitative adhesion information will be obtained.

A number of other specialized adhesion testing methods have been tried, but most apply only to a very limited class of materials. These other methods use many other techniques, such as surface indentation probes or acoustic or thermal shock of the coating to get an idea of the film adhesion. In addition to being applicable only to a small class of materials, all of these techniques are plagued by the lack of a direct relation to adhesive strength and limited use and experience with the technique. Reference 16 reviews a few of the more common methods of adhesion testing.

Hardness

Hardness is often an important property of ceramic films and coatings, especially for protective and tribological applications. Hardness measurements for thick coatings are relatively straightforward to obtain using standard hardness testing methods. However, thin films require special methods, especially for ceramic films where the coating is usually much harder than the underlying substrate. Microindentation methods that use low loads and shallow penetrations are considered essential for thin films, since the indent depth should be 10% or less of the film thickness in order to get an accurate measure of the coating hardness. Deeper indentations may be used if mathematical modeling is used to separate the contributions of the substrate and the coating.[17] However, microindentation techniques require more careful control of experimental parameters and interpretation because of the small loads and indentations used.

Some of the problems with measuring very small indentations may be solved by measuring the loading/unloading response of the indenter tip using microdisplacement measurements, rather than trying to measure the indentation size. This

technique is required when using ultramicroharness (nanoindentation) methods for extremely thin films. Load/displacement methods can also produce information on the elastic and plastic properties of the material being tested, as well. However, the loading/unloading response curves do not directly output a hardness value, but require extensive modeling and precise measurements of very small displacements in order to estimate hardness values. In addition, as the scale of the indentation size decreases, location of the indent becomes very important. Exact definition of the position of the surface and location of the indenter tip near the center or edges of grains or other surface topographical details can dramatically affect the measured results. Reference 18 gives a good overview summary of microindentation methods.

Internal Stress

While internal stress is an important consideration for all coatings, it may be a greater concern for ceramic films for two reasons. The first is that ceramic films and coatings are often deposited at elevated temperatures. It is common to have a mismatch in thermal coefficients of expansion between the coating and the substrate. Consequently, stresses are developed when the deposited films are cooled to room temperature from the elevated deposition temperature, a problem magnified for ceramic materials because of their high elastic modulus values. The second reason internal stress is important for ceramic films is that most ceramic materials are hard and brittle, so stresses are not relieved by deformation. Instead, it is typical for ceramic films or coatings with a large internal stress to buckle, fracture, and delaminate from the substrate in order to relieve the stress within the film. The stress may be compressive or tensile, depending on the relative magnitudes of the expansion coefficients. Even if the film does not immediately fail as a result of stress relief, the long-term stability and lifetime of the coating may be limited by the film's or substrate's ability to accommodate the stress.

The intrinsic stress within the film may be altered by adjusting the deposition or processing parameters. In order to optimize film performance, the analyst might find it necessary to make detailed measurements of film stress. If the substrate is flexible, the stress may be determined by measurement of the substrate deflection following coating. The substrate deflection may be measured by standard stylus, optical, or electrical (capacitor) techniques. A good review of deflection techniques is given in Reference 1, Chapter 12. Alternatively, the film stress may be measured by examining the lattice constants and line broadening of the X-ray or electron diffraction peaks. The latter methods are discussed in References 1 and 3.

3.6 Summary

In this chapter, some of the applications of ceramic films and coatings have been discussed, along with the properties and characterization methods important to those applications. Common deposition methods for ceramic films have been

summarized and compared, including physical vapor deposition (PVD), chemical vapor deposition (CVD), solution and sol–gel techniques, and thermal spray processing. Some of the special problems and concerns of hard carbon coatings have been detailed. Physical characterization methods for ceramic coatings have been summarized, including information on density, porosity and voids, morphology, thickness, and surface finish. Techniques have been discussed for performing chemical characterizations of ceramic films, including elemental analysis, chemical state analysis, and microstructure. Finally, problems and methods have been summarized for mechanical characterization of ceramic coatings, including adhesion, hardness, and internal stress. Although other specialized characterization methods exist for some applications of ceramic films and coatings, this chapter addresses the characterization methods and problems for the properties important to most ceramic films and coatings. References have been chosen to help the reader gain more information on the specific properties and methods discussed in this chapter and to help the reader begin the search for information not covered in this chapter that may be important for the reader's application.

Acknowledgments

A portion of this work was completed at Sandia National Laboratories supported by the U.S. Department of Energy under Contract DE-AC04-76DP00789.

References

1 L. I. Maissel and R. Glang. *Handbook of Thin Film Technology*. McGraw-Hill, New York, 1983. Reissue.

2 R. F. Bunshah. *Deposition Technologies for Films and Coatings*. Noyes Publications, Park Ridge, NJ, 1982.

3 K. J. Klabunde. *Thin Films from Free Atoms and Particles*. Academic Press, Orlando, FL, 1985.

4 C. J. Brinker, G. C. Frye, A. J. Hurd, and C. S. Ashley. *Thin Solid Films*. **201**, 97–108, 1991.

5 T. N. Rhys-Jones. *Surface and Coatings Technology*. **43/44**, 402–415, 1990.

6 H.-C. Tsai and D. B. Bogy. *Journal of Vacuum Science and Technology*. **A5**, 3287–3312, 1987.

7 D. C. McIntyre, J. E. Greene, G. Hakansson, J. E. Sundgren, and W. D. Munz. *Journal of Applied Physics*. **67**, 1542–1554, 1990.

8 M. Alam. New Mexico Institute of Mining and Technology, Socorro, New Mexico. Personal communication.

9 I. Sherrington and E. H. Smith. *Wear*. **125**, 271–288, 1988.

10 I. Sherrington and E. H. Smith, *Wear*. **125**, 289–308, 1988.

11 D. E. Peebles and L. E. Pope. *Journal of Materials Research*. **5**, 2589–2598, 1990.

12 H. H. Madden and G. C. Nelson. *Applications of Surface Science*. **11/12**, 408–419, 1982.

13 H. H. Madden and W. O. Wallace. *Surface Science*. **172**, 641–667, 1986.

14 D. R. Tallant and D. E. Peebles. Sandia National Laboratories. Personal communication.

15 A. J. Perry. *Surface Engineering*. **3**, 183–190, 1986.

16 D. S. Rickerby. *Surface and Coatings Technology*. **36**, 541–557, 1988.

17 P. J. Burnett and D. S. Rickerby. *Surface Engineering*. **3**, 69–76, 1987.

18 P. J. Blau. "Microindentation Hardness Testing of Coatings: Techniques and Interpretation of Data." In *American Vacuum Society Series 2: Physics and Chemistry of Protective Coatings*. (G. Lucovsky, Series Ed.; W. D. Sproul, J. E. Greene, and J. A. Thornton, Eds.) American Institute of Physics Conference Proceedings No. 149, New York, 1986, pp. 1–21.

4

Consolidation of Ceramic Thick Films

TERRY J. GARINO

Contents

4.1 Introduction

Films of ceramic materials are generally divided into two groups: thick films and thin films. These categories differ not only in film thickness but also in the ways they are fabricated. From 10 to greater than 100 μm thick, thick films are made by processes analogous to those generally used to make bulk ceramics: forming a ceramic powder into a desired shape and then heating to sinter the particles together to produce a dense ceramic. Thin films are 0.1–10 μm thick and are made by vacuum techniques such as sputtering and evaporation, chemical vapor deposition, or sol–gel techniques. Ceramic thick films can be either deposited on a substrate by the screen printing process or fabricated as freestanding films by the tape-casting process.

Ceramic thick films are most often used in applications where their electrical properties are exploited. In these applications, the ceramic thick films usually serve as either insulators, resistors, or capacitors. However, in many of these applications, especially those involving multilayer ceramics made from tape-cast films, the mechanical or thermal properties of the ceramic must also be considered.

Ceramic films made by screen printing are used in hybrid circuits,[1, 2] generally as resistors, dielectrics, or capacitors, but interest in sensor and superconducting

applications is growing. As mentioned earlier, these films are deposited as particulate or green films on a nonporous substrate on which they will remain as part of the hybrid circuit. Also, screen-printed films generally contain at least two phases: the electrically active phase, often ruthenium oxide, and a phase, usually a glass, that facilitates low-temperature sintering.

Ceramic thick films made by tape casting are used to fabricate multilayer ceramic (MLC) devices. By far the two most important such devices are MLC capacitors and MLC packages for integrated circuits.[3–5] In MLC capacitors, layers of phase-pure, high-dielectric constant ceramic alternate with metal electrode layers. In MLC packages, the ceramic phase serves as electrical insulation between conducting metal lines and may contain a relatively small amount of glass.

4.2 Thick Film Processing

In order for the discussion of the characterization of ceramic thick film consolidation to be facilitated, the processes used to make these films is briefly outlined. Both types of films, screen-printed films for hybrid circuits and tape-cast films for MLC devices, undergo similar processing steps. In both cases a ceramic powder is mixed with a solvent, organic additives such as a dispersant and a binder, and possibly with inorganic additives such as dopants or glass powder. The green film is then formed from the suspension either by screen printing or tape casting and the solvent is removed by drying. In both cases, the films are eventually heated at moderate temperature to volatilize the organic additives and then at higher temperature for sintering.

Screen printing[1, 2] is done using a very fine mesh screen. The suspension to be printed, called an ink or a paste, is forced through the screen onto the substrate with a squeegee. Often, it is desired to print a pattern instead of a continuous sheet. This is accomplished by masking the screen so that the desired pattern is formed by the unmasked holes. The rheological properties of the ink must be controlled such that it flows under the shear stress during squeegeeing but then does not flow once the screen is removed. This allows the pattern defined by the screen to remain intact. Once the screen is removed, the film is allowed to dry prior to thermal processing.

Tape casting[3–6] is performed using a doctor blade, a uniform cross section metal blade whose length determines the width of the tape-cast sheet. The edge of the blade is held parallel to the casting surface at a carefully controlled distance which determines the thickness of the tape-cast sheet. The suspension is contained in a reservoir on one side of the blade and a carrier film, often mylar, passes along the casting surface under the blade, starting from the side with the suspension. The film is dried and then cut in smaller pieces. Via holes may be punched in the pieces (for MLC packages) and metal lines or layers are then screen-printed on them. Finally, the sheets are stacked and laminated together prior to thermal processing.

4.3 Characterization of Ceramic Thick Film Consolidation

In many respects, the characterization of the consolidation of ceramic thick films is similar to that of bulk ceramics, which is discussed in Chapter 5. However, several important features of thick films make them unique. Their small thicknesses make some characterization techniques inapplicable and sample preparation for other characterization techniques more difficult. Also, in both screen-printed and tape-cast structures, the ceramic thick film is in intimate contact with one or more dissimilar materials such as a metal. This contact can produce interdiffusion and reactions between these phases.

Stress can be a more important factor in thick films than in bulk ceramics—both the stress generated during processing that can cause defects or failure of the film and the residual stress in the film after processing that can affect the film's properties. Stress can be generated by a variety of processes that occur during thick film processing. The removal of solvent by drying a screen-printed or tape-cast layer on the surface of a substrate that, due to the adhesion of the layer to the substrate, constrains the in-plane shrinkage of the layer creates tensile stress in the layer. Similarly, tensile stress develops during sintering of a screen-printed film since the in-plane shrinkage due to densification is also constrained by the substrate. In MLC ceramic devices, stress is generated by differential sintering. Differential sintering occurs when the different materials in the device, for example the ceramic and metal layers, densify at different rates, at different temperatures, or to a different extent. Also, in both screen-printed and tape-cast devices, mismatch in the thermal expansion coefficients between the various different materials in the device also generates stress. This chapter emphasizes these unique features of the characterization of ceramic thick films.

Characterization of Films Before Thermal Processing

Thickness and density Two of the most important properties of unfired ceramic thick films are thickness and relative density. For relatively thick films, thickness can be measured directly with a micrometer, after subtracting the thickness of the substrate for screen-printed films and that of the mylar carrier sheet for tape-cast films. For thinner films, and for greater accuracy with thicker films, a profilometer can be used to measure the thickness by profiling from the surface of the film to the surface of the substrate, crossing a sharp film edge. If a profilometer is not available or if the film is thicker than the maximum the profilometer is capable of measuring, the thickness may be determined using an optical microscope. This is accomplished by focusing on the substrate surface, noting the position of the fine focus knob, and then turning the fine focus knob until the top of the film is in focus. The thickness can then be determined by comparing the difference in the fine focus setting with the difference for standard of known thickness.

The relative density of the film can be calculated from the mass of a known area and the thickness. Another method for determining green density is to determine the mass of a liquid needed to saturate a film of known mass. The volume of the pores in the film can then be calculated from the mass of the liquid and its density. To facilitate penetration of the liquid into the pores and to avoid damaging the film, a low surface-tension liquid should be used. Also, the liquid should not dissolve any of the organic components in the film. Both thickness and density can vary with location in a ceramic thick film so that numerous measurements are necessary to characterize the film completely. Relative density can also vary in the thickness direction of a thick film. This can produce film warpage during sintering. The variation in green density with thickness can be determined by repeatedly measuring the density after progressively thinning the film by very careful polishing. Finally, the density and the characteristics of the pores can be determined using either mercury porosimetry or gas adsorption, just as in bulk ceramics.

Stress measurement in unfired films During forming of ceramic thick films, processes such as drying can produce transient stresses in the film that can cause cracking. They may also lead to the presence of residual stress in the unfired film. These stresses are generally quite low in magnitude, on the order of 1 MPa or less. The magnitude and sign (tensile or compressive) of the stress in thick films can be measured either directly using X-ray diffraction,[7] if the particles in the film are crystalline, or indirectly by measuring the curvature of the substrate, if the film is attached to a rigid substrate. Since the substrate may have an initial curvature, its curvature without the film present must be measured so that the net change in curvature can be used to determine the stress in the film.

If the amount of deflection at the center of the sample is small (<10%) compared with the thickness of the substrate, if the effective Young's modulus of the film and the substrate are approximately equal, $E_r = [E_f/(1-\nu_f)]/[E_s/(1-\nu_s)] \sim 1$, and if the film is much thinner than the substrate, the magnitude of the stress, σ, is related to the radius of curvature of the substrate, R, by the relation[8]

$$\sigma = \frac{t_s^2 E_s}{6(1-\nu)Rt_f} \tag{4.1}$$

where t_f is the thickness of the film, t_s is the thickness of the substrate, and E_s and ν_s are the Young's modulus and Poisson's ratio, respectively, of the substrate and E_f and ν_f are the same for the film. If the modulus ratio is not about 1 or if the thickness ratio, $t_r = t_f/t_s$ is not much less than one, the right side of Equation 4.1 must be multiplied by the factor $(1 + 4E_r t_r - t_r)$.[9] If the amount of deflection at the center is not small compared with the substrate thickness, a still more complicated expression must be used.[10]

The curvature of the substrate can be determined by a variety of techniques. For all of these techniques, to increase the sensitivity of the curvature measurement, a thin substrate, or the order of 100 μm thick, may be used, keeping in mind that

the proper equation must be used if the deflection is on the order of the substrate thickness. If the substrate is a single crystal, such as a silicon wafer, its curvature can be determined by measuring the stress in substrate using X-ray diffraction.[7] A profilometer can be used to determine the curvature simply by scanning across the substrate, which may need to be supported at three points to keep it from rocking during the scan. The stylus load should be set as low as possible so that the contact with the stylus does not cause substrate deformation.

For making stress measurements in situ during drying, optical methods of determining substrate curvature are useful. For example, the substrate, which must have a reflecting bottom surface, can be placed on a transparent optical flat and illuminated from below with monochromatic light so that interference fringes (Newton's rings) form. Photographic or video images can be taken of the ring pattern and then analyzed to determine the curvature. This technique was used by Chui and Cima to measure the stress during drying of films of aqueous alumina suspensions.[11] As shown in Figure 4.1, they found that the stress rises rapidly to about 1 MPa, at which the particles form a rigid network, and then gradually decreases as the water meniscus moves through the film. Using this technique, they were able to correlate the magnitude of the stress with factors such as the average particle size of the powder and the surface tension of the water (which was varied using surfactants). Another optical technique involves reflecting two parallel He–Ne laser beams perpendicularly off the substrate, which again must have a reflecting surface, and measuring the separation of the beams at a fixed distance from the substrate. The curvature can then be calculated from initial and final beam separations

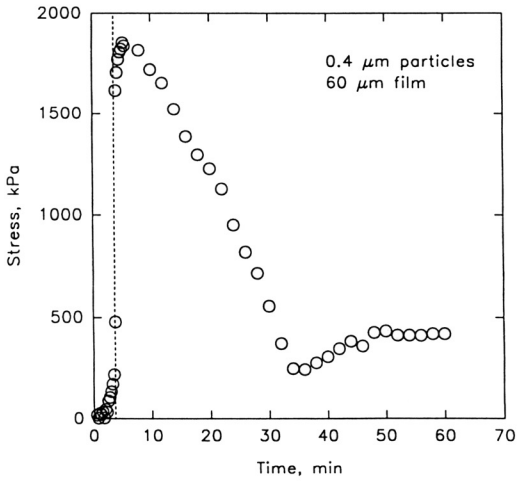

Figure 4.1 **The stress in an alumina particle thick film uniformly saturated with water during drying as a function of time determined using an interference technique to measure the substrate curvature. The rapid rise in stress occurs as the meniscus enters the film.**

and the distance at which the final separation is measured.[12] Finally, various other techniques for determining curvature have been used,[13] and there are several commercially available pieces of equipment that measure substrate curvature.[14]

Characterization of Thick Films During Thermal Processing

Thermal processing of thick films can be divided into low-temperature processing—designed to remove the substantial amount of organic binders, plasticizers, and dispersants usually present in films—and high-temperature processing—designed to densify the films by the sintering process and to achieve the required electrical or other properties. Low- and high-temperature processing may be done in the same firing schedule or in two separate schedules which may be performed in different furnaces. Generally, the low-temperature heat treatment will be performed in an oxygen-containing atmosphere such as air to facilitate pyrolysis, whereas the high-temperature treatment may be done in an inert atmosphere to prevent oxidation of any non-noble metals present. Since different processes of interest occur during the two types of heat treatment, it is useful to consider the characterization of each separately.

Organic burnout In general, the same techniques used to characterize organic burnout in bulk ceramics can be applied to thick films since these techniques are compatible with relatively small sample size and since burnout is not greatly affected by the presence of the substrate so the film can be removed from the substrate prior to characterization. Weight loss can be measured as a function of temperature using thermal gravimetric analysis (TGA). Isothermal weight loss as a function of time can also be monitored. Differential thermal analysis (DTA) can be performed separately or simultaneously with TGA to determine the temperatures at which endo- or exothermic reactions occur. The gaseous reaction products produced during heating can be analyzed with Fourier transform infrared spectroscopy (FTIR) or gas chromatography/mass spectroscopy (GC/MS). Residual carbon content after low-temperature heat treatment can be measured using LECO combustion analysis.

Sintering shrinkage As already mentioned, sintering occurs during high-temperature thermal treatment, producing film densification. For screen-printed films on a substrate, the constraint of the substrate limits the shrinkage to the direction perpendicular to the plane of the film. Because shrinkage is not allowed in the plane of the film, a tensile stress is produced in the film that affects its shrinkage rate in the thickness direction and that can cause the film to crack. On the other hand, tape-cast films are not attached to a substrate and therefore shrink in all three directions, although the amount of shrinkage may differ in each direction. However, since tape-cast layers are used in multilayer devices that contain layers of other materials such as metals, stress can develop due to differential sintering or thermal expansion during high-temperature heat treatment. Therefore, it is important to measure the shrinkage behavior as a function of temperature during heating and with time at the soak temperature for the individual films present in the multilayer

device. The stress due to differential sintering can then be minimized by adjusting the shrinkage of all materials to match each other by control of the factors, such as particle size and dopant concentration, that affect sintering behavior.

Shrinkage during sintering of bulk ceramics is usually measured with a dilatometer. However, this technique is generally not applicable to thick films: the amount of shrinkage in the thickness direction is too small (except if a large number of tape-cast layers are laminated together) and tape-cast films are not rigid enough in the plane of the film to support the load of the dilatometer push rod. Therefore, special measurement techniques must be used.

A laser reflectance technique has been used to measure the in situ shrinkage during sintering of ceramic thick films on rigid substrates.[15] In this technique, a small piece of a transparent material such as sapphire, which has parallel, polished surfaces, is placed on the film and another piece of the same material with the same thickness is placed directly on the substrate where the film has been removed. A third piece is placed resting across the first two so that the angle this piece makes with the first two depends on the film thickness. This angle can be determined by shining a He–Ne laser perpendicularly at the film through the two pieces of transparent material and then measuring the distance between the reflections of the beam from each piece at a distance of several meters from the sample. This technique was used by Garino and Bowen[15] to study the effect of the constraint of the substrate on the densification behavior of ceramic crystalline and glass-particle thick films. They compared the shrinkage of the films on the substrates in the thickness direction to that of the same films after removal from the substrate both in the plane of the film and in the thickness direction. The results indicated that the densification of glass powder is impeded only by the amount expected from the stress caused by the constraint, whereas the densification of the crystalline powders was much more severely impeded.

There are several ways to measure the in-plane shrinkage of a tape-cast film during sintering. The first method[16] utilizes an optical microscope with a long-working-distance lens that is used to view the film as it sinters on a hot stage. The film rests on top of a material such as graphite to which it will not adhere. The in-plane dimensions of the film can thus be determined directly from the image produced by the microscope. In this method, care must be taken so that film warpage is minimal during sintering. A second method[17] involves hanging a strip of the film vertically in a furnace by gripping it on the top and loading from a collar attached to a wire at the bottom with a load large enough to keep the film taut but small enough not to affect the sintering behavior. A traveling microscope can then be used to measure the position of the tip of the wire, which moves upwards by an amount equal to the shrinkage of the film between the grip and the collar.

A good illustration of the issues involved in cofiring MLCs is found in Nishigaki and Fukuta.[18] They first studied the sintering behavior of a $CaO–Al_2O_3–SiO_2–B_2O_3$ glass powder with and without added Al_2O_3 powder by using shrinkage measurements in conjunction with DTA, X-ray diffraction, scanning electron

microscopy (SEM), and transmission electron microscopy (TEM) (see Figure 4.2). The shrinkage data indicated that, when the alumina powder was added, the sintering schedule produced a much higher final density. The TEM electron diffraction and X-ray diffraction indicated that the glass crystallized to anorthite instead of wollastonite when the excess alumina was present. The DTA indicated that excess alumina dissolved in the glass during heating, which raised the temperature of crystallization so that additional sintering could occur while the material was still amorphous. They also measured the shrinkage behavior of the silver conductor powder both by itself and in a multilayer structure with the glass–alumina mixture. They found that the silver by itself began shrinking about 100 °C below that at which the ceramic by itself did and that the multilayer structure began shrinking at an intermediate temperature because the silver exerted a tensile stress on the glass that lowered its sintering temperature.

Stress during sintering As already mentioned, stress develops in a sintering film constrained by a substrate because shrinkage is limited to the thickness direction. The magnitude of the stress can be measured in situ using the techniques described earlier while the film is heated on a hot stage or in a furnace. If a technique that measures the curvature of the substrate is used, the curvature must be measured both with and without the ceramic thick film present so the net curvature due to the stress in the film can be used to calculate the magnitude of the stress. For example, if the ceramic film is on top of a metal electrode layer, thermal expansion mismatch between the substrate and the metal layer during heating will cause the substrate to bend in addition to the bending caused by the sintering of the thick film.

Characterization of Sintered Thick Films

The thickness, density, and residual stress in sintered films can be determined by the methods described above. The X-ray diffraction method of determining stress is generally more suitable for sintered films since it does not require the removal of the film, as do the substrate curvature methods. The surface roughness can be measured with a profilometer, whereas the adhesion of the film to the substrate can be determined by a pull test, in which a wire is bonded to the film and then pulled with the force needed to remove the film from the substrate. The amount of camber or warpage can also be determined with a profilometer. Grain and pore sizes can also be determined by the same techniques used for bulk ceramics.

The sintered microstructure of thick film ceramic devices can be quite complex. This is caused by two factors: (1) the ceramic itself may be multiphase, such as low-firing glass–ceramic packaging material; and (2) dissimilar materials, such as ceramics and metals, are in contact during the high-temperature sintering process. Therefore, a variety of characterization techniques must be used in concert to determine adequately the phase and composition distributions in these materials. The following examples illustrate this point.

A good example of characterizing a ceramic film with a complex microstructure is the previously discussed work of Nishigaki and Fukuta.[18] First, they used X-ray

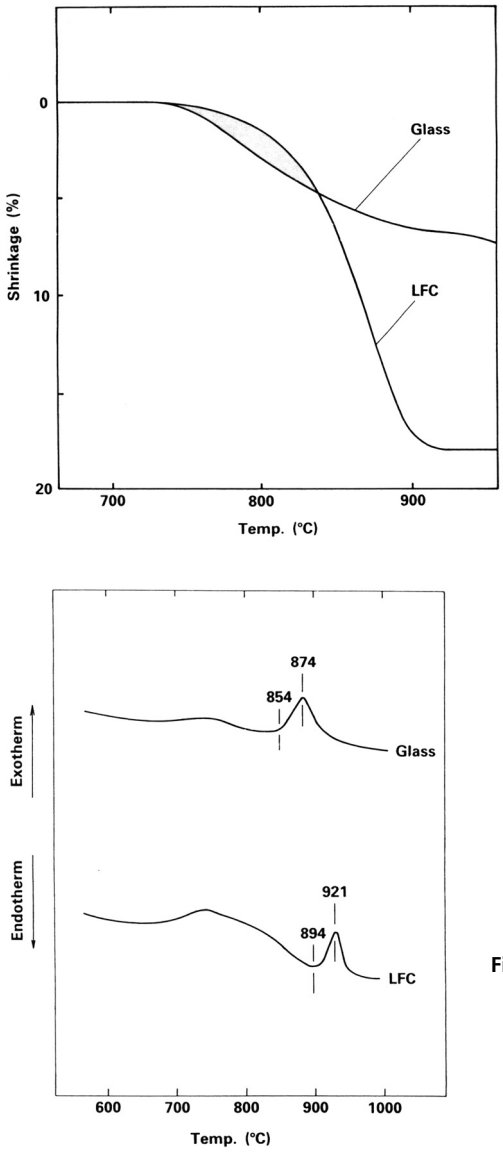

Figure 4.2 **The (*upper*) shrinkage and (*lower*) DTA curves of thick films of glass powder with and without added alumina powder showing that the alumina increases the crystallization temperature, thus allowing increased densification.**

diffraction to determine which phases were present after sintering a glass ceramic powder either by itself or mixed with alumina powder at 880 °C. They found that, with a soak time of 20 min, the film without added alumina contained the undesirable wollastonite phase, whereas the one with alumina contained the desirable anorthite phase, in addition to the alumina. TEM and SEM were then used to characterize the microstructures. Both samples were found to contain a residual glass phase, and electron diffraction and energy-dispersive X-ray analysis (EDX)

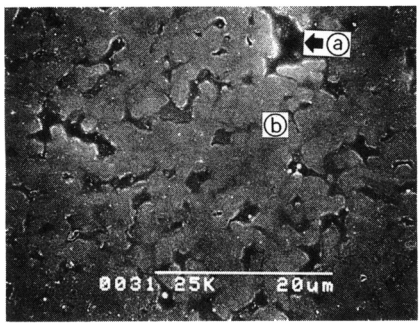

(a)

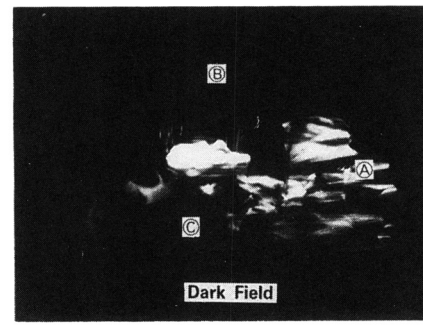

(b)

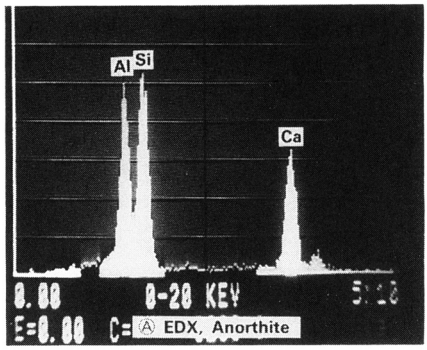

(c)

Figure 4.3 **(*a*) An SEM micrograph and (*b*) a dark field TEM micrograph of the microstructure of sintered glass–alumina thick films showing the presence of anorthite, as indicated by (*c*) the EDX result.**

were used to determine that the anorthite in the alumina-containing film grew in a network surrounding the alumina particles, indicating that some of the alumina dissolved in the glass and changed its composition so that anorthite crystallized instead of wollastonite (see Figure 4.3).

An example of more subtle microstructural features that can strongly affect the properties of thick film ceramics is given in the work of Dettmer and Charles.[19] They studied aluminum nitride substrates, which are of interest due to their high thermal conductivity as compared with the standard substrate material, alumina. They used secondary ion mass spectrometry (SIMS) to characterize the chemical composition of AlN substrates from two different manufacturers, since SIMS is able to detect relatively light elements. As shown in Figure 4.4, they found that the lower thermal conductivity material had a higher oxygen content than the other material. This is consistent with the results of others that oxygen atoms in the AlN lattice disrupt phonon movement, thus decreasing thermal conductivity.

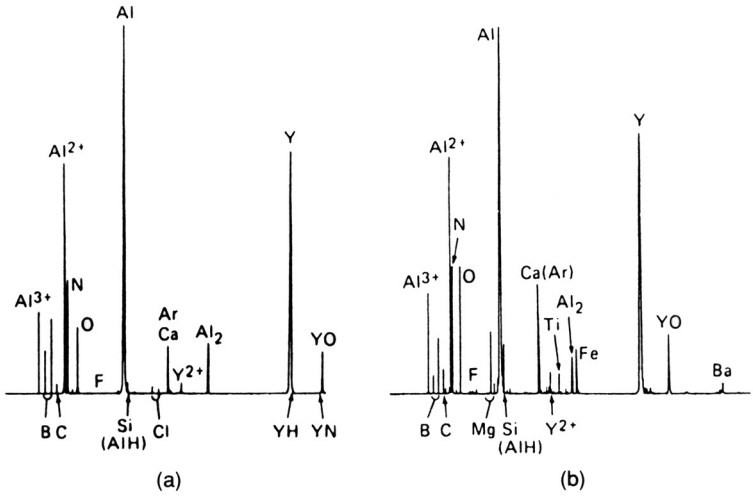

Figure 4.4 **The SIMS analysis of AIN substrates from two different sources indicating that the higher thermal conductivity substrate, (*a*), has a lower oxygen content, consistent with previous results on the effect of oxygen of AIN thermal conductivity.**

As previously mentioned, ceramic thick films generally are used in devices which contain metals or other ceramics or both. This intimate contact between dissimilar materials at the high temperatures necessary for sintering can lead to reactions or diffusion between the materials. The characterization techniques useful for analyzing the reactions between ceramics and metals in thick film structures depend on the extent of reaction, which can vary greatly. For example, Kurokawa et al.[20] found very limited reaction between aluminum nitride and tungsten in a cofired multilayer substrate. They used SEM, TEM, and scanning transmission electron microscopy (STEM) to determine that there were no reaction products formed either as bulk or grain boundary phases. The identification of phases in TEM images was done using bright-field images, dark-field images, and selected area diffraction. They also looked at interdiffusion at AlN/W interfaces. Energy-dispersive electron microprobe analysis using the SEM showed that on the micron scale there was no interdiffusion, as shown in Figure 4.5*a*. However, Figure 4.5*b* shows that the higher resolution energy-dispersive X-ray analysis in the STEM indicated that tungsten diffused about 200 nm into the AlN.

A system in which the interdiffusion was much more extensive was studied by Kriven and Risbud,[21] who studied the reaction between copper and cordierite glass ceramics. They used cathodoluminescence to observe the intensity of the fluorescence from the Cu^+ ions that diffused into the glass. Quantitatively, electron microprobe data indicated that the copper concentration 100 μm from the interface was *7* atom %, although the backscattered electron image in the SEM did not indicate the presence of Cu particles, thus confirming the presence of Cu^+.

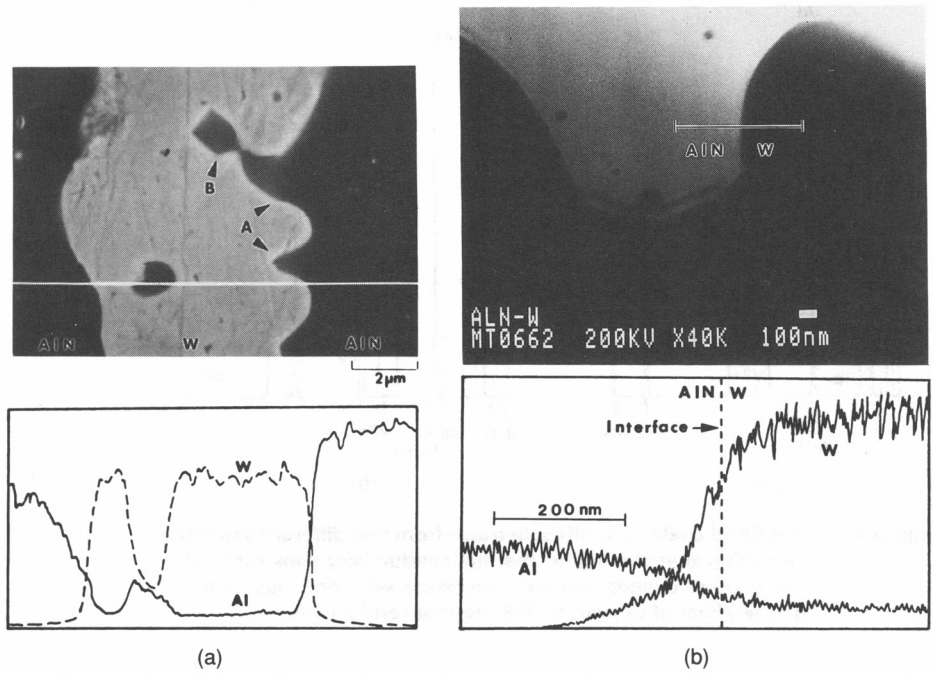

Figure 4.5 **The interface between AIN and W in a cofired multilayer ceramic observed (*a*) with SEM and electron microprobe, which does not indicate interdiffusion, and (*b*) with STEM and EDX, which does indicate interdiffusion due to its higher resolution.**

However, copper-containing crystallites were observed using backscattered SEM, TEM, and energy-dispersive electron analysis on samples heated to a higher temperature, which caused the glass to crystallize. Kriven and Risbud tried to determine the oxidation state of copper in the precipitates using electron energy-loss spectroscopy (EELS), but their sample was too thick. However, they were able to identify the precipitates as metallic copper using convergent beam electron diffraction and selected area diffraction in the TEM.

It is also possible for the ceramic material to be affected by the metal even if no reaction or interdiffusion takes place between them. For example, Takahara[22] studied cofired lead iron tungsten niobate dielectrics with Ag–Pd electrodes for MLC capacitor applications and found that, even though no interaction between the ceramic and metal took place, the resistivity of the ceramic decreased by four orders of magnitude when the metal was present during sintering. From X-ray fluoresence analysis of the zirconia powder in which the sample was sintered, he found that lead, iron, and tungsten were expelled from the ceramic during cofiring. Takahara found that the resistivity was increased to an acceptable value by doping the ceramic with manganese oxide. He used X-ray absorption fine structure (EXAFS) analysis to determine the location of the manganese in the sintered sample

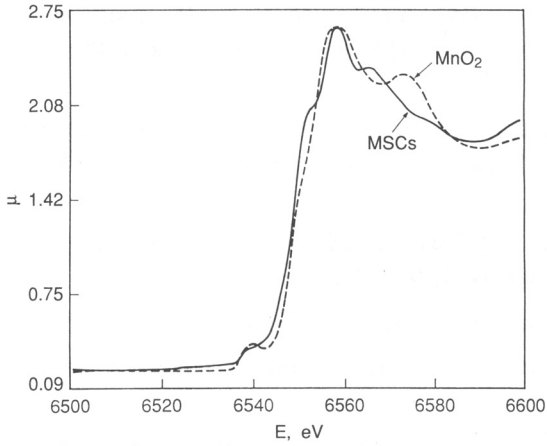

Figure 4.6 **The EXAFS spectra of lead iron tungsten niobate with and without added MnO_2. From the distances to coordinating atom calculated from this spectra, it was determined that the MnO_2 resided at the grain boundaries.**

(see Figure 4.6). They concluded that, since the second and third coordinating atoms around the Mn did not correspond to Pb, Nb, or W, the Mn had diffused to the grain boundaries, apparently compensating for the valence of the expelled elements along the way.

4.4 Summary

The characterization of ceramic thick films requires the use of special techniques in addition to those normally used to characterize bulk ceramics. This chapter has focused on these special techniques. The reader is referred to the following chapter for more information on the standard characterization techniques for ceramics, since many of them are also applicable to thick films.

References

1 R. D. Jones. *Hybrid Circuit Design and Manufacture*. Marcel Dekker, New York, 1982, Chapts. 1–4.

2 R. E. Cote and R. J. Bouchard. In *Electronic Ceramics*. (L. Levinson, Ed.) Marcel Dekker, New York, 1988, Chapt. 6.

3 B. Schwartz. In *Electronic Ceramics*. (L. Levinson, Ed.) Marcel Dekker, New York, 1988, Chapt. 1.

4 M. Kahn, D. P. Burks, I. Burn, and W. Schulze. In *Electronic Ceramics*. (L. Levinson, Ed.) Marcel Dekker, New York, 1988, Chapt. 4.

5 R. R. Tummala. In *Microelectronics Packaging Handbook*. (R. R. Tummala and E. J. Rymaszewski, Eds.) Van Nostrand Reinhold, New York, 1989, Chapt. 7.

6 R. E. Mistler, D. J. Shanefield, and R. B. Runk. In *Ceramic Processing Before Firing*. (G. Onoda and L. Hench, Eds.) John Wiley and Sons, New York, 1978, Chapt. 30.

7 T. Vreeland, Jr., A. Dommann, C.-J. Tsai, and M.-A. Nicolet. *Proceedings*. Materials Research Society Symposia. **130**, 3–12, 1989.

8 G. G. Stoney. *Proc. R. Soc. London Ser. A*. **82**, 172, 1909.

9 A. Brenner and S. Senderoff. National Bureau of Standards No. RP1954 42, 105–123, Feb. 1949.

10 D. E. Fahnline, C. B. Masters, and N. J. Salamon. *J. Vacuum Science and Tech*. **A9**, 2483–2487, 1991.

11 R. Chui and M. Cima. "Drying of Granular Ceramic Films 2: Drying Stress and Saturation Uniformity." Submitted to *J. Am. Ceramic Soc*.

12 E. Kobeda and E. Irene. *J. Vacuum Science and Tech*. **B4**, 720, 1986.

13 R. J. Scheuerman. In *Thin Film Dielectrics*. (F. Vratny, Ed.) The Electrochemical Society, New York, 1969, pp. 561–576.

14 A. Lahav and K. Grim. *J. Appl. Phys*. **67**, 15, 1990.

15 T. J. Garino and H. K. Bowen. *J. Am. Ceramic Soc*. **73**, 251–257, 1990.

16 T. Cheng and R. Raj. *J. Am. Ceramic Soc*. **72**, 1649–1655, 1989.

17 T. Cheng and R. Raj. *J. Am. Ceramic Soc*. **71**, 276–280, 1988.

18 S. Nishigaki and J. Fukuta. In *Ceramic Substrates and Packages for Electronic Applications: Advances in Ceramics*. Vol. 26 (M. Yan, K. Niwa, H. O'Bryan, Jr., and W. Young, Eds.) The American Ceramic Society, Westerville, OH, 1989, p. 199.

19 E. S. Dettmer and H. K. Charles, Jr. In *Ceramic Substrates and Packages for Electronic Applications: Advances in Ceramics*. Vol. 26 (M. Yan, K. Niwa, H. O'Bryan, Jr., and W. Young, Eds.) The American Ceramic Society, Westerville, OH, 1989, p. 87.

20 Y. Kurokawa, C. Toy, and W. Scott. *J. Am. Ceramic Soc*. **72**, 612–616, 1989.

21 W. Kriven and S. Risbud. *Proceedings*. Materials Research Society Symposia. **40**, 323–328, 1985.

22 H. Takahara. *J. Am. Ceramic Soc*. **72**, 1532–1535, 1989.

5

Consolidation of Bulk Ceramics

KEVIN G. EWSUK

Contents

5.1 Introduction

In the manufacture of advanced ceramics, chemical composition and microstructure are specified to optimize the mechanical, electrical, dielectric, optical, thermal, physical, or magnetic properties of the finished product for a given application. The optimum properties are achieved by defining and developing processes to produce the target microstructure, and by controlling processing to minimizing the concentration (i.e., number) and scale (i.e., size) of the defects in the finished product. The tolerance of a finished ceramic product to defects determines the degree of control that must be exercised during processing. To manufacture ceramics with reliable and reproducible properties, it is imperative that process–microstructure–property relations be understood and controlled during the various stages of processing. Processing–microstructure, microstructure–property, and processing–property relationships can be determined by characterizing a ceramic during processing and after final thermal consolidation. The characterization and properties of a ceramic body during the various stages of processing can also provide metrics to assess process reproducibility and to establish process tolerances for manufacturing advanced ceramics.

5.2 Ceramic Consolidation

Consolidation is an important part of ceramic processing that consists in processes ranging from green body (i.e., not fired or sintered) forming to thermal consolidation (e.g., sintering). The consequences of the consolidation processes are densification and microstructure development of the ceramic body.

Many physical and chemical changes occur during ceramic consolidation, ranging from macro-scale changes in the volume of the entire ceramic body, to micro-scale changes in the size or shape of the individual grains that comprise the ceramic body. The sum of the changes that occur during consolidation determines the microstructure and properties of the finished product.

To manufacture reliable ceramic products with the desired properties, it is necessary to understand and control densification and microstructure development. This dictates a need to understand and control ceramic consolidation. It is important to understand the physical and chemical changes that occur during consolidation, and recognize and characterize the critical features and changes that occur in a ceramic body during consolidation.

For the purpose of this chapter, ceramic consolidation is subdivided into three stages, including (1) green ceramic body forming/fabrication, (2) pre-sinter thermal processing, and (3) sintering. This chapter details the processes and products of these three stages of ceramic consolidation, emphasizing the important physical and chemical features and changes that occur during each stage, and the characterization tools that can be employed to understand, monitor, and help control consolidation. Throughout this chapter, specific characteristics and tools used to characterize the consolidation of alumina (Al_2O_3), lead zirconate titanate (PZT), and ceramic-filled-glass (CFG) composites are used as examples.

Green Body Fabrication

The forming/fabrication step in ceramic processing involves the consolidation, bonding, and molding of individual ceramic particles† to produce a cohesive body of the desired size and shape.[1–3] Green ceramic bodies can be fabricated with free flowing dry or semi-dry powders[1] (e.g., dry[4] and isostatic pressing[5]), deformable plastic bodies (e.g., extrusion[1] and injection molding[6, 7]), printable pastes (e.g., screen printing[1]), and fluid slurries (e.g., slip[1, 8] and tape casting[9, 10]). All ceramic forming operations employ a forming pressure to promote particle rearrangement and compaction during the shaping operation, such that particle coordination, green density (i.e., the bulk density of the compact prior to sintering), and strength increase, while the concentration and size of the porosity in the compact decrease.

† For simplicity, this chapter focuses on particulate ceramic body forming and consolidation; however, the principles described are generally applicable to ceramic forming and consolidation.

Processing aids[1] such as liquids, binders, plasticizers, and lubricants are often used to improve particle flow and compaction during forming and to provide additional strength to the formed green body.

During ceramic forming, it is desirable to achieve a high density to minimize density variations and the size and concentration of defects in the formed body and to minimize the total volume of porosity within the compact for the subsequent sintering process.

Pre-Sinter Thermal Processing

Pre-sinter thermal processing involves heating a green ceramic typically to less than or equal to one-half its sintering temperature to extract the processing aids used in forming and to decompose powder precursors to achieve the desired stable form prior to sintering; for example, $MgNO_3$ + heat → MgO + NO_2(g). Pre-sinter thermal processes can include the removal of the liquid used in paste or slurry forming (i.e., drying), extraction of physisorbed and chemisorbed moisture from fine particle surfaces, removal of the water of crystallization, chemical decomposition or dissociation of organic processing additives (i.e., binder burnout), burnout of organic impurities in the raw materials or impurities introduced during processing, and decomposition of powder precursors or additives (e.g., nitrates, carbonates, etc.). The removal of liquid from a ceramic body is typically accomplished in a separate, pre-sintering drying step.[1, 11–13] Organic burnout,[14] dehydration,[1] and decomposition[1] can be accomplished in a separate pre-sinter heat treatment at a temperature well below the sintering temperature, or in a controlled series of ramps and soaks (i.e., controlled heating to a given temperature and holding for a given time) while heating to the sintering temperature in a single, continuous heat treatment process.

Pre-sinter thermal processing is a critical step in the ceramic consolidation process, since improper technique can damage or destroy a ceramic compact. Improper or uncontrolled drying can lead to differential shrinkage, resulting in warping, density gradients, and drying cracks in the green compact. If the drying temperature is too high, catastrophic failure of the green compact can occur due to the explosive evolution of gaseous species within the body. Organic decomposition can also generate gaseous products that may be hundreds of times the volume of the ceramic part; consequently, to prevent catastrophic stresses from developing within a ceramic body during decomposition, organics must be removed gradually, prior to sintering to high relative density when the permeability of the ceramic body is relatively high.

Incomplete drying or burnout during pre-sinter thermal processing can contribute to the uncontrolled evolution of a gas from residual liquid and organic processing aids during sintering, resulting in bloating, warping, or the catastrophic failure of the ceramic part. Additionally, incomplete binder burnout can result in residual carbon particles that can degrade or alter the properties of the sintered product.

Sintering/Thermal Consolidation

The desired, in-use properties (i.e., mechanical, electrical, dielectric, optical, thermal, physical, and magnetic) of a ceramic are generally only realized after a dense, cohesive body is produced by thermal consolidation. The properties of a finished ceramic body are largely dependent on the degree of densification achieved and the microstructure produced during thermal consolidation; consequently, thermal consolidation is one of the most critical steps in ceramic processing.

Most ceramics are consolidated by a process described as sintering,[1, 2, 15–17] in which thermally activated material transport transforms a powder compact of loosely bound particles into a dense, cohesive body. Sintering, which is generally considered synonymous with densification, is usually accomplished by heating a powder compact to approximately two-thirds of its absolute melting temperature and holding it at that temperature for a prescribed time. A ceramic powder compact can also be sintered by subjecting it to an externally applied pressure and heating simultaneously (e.g., hot pressing and hot isostatic pressing). In comparison to conventional sintering, pressure sintering offers the advantage of a lower sintering temperature and shorter sintering time. Additionally, higher end-point densities are often obtained by pressure sintering.

A ceramic sinters as a result of the thermodynamic driving force to minimize the Gibb's free energy, G, of the system.[18] Under the influence of elevated temperature or pressure or both, atoms migrate to lower-energy, thermodynamically more stable positions within the compact to decrease the volume free energy of the system.

In a powder compact, excess volume free energy is present primarily in the form of excess pore surface or interfacial energy (i.e., liquid–vapor and solid–vapor interfaces); consequently, the driving force for sintering can be approximated by

$$dG = \sum \gamma_i \cdot dA_i \tag{5.1}$$

where γ_i, is the interfacial energy and A_i is the interfacial area. Material transport during sintering decreases the interfacial area of a powder compact and decreases the chemical potential differences (e.g., between the grain boundary and the bulk) within the system.

The microstructure of a sintered ceramic and microstructure development during sintering are also controlled by the thermodynamics of the system. Thermodynamics determines what interfaces are formed, what porosity can be eliminated, the size and shape of the grains and pores, and whether or not densification occurs during sintering.

Microstructurally, the material transport occurring during sintering manifests itself as grain boundary formation, interparticle pore shrinkage and annihilation, particle compact densification, and grain growth. Initially, interparticle necks and grain boundaries form, creating a three-dimensional array of approximately cylindrical, interconnected pore channels. These pore channels shrink in diameter during intermediate-stage sintering, and ultimately pinch off to form closed,

isolated, approximately spherical pores for final-stage sintering. Additional pore shrinkage and grain growth occur during final-stage sintering.

Chemical impurities inadvertently or intentionally introduced during processing often migrate to the boundaries between grains during sintering. Chemical impurities may alter the mechanisms of material transport and enhance or impede densification, create second-phase precipitates that pin grain boundaries and impede grain growth, or create a grain boundary phase that alters the properties of the finished product.[19, 20] Chemical impurities that are intentionally added to a system to promote sintering or control grain growth are referred to as dopants or sintering aids.

Ceramics can be densified by solid-state,[21] liquid-phase (LPS),[22] and viscous[13] sintering. Pure alumina, which sinters by solid-state diffusion, requires a relatively high temperature (i.e., 1500–1800 °C) and long time (i.e., 1–5 h) to density.[1, 23, 24] In contrast, because material transport occurs much faster by viscous flow, glasses can be densified at <1000 °C in minutes.[1] Because material transport occurs faster in liquids than in solids, chemical additions that form second-phase liquids during sintering are often used in ceramic powder processing to promote faster densification at lower temperatures. Alumina can be sintered faster and at temperatures hundreds of degrees lower with 0.5–6 wt % of an additive that forms a liquid phase during sintering.[1] The sintering temperature is reduced to ≥1000 °C in a ceramic filled-glass (CFG) composite consisting of ≥50 vol % glass.[25]

Although a liquid or viscous glass phase can enhance densification during sintering, there is often a trade-off with the physical properties. For example, residual glass and foreign crystalline phases present in 94–99.5% alumina bodies degrade the flexural strength.[3, 23, 26] Additionally, grain growth typically occurs faster and is more difficult to control during liquid-phase sintering. Ideally, the processing aids and sintering conditions are optimized and controlled to achieve rapid densification while control is maintained over the microstructure development during sintering.

In solid-state sintered ceramic systems, densification and microstructure development can be assessed on the basis of the dihedral angle, θ, formed as a result of the surface energy balance at the pore–grain boundary intersection,

$$\theta = 2\cos^{-1}\left(\frac{\gamma_{ss}}{2\gamma_{sv}}\right) \tag{5.2}$$

where γ_{ss} and γ_{sv} are the solid–solid and solid–vapor interfacial energies, respectively (see Figure 5.1). Pore shrinkage and densification are favored by a high dihedral angle, and, theoretically, θ must be >70.4° to achieve a relative density of 100% during sintering. The larger the dihedral angle, the larger the intergranular pores that can be eliminated during sintering; however, above a critical pore size, thermodynamics and kinetics limit pore shrinkage and densification.[27–29]

In liquid-phase sintered ceramic systems, densification and microstructure development can be assessed on the basis of the contact angle, ϕ, formed as a result of

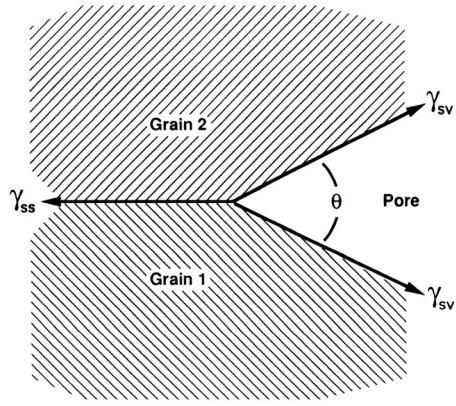

Figure 5.1 An illustration of the equilibrium dihedral angle, θ, formed at a pore–grain boundary intersection during solid-state sintering.

the interfacial energy balance at the solid–liquid–vapor intersection

$$\phi = \cos^{-1}\left(\frac{\gamma_{sv} - \gamma_{sl}}{\gamma_{lv}}\right) \tag{5.3}$$

where γ_{sl} and γ_{lv} are the solid–liquid and liquid–vapor interfacial energies, respectively. A small contact angle favors wetting (i.e., the liquid coats the solid surface) and densification during LPS, and ϕ must be <60° to achieve theoretical density during LPS.[22]

The primary objective of sintering is to produce a cohesive body of the desired size and shape with a microstructure that optimizes the desired in-use properties. For ceramics, this often translates to a high relative density body (i.e., theoretical or nearly theoretical density) composed of fine (i.e., micrometer size), uniform-size grains.

5.3 Characterization of Ceramics

Ceramic characterization[1, 30–32] can range from a process as simple as determining the bulk density of a green powder compact from its mass and dimensions, to a process as complicated as identifying the composition and structure of a submicron size crystal in a dense ceramic matrix using analytical electron microscopy (AEM). Some of the important characteristics evaluated during ceramic consolidation are outlined in Figure 5.2.

During consolidation, both the chemical and physical characteristics of a ceramic are important. Primarily physical changes occur during the green forming process; consequently, physical characteristics including density and pore structure are the most important during the forming stage of consolidation. Chemical changes primarily occur during pre-sintering thermal processing, making composition the critical characteristic during this stage. Appreciable chemical and physical

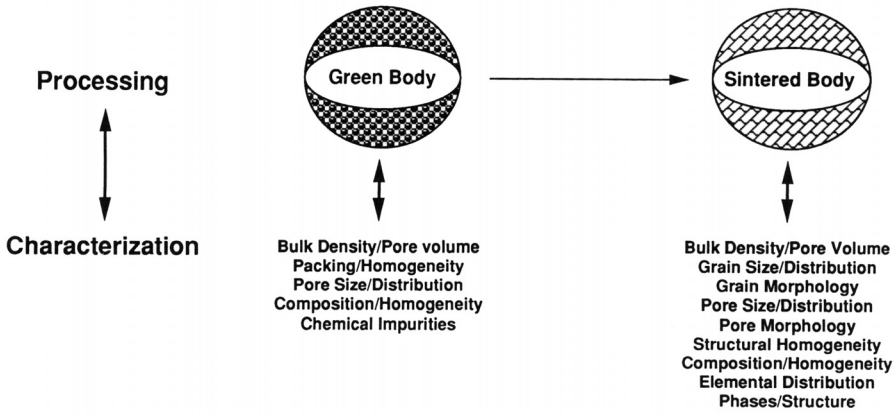

Figure 5.2 **Characteristics evaluated during ceramic consolidation to identify and control processing–microstructure–property relationships.**

changes can occur during sintering, so both chemical and physical characteristics are important during the final stage of consolidation.

Some of the important chemical and physical characteristics of a ceramic body during the consolidation stages of ceramic processing, and some of the pertinent characterization tools that can be used to assess process reproducibility and the consequences of consolidation are summarized in Tables 5.1 and 5.2.

Characteristics and Characterization of Green Ceramic Compacts

Important chemical characteristics of a green powder compact after forming include bulk chemical composition and chemical homogeneity. Bulk composition and any chemical contaminants acquired during processing can be identified with inductively coupled plasma emission spectroscopy (ICP),[33] X-ray diffraction (XRD),[34] and X-ray fluorescence spectroscopy (XRF)[33] (e.g., using scanning electron microscopy [SEM] in combination with electron or wavelength dispersive spectroscopy [EDS or WDS]). Atomic absorption spectroscopy (AAS)[33] can also be used to analyze composition; however, it is limited by being a single-element technique. Optical microscopy (OM) and electron microscopy (e.g., SEM/backscatter, or SEM with EDS dot maps) offer means of assessing chemical homogeneity. Major chemical contaminants and compositional heterogeneities may be avoided by employing controlled clean room–type processing and proper mixing techniques.

Important physical characteristics of a ceramic body after green forming include size, shape, and density. The volume and size of the green body are determined by the forming mold or die. Density is determined by the particle packing, which is determined by the forming technique and pressure. Pore volume, size, and size distribution are determined by the size and shape of the particles and the particle packing.

Particle packing may be the single most important physical characteristic of a powder compact. Improved particle packing increases particle coordination and the

Characteristic	Characterization Tool
Bulk composition	Inductively coupled plasma emission spectroscopy (ICP) Wet chemical analysis Atomic absorption (AA) X-ray diffraction (XRD) X-ray fluorescence (XRF) Neutron activation analysis (NAA)
Impurity composition/ concentration	Inductively coupled plasma emission spectroscopy (ICP) Atomic absorption spectroscopy (AAS)
Elemental distribution/ local chemistry	Optical microscopy (OM) Scanning electron microscopy (SEM) and energy-dispersive spectroscopy (EDS) or wavelength dispersive spectroscopy (WDS) Electron probe microanalysis (EPMA) Transmission electron microscopy (TEM) Analytical electron microscopy (AEM) scanning TEM (STEM) with EDS and electron energy loss spectroscopy (EELS) X-ray absorption spectroscopy (XAS)
Surface/interface chemistry	X-ray photoelectron spectroscopy (XPS, ESCA) Auger electron spectroscopy (AES) Secondary ion mass spectroscopy (SIMS) Ion scattering spectroscopy (ISS) Ultraviolet photoelectron spectroscopy (UPS) Infrared spectroscopy (IR) Raman spectroscopy
Drying and thermochemical events (decomposition and dehydration)	Thermomechanical analysis (TMA) Dilatometry Thermogravimetric analysis (TGA) Differential thermal analysis (DTA) Differential scanning calorimetry (DSC) Gas chromatography/mass spectroscopy (GC/MS)

Table 5.1 Chemical characteristics and tools for characterizing the chemical characteristics of ceramics.

relative density of the compact, which increases the number of material transport paths for densification while decreasing the concentration, size, and size distribution of the pores present in the powder compact. Consequently, in closely packed particle compacts, densification occurs faster, to higher end-point densities, and with less overall volume shrinkage during sintering. Uniform particle packing in a green compact ensures uniform densification and shrinkage during sintering.

Characteristic	Characterization Tool
Density	Density by dimension and mass Hydrostatic weighing (Archimedes' method) Pycnometry (displacement) Comparison with heavy liquids
Densification (kinetics)	Thermomechanical analysis (TMA) Dilatometry
Porosity (volume, size, and distribution)	Mercury porosimetry (intrusion)
Surface area/porosity	BET gas adsorption Permeametry Small angle neutron scattering (SANS) Small angle X-ray scattering (SAXS)
Density homogeneity	Mercury porosimetry Optical microscopy Scanning electron microscopy (SEM) X-ray radiography Ultrasound Magnetic resonance imaging (MRI) Die penetration
Particle/grain size, distribution, morphology, and texture	Optical microscopy (OM) and quantitative stereology Scanning electron microscopy (SEM) and quantitative stereology Transmission electron microscopy (SEM) Scanning transmission electron microscopy (STEM) X-ray diffraction (XRD)
Phase identification/ molecular structure	X-ray diffraction (XRD) Electron diffraction (ED) Fourier transform infrared spectroscopy (FTIR) Raman spectroscopy Extended X-ray analysis fine structure (EXAFS) Neutron diffraction
Thermal events (phase transitions and transformations)	Differential thermal analysis (DTA) Differential scanning calorimetry (DSC) Thermomechanical analysis (TMA) Dilatometry

Table 5.2 Physical characteristics and tools for characterizing the physical characteristics of ceramics.

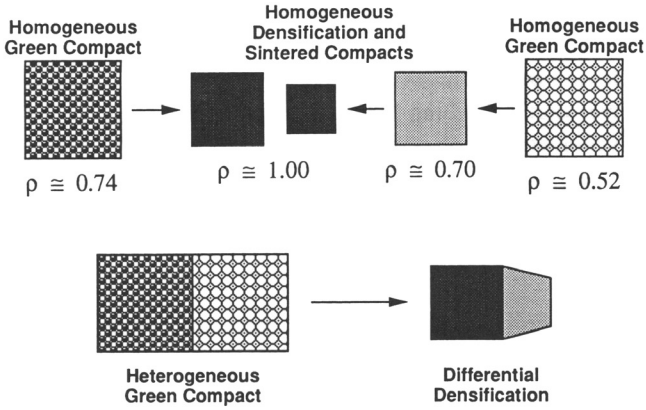

Figure 5.3 **An illustration of homogeneous and heterogeneous densification during green powder compact sintering. Homogeneous densification, which is achieved with uniformly packed powders, results in a volume decrease without a change in shape. A lower green density compact experiences a greater overall volume shrinkage on sintering to theoretical density. Heterogeneous densification, which occurs when density variations exist within the green compact, also results in a volume decrease; however, lower density regions can be physically constrained from sintering to theoretical density, resulting in shape distortion and incomplete densification.**

Packing heterogeneities due to the presence of agglomerates (i.e., densely packed fine-particle clusters) or density gradients created during forming are undesirable because they promote differential or heterogeneous densification within the ceramic body. This often results in warping, the formation of critical defects, exaggerated grain growth (i.e., the growth of a few grains to ≥10 times the average grain size), and incomplete densification during sintering. To avoid the deleterious consequences of heterogeneous densification, ceramic fabrication processes are usually designed and controlled with the intent of optimizing green density while minimizing density gradients during forming. Examples of the consequences of uniform and heterogeneous densification are illustrated and compared in Figure 5.3.

Macroscopically, the particle packing in a powder compact can be assessed on the basis of the relative density of the compact. Relative density, ρ/ρ_{th}, which is the bulk density,† ρ, divided by the true or theoretical density,‡ ρ_{th}, defines the volume of porosity present in the compact that must be eliminated during sintering to achieve theoretical density. The true density of a material can be determined by pycnometry (i.e., fluid displacement) on a finely crushed sample.[35, 36] The bulk

† $\rho = M_s/(V_s + V_v)$, where M_s is the mass of the solids, V_s is the volume of the solids, and V_v is the volume of porosity.

‡ $\rho_{th} = M_s/V_s$.

density of a green powder compact consisting of interconnected porosity that is open to the compact surface is easily determined from the measured mass and bulk dimensions of the compact.[37] Bulk density can also be determined by hydrostatic weighing[35] (Archimedes' method), either by preventing liquid penetration into the open porosity with a thin surface coating of wax, or by accounting for the volume of liquid that infiltrates the open porosity by considering the difference in mass between the sample dry and saturated with liquid.

The processing techniques and additives used in forming a ceramic powder compact largely determine the relative (green) density and subsequent sintering behavior of the compact. Figures 5.4 and 5.5 illustrate the effects different binder systems and uniaxial die pressing pressure can have on the green density and the subsequent densification of alumina during sintering. It is well known that pore volume and size decrease[38, 39] and that the finer and more uniform pore structure in higher green density compacts contribute to more uniform densification and higher end-point densities on sintering.[40–42] Figure 5.4 illustrates how the green density of an alumina powder compact increases with increasing die pressing pressure; Figure 5.5 shows that higher sintered densities are achieved in the higher green density compacts.

Mercury porosimetry provides a more quantitative method of characterizing the porosity in a particle compact. Bulk density, pore volume, mean pore size, and the pore size distribution of a powder compact can all be determined by mercury porosimetry.[36, 43, 44]

The mercury porosimetry results presented in Figure 5.6 illustrate the influence of particle size and size distribution on the size and size distribution of the porosity in green ceramic filled glass (CFG) composites consisting of 65 vol % of 0.4–1.5-μm median particle size alumina and 35% borosilicate glass. The porosimetry results reveal that a relatively broad size distribution of pores exist within the green powder compacts and that pore size distribution and mean pore radius decreases with the substitution of fine alumina for the coarse in the CFG composites. The mean equivalent cylindrical pore radius, r_e, and surface-volume mean equivalent spherical particle radius, R_{sv}, of a powder compact consisting of ≥1-μm particles are proportional to one another and related by the fractional porosity, ε, of the powder compact by

$$r_e = R_{sv} \cdot \frac{2}{3} \cdot \frac{\varepsilon}{1 - \varepsilon} \tag{5.4}$$

Consequently, for the same fractional porosity (i.e., relative density), pore size increases proportionally with increasing particle size, and finer pores are expected in compacts composed of finer particles.[43] Using Equation 5.4, one can approximate the mean pore size in a powder compact solely on the basis of the mean size of the particles in the compact and its relative density.

The mean pore size in a powder compact is proportional to the square root of the mean velocity at which a viscous fluid will flow through that compact, and

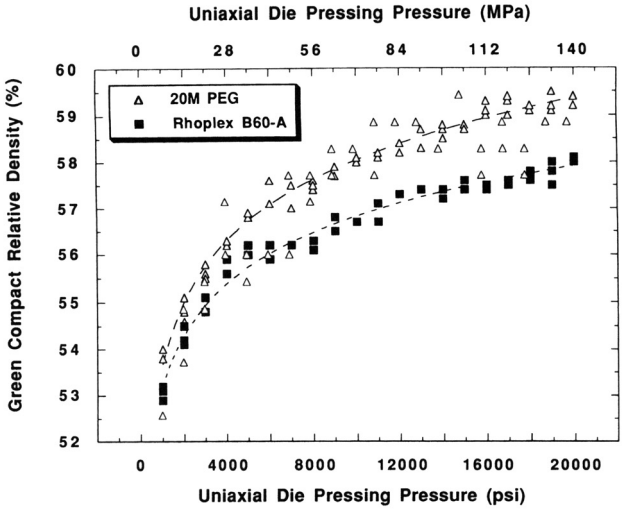

Figure 5.4 **Green density of a 0.35-μm median particle size alumina compact as a function of uniaxial die pressing pressure. At comparable pressing pressures, higher green densities are achieved with 2 vol % of 20 M PEG wax binder as compared with Rhoplex B60-A acrylic wax emulsion. Green density increases proportionally with the log of the applied pressure for both systems.**

inversely proportional to its surface area; consequently, powder compact surface areas determined by permeametry[43] and gas adsorption[36, 43, 45] can also provide information about the porosity of a powder compact. In contrast to mercury porosimetry, however, permeametry measurements provide only mean pore size information, and the accuracy of the results can vary depending on the volume and distribution of the porosity present.

The Fisher sub-seive sizer employs permeametry in a relatively quick and simple technique to determine the volume specific surface area, S, of a powder compact. In combination with the pore volume of the compact, V_v, the mean equivalent radius, r_e, of the macropores (>1000 Å radius) in a dense green powder compact composed of micron-size particles can be estimated from

$$r_e = \frac{2V_v}{S} \tag{5.5}$$

Gas adsorption measurements using the BET method offer an alternate, more precise method of determining S, as well as the size and size distribution of mesopores (8–1000 Å) in a powder compact. Comparisons of the mean pore radius of high green-density CFG composites composed of micron-size particles determined by mercury porosimetry[25] and from surface area measurements using Equation 5.5[46] show good agreement.

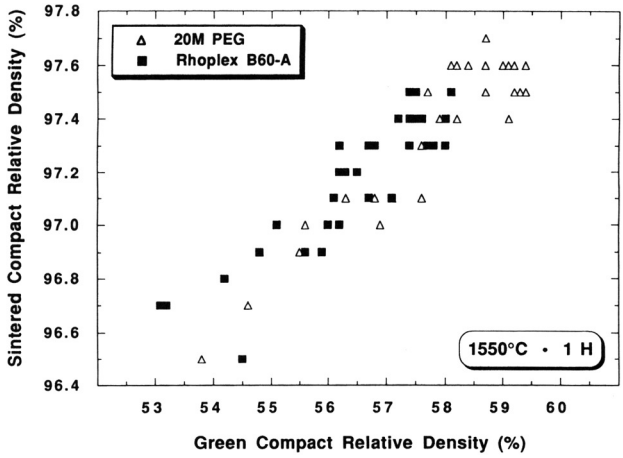

Figure 5.5 **Sintered density of 0.35-μm median particle size alumina as a function of green density (and uniaxial die pressing pressure). Higher sintered densities are achieved in the higher green density bodies produced with the 20 M PEG wax binder and in the higher green density bodies formed at the higher pressing pressures.**

Additional techniques for characterizing porosity in porous compacts include small-angle neutron scattering (SANS),[30, 47, 48] small-angle X-ray scattering (SAXS),[49] and microscopy coupled with quantitative stereology.[50, 51] Ultrasound, X-ray radiography, and magnetic resonance imaging (MRI) have also been used to characterize porous compacts.[30]

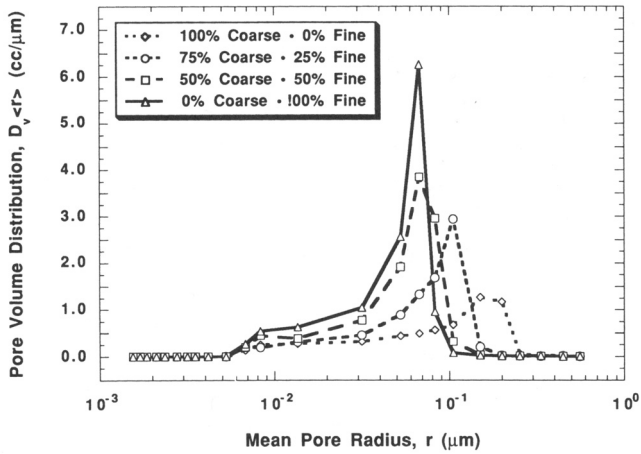

Figure 5.6 **Mercury porosimetry results showing the pore volume distribution in green CFG composite bodies composed of 35 vol % glass and 65% "coarse," 1.5 μm (100:0), "fine," 0.4 μm (0:100) alumina filler, or mixtures thereof.[25]**

Characterization of Pre-Sinter Thermal Processes

Pre-sinter thermal processes typically involve weight changes and thermochemical reactions. Two important pre-sinter thermal processes include drying and binder burnout.

Drying can be characterized by monitoring weight loss or volume shrinkage with time. Weight loss during drying can be characterized using thermogravimetric analysis (TGA). Thermomechanical analysis (TMA) or dilatometry can be used to monitor shrinkage during drying and help define the heating rates, drying times, and temperatures required to yield the desired size and shape product for sintering. Optical imaging techniques can also be useful to monitor the movement of the liquid–vapor drying front and to asses the kinetics of drying.

Organic binder removal can be characterized using thermal analysis and spectroscopy techniques.[34] Thermogravimetric analysis (TGA) is commonly used to characterize weight loss as a function of heating conditions during binder burnout.[52, 53] Differential thermal analysis (DTA) and differential scanning calorimetry (DSC) are used to characterize thermochemical, binder decomposition reactions during heating.[54, 55] Gas chromatography/mass spectroscopy (GC/MS) and Fourier transform infrared spectroscopy (FTIR) are used to analyze the products of binder burnout and to better define the burnout process for specific binders.[54–56] Thermomechanical analysis (TMA) has been used to characterize volume changes during burnout.[52]

In addition to characterizing binder decomposition, thermal analysis is also useful to characterize precursor powder decomposition and dehydration prior to sintering.

Characteristics and Characterization of Sintered Ceramics

Sintering is undoubtedly the most complicated consolidation process and, consequently, one of the most difficult to characterize. The chemical and physical changes that occur during sintering include chemical reactions to form new compounds, chemical changes through vaporization and oxidation, densification, physical changes in the pore and grain size and morphology, the formation of interfaces/grain boundaries, phase transitions such as melting and crystallization, phase transformations (e.g., $\alpha \leftrightarrow \beta$ quartz), grain rearrangement, and liquid phase redistribution (i.e., during LPS).

Microscopy may be the most versatile and most widely used method of characterizing sintering. However, because of the broad range of chemical and physical changes that occur during densification and microstructure development, microscopy is often supplemented with a variety of other characterization techniques.

As in a green ceramic body, important chemical characteristics of a powder compact during and after sintering include bulk chemical composition, chemical homogeneity, and the compositions and concentrations of impurities or undesired phases. Composition can be characterized by ICP,[33] XRD,[34, 57] and XRF.[33]

Chemical homogeneity can be evaluated using OM, SEM in the backscatter mode or with EDS dot maps, and scanning acoustic microscopy (SAM).[58] Phase distribution and chemical homogeneity can also be assessed with micrographs and quantitative stereology.[51, 59, 60]

Chemical information about the surfaces and interfaces of sintered ceramics can be obtained using electron probe microanalysis (EPMA),[61] Auger electron spectroscopy (AES),[61] X-ray photoelectron spectroscopy (XPS or ESCA),[61] ion scattering spectroscopy (ISS),[31] secondary ion mass spectroscopy (SIMS),[31] and ultraviolet photoelectron spectroscopy (UPS).

Phase evolution during sintering and subsequent thermal processing can be characterized with XRD[62] and DTA.[63, 64] The crystalline products of phase transitions and phase transformations in excess of a few percent can be identified by XRD, while information concerning thermochemical reactions, including reaction rates, temperatures, and whether the reactions are endothermic (e.g., melting) or exothermic (e.g., crystallization), can be obtained by DTA.[34]

Relatively large (i.e., micrometer size) regions of minor concentrations of nonprimary or segregated phases in a sintered ceramic can be characterized using SEM and EDS spot imaging, or EPMA. A combination of SEM and EPMA is useful to identify foreign or unusual phases and structures in a microstructure and to obtain information about the mechanisms of densification. An example is presented in the SEM micrographs in Figure 5.7, which show distinct microstructural differences in and about macropores in sintered and HIPed PZT. EPMA determined that, while the composition of the sintered PZT is homogeneous, a lead-rich liquid migrates to the macropores, and lead-rich crystals form within macropores during HIP-ing.[65, 66] By analyzing phase diagrams for PZT it was determined that a lead-rich liquid phase forms as a result of the slight excess concentration of PbO in the starting powder.[67, 68] The lead-rich liquid forms by pressure-enhanced dissolution

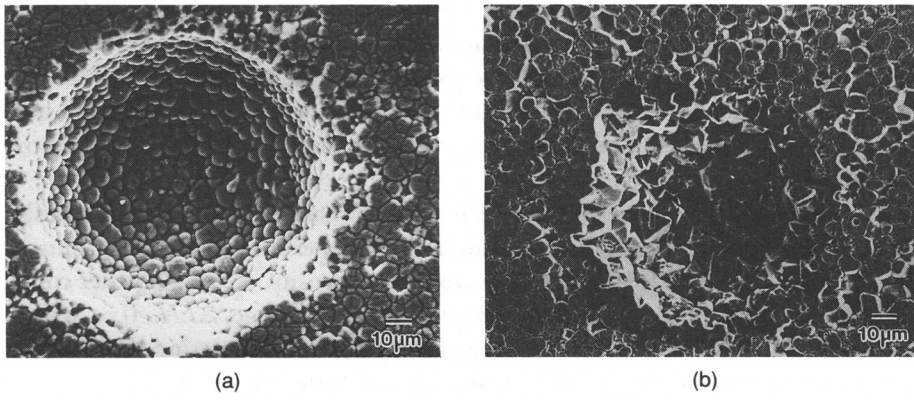

Figure 5.7 **SEM micrograph of a macropore in PZT (*a*) after sintering for 60 min at 1320 °C in oxygen and (*b*) after HIPing for 45 min at 1300 °C and 21 MPa in oxygen.[65, 66]**

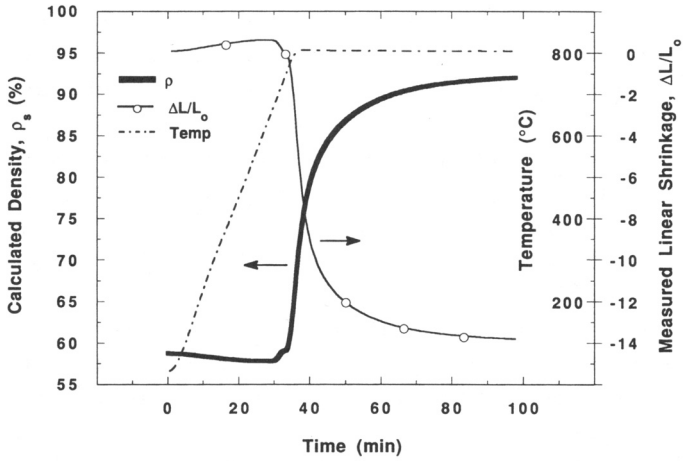

Figure 5.8 **Thermomechanical analysis (TMA) plot of the linear shrinkage and densification of a CFG composite containing 50 vol % glass as a function of time at 800 °C.[25]**

during HIPing, promoting densification of the PZT by liquid redistribution, dissolution-reprecipitation, and grain rearrangement. The tetragonal crystals within the macropores are lead titanate crystals that precipitate from the lead-rich liquid. The piezoelectric properties of PZT are extremely sensitive to composition,[67] and, while the addition of PbO to PZT can enhance sinterability and compensate for PbO vaporization during sintering,[69, 70] too much PbO can severely degrade the properties of PZT. Microstructural and chemical analyses revealed that, in combination with pressure during sintering, a slight excess of PbO in PZT can improve densification without deleteriously affecting properties.

Minor concentrations of foreign compositions at grain boundaries and three-grain junctions in a sintered ceramic can be characterized using transmission electron microscopy (TEM)[71] and electron diffraction, scanning transmission electron microscopy (STEM)[71] with EDS or electron energy loss spectroscopy (EELS), and AES.[71]

Information on grain boundary structure, the structure of second-phase precipitates, and crystal defects can be obtained using high-resolution electron microscopy (HREM).[72]

Densification during sintering can be indirectly characterized by continuously monitoring the linear shrinkage of a sample with time during sintering using a TMA or dilatometer. Based on the measured green density, ρ_g, of a powder compact, and the normalized, measured linear dimensional change, $\Delta L/L$, (i.e., where L is the sample length and ΔL is the change in length) during sintering, the density, ρ_s, of the ceramic can be approximated at any time during sintering.

$$\rho_s = \frac{\rho_g}{(1 - \Delta L/L)^3} \tag{5.6}$$

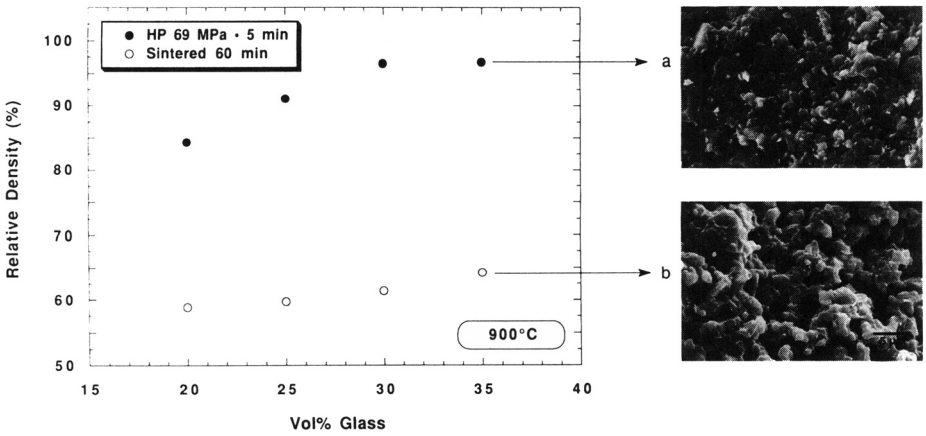

Figure 5.9 **A comparison of the densification and microstructures of (*a*) vacuum hot pressed (HP) and (*b*) sintered alumina-filled borate glass composites containing 20–35 vol % glass.[46] Higher densities are achieved by hot pressing.**

Consequently, TMA can provide valuable information concerning the kinetics of densification as well as the extent of densification during sintering.[73] Figure 5.8 shows the densification of a CFG composite during heating to and soaking at 800 °C for 1 h. Consistent with rapid glass redistribution by infiltration and rapid densification by grain rearrangement, densification occurs rapidly during the initial and intermediate stages of sintering. The rate of densification decreases appreciably during final-stage sintering when material transport is controlled by the viscous flow of the high-viscosity ceramic-filled-glass dispersion.[74]

Although more labor-intensive and less efficient, information on the densification kinetics and densification can also be obtained from density measurements on different individual samples as a function of time for otherwise identical sintering conditions. Bulk density measurements on ≤92% dense sintered samples containing open porosity can be determined from the measured mass and dimensions of the compact,[37] while Archimedes' method[35] works well for closed pore, >92% dense bodies. The density of closed pore samples can also be determined by pycnometry (e.g., helium pycnometry),[35, 37] mercury porosimetry,[37] and by the sink-float method[35] (i.e., whereby the buoyancy of the sample is assessed and compared in different density liquids). Density can also be estimated from micrographs using quantitative stereology.

Densification data coupled with microstructure information can also provide valuable information about the mechanisms of densification and the conditions required to achieve the desired level of densification during sintering. As shown in Figure 5.9, in comparison to conventional sintering, higher densities are achieved with comparable glass concentrations in hot pressed samples that are densified under an externally applied pressure. The densification data indicate that >95% dense CFG composites can be produced with as little as 30 vol % glass; however,

the SEM micrographs indicate that an externally applied pressure is required to induce grain rearrangement to realize this densification. The dense CFG composite skeletal structure of the sintered composite indicates that glass redistribution occurs during the early stages of sintering to eliminate the fine pores between alumina particles, leaving behind larger pores in the composite microstructure where the glass originally resided. In absence of an external pressure to collapse the large pores, additional densification must occur solely by surface tension-driven viscous flow; however, the viscosity of the CFG composite skeletal structure containing only 30–35% glass is too high for additional densification to be realized during conventional sintering.[74]

Pressure sintering can also be useful to further density sintered ceramics. The density of liquid-phase sintered PZT was improved from ~97% to ~98% of theoretical density by HIPing for 7.5–60 min at 1300 °C and 7–21 MPa.[65, 66] Consistent with the microstructural evidence of liquid formation and redistribution (Figure 5.7), and the preferential annihilation of the fine, submicrometer porosity within the microstructure, the majority of densification occurs rapidly, within the first few minutes of HIPing.

The inability to achieve theoretical density during HIPing is, in part, attributed to the incomplete elimination of the gross macroporosity in the PZT microstructure. Using SEM and quantitative stereology[51, 52, 75] (i.e., the average lineal intercept method) it was determined that macropores in the PZT shrink but are not eliminated during HIPing. SEM analysis of the PZT revealed that, as has been observed in other liquid-phase sintered systems,[76, 77] macropore shrinkage occurs by migration of liquid into the macropores during HIPing (Figure 5.7). The liquid phase is critical to the macropore shrinkage observed during HIPing, since similar experiments conducted on solid-state sintering alumina show that HIPing has little effect on the macroporosity.[28, 29] The densification and microstructural evidence for the PZT system indicate that, while there was enough liquid to decrease the size of the macropores in the PZT microstructure during HIPing, there was insufficient liquid present to eliminate them.

Reducing the size of the macropores in the PZT microstructure by pressure enhanced liquid-phase sintering improves the dielectric breakdown strength of the PZT; however, presumably due to the minor concentration of non-PZT phase present in the microstructure, the piezoelectric properties are not deleteriously affected.

The evolution of the open-pore structure of a powder compact during sintering can be characterized using mercury porosimetry and gas adsorption, and such information can also be useful in elucidating sintering mechanisms. The results from mercury porosimetry analyses conducted on CFG composites as a function of sintering time show that the fine porosity in the composite microstructure is preferentially eliminated and that a narrow distribution of larger, 0.3–0.4-μm radius pores are created during initial-stage sintering[25] (Figure 5.10). As sintering progresses, the volume and size of the larger porosity slowly decrease. The preferential

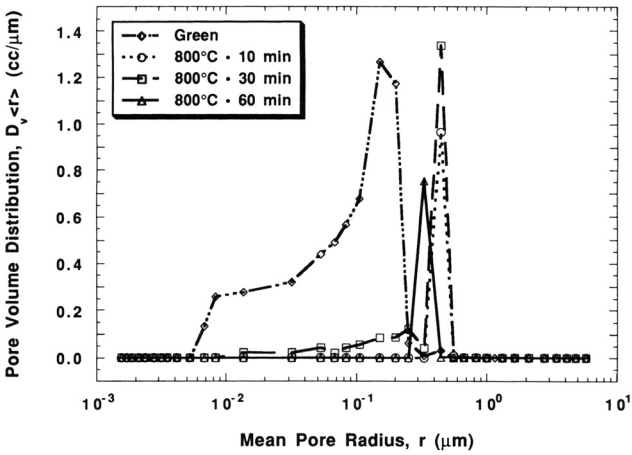

Figure 5.10 Mercury porosimetry results showing the microstructural evolution of a CFG composite composed of 35 vol % glass and 65% alumina as a function of time during sintering at 800 °C.[25]

and rapid annihilation of the fine porosity during sintering supports the hypothesis of glass redistribution by infiltration during initial-stage sintering, and the formation of larger pores during initial-stage glass redistribution is also consistent with this model and microstructural evidence.[46]

Pore structure evolution during sintering can also be characterized using SANS,[30, 47] SAXS,[49] and microscopy coupled with quantitative stereology.[50, 51]

Grain size, size distribution, and shape, and the changes that occur during sintering can be characterized using microscopy coupled with quantitative stereology.[51, 59, 60, 75] XRD can also be used to characterize grain size.

The equilibrium dihedral angle formed at pore-grain boundary intersections in a ceramic during sintering can be characterized using SEM.[78, 79]

To determine if a liquid wets a solid and will favor densification by LPS, contact angles can be measured using the sessile drop method.[61, 80]

The aesthetic quality of a sintered ceramic is also an important physical characteristic. Surface imperfections such as blemishes, blisters, burrs, or cracks are generally characterized by visual inspection.[81] Camber (i.e., waviness or bow) can be assessed from the physical dimensions of the ceramic. Surface roughness can be characterized using profilometry.[31, 61]

Internal defects such as cracks, delaminations, large processing related voids, and density gradients in a sintered ceramic can be characterized using microscopy, ultrasound, X-ray radiography, and neutron scattering.[30]

The hermeticity of a sintered ceramic is particularly important in electronic components. Fine size, open porosity or surface cracks in sintered ceramics can be characterized by the bubble test[82] or by dye penetration.[83] The hermeticity of closed-porosity sintered ceramics can be characterized using the helium leak test.[84, 85]

5.4 Summary

The processes employed in manufacturing a ceramic are defined and controlled with the intent of producing a product with properties suited to a specific application. Processing, microstructure, and properties are all interrelated, and it is important to understand these relationships to manufacture a high-quality, reliable product. Processing–microstructure, microstructure–property, and processing–property relationships can be identified, monitored, and controlled by characterizing the ceramic body during the various stages of processing and after final thermal consolidation. By understanding processing–microstructure–property relationships, it is possible to modify and optimize properties and identify and correct processing deficiencies when less than optimal properties are obtained.

Ceramic consolidation processes include green body forming, pre-sinter thermal processing, and sintering. During consolidation, a variety of chemical and physical changes can occur, including pore shrinkage and elimination, densification, and grain growth. Many of the changes that occur during consolidation can be characterized using microscopy. Ceramic consolidation can be characterized more quantitatively using microscopy in conjunction with other characterization techniques, including spectroscopy, pycnometry, porosimetry, gas adsorption, thermal analysis, and stereology.

References

1 J. S. Reed. *Introduction to the Principals of Ceramic Processing*. John Wiley & Sons, New York, 1988.

2 D. W. Richerson. *Modern Ceramic Engineering*. Marcel Dekker, New York, 1982.

3 J. M. Herbert. In *Ceramic Dielectrics and Capacitors*. Electrocomponent Science Monographs, Vol. 6. Gordon and Breach Science Publishers, New York, 1985.

4 J. S. Reed and R. B. Runk. In *Ceramic Fabrication Processes*. Treatise on Materials Science and Technology, Vol. 9. (F. F. Y. Wang, Ed.) Academic Press, New York, 1976, pp. 71–93.

5 G. F. Austin and G. D. McTaggart. In *Ceramic Fabrication Processes*. Treatise on Materials Science and Technology, Vol. 9. (F. F. Y. Wang, Ed.) Academic Press, New York, 1976, pp. 135–151.

6 J. A. Mangels. *Ceram. Eng. Sci. Proc.* **3** (9–10), 529–537, 1982.

7 R. M. German and K. F. Hens. *Bull. Am. Ceram. Soc.* **70** (8), 1991.

8 R. E. Cowan. In *Ceramic Fabrication Processes*. Treatise on Materials Science and Technology, Vol. 9. (F. F. Y. Wang, Ed.) Academic Press, New York, 1976, pp. 153–171.

9 R. E. Mistler, D. J. Shanefield, and R. B. Runk. In *Ceramic Processing Before Firing*. (G. Y. Onoda, Jr., and L. Hench, Eds.) John Wiley & Sons, New York, 1978, pp. 411–448.

10 J. C. Williams. In *Ceramic Fabrication Processes*. Treatise on Materials Science and Technology, Vol. 9. (F. F. Y. Wang, Ed.) Academic Press, New York, 1976, pp. 173–197.

11 J. S. Reed. In *Ceramics and Glasses*. Engineering Materials Handbook, Vol. 4. ASM International, Materials Park, OH, 1991, pp. 130–134.

12 W. E. Brownell. In *Structural Clay Products*. Applied Mineralogy, Vol. 9. Springer-Verlag, New York, 1976, pp. 101–125.

13 C. J. Brinker and G. W. Scherer. In *Sol-Gel Science, The Physics and Chemistry of Sol-Gel Processing*. Academic Press, New York, 1990.

14 L. Hermansson. In *Ceramics and Glasses*. Engineering Materials Handbook, Vol 4. ASM International, Materials Park, OH, 1991, pp. 135–140.

15 R. L. Coble and J. E. Burke. In *Progress in Ceramic Science, Vol. 3*. (J. E. Burke, Ed.) MacMillan, New York, 1963, pp. 197–251.

16 F. Thümmler and W. Thomma. *J. Inst. Metals*. **12**, 69–108, 1967.

17 J. E. Burke and J. H. Rosolowski. In *Reactivity of Solids*. Treatise on Solid State Chemistry, Vol. 4. (N. B. Hannay, Ed.) Plenum Press, New York, 1976, pp. 621–659.

18 C. Herring. In *The Physics of Powder Metallurgy*. (W. E. Kingston, Ed.) McGraw-Hill, New York, 1949, pp. 143–179.

19 C. A. Handwerker, P. A. Morris, and R. L. Coble. *J. Am. Ceram. Soc*. **72** (1), 130–136, 1989.

20 J. E. Blendell and C. A. Handwerker. *J. Cryst. Growth*. **75** (11), 138–160, 1986.

21 R. L. Coble. *J. Appl. Phys*. **32** (5), 787–792, 1961.

22 R. M. German. *Liquid Phase Sintering*. Plenum Press, New York, 1985.

23 W. H. Gitzen. *Alumina as a Ceramic Material*. The American Ceramic Society, Westerville, OH, 1970, pp. 127–131.

24 R. L. Coble. *J. Appl. Phys*. **32** (5), 793–799, 1961.

25 K. G. Ewsuk and L. W. Harrison. In *Ceramic Powder Science III*. Ceramic Transactions, Vol. 12. (G. L. Messing, S. Hirano, and H. Hausner, Eds.) The American Ceramic Society, Westerville, OH, 1990, pp. 639–648.

26 E. Dörre and H. Hübner. *Alumina, Processing, Properties, and Applications*. Springer-Verlag, New York, 1984, p. 218.

27 W. D. Kingery and B. Francois. In *Sintering and Related Phenomena*. (G. C. Kuczynski, N. A. Hooton, and C. F. Gibbon, Eds.) Gordon and Breach Science Publishers, New York, 1965, pp. 471–498.

28 K. G. Ewsuk. "Final Stage Densification of Alumina During Hot Isostatic Pressing." Ph. D. dissertation, Pennsylvania State University, University Park, 1986.

29 K. G. Ewsuk and G. L. Messing. In *Hot Isostatic Pressing: Theories and Applications*. (R. J. Schaefer and M. Linzer, Eds.) ASM International, Materials Park, OH, 1991, pp. 23–33.

30 J. B. Wachtman. In *Advanced Characterization Techniques for Ceramics*. Ceramic Transactions, Vol. 5. (W. S. Young, G. L. McVay, and G. E. Pike, Eds.) The American Ceramic Society, Westerville, OH, 1989, pp. 3–30.

31 V. A. Greenhut. In *Ceramics and Glasses*. Engineering Materials Handbook, Vol. 4. ASM International, Materials Park, OH, 1991, pp. 24–28.

32 *Characterization of Ceramics*. Ceramics and Glass: Science and Technology, Vol. 3. (L. L. Hench and R. W. Gould, Eds.) Marcel Dekker, New York, 1971.

33 J. E. Enrique, E. Ochandio, and M. F. Gazulla. In *Ceramics and Glasses*. Engineering Materials Handbook, Vol. 4. ASM International, Materials Park, OH, 1991, pp. 549–556.

34 C. A. Sorrell. In *Ceramics and Glasses*. Engineering Materials Handbook, Vol. 4. ASM International, Materials Park, OH, 1991, pp. 557–563.

35 N. A. Pratten. *J. Mater. Sci*. **16**, 1737–1747, 1981.

36 S. Lowell and J. E. Shields. In *Powder Surface Area and Porosity*. 2nd ed. (B. Scarlett, Ed.) Chapman and Hall, New York, 1984.

37 J. E. Shields. In *Ceramics and Glasses*. Engineering Materials Handbook, Vol. 4. ASM International, Materials Park, OH, 1991, pp. 580–584.

38 N. G. Stanley-Wood and M. E. Johansson. *Analyst*. **105**, 1104–1112, 1980.

39 A. Roosen, S. Sumita, and H. K. Bowen. In *Ceramic Microstructures '86, Role of Interfaces*. Materials Science Research, Vol. 21. (J. A. Pask and A. G. Evans, Eds.) Plenum Press, New York, 1987, pp. 433–446.

40 H. Palmour III, M. Geho, R. L. Russell, and T. M. Hare. "Study of Do Effects on Subsequent Densification Behavior in Spinel and Alumina Ceramics." In *Solid State Phenomena*, Vols. 25 and 26. (A. C. D. Chaklader and J. A. Lund, Eds.) Trans Tech Publications, Brookfield, VT, 1992, pp. 37–44.

41 M. A. Occhionero and J. W. Halloran. In *Sintering and Heterogeneous Catalysis*. Materials Science Research, Vol. 16. (G. C. Kuczynski, A. E. Miller, and G. A. Sargent, Eds.) Plenum Press, New York, 1984, pp. 89–101.

42 M. D. Sacks, T. S. Yeh, and S. D. Vora. In *Ceramic Powder Processing Science*. (H. Hausner, G. L. Messing, and S. Hirano, Eds.) Deutsche Keramische Gesellschaft e. V. Köln, 1989, pp. 693–704.

43 T. Allen. In *Particle Size Measurement*. 3rd ed. Chapman and Hall, New York, 1981.

44 D. N. Winslow. *J. Colloid and Interface Science*. **67** (1), 42–47, 1978.

45 S. J. Gregg and K. S. W. Sing. In *Adsorption, Surface Area, and Porosity*. Academic Press, New York, 1967, pp. 1–34, 121–194.

46 K. G. Ewsuk, L. W. Harrison, and F. J. Walczak. In *Ceramic Powder Science II*. Ceramic Transactions, Vol. 1. (G. L. Messing, E. R. Fuller, Jr., and H. Hausner, Eds.) The American Ceramic Society, Westerville, OH, 1988, pp. 969–977.

47 K. A. Hardman-Rhyne and N. F. Berk. *Physica*. **13B**, 223–225, 1986.

48 K. A. Hardman-Rhyne and N. F. Berk. *J. Am. Ceram. Soc*. **69** (11), c285–287, 1986.

49 A. Emmerling, R. Gerlach, R. Goswin, J. Gross, G. Reichenauer, J. Fricke, and H.-G. Haubold. *J. Appl. Cryst*. **24**, 781–787, 1991.

50 H. Landspersky. *Sci. Sintering*. **6** (3), 163–174, 1974.

51 E. E. Underwood. *Quantitative Stereology*. Addison-Wesley, Reading, MA, 1970.

52 D. E. Sproson and G. L. Messing. In *Ceramic Powder Science II*. Ceramic Transactions, Vol. 1. (G. L. Messing, E. R. Fuller, Jr., and H. Hausner, Eds.) The American Ceramic Society, Westerville, OH, 1988, pp. 528–537.

53 M. R. Barone, J. C. Ulicny, R. R. Hengst, and J. P. Pollinger. In *Ceramic Powder Science II*. Ceramic Transactions, Vol. 1. (G. L. Messing, E. R. Fuller, Jr., and H. Hausner, Eds.) The American Ceramic Society, Westerville, OH, 1988, pp. 575–583.

54 Y. N. Sun, M. D. Sacks, and J. W. Williams. In *Ceramic Powder Science II*. Ceramic Transactions, Vol. 1. (G. L. Messing, E. R. Fuller, Jr., and H. Hausner, Eds.) The American Ceramic Society, Westerville, OH, 1988, pp. 538–548.

55 W. K. Shih, M. D. Sacks, G. W. Scheiffele, Y. N. Sun, and J. W. Williams. In *Ceramic Powder Science II*. Ceramic Transactions, Vol. 1. (G. L. Messing, E. R. Fuller, Jr., and H. Hausner, Eds.) The American Ceramic Society, Westerville, OH, 1988, pp. 549–558.

56 M. J. Cima and J. A. Lewis. In *Ceramic Powder Science II*. Ceramic Transactions, Vol. 1. (G. L. Messing, E. R. Fuller, Jr., and H. Hausner, Eds.) The American Ceramic Society, Westerville, OH, 1988, pp. 549–558.

57 I. C. Madsen, R. J. Finney, R. C. A. Flann, M. T. Frost, and B. W. Wilson. *J. Am. Ceram. Soc*. **74** (3), 619–624, 1991.

58 M. Hoppe and J. Bereiter-Hahn. *IEEE Trans. on Sonics and Ultrasonics*. **SU-32** (2), 289–301, 1985.

59 R. T. DeHoff. In *Characterization of Ceramics*. Ceramics and Glass: Science and Technology, Vol. 3. (L. L. Hench and R. W. Gould, Eds.) Marcel Dekker, New York, 1971, pp. 529–553.

60 S. W. Freiman. In *Characterization of Ceramics*. Ceramics and Glass: Science and Technology, Vol. 3. (L. L. Hench and R. W. Gould, Eds.) Marcel Dekker, New York, 1971, pp. 555–579.

61 L. Berrin and R. C. Sundahl. In *Characterization of Ceramics*. Ceramics and Glass: Science and Technology, Vol. 3. (L. L. Hench and R. W. Gould, Eds.) Marcel Dekker, New York, 1971, pp. 583–624.

62 T. J. Headley and R. E. Loehman. *J. Am. Ceram. Soc*. **67** (9), 620–625, 1984.

63 W. F. Hammetter and R. E. Loehman. *J. Am. Ceram. Soc*. **70** (8), 577–582, 1987.

64 W. E. Brownell. In *Structural Clay Products*. Applied Mineralogy, Vol. 9. Springer-Verlag, New York, 1976, pp. 126–164.

65 K. G. Ewsuk. "The Effects of Hot Isostatic Pressing on Microstructure and Properties of Sintered Lead Zirconate Titanate." M.S. dissertation, Pennsylvania State University, University Park, 1982.

66 K. G. Ewsuk and G. L. Messing. *J. Mater. Sci*. **19**, 1530–1534, 1984.

67 B. Jaffe, W. R. Cook, Jr., and H. Jaffe. *Piezoelectric Ceramics*. Academic Press, New York, 1971.

68 S. Fushimi and T. Ikeda. *J. Am. Ceram. Soc*. **50** (3), 129–132, 1967.

69 A. I. Kingon and J. B. Clark. *J. Am. Ceram. Soc*. **66** (4), 253–256, 1983.

70 A. I. Kingon and J. B. Clark. *J. Am. Ceram. Soc*. **66** (4), 256–260, 1983.

71 H. F. Fischmeister. In *Ceramic Microstructures '86, Role of Interfaces*. Materials Science Research, Vol 21. (J. A. Pask and A. G. Evans, Eds.) Plenum Press, New York, 1987, pp. 1–14.

72 M. Rühle, G. Necker, and W. Mader. In *Advanced Characterization Techniques for Ceramics*. Ceramic Transactions, Vol. 5. (W. S. Young, G. L. McVay, and G. E. Pike, Eds.) The American Ceramic Society, Westerville, OH, 1989, pp. 341–359.

73 R. M. German. *Liquid Phase Sintering*. Plenum Press, New York, 1985, p. 9.

74 K. G. Ewsuk. In *Materials and Processes for Microelectronic Systems*. Ceramic Transactions, Vol 15. (K. M. Nair, P. Pohanka, and R. C. Buchanan, Eds.) The American Ceramic Society, Westerville, OH, 1990, pp. 279–295.

75 R. L. Fullman. *Trans. Met. Soc. AIME*. **197** (3), 447–452, 1953.

76 O. H. Kwon and G. L. Messing. *J. Am. Ceram. Soc*. **67**, C43–45, 1984.

77 W. A. Kaysser. In *Ceramic Powder Science II*. Ceramic Transactions, Vol. 1. (G. L. Messing, E. R. Fuller, Jr., and H. Hausner, Eds.) The American Ceramic Society, Westerville, OH, 1988, pp. 955–968.

78 C. A. Handwerker, J. M. Dynys, R. M. Cannon, and R. L. Coble. *J. Am. Ceram. Soc*. **73** (5), 1365–1370, 1990.

79 C. A. Handwerker, J. M. Dynys, R. M. Cannon, and R. L. Coble. *J. Am. Ceram. Soc*. **73** (5), 1371–1377, 1990

80 R. E. Johnson, Jr., and R. H. Dettre. In *Surface and Colloid Science, Vol 2*. (E. Matijevic, Ed.) Wiley-Interscience, New York, 1969, pp. 85–153.

81 "Definitions of Terms Relating to Surface Imperfections on Ceramics," *Annual Book of ASTM Standards*, ASTM F 109–73. American Society for Testing and Materials, Philadelphia, 1981.

82 "Recommended Practices for Determining Hermeticity of Electron Devices by a Bubble Test," *Annual Book of ASTM Standards*, ASTM F 98–72. American Society for Testing and Materials, Philadelphia, 1981.

83 "Recommended Practices for Determining Hermeticity of Electron Devices by Dye Penetration," *Annual Book of ASTM Standards*, ASTM F 97–72. American Society for Testing and Materials, Philadelphia, 1981.

84 "Recommended Practices for Determining Hermeticity of Electron Devices with a Helium Mass Spectrometer Leak Detector," *Annual Book of ASTM Standards*, ASTM F 134. American Society for Testing and Materials, Philadelphia, 1981.

85 "Test Methods and Procedures for Microelectronics," MIL-STD 883, Method 1014.2, Naval Publications and Forms Center, Philadelphia, 1977.

6

Inorganic Glasses and Glass-Ceramics

RICHARD K. BROW

Contents

6.1 Introduction

Two material characteristics separate glasses from other solids: (1) glasses have noncrystalline structures and, (2) instead of melting when heated, a solid glass slowly transforms to a liquid in a temperature range defined as the glass transition.

The short-range (polyhedral level) bond structure of glasses and crystals are similar. For example, the structure of amorphous silica consists of silicon tetrahedra linked by bi-coordinated oxygen, the same short-range bonding as found in crystalline quartz. Recent neutron diffraction studies reveal that the intratetrahedral bond-lengths and angles in fused silica are virtually identical to those in crystalline polymorphs. However, the atomic arrangements (e.g., intertetrahedral bonding) in a glass are indistinct much beyond the polyhedral level. Crystalline solids have repeating atomic arrangements that are defined by the unit cell and can be quantitatively characterized using X-ray or electron diffraction techniques. The broad distributions of the interpolyhedral bond-lengths and angles in a glass structure result in essentially an infinite unit cell that produces very broad, indistinct large angle X-ray or electron diffraction patterns. The properties of polycrystalline materials are often controlled by the chemistry of their grain boundaries; there are no grain boundaries in glasses.

The transition from a solid glass to a liquid (the glass transition) is kinetically sluggish and thermodynamically distinct from that of a crystalline solid. Crystalline

materials undergo a first-order transition to a liquid when heated through their melting point, whereas the glass transition is of a higher thermodynamic order.

The two unique features of glass (i.e., the noncrystalline structure and the glass transition) are usually considered "bulk" phenomena and thus are not typically probed using surface-sensitive spectroscopic techniques. However, as discussed in Section 6.3, local bonding information can be obtained using surface techniques like X-ray photoelectron spectroscopy (XPS). The glass transition is usually studied using thermal analytical techniques (e.g., differential scanning calorimetry). In some cases (particularly for low-transition-temperature glasses), dynamic information can by obtained by surface-sensitive probes, including photons and neutrons.

Glasses can be prepared from a wide variety of materials, including metals (Fe–B–P alloys, Au_4Si, Pd_4Si, etc.), organics (e.g., polyethylene, poly[vinyl chloride], etc.) and inorganic compounds. These latter materials include technologically important compositions based on oxides, chalcogenides, and halides. In this review, we discuss the characterization of inorganic glasses; techniques discussed in other chapters that have been developed to analyze the surfaces of conventional metals and polymers work equally well for glassy metals and polymers.

In general, surface analytical techniques are most often used to correlate the nature of glass surfaces with surface-dependent material properties. For example, the mechanical strength of a glass is dependent on the size and distribution of surface microcracks. Interactions between these cracks and the ambient atmosphere weaken a glass through the process of subcritical crack growth. In addition, chemical bonding of materials to glass (i.e., attaching silane coupling agents when preparing glass/polymer "fiberglass" composites; bonding glass to metal or glass-to-ceramic for hermetic packages) is dependent on surface chemistry. The ability of a glass fiber to transmit light is dependent on controlling the composition of the fiber surface to produce the necessary refractive index profile. The chemical durability of a glass is controlled by surface reactions with the ambient liquid or gas. This latter example is discussed in greater detail in Section 6.4.

Microanalytical techniques are also useful for characterizing heterogeneities in bulk glasses. Processing defects, including stones and striae (resulting from unmelted raw materials or from furnace refractories), bubbles, and crystallized regions, can be characterized by analytical electron microscopic, including micro-diffraction. Such techniques are useful for characterizing distinctly different phases in glasses that have been purposely crystallized (glass-ceramics) or that have phase-separated (e.g., Vycor, Pyrex). A study of the nucleation and growth of crystalline phases in a technologically useful glass-ceramic composition will be reviewed in Section 6.5.

6.2 Possible Surface Analytical Artifacts

Because most technologically useful glasses are electrically insulating, care must be taken when using charged particles as an analytical probe. For example, Figure 6.1

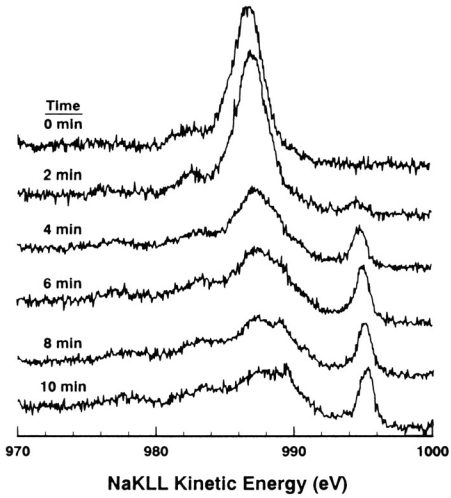

Figure 6.1 **NaKLL spectra collected from a $30Na_2O{\cdot}70SiO_2$ glass bombarded by a 3 keV, 0.50 mA/cm^2 electron beam for various times. Note the development of the peak near 994 eV due to Na^0.**

shows the X-ray induced Na-KLL spectra from a 30 mole % Na_2O, 70 mole % SiO_2 glass surface bombarded by a 3 keV, 0.5 mA/cm^2 electron beam. The broad peak near 987 eV in the spectrum from glass that was freshly fractured in vacuum prior to exposure to the electron beam is typical for sodium involved in ionic bonds with oxygen, as expected from the atomic structure of sodium silicate glasses. Exposure to the electron beam has two effects on the surface sodium: (1) Na is depleted from the surface, and (2) much of the remaining sodium has been reduced to the metallic form, as indicated by the new peak near 994 eV. The sodium depletion results from the migration of Na^+ ions away from the charged glass surface. This effect is well known and can be compensated for in Auger electron spectroscopy (AES) or in analytical scanning electron microscopy (ASEM) by using defocused primary electron beams with reduced current densities or by cooling the samples to liquid nitrogen temperatures to reduce the Na mobility.[1] Oxygen outgassing from electron bombarded glass surfaces is another well-known artifact.[2]

"Inert" ion beams can also affect the surface composition and structure of inorganic glasses. Figure 6.2 shows the effect of a 2.5 keV Ar-ion beam with different current densities on the surface sodium concentration (measured by XPS) of the $30Na_2O{\cdot}70SiO_2$ glass mentioned previously. Again, there is a systematic depletion of sodium, the rate of which is dependent on the beam current density. The sodium depletion is dependent on both charge-induced migration of Na^+ ions and preferential sputtering of the different oxide components of the glass.[3] Modifications to the atomic bonding of glass surfaces often accompany the compositional changes. The O 1*s* spectra of Ar^+-bombarded alkali silicate glass show increasing concentrations of bridging oxygen, relative to nonbridging oxygen, as the surface becomes

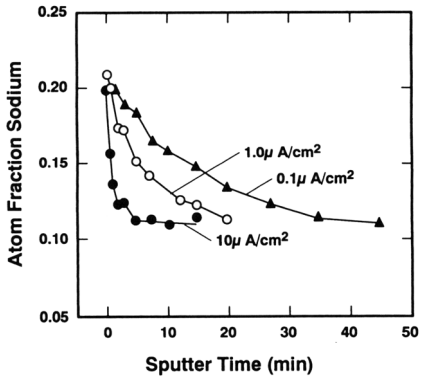

Figure 6.2 **Surface concentration of sodium on a $30Na_2O{\cdot}70SiO_2$ glass initially fractured in vacuum, then bombarded by a 2.5 keV Ar-ion beam operated at various current densities. (From Reference 3.)**

alkali depleted.[3, 4] This is consistent with an increase in surface structural polymerization caused by the decrease in the alkali-to-silicon ratio. Clearly, such behavior must be considered when one employs ion beams to obtain depth profiling information (i.e., in secondary ion mass spectrometry [SIMS] experiments or when one uses ion beams with other surface sensitive spectroscopies like AES or XPS). These effects can be mitigated by neutralizing the surface with low-energy electrons or by using neutral particle beams.

Transition metals can be incorporated into glasses, and their oxidation states might be affected by the surface analytical probe. For example, Figure 6.3 shows the Cu 2*p* spectra collected from a 50 mole % CuO·50 mole % P_2O_5 glass melted under reducing (*top*) and oxidizing (*middle*) conditions; both spectra were collected after short exposure times to the 300 W Mg–Kα X-ray source. The reduced glass

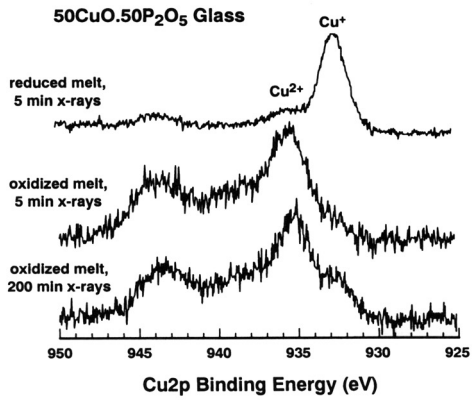

Figure 6.3 **Cu 2*p* spectra (5 min, 300 W Mg–kα X-rays) collected from a $50CuO{\cdot}50P_2O_5$ glass melted in reducing (*top*) and oxidizing (*middle*) conditions; the latter sample was then exposed to the X-ray source for 200 min, after which the Cu 2*p* spectrum (*bottom*) shows the development of a Cu^+ peak.**

spectrum is dominated by a peak near 934 eV, due to Cu^+, whereas the oxidized sample has a Cu 2*p* binding energy near 937 eV due primarily to Cu^{2+}. When this latter sample is exposed to the X-rays for 200 min (typical for a number of different high-resolution spectra from a single sample), a shoulder on the Cu 2*p* spectrum (*bottom*) due to Cu^+ clearly develops. Cu^{2+} (and other transition ions) is susceptible to X-ray-induced reduction. Operating with a lower X-ray power minimizes this effect.

Finally, it is worth emphasizing that the composition and structure of glass surfaces can be distinctly different from the bulk characteristics, even if the surface has been exposed to ambient conditions for only short times. An extreme example is shown in Figure 6.4, where survey spectra from the surface of a B_2S_3 glass (developed for IR transmitting applications) fractured in vacuum (Figure 6.4*a*) are compared with those collected from the same sample after exposure to air for approximately 1 min (Figure 6.4*b*). This very hygroscopic sample readily reacted with the ambient water vapor to form an oxide surface layer that is depleted in S. The increase in the B 1*s* binding energy of the oxidized sample (from ~192.0–193.5 eV, relative to a C 1*s* energy of 284.8 eV due to adventitious carbon) is consistent with the greater ionicity of the B–O bond compared with a B–S bond.

More conventional, chemically stable glasses also have modified surfaces relative to their bulk as a result of interactions with the ambient atmosphere. In a review of glass and ceramic surface analyses, Pantano[5] has shown that commercial sodalime silicate glasses exposed to the ambient have carbonaceous overlayers (consisting of both hydrocarbon and carbonate phases) on surfaces that are alkali-depleted as a result of interactions with atmospheric water and carbon dioxide. Pantano uses techniques including XPS, AES, ion scattering spectrometry (ISS), SIMS, and sputtered-induced photon spectrometry (SIPS) to qualitatively and quantitatively characterize these surface layers.

For additional information about potential problems that can be encountered during the surface analysis of glass, the reader is directed to several reviews available

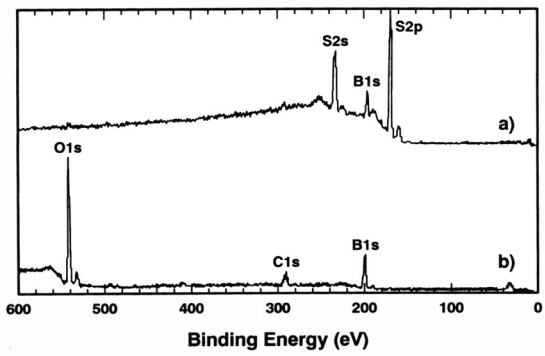

Figure 6.4 **Survey photoelectron spectra from a B_2S_3 glass (*a*) fractured in vacuum, then (*b*) exposed to air for 1 min.**

in the literature.[6–9] The recent *Proceedings of the Tenth University Conference on Glass Science*[10] contain over 30 papers on the physics and chemistry of glass surfaces with a particular emphasis on characterization. Several references from these *Proceedings* are included in the following examples.

6.3 XPS Studies of Bonding in Glass

As mentioned already, the local atomic bonding of atoms in a glass is comparable to that in the corresponding crystal; in general, cations and anions form similar polyhedral arrangements in crystalline and amorphous materials. The structural similarity breaks down at the level at which the polyhedra are arranged; crystals have symmetric polyhedral arrangements, whereas glasses do not. As a result, diffraction techniques that precisely locate the relative positions of ions in a crystal cannot provide comparable information about the long-range atomic structure of glass.

Several surface-sensitive techniques can provide details about bonding in amorphous materials. Such information complements structural analyses obtained by traditional bulk analytical techniques like Raman and infrared spectroscopy, solid state nuclear magnetic resonance spectroscopy, and Mössbauer spectroscopy.

X-ray absorption techniques, including EXAFS and XANES, have been used to characterize cationic polyhedra in a variety of glasses (see the review by Greaves[11]); for example, these analyses have revealed a degree of alkali and alkaline earth clustering in silicate glasses, suggesting new mechanisms for many transport-dependent properties. Information about atomic arrangements can be obtained by characterizing the mass-to-charge ratio of ionized species sputtered from glass surfaces during neutral-beam SIMS experiments.[7] ESR (electron spin resonance) measurements of powders can be used to characterize electronic defects associated with glass surfaces.[12] Finally, XPS is a powerful tool for quantitatively characterizing bonding in simple glasses. Several examples of anion-substituted phosphate glasses are discussed below; the literature contains many other XPS studies of a wide range of glass compositions.

Careful sample preparation is critical for obtaining useful structural information from surface-sensitive techniques such as XPS. We have found that fracturing the glass sample in vacuum immediately before analysis produces a surface with a structure and composition that is most representative of the bulk. For reasons already outlined, polished samples or samples exposed to the ambient have compositionally and structurally altered surfaces that yield misleading results. Surfaces that are created by inert ion sputtering in vacuum also are altered relative to the bulk.

Because most inorganic glasses are electrically insulating, some sort of charge referencing must be done in order to compare accurately binding energies measured from different samples. Binding energies can be corrected by referencing the C 1*s* peak for adventitious carbon at 284.8 eV.[13] However, this procedure is generally unsatisfactory, particularly for samples fractured in vacuum that generally exhibit very little C 1s intensity. Charging can also be compensated for by referencing the

binding energies of different intense peaks to those reported for similar materials. However, as reported by Tasker et al.,[14] subtle structural information might be lost when this charge correction technique is employed. Instead, they suggest depositing Au dots on the glass surface and, in conjunction with a low-energy electron flood gun, using the Au 4*f* binding energy as a reference.

Two types of oxygen ions are present in binary alkali (or alkaline earth) phosphate (or silicate) glasses: those that link neighboring P-tetrahedra (labeled "bridging oxygen") and those that are bonded to only one tetrahedron (nonbridging oxygen). These latter oxygens are charge-compensated by neighboring alkali or alkaline earth cations. Adding an alkali oxide to a phosphate glass increases the concentration of nonbridging oxygen; the resulting depolymerization of the phosphate network significantly affects a variety of properties. Quantitative structural analyses show that the bridging-to-nonbridging oxygen ratio (BO/NBO) in binary alkali phosphate glasses ($xR_2O \cdot (1 - x)P_2O_5$) depends on the mole fraction of R_2O (the quantity x) according to

$$\text{BO/NBO} = 0.5(3 - 4x) \tag{6.1}$$

Note that Equation 6.1 also works for divalent oxides (R'O) added to P_2O_5.

Contributions from the bridging and nonbridging oxygens are easily distinguished in the O 1*s* spectra from binary phosphate glasses (Figure 6.5*a*); the more ionic nonbridging oxygen has an O 1*s* binding energy approximately 2 eV lower than the bridging oxygen. The areas of each respective contribution can be measured to provide a BO/NBO ratio that is in excellent agreement (Figure 6.5*b*) both with results obtained by other spectroscopic techniques (in this case, by ^{31}P MAS NMR spectroscopy[15]) and with the predictions of Equation 6.1. Comparable

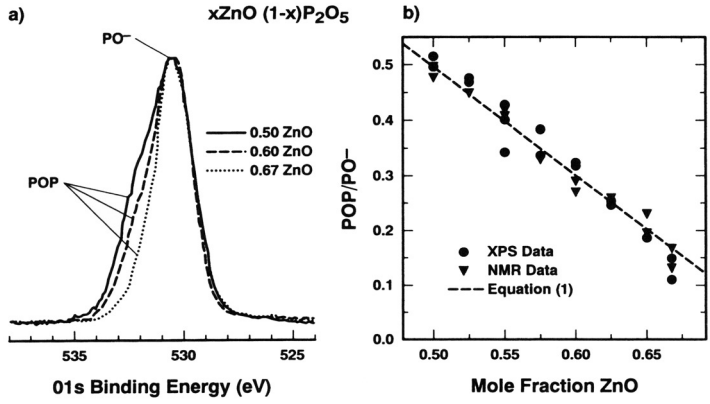

Figure 6.5 **(*a*) O 1*s* spectra from several xZnO·$(1 - x)P_2O_5$ glasses; (*b*) quantitative bridging-to-nonbridging oxygen ratios determined from the O 1*s* spectra and from ^{31}P MAS NMR. The dashed line is the predicted ratio based on Equation 6.1.**

structural information is described in an XPS study of sodium silicate and sodium aluminosilicate glass.[14]

Significant concentrations of other anions, including N and F, can be substituted for O in phosphate glasses, and analyses of the O 1*s* (and the N 1*s* or F 1*s*) spectra provide valuable information about how such incorporations modify the glass structure. For example, N-incorporation systematically reduces the BO\NBO ratio in a $NaPO_3$ base glass in a way that suggests that both BO and NBO are replaced by N-species.[16] Fluorine, on the other hand, preferentially replaces bridging oxygen to form P–F bonds (confirmed by the F 1*s* spectra).[17] The resulting extensive structural depolymerization is consistent with the large decrease in glass transition temperature and significant increase in thermal expansion coefficient with F-incorporation.

Multiple F-sites can also be characterized in more complex fluorophosphate glasses. Figure 6.6 shows the F 1*s* spectra from a sodium aluminophosphate-base glass with different levels of F-incorporation. After charge referencing and comparing the two binding energy peaks with those collected from various standard samples, the peak at ~688.3 eV is attributed to F bonded to P and the peak at ~685.5 eV is from F bonded to Al. Quantitative analyses of the relative peak areas[17] reveal that, when F is added to an aluminophosphate glass, it first bonds to Al. Once all Al sites are saturated, additional F then bonds to P. Similar XPS information about F-bonding has been reported for other glass systems.

6.4 Corrosion in Water

The interactions between glass surfaces and water, both liquid and vapor, produce altered surface layers that range in scale from a monolayer to several millimeters

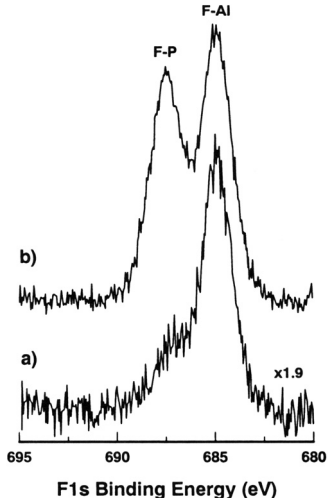

Figure 6.6 **F 1*s* spectra from a sodium aluminophosphate glass containing (*a*) 5 wt % F and (*b*) 15 wt % F. (From Reference 22.)**

thick and thus can be studied by nearly any analytical tool. In this section, we will review several corrosion studies that employ a number of different techniques.

Water Vapor

Water vapor is chemisorbed to pristine silica surfaces, forming silanol (Si–OH) bonds. Investigators can qualitatively analyze different silanol species, including free hydroxyls and vicinal (hydrogen bonded) hydroxyl groups, using a variety of vibrational spectroscopic techniques. For high-surface-area silicas (e.g, Cab-O-Sil, sol-gel SiO_2), IR and Raman spectroscopic studies show that the formation of silanol species can be correlated with the disappearance of spectral features associated with strained siloxane linkages. The strained bonds are believed to result from the presence of 2- and 3-membered siloxane rings, perhaps concentrated at the glass surface.[18, 19] For example, Figure 6.7 shows the Raman spectra collected from a high-surface area, sol–gel-derived amorphous silica sample originally dried at 600 °C in vacuum. This drying step creates a significant concentration of strained siloxane bonds, as revealed by the sharp peak at 608 cm^{-1} (labeled "D2"). When this sample is exposed to water vapor, the D2 signal decreases and the peak at ~3740 cm^{-1} increases; this latter feature is due to the SiO–H stretch. These spectral changes can be summarized by the following chemisorption reaction[18]:

$$\text{Si–O–Si} + H_2O \rightarrow \text{Si–OH HO–Si} \tag{6.2}$$

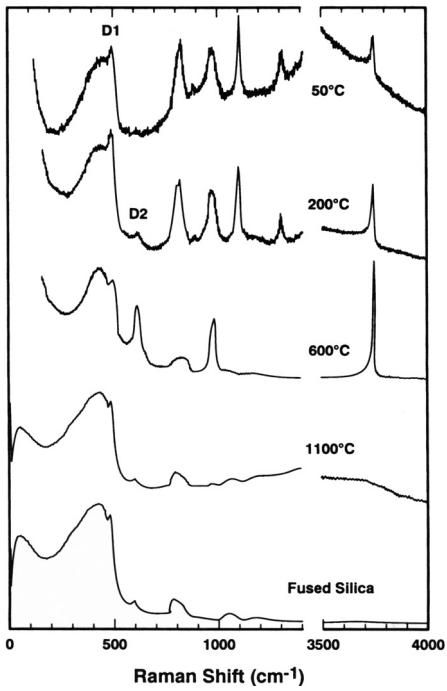

Figure 6.7 **Raman spectra of SiO_2 gels dried at 50 °C, heated to 200 °C or 600 °C, or fully consolidated at 1100 °C. (From Reference 19.)**

where Si–O–Si represents a strained siloxane surface site. ^{29}Si MAS NMR spectroscopy, including ^{1}H cross-polarization experiments, provides complementary information about the changes in the surface structure of these materials.[19]

Further exposure of glass surfaces to water vapor results in the formation of physisorbed water layers. These layers have their own vibrational signatures in the IR. In addition, the analyst can obtain quantitative adsorption information using both microbalance and modified BET techniques; two recent papers describe such analyses on SiO_2 optical fibers and on E-glass fibers.[20, 21] Such studies have more than academic interest; developing an understanding of the chemical and physical adsorption of water on glass surfaces is crucial to controlling a variety of technological properties, from the ultimate strength of a glass fiber (influenced by stress corrosion interactions between the fiber and adsorbed water) to the wettability and adhesion of polymer matrix materials in fiberglass composites.

Aqueous Solutions

The surfaces of multicomponent glasses are significantly altered when exposed to aqueous solutions; the extent of the alteration layer is dependent on a variety of parameters, including the glass composition, the duration of exposure, the temperature and pH of the solution, and the ratio of the glass surface area to the solution volume. This section is not intended to be a discussion of the aqueous corrosion of glass; rather, several different studies are mentioned to provide an overview of the analytical tools that characterize such interactions.

The initial interaction between many different silicate, borate, or phosphate glasses and water often involves an exchange between the glass ions and protonated water (H_3O^+) to produce hydrated surface layers. The compositional profiles within these corrosion layers have been characterized by many different analytical probes. Neutral primary beam-SIMS (NPB-SIMS) is particularly useful for measuring Na-profiles in the outermost (<100 nm) surface layers. Neutral Ar^0 particles have much less effect on mobile Na^+ ions in the insulating glass surface and thus are less likely to produce analytical artifacts than is the case for conventional SIMS. Reference 22 contains good examples of Na profiles obtained by NPB-SIMS from soda-lime silicate surfaces corroded in 90 °C water. Na-profiles in thin (<100 nm) corrosion layers have also been measured using AES or XPS or both in conjunction with ion milling.

Because hydrogen often is incorporated into corroded glass surfaces, the characterization of H profiles is important to understanding corrosion behavior. SIMS and SIPS are useful for characterizing H in near surface (<1 μm) layers (e.g., see Reference 23).

Ion scattering techniques are useful for characterizing corrosion layers. ISS provides information about the outermost monolayer. ERD (elastic recoil detection) is sensitive to light elements in a heavy matrix and thus provides useful H and Li profile information. Rutherford backscattering spectrometry (RBS), on the other hand,

is suitable for the analysis of heavy elements in a light matrix and thus can provide complementary information about the distribution of other glass-forming and modifying ions. Nuclear reaction analyses (NRA) also provide profile information about specific elements (e.g., H analysis by $^{1}H + {}^{15}N \rightarrow {}^{12}C + {}^{4}He + 4.43$ MeV γ-radiation). In an interesting study illustrating the advantages of employing a variety of analytical techniques, Bach et al.,[24] used SIMS, IBSCA (or SIPS), RBS, and NRA to characterize fully the hydrated corrosion layers on a $SiO_2 \cdot BaO \cdot B_2O_3$ glass.

The complementary nature of RBS and ERD analyses is illustrated in Figure 6.8, which shows Na and H depth profiles of the surface layers that form on sodium borosilicate glass corroded in pH 8 aqueous solutions for various times.[25] Na is depleted from the outermost surface and replaced by H at approximately a one-to-one ratio. ERD analyses of B-profiles show no B-depletion, and RBS analyses show no significant Si-loss at pH 8; however, the corrosion mechanism is dependent on solution pH.[25]

Depending on the experimental conditions, complex reactions can occur at the liquid–glass interfaces. For example, dissolution/reprecipitation reactions might produce surface species that can be characterized by microanalytical techniques. Figure 6.9*a* shows an optical micrograph of the surface of a complex iron-barium-phosphate glass after several months in 70 °C deionized water. The light-colored regions are corrosion reaction products. EDS analyses (Figures 6.9*b* and 6.9*c*) show that these

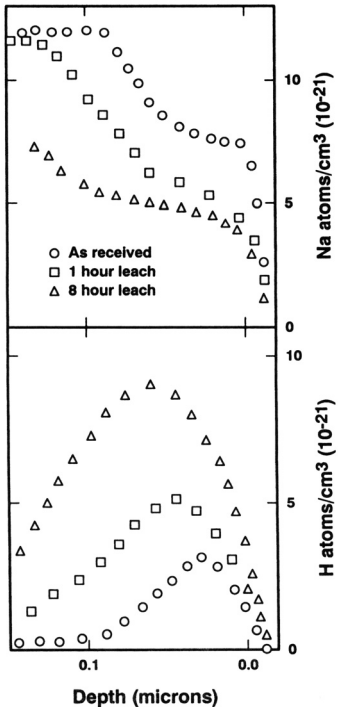

Figure 6.8 **Na (by RBS) and H (by ERD) depth profiles of the surfaces of a sodium borosilicate glass leached in a pH 8 aqueous solution at 70 °C for various times. (From Reference 25.)**

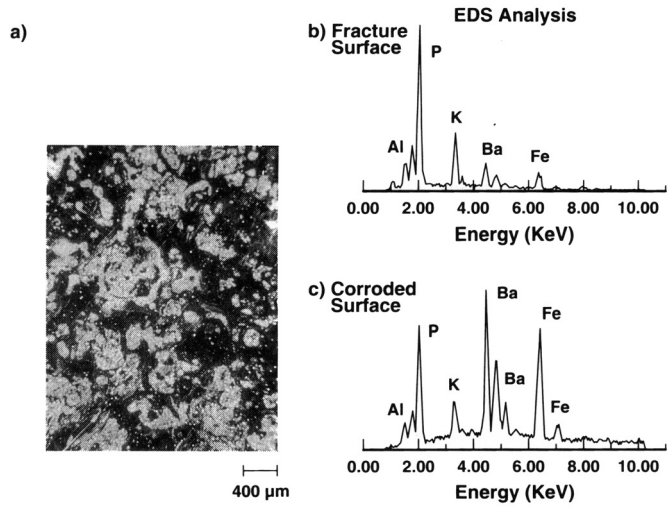

Figure 6.9 **(*a*) Optical micrograph of the surface of a barium–iron–phosphate glass corroded in water for several months; (*b*) energy-dispersive X-ray spectra of the bulk glass, and (*c*) the corrosion product which shows enhanced Fe and Ba concentrations on the surface.**

regions are rich in Fe and Ba, relative to the bulk glass, suggesting that hydrated Fe and Ba species have precipitated on the corroded glass surface. Such surface species might be further analyzed by X-ray diffraction and fluorescence techniques.

6.5 Glass Crystallization

A common processing defect associated with glass formation is the presence of crystallized regions; such regions may result from bulk or surface devitrification or may be due to unmelted raw materials or undissolved refractory phases. Analytical optical and electron microscopic techniques are most useful in identifying these phases.

In some cases, glass crystallization is desirable. Glass-ceramics are a class of materials that are processed and formed as glasses and then are carefully crystallized to

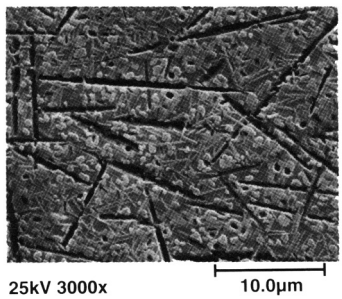

Figure 6.10 **Scanning electron micrograph of a crystallized lithium aluminosilicate glass after etching in HF.[26]**

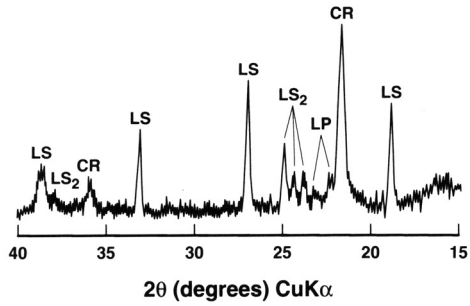

Figure 6.11 XRD spectrum of the crystallized glass-ceramic showing the presence of cristobalite, lithium metasilicate, lithium disilicate, and lithium orthophosphate phases.

obtain the properties of a ceramic. An example of the characterization of one glass-ceramic composition is described below; the details of this examination can be found in Reference 26.

Certain compositions in the $Li_2O{\cdot}Al_2O_3{\cdot}SiO_2$ system form glass-ceramics that can be used in high thermal expansion (140×10^{-7}/°C), high-strength sealing applications. Figure 6.10 shows a scanning electron micrograph of one such composition after the appropriate crystallization cycle. X-ray diffraction analyses (Figure 6.11) indicate that the high thermal expansion of the crystallized material is due to the formation of cristobalite (the equiaxed crystallites in Figure 6.10) and lithium metasilicate (the heavily etched platelets in Figure 6.10). Other crystalline phases that can be detected are lithium disilicate and lithium orthophosphate; both are present as small platelets in Figure 6.10.

A careful study of the heat treatment cycle required to form the glass-ceramic indicates that different crystalline phases epitaxially grow on heterogeneous Li_3PO_4 crystal surfaces. This is illustrated by the transmission electron micrograph shown in Figure 6.12. Crystal lattice orientations given in Figure 6.12 were determined by electron diffraction techniques and confirm the epitaxial growth mechanism.[26]

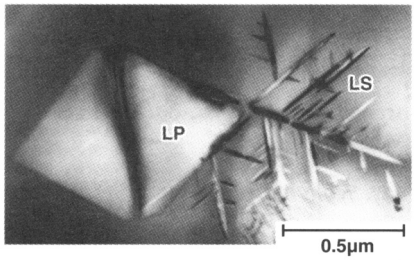

Figure 6.12 Transmission electron micrograph showing the epitaxial growth of lithium metasilicate (LS) on a lithium orthophosphate (LP) crystal in a glass-ceramic heated through a typical thermal cycle.[26]

Acknowledgment

The author wishes to thank a number of his Sandia colleagues, including G. W. Arnold, R. E. Loehman, and D. R. Tallant, for contributing their original research results to this chapter.

References

1 C. G. Pantano, D. B. Dove, and G. Y. Onoda. *J. Vac. Sci. Technol*. **13** (1), 414–418, 1976.

2 J. L. Lineweaver. *J. Appl. Phys*. **34** (6), 1786–1791, 1963.

3 R. K. Brow. *J. Non-Cryst. Solids*. **107**, 1–10, 1988.

4 R. K. Brow. *J. Vac. Sci. Technol. A*. **7** (3), 1673–1676, 1989.

5 C. G. Pantano. *Bull. Amer. Ceram. Soc*. **60** (11), 1154–1167, 1981.

6 H. Bach. *Fresenius Z. Anal. Chem*. **333**, 373–382, 1989.

7 C. G. Pantano. *Rev. Solid State Sci*. **3** (3, 4), 379–408, 1989.

8 H. Bach. *Glastech. Ber*. **56** (1), 1–18, 1983.

9 C. G. Pantano, J. F. Kelso, and M. J. Suscavage. In *Advances in Materials Characterization*. (D. R. Rossington, R. A. Condrate, and R. L. Snyder, Eds.) Plenum Press, New York, 1982, pp. 1–38.

10 *Proceedings*. The 10th University Conference on Glass Science. *J Non-Cryst. Solids*. **120**, 1989.

11 G. N. Greaves. In *Glass: Science and Technology*, Vol. 4B. (D. R. Uhlmann and N. J. Kreidl, Eds.) Academic Press, San Diego, 1990, pp. 1–76.

12 D. L Griscom. In *Glass: Science and Technology*, Vol. 4B. (D. R. Uhlmann and N. J. Kreidl, Eds.) Academic Press, San Diego, 1990, pp. 151–251.

13 "Practice for Reporting Spectra in ESCA," *Annual Book of ASTM Standards*, E 1015-84. American Society for Testing and Materials, Philadelphia, 1984.

14 G. W. Tasker, D. R. Uhlmann, P. I. K. Onorato, M. N. Alexander, and C. W. Struck. *J. Phys*. **46** (12), C8-273–C8-280, 1985.

15 R. K. Brow, R. J. Kirkpatrick, and G. L. Turner. *J. Non-Cryst. Solids*. **116**, 39–45, 1990.

16 R. K. Brow, M. R. Reidmeyer, and D. E. Day. *J. Non-Cryst. Solids*. **99**, 178–189, 1988.

17 Z. A. Osborne, R. K. Brow, and D. R. Tallant. In "Properties and Characteristics of Optical Glass II." *Proceedings*. SPIE 1990 International Symposium on Optical and Optoelectronic Applied Science and Engineering. **1327**, 203–211, 1990.

18 B. C. Bunker, D. M. Haaland, T. A. Michalske, and W. L. Smith. *Surf. Sci*. **222**, 95, 1989.

19 C. J. Brinker, R. K. Brow, D. R. Tallant, and R. J. Kirkpatrick. *J. Non-Cryst. Solids*. **120**, 26–33, 1990.

20 G. M. Nishioka. *J. Non-Cryst. Solids*. **120**, 34–39, 1990.

21 L. A. Carman and C. G. Pantano. *J. Non-Cryst. Solids*. **120**, 40–46, 1990.

22 H. J. Franek and G. H. Frischat. *J. Non-Cryst. Solids*. **42**, 561–568, 1980.

23 I. S. T. Tsong. In *Advances in Materials Characterization*. (D. R. Rossington, R. A. Condrate, and R. L. Snyder, Eds.) Plenum Press, New York, 1982, pp. 39–57.

24 H. Bach, K. Grosskopf, P. March, and F. Rauch. *Glastech. Ber*. **60** (1), 21–46, 1987.

25 B. C. Bunker, G. W. Arnold, D. E. Day, and P. J. Bray. *J. Non-Cryst. Solids*. **87**, 226–253, 1986.

26 T. J. Headley and R. E. Loehman. *J. Amer. Ceram. Soc*. **67** (9), 620–625, 1984.

7

Ceramic Microstructures

ALTAF H. CARIM

Contents

7.1 Introduction

Regardless of whether the application is structural, electronic, optical, or refractory, the performance of a given ceramic material is intimately linked to its microstructure. The arrangement of phases, interfaces, and defects on the microscopic and submicroscopic scale governs a wide range of properties, including everything from fracture toughness to superconducting current densities. This chapter presents an introduction to the microstructural features that are of interest in ceramic materials and discusses the appropriate techniques for analyzing particular types of microstructural problems.

A wide variety of features define the microstructure of a solid. In the following discussion, information on three-dimensional components such as grains, inclusions, and pores is considered first. This includes the shapes, sizes, and distributions of all structurally or chemically distinct phases. One section focuses specifically on the growth of crystalline grains and on some different morphologies that may result. In multiphase systems, the connectivity of each type of phase may need to be considered. Three-dimensional secondary phases include fine amorphous or crystalline inclusions and boundary layers, which are particularly prevalent in

ceramic materials. Finally, the extent of porosity—the presence of intrinsic or processing-induced voids within the material—is critical in the fabrication of ceramic bodies and in their electromagnetic and mechanical behavior.

On a two-dimensional level, there are also several types of important microstructural features. Grain boundaries and interfaces between dissimilar phases control the properties of many systems. Defects, such as twins, stacking faults, and domain boundaries, often develop along specific habit planes in crystalline materials.

The most common one-dimensional features are dislocations. The generation and motion of dislocations, though not as important as in most metal systems, are still central issues with respect to plastic deformation and the production of planar defects in ceramics. Such defects also form readily during film or crystal growth, as a result of thermal expansion mismatches, and to relieve lattice mismatch at interfaces.

Finally, there are zero-dimensional or point defects that could also be considered part of the microstructure of the material. These include vacancies or foreign atoms substituting at atomic positions in a crystal lattice as well as interstitial atoms residing in between the normal atomic sites. They are not discussed further in this chapter, partly due to limited space and partly because they are not amenable to observation by the same sorts of microscopic techniques typically used to define the other aspects of the material microstructure. More information can readily be found in the many existing treatises on point defects and crystal chemistry in the literature.[1]

The various microstructural features discussed above are presented in further detail below, and a number of illustrative examples are provided. The following section specifically addresses methods of phase identification with respect to both crystal structure and chemical composition. Finally, the chapter concludes with a brief description of stereology—the quantitative extraction of information about a three-dimensional solid from the two-dimensional images of sections or surfaces that are normally available.

7.2 Bulk Microstructural Features

Grain Size, Shape, and Growth

There are many possible shapes and arrangements for individual grains in a crystalline material. A familiar type of microstructure, similar to that often seen in metals, is shown in Figure 7.1. This image is a scanning electron micrograph of a titania (TiO_2) surface that has been polished and then thermally etched. A number of grains and their boundaries are visible, along with several pores situated upon the boundaries (dark elliptical areas). For optical microscopy or scanning electron microscopy (SEM) of single-phase samples such as this one, either thermal or chemical etching is usually necessary in order to delineate the grain boundaries. In multiphase samples, on the other hand, the optical and chemical differences between the distinct compounds make phase boundaries evident.

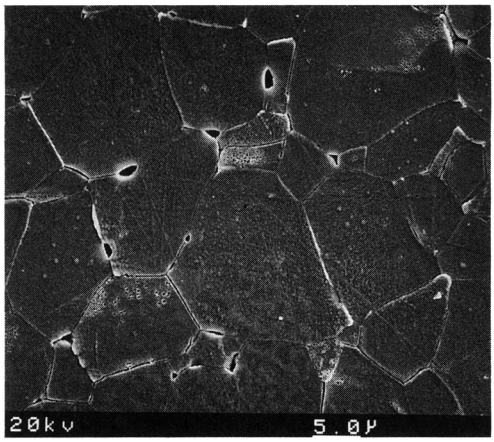

Figure 7.1 **Scanning electron micrograph of the grain sizes and shapes for a sintered compact of TiO_2. Grain boundaries have been revealed by thermal etching. Occasional pores are seen, situated along the grain boundaries or at triple points. (Courtesy of D. Hague, The Pennsylvania State University.)**

Whatever their initial size, almost all grains eventually succumb to grain growth at elevated temperatures. The reduction of grain boundary interfacial energy provides the driving force for straightening out curved boundaries, and the resulting growth of the average grain size by dissolution of the smallest grains is regulated by the atomic diffusion across boundaries. This process is therefore exponentially dependent on the temperature of the heat treatment. Grain shape is important in this process, since polyhedral grains with few sides tend to shrink while those with more sides and concave boundaries generally grow. The rate of grain growth is also inversely proportional to grain size itself, and thus the change in average grain diameter from the original grain size ($\Delta d = d - d_0$) should be proportional to the square root of time. In real samples, however, this dependence is often modified by the presence of inclusions or sample size limitations which slow the grain growth. So-called abnormal or discontinuous grain growth, sometimes referred to as secondary recrystallization, may also occur; this is a phenomenon in which a few very large, many-sided grains grow rapidly at the expense of smaller ones due to the high curvature at the boundaries between grains of very different sizes.[2]

Finally, individual grains can occasionally take on highly unusual shapes. In Figure 7.2, a transmission electron microscope (TEM) image of a Pb–Zr–Ti–O thin film is presented. The light phase in the background consists of a phase with the pyrochlore structure, while each roughly circular region associated with the darker phase is actually a single crystal, albeit porous, with a perovskite-type unit cell. The basis for these determinations is discussed below in the section on phase identification. All of the filamentary portions within each darker circle (actually a

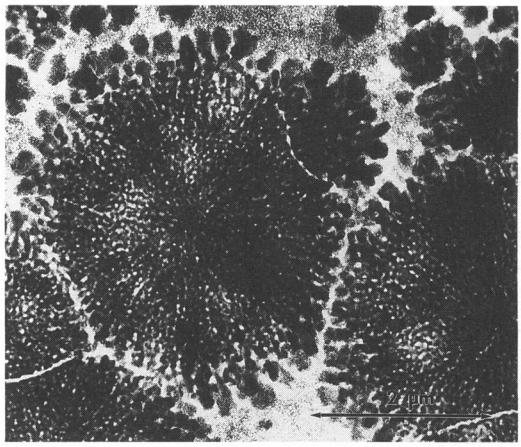

Figure 7.2 **Transmission electron micrograph showing the "rosette"-shaped single-crystalline grains of perovskite phase (*dark*) and the surrounding fine-grained pyrochlore matrix (*light*) in a thin film of lead zirconate titanate (overall composition $PbZr_{0.53}Ti_{0.47}O_3$).**

pill-box shape in three dimensions) of perovskite are of the same crystallography orientation and are interconnected.

Connectivity

For multiphasic materials, a full understanding of their three-dimensional microstructure also includes a knowledge of how the separate phases are linked together. This is particularly important in electronic and magnetic ceramics, for which issues such as electronic transport along continuous pathways are central to the performance of the material.[3] The degree of connectivity is usually expressed as the number of dimensions (out of the usual three orthogonal spatial directions) in which each phase is self-connected.[4] For instance, isolated particles of one phase in another, such as ceramic particulates distributed in a metal matrix composite, would constitute a microstructure with 0–3 connectivity, since the inclusions are not continuous in any dimension but the matrix is fully continuous in three dimensions. Similarly, a composite with a uniaxial arrangement of continuous fiber reinforcements would be 1–3 and a multilayered material (such as thin-film X-ray mirrors or quantum well heterostructures—or, in a less exotic vein, plywood) would be 2–2. One particular area of interest is the change in properties at the percolation limit, where the amount of a dispersed second phase becomes large enough to force connections between the dispersoids, altering the connectivity of a composite material from 0–3 to 3–3. The percolation limit can be directly distinguished by sufficiently careful microstructural evaluations, especially with depth-sensitive tools such as scanning acoustic microscopy, or indirectly by the way in which the connectivity change influences electrical or mechanical behavior.

Boundary Layers and Inclusions

Thin layers of amorphous material (or, occasionally, crystalline reaction products) that entirely coat grain boundaries are especially prevalent in ceramics, and inclusions at boundaries are seen in many heterogeneous materials. The presence of a glassy (amorphous) phase at the boundary is generally associated with the segregation of an impurity species to that region. The impurity destabilizes the crystalline regularity of the bulk compound and thus, effectively, a film of glass is formed, which wets the boundary. Well-known examples include silicate boundary layers in ZrO_2 and amorphous oxide and oxynitride interlayers, sometimes containing Y, in Si_3N_4.[5, 6] The most common sources of these impurities are the sintering aids that are incorporated in the ceramic and the milling media that are used to reduce the particle size in the starting powder.

Precipitates on grain boundaries can be a major factor in inhibiting grain growth, since the migration of a boundary is hampered when it is pinned by second-phase particles. Inclusions also affect the mechanical properties of the ceramic via interactions with dislocations and point defects, and precipitate stress fields may influence the further segregation of other species dissolved within the grains.

Porosity and Density

Pores in ceramic materials arise largely from processing. Grain boundary pores, for example, are evident in Figure 7.1. The sintering of powders nearly always leaves behind residual porosity that is hard to remove without applying pressure during firing. As a result, full density may be difficult to achieve. The actual density thus provides one measure of the porosity, with the efficacy of sintering often expressed by the percentage of theoretical density (the nominal value calculated from the crystal structure and lattice parameters) that has been attained. The pore volume fraction can also be determined from lineal or areal analysis of polished sections as described below. Another measure for porosity is the surface area associated with the material, usually given in area per unit mass. Applications for which this is particularly important include catalyst supports and molecular sieve materials (such as zeolites), which are highly porous. In some cases, a critical distinction must be made between open and closed porosity. The former corresponds to a 3–3 connectivity in which the pores can all be accessed from the surface. The latter is a 0–3 situation and will result in reduced density; however, the apparent surface area as measured by infiltration or immersion techniques will be quite low—perhaps several square meters per gram rather than several hundred square meters per gram—due to the isolation of the pores. Closed pores, which predominate at densities above about 90% of the theoretical density, are a major impediment to achieving full density during sintering since they are no longer linked to the surface and thus a major diffusion path has been deactivated. In addition to overall pore volume, the size of individual pores may also be of interest in assessing their effects on further processing and on materials behavior. The

final section of this chapter, on quantitative stereology, discusses the measurement of pore size.

7.3 Interfaces and Planar Defects

Grain Boundaries and Domain Boundaries

In addition to the effects on segregation and precipitation that were mentioned earlier, the total area, orientations, and atomic structure of grain boundaries in ceramics can influence both processing and properties. As an example, the flow of electrical current across single grain boundaries in the high-temperature oxide superconductors has been studied in an elegant experiment utilizing thin-film $YBa_2Cu_3O_{7-x}$ bicrystals.[7] It was found that the ratio of critical current density flowing across a boundary to the average of the bulk values for the two adjacent grains was inversely proportional to the misorientation angle. In other words, as the grain boundary angle increased, the transport became more restricted. This has important consequences with respect to the texturing of polycrystalline ceramic superconductors. It is also important to keep in mind that the distribution of grain boundaries is not random; special grain boundaries that exhibit better matching across the interface are often more common than those at which there is no crystallographic relationship. A number of means are used to quantify these special boundaries. Most deal with either the spacing of interfacial dislocations required to accommodate the tilt and/or twist between the two grains, or the number of atoms on either side that are in registry across the boundary versus those that are not.

Domain boundaries can also be thought of as special types of grain boundaries. Two types are illustrated in Figure 7.3. The development of an ordered phase from an amorphous melt or solid, or during deposition on a substrate, may involve many nucleation sites. If the growth of the initial clusters occurs in such a way that they are oriented identically but are translationally offset by part of a unit cell, they will share an imperfect interfect when they impinge. The various separately nucleated regions are known as domains, and the interfaces where they meet are antiphase domain boundaries.

Separation into distinct domains can also occur in slightly distorted structures, such as ferroelectric oxides. Many perovskite-based unit cells, such as $BaTiO_3$, are tetragonal below the Curie temperature, with the central ion displaced slightly from the middle of the cell towards one of the face centers. Since there are different directions in which the ion can be shifted, and since unit cells with like orientations tend to be clustered together rather than intimately intermixed, one can observe distinct ferroelectric domains with corresponding domain walls. The location, shape, and movement of these boundaries with applied electric fields or mechanical forces are of particular interest for the many transduction, memory, and optical applications in which ferroelectric materials are used. Ferromagnetic materials are similarly organized into domain structures.

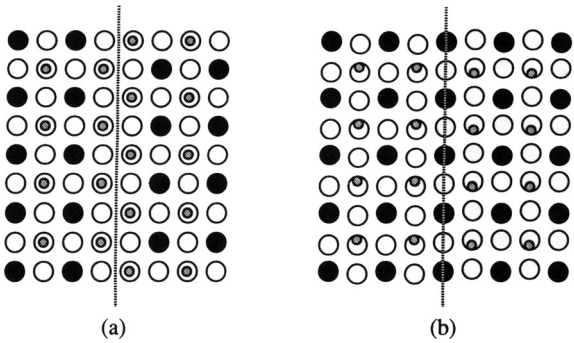

Figure 7.3 **Schematic illustration of (*a*) an antiphase domain boundary in a cubic perovskite structure for an ABO_3 material, and (*b*) a ferro-electric domain boundary in a material with a distorted perovskite cell such as $BaTiO_3$, which is tetragonal below the Curie temperature. Each sketch shows the projected atomic positions along a viewing direction corresponding to the a-axis, or [100], of the crystal structure. A atoms are dark, B atoms are grey, and oxygen atoms are the large white circles.**

Heterogeneous Interfaces

The simplest heterogeneous interface is a surface, which can nonetheless be quite complex indeed. Faceting of a surface may occur along particular crystallographic planes, and the structure of the surface layer of atoms may be different from that in the bulk due to relaxation and reconstruction of dangling bonds. Similar considerations apply to the grain boundaries mentioned previously as well as to other heterogeneous interfaces.

In the case of faceting, lattice planes with high surface or interfacial energies tend to separate into alternating, localized regions corresponding to low-energy interfaces. Figure 7.4 shows a TEM image of faceting for a SiC inclusion in an Al matrix. Each of the steps lies along a well-defined set of atomic planes corresponding to low-energy terminations of the SiC structure. The reorganization of planar crystal surfaces or interfaces into a set of facets has a number of consequences: it increases the total boundary area, which can modify chemical segregation; it influences mechanical properties and adhesion across the boundary; and it affects the lattice matching at any given point along the boundary.

Although interatomic relaxation and reconstruction may occur at solid–solid interfaces, the topic of epitaxy is a more prominent issue and has been of great interest for a number of years now.[8] Formation of an epitaxial relationship implies that one crystalline phase (often in thin-film form) is nucleated and grown upon another (a substrate) in such a way that a well-defined macroscopic orientation relationship occurs between the two as a result of lattice and chemical matching at the interface. The uniform formation of an appropriately oriented single-crystalline overlayer is of paramount concern in reliable fabrication of electronic and optical

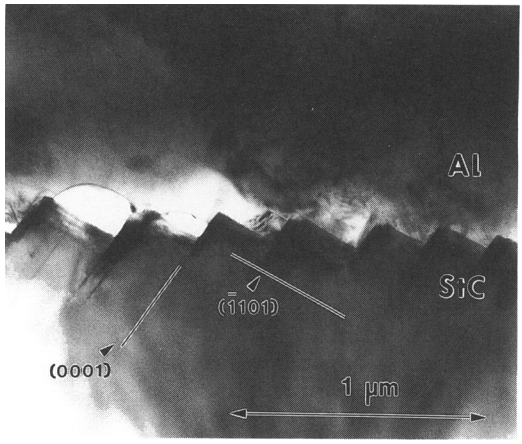

Figure 7.4 **Facets at the edge of a SiC grain embedded in an Al matrix. The SiC planes along which the steps lie have the indicated indices. Stacking faults along the basal (0001) planes are seen extending into the SiC from the step edges on the left side of the micrograph.**

devices. For instance, epitaxial growth of oxide superconductors on specific ceramic substrates is very desirable for microwave and other applications. A high-resolution TEM image of the $YBa_2Cu_3O_{7-x}$ superconductor deposited on a $LaAlO_3$ substrate is presented in Figure 7.5.[9] A direct correspondence between the crystallography in the film and that in the substrate is evident, although there are some irregularities in the film corresponding to interfacial and internal defects. The (001) planes of both the orthorhombic superconductor and the nearly cubic $LaAlO_3$ are parallel to the interface, and the *a*- and *b*-axes ([100] and [010] directions) of the $YBa_2Cu_3O_{7-x}$ are aligned with the same $LaAlO_3$ directions in the interfacial plane. This orientation relationship at the interface persists over the entire sample; other studies have shown that it is disturbed only by foreign particles or preexisting steps at the substrate surface.

Stacking Faults and Twins

Planar defects within individual grains are also important components of the microstructure. Stacking faults, in which the normal sequence of layers is locally disturbed by the insertion, removal, or partial translation of a single atomic plane, are readily revealed in most materials by etching or by TEM. They often occur as growth defects in thin films, although it is also possible for them to be induced by further processing or environmental effects. As an example, basal-plane stacking faults propagate into the SiC crystal from the step edges in Figure 7.4. The accumulation of vacancies or interstitials on a single plane produces a dislocation loop enclosing a fault, which is intrinsic if it results in a missing plane (vacancies)

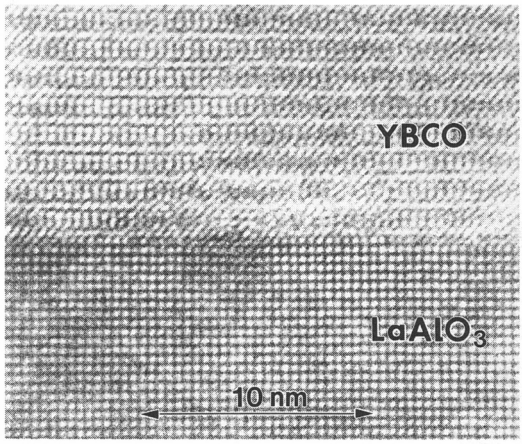

Figure 7.5 **High-resolution TEM image of the interface for an $YBa_2Cu_3O_{7-x}$ film (YBCO) grown on a single-crystal $LaAlO_3$ substrate. The geometrical lattice mismatch at the growth temperature is only a few percent, allowing a clear epitaxial relationship to develop.[9]**

and extrinsic if an extra plane is inserted (interstitials). Therefore, any damage mechanism that generates such point defects may produce stacking faults as well. Ion implantation in semiconductor fabrication, neutron irradiation in nuclear waste containment applications, and reactions requiring large free volume changes are examples of such processes. In some cases the growth, shrinkage, or annihilation of the faults can be utilized to evaluate the kinetics of the damage mechanism.

Twins are planar crystal defects across which the local structure of the crystal on one side is a mirror image of that on the other side. Deformation twins commonly occur as a means of accommodating shear strains, while growth twins typically arise from the nucleation of a single incorrect layer and subsequent reversal of the order of planes. The presence of twins can sometimes be discerned purely from the external shape of a crystal, as well as by TEM or etching experiments. Readily twinned ceramics include calcite, sphalerite, graphite, and some of the high-temperature oxide superconductors. In the last, the spacing of twin boundaries is related to the degree of orthorhombicity in the unit cell and is thus indicative of the oxygen content.

7.4 Dislocations

The primary one-dimensional or line defects seen in solids are dislocations. In general, dislocation formation and motion require more energy in ceramics than in metals. This is due to the complex atomic structures of ceramics, which often have large unit cells, and to the typically strong and localized bonding between atoms in

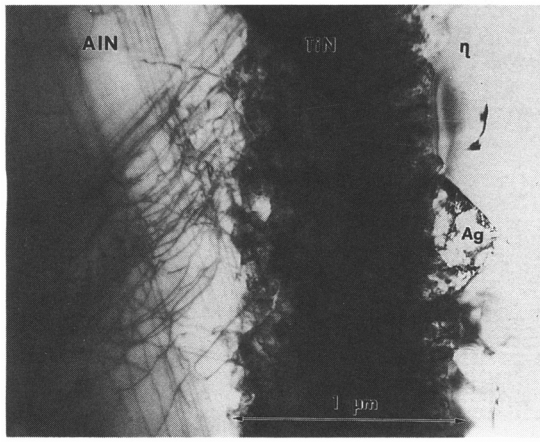

Figure 7.6 **Dislocations generated in AlN as a result of thermal expansion coefficient mismatches during the cooling of a joint containing a metallic interlayer from the joining temperature.[11] The TiN, η, and Ag regions are reaction products from the joining process.**

ceramics. With respect to the first of these, the energy associated with a dislocation is proportional to the square of the magnitude of the Burgers vector **b**, $E\alpha[\mathbf{b}]^2$ (see Reference 10). Since the displacement **b** typically corresponds to a lattice translation vector in the unit cell, it is usually larger for ceramic compounds than for metals, and dislocations are correspondingly harder to create. Furthermore, the interatomic bond strength is typically greater in ceramics due to ionic or covalent bonding. Dislocations cannot travel easily through ceramics since their motion requires the breaking and re-forming of such bonds along the dislocation line. Broken bonds or perpendicular steps (jogs) along the linear defect may also give rise to effective electrical charges for dislocations in ionic compounds.

The ease of dislocation generation and motion is intimately related to a material's ability to deform plastically. Consequently, knowledge of how dislocations are distributed in a ceramic often can be used to evaluate prior deformation. For instance, dislocations in many oxides are located in close-packed planes of oxygen atoms, and so these planes are associated with slip. Nonoxides may also sustain line defects after mechanical damage or thermal shock, and the location of dislocation clusters often reveals regions of localized deformation. As an example, Figure 7.6 shows dislocations created in an AlN substrate after reactive bonding of two such substrates with a Ag–Cu–Ti foil at high temperature. Reaction products at the interface provide a strong series of chemical bonds, but the variation in thermal expansion coefficients across the joint leads to local damage during the cool-down from the joining temperature.[11] In this particular study, it was found that only the top (bonded) layer of AlN grains actually deformed, for it contained the thermal mismatch dislocations. Subsequent cracking occurred at the set of grain boundaries

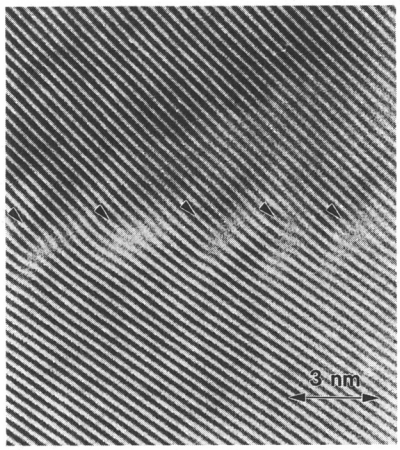

Figure 7.7 **Dislocation array at an asymmetric low-angle boundary in ZrO_2. The individual lattice planes are distinguished in this high-resolution transmission electron micrograph. Each arrow indicates the termination of a lattice plane in an interfacial dislocation.**

between the highly defective interfacial grains and the next layer of nearly defect-free grains farther removed from the interface.

If a number of dislocations line up in a row, a low-angle grain boundary or so-called subgrain boundary will result. The high-resolution image of Figure 7.7 displays a low-angle (nonsymmetric) grain boundary in a sintered compact of zirconia and also reveals the termination of individual lattice planes at interfacial dislocations. The regular spacing of dislocations in the interface accommodates the slight misorientation of the two adjoining regions. Reorganization into subgrains results in an energetically more favorable situation than having individual dislocations scattered throughout the crystal. Subgrain boundaries can also be readily distinguished by diffraction-contrast imaging in the TEM showing the curtain-like array of dislocations or by electron diffraction techniques which indicate the tilt or twist between the crystal orientations on either side of the boundary.

7.5 Methods of Phase Identification

In practice, nearly the entire array of characterization tools has been employed to determine the identities of unknown phases. The ensuing discussion begins by addressing the microstructural examination of phase distributions. Full identification of any particular phase in the microstructure requires knowledge of both crystal structure and chemical content; each of these topics is discussed with respect to the types of analyses best suited to obtaining the necessary information. Both elementary techniques and advanced analytical approaches are mentioned; one should

keep in mind that increasingly complex methods usually require more time and have higher costs!

Phase Distribution

Most materials are multiphase, and the analyst's first task prior to identifying particular phases is understanding the distribution and location of the various phases that are present. For this purpose, optical microscopy (OM) is often the most appropriate initial step in microstructural characterization. Differences in reflectivity (or light transmission, for thin transparent samples) allow one to distinguish between distinct phases in the microstructure. Samples can also be viewed between crossed polarizing filters, allowing transmission only from optically birefringent crystals. Other specialized techniques, such as interference contrast, allow the analyst to observe very small changes in surface height across an uneven specimen. Beyond the approximately half-micron resolution limit of conventional OM, SEM can serve a similar function. In addition to showing the surface topography in fractured or as-grown samples, SEM can delineate the boundaries of submicron phase fields if polished surfaces are examined. The contrast arises from differences in the generation of secondary or backscattered electrons by the chemically and structurally distinct regions.

Examination of the phase distribution on an even finer scale—down to the atomic level—may require TEM. Contrast between different materials can arise simply due to differences in electron scattering, with increased scattering, and thus reduced transmission, generally correlated with heavier elements. More commonly, however, diffraction contrast is predominant. Diffraction events are sensitive to crystallographic orientation and distortion, making it possible to distinguish between phases by limiting the specific diffraction phenomena that contribute to the image.

In many cases, the biggest difficulty in TEM is the preparation of suitable samples. First, specimen preparation for TEM is generally difficult, tedious, and destructive. Methods that work for one material may not be adequate for another. There are also potential problems with introducing artifacts such as dislocations and other defects during the grinding, polishing, or ion milling (sputtering) steps. Furthermore, since the specimen volume examined is so small, one must take care to confirm that the region examined is representative of the overall sample. Although not well-suited for routine analysis of large numbers of samples, TEM is an extraordinarily powerful method for phase identification and microstructural evaluation as long as selected specimens provide the desired information and concerns about the sample integrity can be appropriately addressed.

SEMs, electron microprobes, and TEMs with suitable X-ray dispersive spectroscopy equipment can be used to evaluate the chemical compositions of phases, as described below. These instruments provide very powerful methods for examining phase distribution: X-ray maps of a particular area can be obtained by rastering the

electron beam, producing a visual image of the relative proportions of one or more elements across the field of view.

Crystal Structure of Phases

Crystal structure can be unambiguously identified using X-ray diffraction (XRD). In the simplest case, for a homogeneous single-phase material, one can confirm that the observed compound is the expected one by comparing the location of diffraction peaks with known, tabulated structural data. XRD is often the appropriate starting point for phase identification in multiphase materials as well. One can, in principle, determine the number and type of all major phases present. In some cases this is still insufficient; one may need to identify the structure of individual regions (grains, inclusions, interfacial layers). This cannot be accomplished by XRD because of the lack of spatial resolution. There are other limitations as well: compounds that are present in small quantities but which may be an important part of the microstructure, such as fine internal precipitates, often cannot be detected at all by X-ray methods. Amorphous regions are also not analyzed.

OM is incapable of providing direct information on atomic structure because the wavelength of visible light is orders of magnitude larger than the typical unit cell lattice parameters. Indirectly, however, one can make some inferences. For instance, as stated above, only birefringent materials will be imaged in transmission when placed in a polarizing microscope, and thus it is possible to conclude that the phases seen are neither amorphous nor cubic since such materials are not optically anisotropic. Information on crystal structure is not readily available in SEM either, although under some special circumstances electron-channeling patterns that reflect the structure can be obtained.

TEM is one technique capable of assessing atomic structure over much smaller areas than can be analyzed by XRD. Crystallographic information is provided by the diffraction events taking place within the sample, which lead to the formation of an electron diffraction pattern. Selected-area diffraction patterns are most common, with the source of the diffracted and transmitted electrons being constrained to the area of interest on the sample by an aperture. If the grain size is small and if the material only contains one or two phases, a ring pattern can be obtained using a large objective aperture that allows the signal from many grains to be included. Such a pattern is analogous to a Debye–Scherrer X-ray pattern and includes rings of intensity from all diffracting planes in the selected area. Consequently, a ring pattern allows determination of all interplanar spacings, although it sacrifices angular information.

Selected-area diffraction patterns exhibiting discrete, periodic spots arise from single-crystal grains or particles, in analogy to X-ray Laue patterns. They provide lattice spacings from the diffracting planes which contain the beam direction as well as the interplanar angles between these planes. Examples of both ring and spot patterns are shown in Figure 7.8. These diffraction patterns were recorded from the

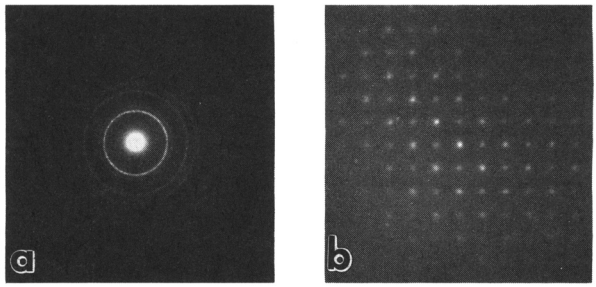

Figure 7.8 **Selected-area electron diffraction patterns allowing identification of the two distinct phases in the Pb–Zr–Ti–O film from Figure 7.2. (*a*) Ring pattern from the pyrochlore phase that constitutes the fine-grained matrix (*lighter areas*). (*b*) Spot pattern obtained along [001] in a single "rosette" of the nearly-cubic perovskite structure (*darker areas*).**

Pb–Zr–Ti–O film pictured in Figure 7.2. Analysis of the ring pattern, taken from a light region containing many nanometer-scale grains, indicates that it arises from a cubic pyrochlore phase with a lattice parameter of 1.04 nm. The spot pattern was obtained by limiting the electrons to one of the porous, dark areas with a selected-area aperture. The fourfold symmetry, the interplanar spacings derived from the spot separations, and the interplanar angles all indicate that the pattern corresponds to the [001] direction in a (nearly) cubic perovskite-type unit cell for $Pb(Zr,Ti)O_3$ with a lattice parameter of about 0.40 nm. Thus, both phases in this complex microstructure were readily identified by electron diffraction in the TEM. Phase identifications were confirmed by additional diffraction patterns and compositional analyses by energy-dispersive X-ray spectroscopy.

Due to aperture restrictions, selected area methods are only applicable for examining areas of perhaps 0.5 μm or more in diameter. It is also possible to obtain spot patterns from much smaller areas—down to as little as a nanometer or so in diameter—by using a focused incident electron beam, rather than an aperture, to limit the sample area under examination. Such microdiffraction patterns are somewhat more complex due to the nonparallel illumination, but they may also contain more information. For example, so-called convergent-beam electron diffraction (CBED) patterns provide three-dimensional information about the compound's crystal chemistry and can be used as a sensitive fingerprint for a given atomic structure.[12]

Chemical Composition of Phases

The composition of single-phase materials can be determined by a wide range of wet chemistry techniques and bulk analysis procedures, including such varied methods as atomic absorption spectroscopy, X-ray fluorescence, and magnetic resonance spectroscopy. For most materials, however, the chemical composition of each component in a complex microstructure is of interest. In order to ascertain this,

one must be able to image the microstructure and simultaneously determine composition within some selected portion of it. The most routine method is to employ the SEM. With an energy-dispersive spectrometer (EDS) system attached, elemental analysis can be readily carried out in a specific region by locating the incident beam on the point of interest. The electron microprobe provides similar information in quantitative form, usually employing a slightly different wavelength-dispersive X-ray spectroscopy (WDS) system that provides better resolution but requires much longer analysis times. In each system, the characteristic X-rays generated by interaction of the incident electron beam with the sample are used to determine the elements that are present and their relative quantities. Many phases can be identified in this way, particularly if one has additional information about the sample from knowledge of the raw materials and processing or from other methods such as XRD. One drawback to compositional analysis by SEM or microprobe is that the micron-scale penetration and scattering of the energetic electron beam precludes analysis of particles or areas smaller than this, since the signal from the surrounding volume will necessarily be included.

Once again, the use of TEM may be justified if the regions to be examined are very small (submicron to atomic-level). Because the TEM samples are thin, electron scattering does not lead to an analysis area much broader than the diameter of the beam. Electron diffraction patterns are often sufficient to identify the phases if the chemical species in the sample are few and known. Otherwise, one can use EDS or electron energy-loss spectroscopy (EELS)—both of which can be performed in situ on a suitably equipped TEM—to evaluate the elemental composition of the particle.[13] EELS, as the name suggests, provides a spectrum of the kinetic energy lost by the illuminating electrons as they pass through the sample. Characteristic edges in the energy distribution occur at the energy-loss values corresponding to orbital binding energies in the constituent atoms, since these bound electrons are ionized by energy transfer from the incident electrons. EELS is particularly sensitive to lighter elements (down to atomic number $Z = 3$, lithium); it can yield binding-state information and also provide a means of measuring the sample thickness using the low-energy-loss peaks. Modern EDS systems, on the other hand, are now capable of routinely detecting elements down to $Z = 5$ (boron) and generally are simpler to use and interpret than EELS. By employing suitable standards, EDS can provide excellent quantitative results. EDS also does not require the extremely thin specimen areas necessary for the collection of EELS spectra.

7.6 Stereology for Phase Quantification

It is sometimes necessary to extract quantitative data on three-dimensional features from two-dimensional sections or surface micrographs taken by OM, SEM, or TEM. Such data extraction requires a careful consideration of how the two-dimensional representation samples the true three-dimensional objects. This branch of metrology, or measurement science, is known as stereology.[2, 14] Detailed techniques for the

determination of number, surface area, volume fraction, and other information on arbitrarily shaped particles or inclusions have been developed and are of great utility in biological applications.[15] For ceramics or other solid inorganic materials, however, one can usually employ some simplifying assumptions to reduce the experimental work required to obtain unbiased estimates of microstructural parameters.

A number of variables are of interest in describing microstructure, and the choice of which measure to use may depend on the problem at hand or on the characteristics of the microstructure itself. The most widely used parameter in metallography, and more recently in ceramics, has been the grain size. One of the complications in specifying microstructural measurements is that the dimensionality of both the quantity of interest and the means of measurement must be considered. For instance, "grain size" can refer to the linear diameter, surface area, or volume of grains as measured from linear intercepts, sectional areas in a plane, or from actual volumetric measurements (which are extremely difficult to obtain in practice). Relationships have been derived between many of these measures, although conversion of a measurement based on one variable to a value in a different dimension (say, from intercept lengths measured within grains to the three-dimensional diameters of the grains) requires further assumptions about the grain shape.

Grain Size and Mean Lineal Intercept

Presently, the most common method of specifying grain size is by the mean lineal intercept. For this to be a valid measure, one must sample grains along lines that are randomly oriented across an optical, SEM, or TEM micrograph. Ideally, micrographs are taken from sections cut perpendicular to each other in the material so that measurements in all three specimen dimensions are incorporated. The mean intercept $\overline{L}$ is found simply by $\overline{L} = L_L/N_L$, where the lineal fraction L_L is the length of the line segments falling within the phase of interest per unit length of the test line and N_L is the number of points where the lines intercept the features of interest (grains) per unit length of test line. Note that this approach is applicable for multi-phase samples as well as for single-phase material and so can be used for dispersed particles in air or other media as well as for dense sintered compacts. Similarly, it allows analysis of pore sizes since pores can be regarded as one "phase" within a multiphase sample. The mean lineal intercept provides an experimentally simple method for defining grain size, although the manner in which it corresponds to the actual dimensions of the grains is quite dependent on their shape and size distribution.

For simple cases, the relationship between three-dimensional sizes and $\overline{L}$ can be geometrically determined. It can be shown, for example, that uniformly sized spherical particles have a diameter given by $d = 1.5\overline{L}$. Note also that the internal surface area per unit volume, S_V, is simply related to the mean lineal intercept for a three-dimensional structure of space-filling grains by the equation $S_V = 2/\overline{L}$.

This makes it possible for the analyst to obtain quantities such as the grain boundary area in a polycrystalline material from simple linear measurements on

plane sections. The relationship cited here depends critically on the randomness of the sections used but is independent of grain shape or isotropic arrangement.

Measurements of average grain size by X-ray peak widths can be very useful for bulk powders and sintered ceramics, although care must be taken to compare with an X-ray spectrum of the same compound on the same instrument to accurately determine the instrumental contribution to the line broadening. Unfortunately, this method is not suitable for ceramic thin films because of the interference from substrate peaks and the small volume of sample that is irradiated, giving an insufficient signal-to-noise ratio in most cases. The data provided by X-ray line broadening refer to the average diameter of a three-dimensional grain assuming a spherical particle shape.[14]

Volume Fraction of Phases

Information on the relative quantities of the various phases in the microstructure is also often desirable. These data are most frequently expressed as the volume fraction, V_V, of the features of interest within the microstructure. If one assumes a random sample without substantial anisotropy, one conveniently finds that the volume fraction is equal to the lineal fraction described previously, as well as to the area fraction A_A and point fraction P_P: $V_V = A_A = L_L = P_P$.

The measurement of V_V can then be readily accomplished through point counting, in which one randomly superimposes a grid of points over an image and determines the proportion of them that fall within the phase or features of interest; by the lineal intercept method described previously; or by measurement of areas, which is now readily accomplished with image analysis programs for digitized micrographs such as those produced on an SEM.

7.7 Summary

One of the primary goals of modern materials science is to develop desirable microstructures that provide superior performance through controlled processing. This chapter provides an overview of many features that contribute to the overall microstructure of ceramic materials. In addition to the three-dimensional details of phase distribution that are commonly considered, other structural components including interfaces and defects may play important roles in determining the materials properties. The morphology on a microscopic scale is therefore of keen interest in the study of ceramic properties.

References

1 See, for example, (*a*) R. K. Watts. *Point Defects in Crystals*. Wiley, New York, 1976, and (*b*) R. J. D. Tilley. *Defect Crystal Chemistry and Its Applications*. Chapman and Hall, New York, 1987.

2 W. D. Kingery, H. K. Bowen, and D. R. Uhlmann. *Introduction to Ceramics*. Wiley, New York, 1976, Chapt. 10.

3 D. S. McLachlan, M. Blaszkiewicz, and R. E. Newnham. *J. Amer. Ceram. Soc*. **73**, 2187, 1990.

4 R. E. Newnham, D. P. Skinner, and L. E. Cross. *Mater. Res. Bull*. **13**, 525, 1978.

5 For example, see papers in *Science and Technology of Zirconia II*. Advances in Ceramics, Vol. 12. (N. Claussen, M. Ruhle, and A. H. Heuer, Eds.) The American Ceramic Society, Columbus, OH, 1984.

6 D. R. Clarke, N. J. Zaluzec, and R. W. Carpenter. *J. Amer. Ceram. Soc*. **64**, 601, 1981.

7 D. Dimos, P. Chaudhari, J. Mannhart, and F. K. LeGoues. *Phys. Rev. Lett*. **61**, 219, 1988.

8 *Epitaxial Growth*. (J. W. Matthews, Ed.) Academic Press, New York, 1975.

9 S. N. Basu, A. H. Carim, and T. E. Mitchell. *J. Mater. Res*. **6**, 1823, 1991.

10 D. Hull. *Introduction to Dislocations*. 2nd ed., Pergamon Press, Oxford, 1979.

11 A. H. Carim and R. E. Loehman. *J. Mater. Res*. **5**, 1520, 1990.

12 J. Mansfield. *J. Electron Microsc. Technique*. **13**, 3, 1989.

13 *Principles of Analytical Electron Microscopy*. (D. C. Joy, A. D. Romig, Jr., and J. I. Goldstein, Eds.) Plenum Press, New York, 1986.

14 For detailed treatments of stereological problems, see books such as (*a*) *Quantitative Microscopy*. (R. T. DeHoff and F. N. Rhines, Eds.) McGraw-Hill, New York, 1968, and (b) J. C. Russ. *Practical Stereology*. Plenum Press, New York, 1986.

15 H. J. G. Gundersen. *J. Microscopy*. **143**, 3, 1986.

8

Ceramic Reactions and Phase Behavior

PATRICK K. GALLAGHER

Contents

8.1 Introduction

Solid-state reactivity is a topic of enormous technological importance. It is, however, a complex subject because of the many factors influencing how solid materials react with one another and the atmosphere. These factors are based not only on the thermodynamic or equilibrium considerations that dictate the ultimate products but, more importantly, by the rates and mechanisms established through considerations of heterogeneous kinetics. The interplay between thermodynamics and kinetics leads to an infinite number of final end points depending upon the particular conditions and times of reaction.

As difficult as it may be, it is essential that the synthetic process be controlled to the degree necessary to obtain the desired product. This frequently entails choosing between competing techniques and pathways in order to obtain the following goals:

- achieving the metastable or stable product
- isolating an intermediate product
- reacting to the specified extent, partially or completely
- establishing the macroscopic and microscopic morphology
- controlling the defect structure and impurities.

Composites are of increasing technological importance. They can be partially preformed and assembled or they can be made in situ through controlled reactivity. The key to mastering these and general solid-state synthetic methods is in the control and understanding of the processes at the interfaces.

The initially heterogeneous nature of mixed solid phases dictates that diffusion paths for subsequent reactions are long and dependent upon the geometrical aspects of the assemblage as well as on the specific methods of processing. Generally, high temperatures are required to achieve the desired reactions in a reasonable time. Reaction rates are controlled by many factors other than the temperature, however. Some of these are given in Table 8.1. They are subdivided into those that act primarily through changing the path length and those that alter the activation energy for diffusion.

The factors which lengthen the pathway for diffusion not only slow the reaction, but also can lead to the formation of nonequilibrium intermediate phases. As an example, coarse particles of an equimolar mixture of $BaCO_3$ and SnO_2 will lead to the initial formation of Ba_2SnO_4 rather than $BaSnO_3$. This aspect generally makes chemically prepared mixtures, for example, sol–gel, coprecipitation, and freeze- or spray-dried solution processes, more attractive as synthetic methods.

The concept of "reactivity" is a difficult one to define adequately. Comparison of the reactivity of iron oxides prepared from various starting compounds via several processes indicates that the reactivity depends upon the particular test applied.[1] The relative order of activities determined by (1) solubility in acid at 81 °C, (2) extent of the reaction with lithium carbonate at 490 to 840 °C, and (3) the ability to sinter to high density at 1200 °C is different for each. The reactivity of a powder is a transient phenomenon which dissipates with increasing temperature. To be useful, the test for reactivity has to occur in the specific temperature range associated with the particular activity of interest.

For the purpose of ceramic synthesis, the ability to react with another material is most important. Table 8.2 lists the source of iron oxide and the temperature at which the reaction with lithium carbonate was 85% complete. The temperatures selected for the calcination of each starting compound had been determined by thermogravimetry (TG) as the minimum temperature necessary to completely

Via the Diffusion Path Length	Via the Diffusion Energy
Particle size and aggregation	Temperature
Degree of mixing	Defect structure and purity
Interparticle contacts	Topochemistry-transformations
Intraparticle porosity	External fields
Mechanism/pathway (bulk–surface–vapor)	Mechanism/pathway (bulk–surface–vapor)

Table 8.1 Some factors influencing solid-state reactivity.

decompose the precursor to iron(III) oxide. All the oxides lowered the decomposition temperature of lithium carbonate to some extent. The spread in temperatures, however, reveals a wide range in the relative reactivity among the powders.

Although iron oxide derived from the nitrate was among the most active materials in the two low-temperature tests, it was the least active in the sintering test. Its low-temperature reactivity had led to a partial sintering of the powder into hard agglomerates which were subsequently impossible to sinter to reasonably dense materials. Conversely, the oxides prepared at higher temperatures, such as from sulfates, sintered well but were less reactive at the temperatures below their formation temperature. That potential low-temperature reactivity had been consumed during formation.

In this chapter, the discussion of these topics is divided into three broad categories. The first briefly considers the starting materials and how they might influence the outcome. The second topic concerns phase equilibria and the methods used to establish the situation at equilibrium. The final section discusses how the starting materials transform into the equilibrium products; that is, what factors control the rates and mechanisms during the reaction and what methods and techniques are used to follow the course of the overall reaction process? Clearly, there is considerable overlap between the last two topics, and the experimental techniques in common are covered in the section on equilibrium.

Iron Salt Decomposed	Temperature of Calcination, °C	Temperature of 85% Reaction, °C
Iron(III) sulfate	700	535
Ammonium iron(III) sulphate	660	495
Iron(II) sulfate	720	580
Ammonium iron(II) sulfate	660	490
Iron(III) nitrate	390	570
Ammonium hexacyanoferrate(III)	670	600
Ammonium hexacyanoferrate(II)	480	840
Iron(III) oxalate	325	560
Ammonium trisoxalatoferrate(III)	500	560
Ammonium iron(III) citrate	580	800
Magnatite and EDTA	525	615
Commercial iron(III) oxide		670
Lithium carbonate		950

Table 8.2 **Formation temperatures for the formation of $LiFeO_2$ from mixtures of Li_2CO_3 and α-Fe_2O_3.**

8.2 Starting Materials

The strength of interparticle forces becomes a significant consideration in determining the effective particle size. Aggregation plays a major role in controlling the microstructure of the mixed powder. "Soft" agglomerates will readily break down during the mixing stage, while partially sintered or otherwise strongly bonded "hard" aggregates persist throughout processing. Determinations of the individual crystallite size, aggregation, distribution, and porosity are important for the preceding reasons.

Besides the simple number of interparticle contacts described above, the specific properties of the surface or interface are important. The nature of the species adsorbed, either physically or chemically, on the surface of the reactants can influence the rates of reaction and transfer across the interface. The presence of a liquid phase will alter mass transport. Surface active sites such as edges, corners, or particular crystallographic orientations are important. Dislocations, point defects, and substitutional impurities can alter diffusion to the extent of controlling the rate of reaction. Properties of the surface or near-surface regions are often determined by physical damage occurring during the mixing or grinding stage. Thus, aspects of tribology become relevant.

Many experimental tools and techniques have been developed to determine the chemical composition of the bulk material and to characterize the surface of substances under a wide variety of conditions. Most of these have been described in detail elsewhere in this series. Although these methods are not within the scope of this chapter, the results are necessary to determine the starting points or conditions for the methods described herein. Applications of thermal analysis to the quality of starting materials are deferred until the more extensive discussion of thermoanalytical methods in the section entitled "Determining the Chemical and Structural Aspects."

8.3 Phase Equilibria

General Aspects

Most phase diagrams depict the equilibrium situation as a function of composition, temperature, and, occasionally, pressure. When one or more of the components in the system is gaseous, it is essential to distinguish between the partial pressures of the active components and the total pressure. Diagrams are also prepared that display regions of metastability; however, these are specific for selected situations and processing times.

The general principles and techniques used to establish phase equilibrium are common for both equilibrium and nonequilibrium diagrams. These can be divided into three categories. One pertains to the evaluation of the chemical aspects for the system, for example, composition and structure. The second concerns the determination of the physical conditions within the system, for example, temperature, total pressure, and time. The result of such studies is a description of the variations in

the chemical nature of the system as a function of the physical environment—a phase diagram. When time is no longer a factor, the equilibrium diagram has been attained.

The third category of information is not, strictly speaking, an intrinsic part of the phase diagram. It is necessary, however, for the complete description of the system and its properties. The distribution or arrangement of the phases controls many of the properties, for example, electrical and thermal conductivity, resistance to corrosion, and mechanical properties. Knowledge is essential on both the macro and micro scale. As an example on the macro scale, composite materials are deliberately tailored to optimize these properties, particularly mechanical strength. On the micro scale, grain boundary phases control the electrical conductivity. This can be undesirable, as with insulating carbonate or hydroxide phases in high-temperature superconductors, or beneficial through the deliberate addition of dopants to produce positive temperature coefficient thermistors or more stable capacitors and inductors.

It is generally much easier to make most measurements at room temperature. Consequently, samples are frequently quenched from higher temperatures prior to characterization. The effectiveness of the quench determines the validity of subsequent interpretations. Many factors affect this uncertainty. The assumption that a quenched sample represents the true situation of the sample at the temperature and time it was quenched must always be questioned and confirmed when possible.

Determining the Chemical and Structural Aspects

Describing the chemical nature of the system requires determining the number, composition, and structure of the phases present for each set of physical and chemical conditions specified. Seldom does a single experimental method provide all the needed information. A combination of techniques is required to define the system completely.

Microscopy is the analyst's primary tool to establish the number of phases present in a material. Optical microscopy is a relatively inexpensive and simple method that can be used to distinguish between phases with differing morphology or reflectivity. The sensitivity is very high, provided that a representative sample is viewed. The proverbial needle in the haystack will stand out clearly when in the field of view. As an example, the difference in reflectivity between hematite (α-Fe_2O_3) and magnetite (Fe_3O_4) in a polished sample is dramatic and the basis for an easy way to detect the onset of oxidation or reduction for either pure phase. Similarly, twinning of one of the phases can be used to distinguish between the orthorhombic and tetragonal structures in the superconductor, $Ba_2YCu_3O_{7-x}$. Yet another factor, particle shape, clearly differentiates the whiskers in a composite matrix. Polarized light can be used to enhance detection or to reveal ferroelectric domain structure.

Because of the opaque nature of most materials, optical microscopy is limited to the surface region. Hence, the sample must be cut or abraded to reveal features as a function of depth. Thin sections may be cut to observe features in transmission.

The particle shape of a particular phase is the major means of indicating the individual phases in a powder, although differences in refractive indices can also be exploited.

Scanning electron microscopy (SEM) has many advantages, such as a greater depth of field and higher magnification. The secondary electron emission used to form the image is dependent upon the electrical conductivity of the specimen. Consequently, insulating phases have a much brighter image due to charging effects. This intense brightness is generally undesirable, and a conducting coating is applied to the specimen to alleviate this problem. Again, shape is the predominant aspect used to distinguish individual phases, and only the surface of the sample is accessible. Samples, such as many hydrates, that are unstable in vacuum are not amenable to this technique.

Improvements in SEM technology, however, have recently progressed to the stage that it is now possible to obtain commercial instruments, called environmental scanning electron microscopes (ESEM), which are capable of operation at pressures of several torr and at temperatures greater than 1000 °C. This greatly improves the versatility of the SEM and enhances its applicability to studies of phase equilibria and reactivity with the vapor phase.

Figure 8.1 shows a series of ESEM micrographs taken immediately after an in situ chemical vapor deposition experiment.[2] These pictures clearly indicate how the morphology of the deposited films of diamond on silicon depends upon the experimental conditions. A gas stream, at 15–20 torr, of 1% methane in hydrogen was flowed over a heated filament (2000 °C) to break down the methane into atomic carbon prior to deposition on the heated substrate (850 °C). This process was continued for 30 min to form films with a thickness of about 5 μm. The total pressure was then reduced to 4.3 torr for these pictures.

At the higher flow rates, the film grew as a fine-grained spherical form. At lower flow rates, better crystallized, larger grained, polycrystalline clusters formed. Similar studies can illustrate the detailed morphology during oxidation or reduction processes. Vaporization and condensation phenomena can also be monitored effectively with such an apparatus.

More detailed surface features and topography can be revealed by scanning tunneling microscopy (STM) or atomic force microscopy (AFM). The instruments employing these techniques are capable of resolution at the atomic level. Recent efforts have also shown the feasibility of manipulating and rearranging atoms on the surface. The techniques do not require vacuum and can even be used in solution to study such processes as reactions taking place at the surfaces of electrodes, corrosion, or precipitation/dissolution phenomena.

Transmission electron microscopy (TEM) offers very high resolution and magnification at the expense of considerable inconvenience in sample preparation. In addition to the tedious aspects of the sample preparation, there is concern that thinning the sample to the required degree may also change the nature of it. Nevertheless, the detailed observations possible through TEM are unmatched, and TEM

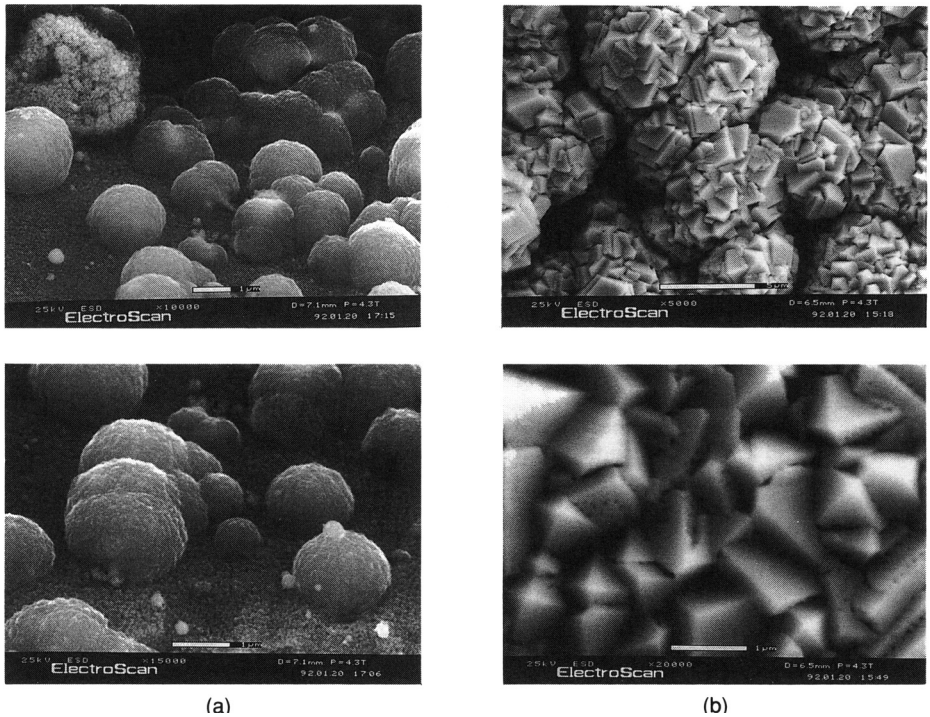

Figure 8.1 **Micrographs of diamond films formed in situ using an ESEM: (*a*) "fuzzy ball" structure and (*b*) polycrystalline structure.**

finds great use in the characterization of solid–solid interfaces. It can detect very minor amounts of additional phases.

The electron diffraction patterns possible with this technique provide the opportunity for detailed structural characterization as well. Irregularities at the grain boundaries—traces of new phases, concentrations of impurities or point defects, special angle grain boundaries, etc.—profoundly influence kinetic processes. Analysts achieve improved understanding of the topochemical processes that may control the nature and rate of the relevant decomposition, nucleation, or growth processes. Epitaxial growth is a specific example. Such preservation or changes in structure across the interface are best established by electron diffraction patterns.

Figure 8.2 illustrates the usefulness of TEM to characterize the critical interfacial boundary between the reinforcing ceramic and the intermetallic phases in a composite structure designed for use in the turbine blades of an advanced high-temperature gas turbine engine.[3] The essential properties at the high temperatures are mechanical strength and toughness, in addition to chemical stability and low weight.

Achieving these goals demands that the interface between the reinforcing and matrix phases exhibit two features. There must be evidence that the materials are thermodynamically compatible under the conditions of formation and use—no

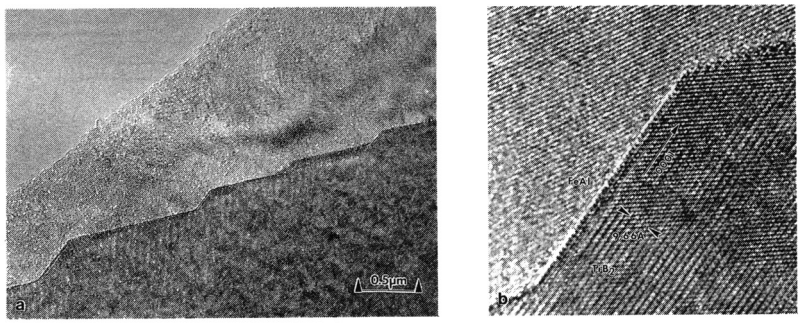

(a) (b)

Figure 8.2 **Images from a high-resolution TEM of the interface created between FeAl/TiB_2 metal matrix composite: (*a*) the faceted interface and (*b*) higher magnification of an individual facet step.**

new phases or weak structures develop at the grain boundaries. Second, the bonding between the phases must have the optimum strength. This bonding must be sufficiently strong to allow the reinforcing phase to strengthen the composite, yet not so strong as to deflect crack propagation along the interface rather than through the reinforcing phase.

The composite in Figure 8.2 was formed by isostatically hot pressing a mixture of powdered FeAl (40 at % Al) and TiB_2 in a 9:1 volume ratio followed by an anneal for 25 h at 1225 °C. The high-resolution electron micrographs reveal the clean interface with substantial bonding indicated by the smooth transition from the initially hexagonal structure of the TiB_2 to a new monoclinic phase. This transformation is thought to be induced by the slight diffusion of iron into the reinforcing phase.

X-ray diffraction is another method often used for phase identification. It is less versatile in that it is generally limited to crystalline materials. The sample preparation required for qualitative results is simple, however, and the technique is more readily applicable than microscopy to powders. It also can provide more specific and detailed information, such as any texturing or ordering of phases in the material. Although the penetration depth of X-rays is significantly greater than for optical wave lengths, the measurements are still restricted to a surface layer. Crushing, sectioning, etc., are necessary to detect interior phases, as before.

Generally, the powder diffraction patterns for different phases are unique and identifiable. The Joint Committee for Powder Diffraction Standards (JCPDS) maintains a large data base in many forms. The files are available on magnetic tape, and several versions of computer software have been developed to obtain and utilize raw experimental X-ray diffraction data. These provide routines for data acquisition, smoothing, plotting, and conversion to d spacings. The resulting converted data files are then used as input for structural determination, pattern searching, subtraction, and phase-identification programs.

Detection of a second phase is on the order of several percent for favorable conditions and much less for very complex mixtures, mixtures of materials having a very similar crystal structure and size, or those containing amorphous or micro-crystalline materials. Detection of small amounts of the defect spinel γ-Fe_2O_3, in matrices of ferrites having the spinel structure, is much more difficult than that of α-Fe_2O_3 (corundum structure).

The reduced X-ray scattering power of the lighter elements limits the ability to accurately establish numbers or positions of such important atoms as carbon, oxygen, and hydrogen in the lattice. Although, neutron diffraction is capable of this, the availability of the method is restricted.

The previous discussion has focused primarily on determining the number of phases present. The specific nature of these phases other than crystallographic structure has not been considered. Although establishing the number of phases by X-ray diffraction is also closely connected with their identification and bonding, mere determination of the pattern characteristic of a particular structure, such as spinel or perovskite, does not establish its chemical composition. The existence of many solid solutions gives rise to very similar patterns derived from totally different chemical compositions.

The diffraction techniques reveal long-range structural order, but not oxidation states. In addition, they provide little information about the nature of the bonding and site symmetry for amorphous or microcrystalline materials. In studies of solid state reactivity, this situation arises frequently. It is precisely this highly disorganized state of matter that is of greatest interest. As the material reacts or decomposes, long-range order is unlikely to be present at the reacting interface or for some ill-defined region following it. Glasses are another class of material for which diffraction techniques are less useful.

A variety of spectroscopic techniques, however, are of value to determine the local bonding and, occasionally, oxidation states of various ions. Frequently, they can perform satisfactory quantitative analysis or estimates as well. Adsorption, emission, and Raman spectroscopy operating from the UV through the IR region of the spectrum can provide such information. These optical spectroscopies can be performed in either a transmission or surface-scattering mode based on the thickness and absorption properties of the specific sample. Nuclear magnetic resonance (NMR), Mössbauer spectroscopy, and electron spin resonance techniques are some other forms of spectroscopy frequently used to determine local bonding and oxidation states of specific species, primarily in the bulk rather than on the surface. These methods are limited to particular atoms or ions and are not universally applicable.

The chemical composition for the solid phases, either individually or collectively, can be determined by traditional chemical analysis or a variety of modern instrumental methods. Such methods have been described elsewhere in this series. One important aspect, when applying these methods to study interfaces and composites, is their ability to provide spatial resolution. Unless the phases can be readily

Property	Technique
Mass	Thermogravimetry (TG)
Apparent mass[a]	Thermomagnetometry (TM)
Volatiles	Evolved gas detection (EGD) Evolved gas analysis (EGA) Thermal desorption
Radioactive decay	Emanation thermal analysis (ETA)
Temperature	Differential thermal analysis DTA
Heat[b] or heat flux[c]	Differential scanning calorimetry (DSC)
Dimensions	Thermodilatometry (TD)
Mechanical properties	Thermomechanical analysis (TMA) Dynamic mechanical analysis (DMA)
Acoustical properties	Thermosonimetry (TS) for emission Thermoacoustimetry for velocity
Electrical properties (resistance, voltage, current, and dielectric)	Thermoelectometry
Optical properties	Thermoparticulate analysis (TPA) Thermooptometry for spectroscopy[d] Thermoluminesence for emission Thermomicroscopy for structure

[a]Change induced by an imposed magnetic field gradient.

[b]Power compensated DSC.

[c]Heat flux DSC.

[d]Absorption, fluorescence, Raman, etc. Non-optical forms of spectroscopy such as NMR, ESR, Mössbauer, etc. are also applicable.

Table 8.3 Principal thermoanalytical methods. (From Reference 4; reproduced by permission of JAI, Inc.)

separated, traditional methods based upon sample dissolution provide only averaged results.

On the other hand, certain instrumental techniques—such as energy-dispersive X-ray fluorescence (EDX) in conjunction with an SEM—can selectively pinpoint particular spots or provide a mapping of the concentration over a planer surface. These techniques enable one to distinguish compositional variances between individual phases or features. Other techniques have the ability to vary the analytical spot size over a wide range. Consequently, they are capable of providing both averaged analysis over a surface or more focused specific information.

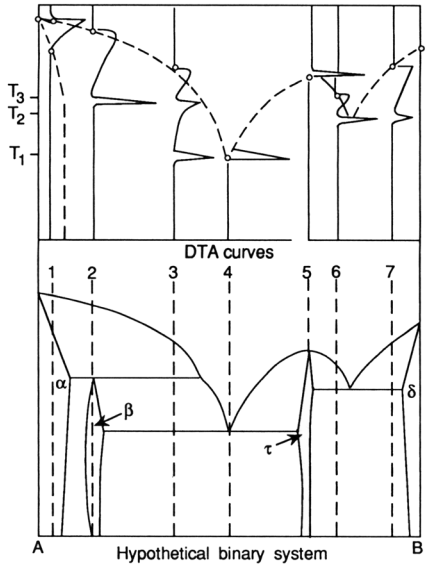

Figure 8.3 **Hypothetical phase diagram and associated DTA curves. (From Reference 5.)**

Nearly all of the methods for analyzing solids are constrained to a limited penetration depth. Consequently, they will fail to detect chemical inhomogeneities below a depth that is dependent upon the particular technique. Analysis of a partially reacted coarse powder or the surface of a sintered disk, for example, is likely to present a highly biased result favoring the exterior layer of product. Magnetic resonance measurements are an exception to this limitation.

Thermoanalytical methods constitute a powerful and versatile collection of techniques for the characterization of ceramic reactions and phase equilibria. Some property of the sample is followed as a function of time or temperature or both while it undergoes a prescribed temperature program. Table 8.3 gives the major thermal methods. The most common methods applied to studies of reactivity in ceramics are TG, differential thermal analysis (DTA), differential scanning calorimetry (DSC), evolved gas analysis (EGA), and dilatometry. The various types of spectroscopy, diffraction, and microscopy can also be conducted on a hot stage in controlled atmospheres.

The uses of these techniques in this section are divided into three categories: (1) general phase equilibria and boundaries, (2) structure and transformations, and (3) chemical composition. The next section discusses the measurement of the system's physical condition or properties. Those physical properties utilized to obtain chemical information are described in this section, however.

Differential thermal analysis (DTA) is a commonly used method to determine the location of phase boundaries. Figure 8.3 shows a hypothetical binary phase diagram and the DTA curves that would be expected for several compositions within the system. The endothermic melting and $solid_1$–$solid_2$ first-order transformations during heating are clearly evident. These peaks are due to the temporary

imbalance in temperature between the sample and reference material established by the absorption or evolution of heat by the sample during the particular endothermic or exothermic event. If the curves are measured during cooling, the direction of the excursions will be the opposite, since the events that occur are proceeding in the reverse direction.

As with many thermoanalytical measurements, there must be a compromise established between such experimental parameters as heating rate and sample size and the quality of the results in terms of sensitivity and accuracy. Faster heating or cooling rates and larger sample sizes will enhance the intensity of the signal (ΔT) and, therefore, the sensitivity. On the other hand, they lead to greater thermal lag between the temperature observed for the event and its actual equilibrium value.

The part of the peak associated with the equilibrium temperature of the event is generally accepted to be the onset temperature or first departure from the baseline. The transition will not start before the equilibrium temperature is reached and may begin significantly later depending upon the kinetics of the situation, such as a tendency toward superheating, supercooling, or other metastabilities. Once the transition has initiated, there is still a finite time required for the sample to convert completely depending upon the enthalpy, thermal transport, and temperature or sample homogeneity. Evidence for these effects is determined by the degree of temperature hysteresis between the onset temperatures during heating and cooling and variations with the heating or cooling rates.

The determination of the initial departure from the baseline is very subjective and dependent upon the quality of the baseline and the amount of amplification. The standard procedure is to report an extrapolated onset temperature measured as the intersection between the extrapolated baseline and the linear extrapolation through the smooth steepest portion of the onset side of the curve. If there is no superheating or cooling, the temperatures measured from the heating and cooling curves will tend to merge as the rate decreases. When differences persist due to metastabilities, a good general rule to consider is that the source of metastability is due to kinetic difficulties in nucleation or formation of the solid phase. Consequently, the cooling curve during precipitation of a solid from either a liquid or second solid phase is more likely to be in error.

Generally, the observation of an exothermic event during heating implies a chemical change such as oxidation or reduction, since most simple thermal decompositions and phase transformations are endothermic. Exothermic events during heating that do not involve changes in chemical composition are due to metastable to stable transformations, such as amorphous to crystalline transformations or the relief of stresses. Such changes are irreversible and, hence, do not occur during cooling or subsequent reheating.

The phase transformations described above have been first-order transformations with measurable enthalpies. Second-order transformations, however, only exhibit a change in heat capacity at the transformation. Examples are many magnetic transitions, the glass transition in polymers, and some crystallographic transitions

where very little atomic movement is necessary to accommodate the rearrangement. Such transitions do not show peaks in the DTA or DSC curves, but rather a step in the baseline. Figure 8.4 presents the DTA curve for a heavy metal fluoride glass. The glass transition near 200 °C is followed by metastable to stable crystallization peaks and then melting peaks at approximately 300 and 400 °C, respectively.

Many of the other thermoanalytical techniques will identify phase transformations, but DTA and differential scanning calorimetry (DSC) are most often used. The same considerations described for DTA apply to DSC. TG measures mass loss as a function of temperature and time. Restricting the discussion at this point to phase boundaries without compositional change limits TG to measuring vaporization processes. Vaporization is thermodynamically reversible and therefore depends on the partial pressure of the component in the atmosphere. If one is uncertain about the specific nature of the gaseous products, then evolved gas analysis (EGA) is used to distinguish between simple vaporization and decomposition.

Thermodilatometry not only measures the thermal expansion of a material but also will indicate the following: phase transformations; shrinkage due to sintering, dehydration, crosslinking, or softening; and expansion due to solvent uptake, precipitation of a second phase, formation of trapped gases, etc. First-order transitions show a discontinuity in volume, whereas second-order transformations exhibit a change in slope of the thermal expansion curve. Softening points can be determined using a pointed probe which will penetrate as the material softens.

Reduction in surface area and open porosity for a powdered sample is not readily measured by dilatometry. Density, BET adsorption isotherms, or emanation thermal analysis (ETA) are the applicable techniques. The latter is accomplished in a scanning temperature mode and, therefore, is capable of more rapidly identifying the significant temperature regimes. ETA involves substantial effort in sample preparation, however. A radioactive gas or its parent must be incorporated into the

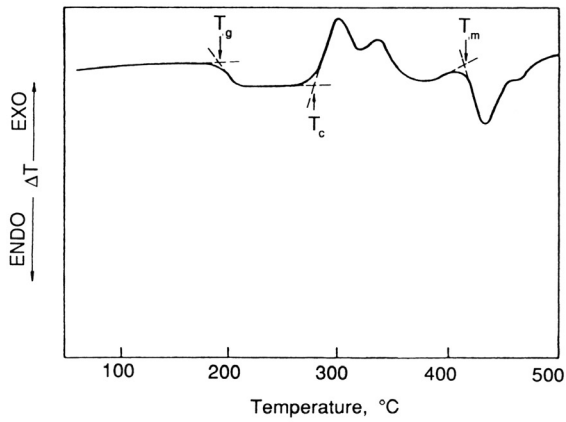

Figure 8.4 DTA curve for a glass ($0.5BeF_2 \cdot 0.3KF \cdot 0.1CaF_2 \cdot 0.1AlF_3$), 25 mg at 20 °C·min^{-1} in N_2.

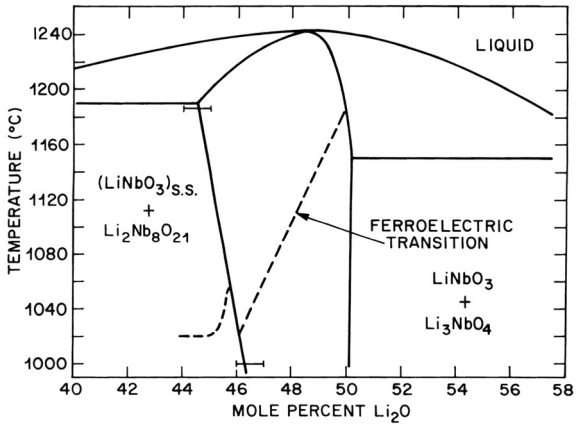

Figure 8.5 Phase diagram for the lithium niobate system.

sample, usually by ion implantation. The radioactivity in the gas stream is measured as the sample is heated. The rate of escape of the gas is proportional to the effective surface area so that regions of sintering or collapsing porosity are indicated by a marked reduction in the radioactivity of the gas stream.

Changes in crystal structure as a function of temperature are frequently measured using hot-stage X-ray diffraction. Isothermal steps of an appropriate size are made and the desired region of 2θ is scanned at each step. Alternatively, the temperature is programmed to change slowly while the region of 2θ is scanned repeatedly. Not only is the transition temperature indicated, but also the specific nature of the transition and the change in lattice parameters as a function of temperature are identified. Thermal expansion can be accurately computed for each crystallographic axis from the lattice parameter data.

Thermoanalytical methods can also be used to derive specific information about the chemical composition of the material as well as its transitions and structure. The liquidus line of the phase diagram is sometimes used to determine composition in relatively simple phase systems. Even in the more complex diagram shown in Figure 8.3, the liquidus temperature to the left of the eutectic (about 50% A) is a unique function of the composition.

Occasionally, solid–solid transformations will be dependent on the specific composition. An example is the tetragonal to cubic transformation in solid solutions of perovskites where Sr or Pb have been substituted for Ba in $BaTiO_3$. The transition temperature measured by DTA or DSC will be indicative of the extent of substitution.

Figure 8.5 shows the phase diagram for the lithium niobate system.[6] There is a wide range of lithium deficiency in lithium niobate. Since electro-optic applications of this material require large crystals having a very uniform composition, it is essential that the congruent composition be known very accurately in order to grow

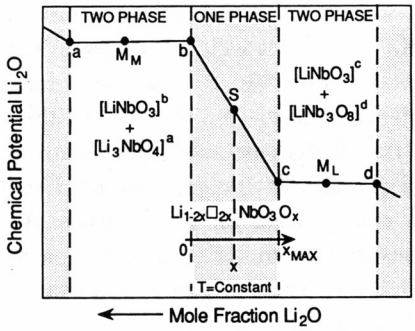

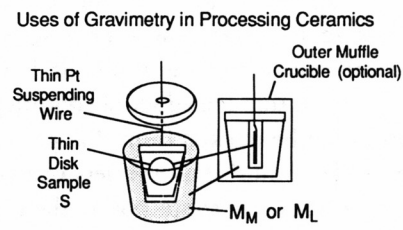

Figure 8.6 **Isothermal compositional dependence of lithium oxide chemical potential in the Li_2O–Nb_2O_5 system.**

such crystals from the melt. The second-order ferroelectric transition temperature, shown as the dashed line in Figure 8.5, has a strong dependence on the lithium content. This transition temperature has been measured by DTA and was used successfully to determine the congruent composition precisely and to correlate the transition temperature with the cation vacancy content of the material.[7]

Holman[8] has also demonstrated that TG can be used for such analyses. This approach is universal because it does not depend on the fortuitous presence of a phase transition. The method is illustrated in Figure 8.6 for the same lithium niobate system. The basis of the method is to vaporize the more volatile component, Li_2O, and follow the associated weight change. The sample is surrounded by a two-phase mixture from either phase boundary. This establishes the vapor pressure of the volatile component, which will transfer to or from the sample, depending on which two-phase mixture is used, until the composition corresponding to the phase boundary is attained. This method, however, is experimentally much more involved and time-consuming than DTA.

The major contribution of TG to the analysis of ceramic materials and phase equilibria is its ability to follow the degree of nonstoichiometry in materials as the temperature, pressure, and atmospheric composition are varied. The scientific literature abounds with examples involving the oxidation of metals[9] or other exchanges of oxygen with the atmosphere.[10] The point defects and valence changes necessary for charge compensation significantly affect diffusion rates and thereby the reactivity of these materials. In addition, frequently there are profound effects on the electrical, magnetic, and thermal properties of the material as the degree of nonstoichiometry varies.

The cuprate systems, renowned for their high-temperature superconducting properties, exhibit a particularly wide range of oxygen nonstoichiometry.[11] Attaining the proper oxygen content is vital to achieving high-T_c superconductivity. The amount of oxygen vacancies in the structure also influences the rates of reaction and, hence, the ease and temperature at which the desired phase is formed.

Determining the oxygen content of a material as a function of temperature, partial pressure of oxygen, and time is straightforward from weight changes as the experimental parameters are varied. It is necessary, however, to know the exact oxygen content at some fixed set of conditions by an independent means. Then the composition can be tracked from that point as the changes are made. This starting point can be determinded by a variety of analytical methods. If composition is fixed by thermodynamics at some point, then TG can be used for this analysis. An example is the $Ba_2YCu_3O_{7-x}$ system where heating the material in hydrogen to about 950 °C will reduce it to a mixture of BaO, Y_2O_3, and Cu. The weight change associated with that reduction is used to calculate the value of x.

For most systems, the range of nonstoichiometry is small, and very accurate data are required to describe the composition adequately. Electronic ceramics are of particular interest in this respect. The magnetic properties and loss can vary dramatically as a result of small changes in the Fe^{2+} to Fe^{3+} ratio and, hence, the oxygen content. The desired ratio is established at the high temperature when the powder is sintered, and then the oxygen partial pressure is programmed to preserve that ratio as the material is cooled. Alternatively, the cooling is sufficiently rapid that the rate of oxygen uptake is small enough to preclude a significant change in its concentration.

Understanding and controlling these processes in electronic ceramics requires knowledge of the variation in both the equilibrium concentrations and the reaction rates as a function of temperature, time, and partial pressure of oxygen. The general procedure is similar to that described earlier for the high-T_c superconductors except that much greater precision is required and higher temperatures are involved. The

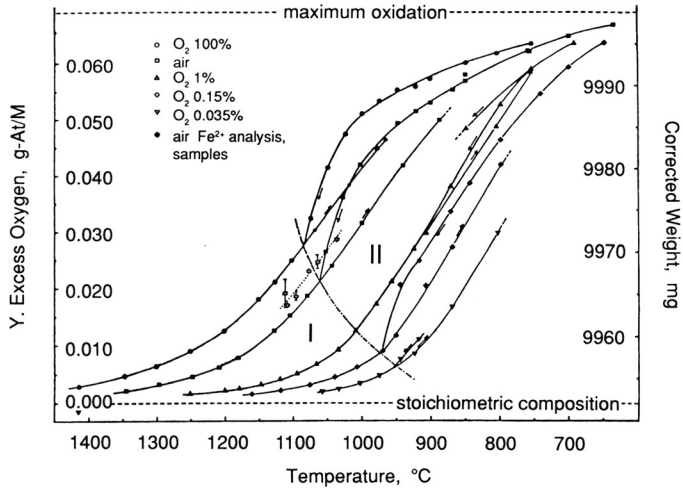

Figure 8.7 **Changes of mass for $Ni_{0.685}Zn_{0.177}Fe_{2.138}O_4 + \gamma$ as a function of temperature and partial pressure of O_2.**

higher temperature adds to the experimental difficulties and uncertainties. Volatility of essential components in the ferrite, for example, ZnO in nickel-zinc ferrite, or even of the supporting and suspension system, for example, PtO, may become significant. Very careful work utilizing blank experiments is necessary to achieve the specified accuracy.

A typical example of these curves is shown in Figure 8.7 for the spinel ferrite, $Ni_{0.685}Zn_{0.177}Fe_{2.138}O_{4+\gamma}$.[12] The weight of a nominally 10-g porous sample is tracked as a function of temperature for different partial pressures of oxygen. Region I is the single-phase region with rapid reversibility for the exchange of oxygen. Region II is the two-phase region where α-Fe_2O_3 precipitates under equilibrium conditions. In Region II, there is obvious metastability during cooling, and the slope does not change, nor does a second phase precipitate. When equilibrated, oxidized samples (two phase) are heated, however, the change in slope at the phase boundary is evident because no metastability occurs in that direction.

Such data are summarized in the form of vant Hoff plots in which a series of isocompositional lines are plotted as a function of reciprocal temperature and log partial pressure. The results for the above system are presented in Figure 8.8.[12] The dashed lines in the right-hand portion represent the metastable (single phase) extensions into the two-phase region. The enthalpy for the oxidation process, Equation 8.1, can be obtained from the slope of the lines in the single-phase region.

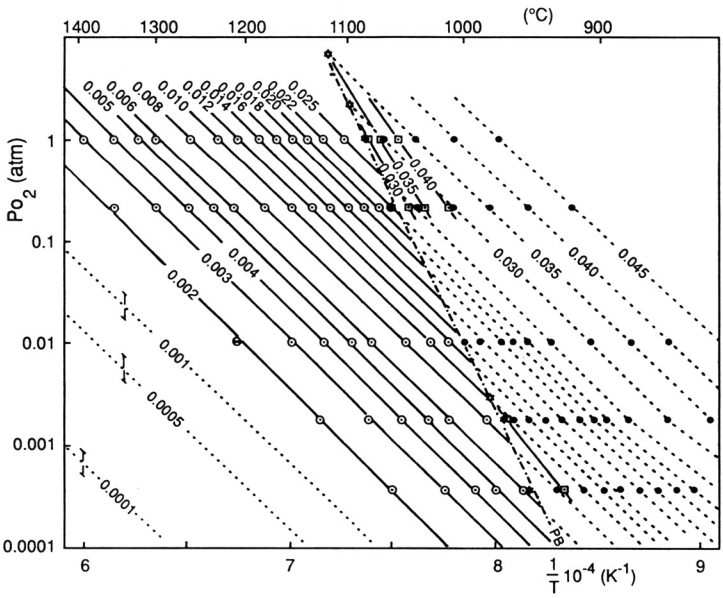

Figure 8.8 Isocompositional plots constructed from data in Figure 8.7. Numbers on the lines represent the value of excess oxygen, γ.

$$M_{1-x}2{+}Fe_x2{+}Fe_23{+}O_42{-} + (\gamma/2)O_2 = M_{1-x}2{+}Fe_{x-2\gamma}{}^{2+}Fe_{2+2\gamma}{}^{3+}O_{4+\gamma}{}^{2-} \quad (8.1)$$

A value of -43.2 ± 0.9 kcal·mol^{-1} is calculated for ΔH.

The desired oxygen content is established during sintering or a subsequent high-temperature anneal. The relevant isocompositional line in Figure 8.8 indicates how the partial pressure of oxygen must change as the sample is cooled in order to preserve the desired oxygen content under equilibrium conditions. In practice, the samples are reasonably dense, however; rapid cooling is frequently all that is required to maintain the high-temperature equilibrium value in the bulk, and only the surface of the sample is oxidized further.

These types of measurements are applicable to a wide range of materials. Following the change in stoichiometry as conditions are varied is not limited to gains or losses of oxygen but can be relevant for other anions or molecular species. Previously it was shown how weight changes associated with the loss of Li_2O were used to investigate the phase composition of $LiNbO_3$. Similarly, the exchange of H_2O, ZnO, PbO, or other volatile molecular species can be studied for other ceramics.

Thermal analysis has been extensively applied to understanding the processing stages of ceramics as well as in studying phase equilibria and reactions. Starting materials may be routinely assayed by TG in order to determine the pickup of moisture and CO_2 during storage. As examples, rare earth oxides are particularly reactive to CO_2 and moisture during storage, while the water content of hydrated salts varies with humidity.

Similarly, the temperature profile for the burn-out of binders, lubricants, and surfactants can be measured by TG. The organic content of raw materials can be measured by TG and verified by EGA. The thickness of coatings such as the carbon used to protect glass fibers hermetically from interaction with the atmosphere can be determined from their weight loss and density.

Determining the Physical Variables

The variables necessary to describe phase equilibria are temperature and pressure for equilibrium; when considering nonequilibrium situations, time is an additional factor. The measurement and standardization for time, however, needs little explanation. Because most phase equilibria are concerned with equilibrium at atmospheric pressure, temperature is the most important physical variable.

The International Temperature Scale (ITS) was developed in 1927 and most recently revised in 1990. The scale ranges from 0.65 K to the upper limit of radiation pyrometry using Plank's law and monochromatic light. Below room temperature, the fixed points defined are based on the vapor pressure relationships of ^{3}He and ^{4}He at the low end through a series of triple points to the triple point of water at 0.01 °C. Above this temperature, the melting/freezing points of pure metals from Ga at 29.7646 °C to Cu at 1084.62 °C are used. The primary reason for revising the temperatures of the fixed points has been the increased purity of the metals rather than improved measuring technology.

There are three official methods for the measurement of temperature, each with a specified range of use. Below the triple point of natural hydrogen (13.8033 K) the gas thermometer is the method of choice. From there to the melting point of silver at 961.78 °C, the electrical resistance of pure platinum is used for interpolation between fixed points. Above this temperature the measurements are based on Plank's radiation law. Thermocouples, however, are the devices most often used in practice. Tables and fitted equations have been extensively developed to relate the emf from the most common types of thermocouples to the ITS. Unfortunately, they have not been revised yet to accommodate the most recent change in the ITS. The interested reader is referred to the second edition of the monograph on temperature by Quinn.[13]

Most experimental measurements of temperature associated with studies of ceramic phase equilibria use thermocouples or, at the highest temperatures, optical pyrometry. Thermoanalytical instruments and hot stages for microscopy, X-ray diffractometers, or spectroscopic investigations use a variety of thermocouples depending upon the range of operation. The fixed points in the region of interest to ceramists are based on melting points and, hence, are readily measured by DTA or DSC. Consequently, the identical instruments regularly used to determine phase equilibria may be directly and conveniently calibrated using primary temperature standards.

The discussion of DTA in the previous section describes the precautions and recommended practices for calculating the melting point from DTA or DSC curves. The advent of instrumentation for simultaneous DTA/TG or DTA/EGA allows the TG and EGA instruments to be calibrated directly as well. Many secondary standards for temperature measurements have also been developed for thermal analysis. These have been based on $solid_1$–$solid_2$ crystallographic transitions or magnetic transitions, that is, Curie or Neel temperatures.

The latter transitions can be readily detected by TG in the presence of a weak magnetic field gradient. The apparent weight gain or loss determined by the direction of the magnetic field gradient vanishes as the material becomes paramagnetic. This measurement of TG in the presence of a magnetic field gradient, called thermomagnetometry (TM), has also been used to detect the formation of magnetic products or intermediates and the consumption of magnetic reactants.

While most measurements are made at essentially atmospheric pressure, there is great scientific and technological interest in both the high-vacuum and high pressure regimes. Low-pressure processing is particularly important in the field of thin film technology—chemical vapor deposition, sputtering, and evaporation methods, etc. Catalysis, energy technologies, and sintering may utilize high pressures. Extremes in pressure considerably complicate the experimental techniques.

Commercial thermal analysis equipment is available to work in the range from about 10^{-6} to 10^{5} torr over restricted ranges of temperature. A wide variety of pressure vessels, autoclaves, and vacuum chambers are readily available for sample treatment and equilibration. These can be fitted with either internal or external

temperature control devices. For special information on vacuum techniques and measurements, the reader is referred to Dushman.[14] Similarly, high-pressure technology is described by Wentorf and DeVries.[15]

8.4 Rates and Mechanisms of Reaction

General Considerations

The study of the reactivity of solids is a complex, fascinating, and frequently controversial topic. Hedvall was a major contributor to the understanding and appreciation of the topic. He listed the following major factors associated with reactivity in his 1934 review[16]:

- heating
- deformation
- impurities in the lattice
- radiation
- changes in crystal structure accompanying phase transformations and decompositions.

These are primarily concerned with the degree of disorder in the solid. Factors which increase this disorder enhance the reactivity of the material. The existence of a brief period of enhanced reactivity during a $\text{solid}_1 \rightarrow \text{solid}_2$ phase transition has been controversial and is referred to as the "Hedvall effect" (see References 17, 18, and references therein). An example in ceramic processing is the use of metastable anatase instead of the stable rutile form of titanium dioxide for the preparation of barium titanate.[19]

The qualitative influence of the factors listed above can be deduced from relatively simple experiments. Quantitative evaluation, on the other hand, requires the measurement of specific rate constants and Arrhenius parameters under the specified conditions. Methods capable of following the concentration of the desired species as a function of time can produce specific rate constants. If the change of mass or heat correlates with concentration, then thermoanalytical techniques are ideally suited. Relevant data can be obtained in either an isothermal or programmed temperature mode of operation.[20] Recent studies suggest that the best approach is to use feedback from the process to determine the heating rate.[21] For TG, the heating rate can be controlled to give a preset rate of weight loss or total pressure, whereas for dilatometry the rate of shrinkage is preset. This latter approach has been particularly valuable in optimizing the conditions for sintering.[22]

Many rate laws have been developed to describe solid–solid decompositions, solid–solid reactions, and gas–solid reactions. Table 8.4 lists some of the most common reaction rate laws expressed as functions of the fraction reacted, α. If the

Rate Law	Equation
Power law	α^n, n = 2, 1, ½, ⅓, ¼
Contracting geometry	$1 - (1 - \alpha)^{1/n}$, n = 1, 2, 3
Erofeev	$-\ln(1 - \alpha)^{1/n}$, n = 1, 1.5, 2, 3, 4
Diffusion controlled, 2D	$(1 - \alpha)\ln(1 - \alpha) + \alpha$
Diffusion controlled, 3D	$(1 - \frac{2}{3}\alpha) - (1 - \alpha)^{2/3}$
Jander	$[1 - (1 - \alpha)^{1/3}]^2$
Prout-Tompkins	$\ln[\alpha/(1 - \alpha)]$
Second order	$1/(1 - \alpha) - 1$
Exponential	$\ln \alpha$

Table 8.4 Common rate laws for heterogeneous kinetics. $f(\alpha) = kt$; α = fraction reacted.

selected model is appropriate, then a plot of that expression versus time will be linear and the slope will equal the specific rate constant, k:

$$f(\alpha) = kt \tag{8.2}$$

Derivations of the rate laws given in Table 8.4 are beyond the scope of this chapter; Reference 20 is recommended for more detail. The equations for contracting geometry are generally most applicable for decompositions. They are based on a reaction interface moving at a steady rate, and the effective overall rate is determined by geometrical considerations. The reaction initiates at a surface and moves inward in one, two, or three dimensions. The exact form of the expression depends on the crystalline anisotropy of the rate constants and the particle shape. The generalized expressions in Table 8.4 are for a uniform cross section progressing linearly, for example, a burning fuse; a circular disk reacting from the edge inward; and an isotropically collapsing sphere for the one-, two-, and three-dimensional cases, respectively.

Rarely, however, do the particle shape, degree of perfection, and anisotropy allow for these precise and invariant values of n. Because of mass and thermal transport, a pile, pressed pellet, or other assemblage of powder may behave as though it were a single particle, that is, reacting from the external surface into the center or bottom of the pile depending on the transport conditions.

The Erofeev rate laws listed in Table 8.4 provide for nucleation and growth under various conditions that take into account impinging and overlapping nuclei. Other rate expressions are predicted for autocatalytic phenomena, and for diffusion

controlled rates through product layers which are based on geometrical assumptions. Kinetics of heterogeneous reactions is a difficult and controversial topic; however, technology frequently requires a minimum predictive capability and understanding of the specific mechanisms occurring in these critical processes.

The simplified Arrhenius expression, Equation 8.3, describes the temperature dependence of the rate constant:

$$kt = Ae^{-E/RT} \tag{8.3}$$

where A is the pre-exponential term, E the apparent activation energy, T the absolute temperature, and R the gas constant. The Arrhenius parameters, A and E, are usually determined from a set of isothermally derived values of k.

The parameters A and E can also be calculated from data taken under non-isothermal conditions. These analyses are derived from mathematical combinations of the various rate laws, the Arrhenius equation, and the heating rate (usually linear with respect to time). Several methods of numerical analysis can determine the parameters from a single dynamic experiment, whereas others require a series of experiments performed at different heating rates.[20] These dynamic experiments are faster and more convenient, but are less flexible and informative, than isothermal studies.

Some precautions are necessary when using non-isothermal experiments. To determine if mass or thermal transport is the rate determining step, measure the rate constants or Arrhenius parameters at different sample sizes, heating rates, and flow rates. Do *not* conclude, based solely on the best fitting rate law, that the mechanism is necessarily the one for which that rate expression was derived. One must confirm the mechanism using other methods, such as microscopy. Bear in mind that the Arrhenius equation is mathematically ill-conditioned and requires very precise data to establish uniquely the values of A and E. More often, a range of A and E values will fit the data in a manner where a high value of E is coupled with a high value of A, predicting virtually the same rate in the temperature region in which the measurements were made. Referred to as "the kinetic compensation effect," this is a topic of extensive discussion.

Decomposition of Precursors

The mechanisms, rates, and reactivity of the products markedly affect the success or failure of a synthesis. The calcination step is usually at atmospheric pressure in a suitably oxidizing, inert, or reducing atmosphere. Even under these straightforward conditions, various effects and reaction paths are still possible.

The atmosphere initially surrounding the sample will change during the course of the decomposition because of the buildup of product gases or the depletion of the reactive gas. The equilibrium decomposition temperature for reversible reactions is determined by the partial pressure of the product. The temperature at the reacting interface, therefore, must increase during the decomposition as the outward

diffusion of the product gases becomes increasingly difficult because of the buildup of products. Reversible reactions common in ceramic syntheses are the decomposition of carbonates, hydroxides, hydrates, and oxides.

The ill-defined nature of the temperature at the reaction interface is exacerbated by the enthalpy of the specific reaction. This energy, which is evolved or absorbed by the reaction, is generally large compared with the heat capacity of the reactants and products. Hence, the actual temperature at the reaction interface may differ substantially from that of the nearby temperature sensor. Consider the oxidation of carbon monoxide that occurs during the decomposition of oxalates in air. The thermocouple near the sample may indicate 300 °C while the actual specimen is glowing a bright red (indicating at least 600 °C). Conversely, for the more typical endothermic decomposition it is necessary to supply heat to maintain the reaction.

The degree and rate of attaining structural order at the reaction interface, particularly on the product side, also influences the reaction. It matters whether the product initially is in an amorphous or microcrystalline state for a significant period of time or whether it orders immediately upon formation. For example, if it is amorphous, then the full effect of the product's lattice energy is not indicated in the apparent activation energy of the process. Such effects are not uncommon. The movement of the decomposition front for even a virtually perfect material is, therefore, established by the complex interactions of the concentration gradients of the reactant or product gases or both, the temperature profile and thermal transport properties of the system, and the degree of order present throughout the reactants and products.

The decomposition of calcium carbonate, Equation 8.4, is a good illustration of these effects:

$$CaCO_3 \rightarrow CaO + CO_2 \tag{8.4}$$

The dependence of the decomposition temperature on the partial pressure of CO_2 obtained by the use of various sample holders has been described by Paulik and Paulik.[23] Each of the sample holders shown in Figure 8.9 provides a different rate of exchange with the flowing atmosphere. The decomposition temperature increases markedly as the degree of mixing is impeded and the partial pressure of the CO_2 builds. This effect and the endothermic nature of the reaction are also shown to have a remarkable influence on the apparent activation energy for this relatively simple reaction as the sample size and heating rate are varied.[24]

These transport effects not only change the temperature and rate of the reaction, but they can even influence the choice of reaction pathways for energetically similar routes. An example is the decomposition of aluminum hydroxide, the mineral Gibbsite, to ultimately form the stable phase of alumina, corundum. The pathway tends to shift among three routes, each having different intermediate crystalline phases of alumina, with changes in starting particle size, heating rate, total pressure, or partial pressure of water vapor.[25]

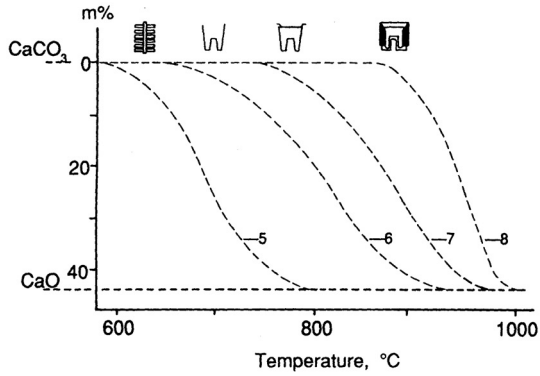

Figure 8.9 Influence of sample holder on the thermal decomposition of $CaCO_3$.

The particle size and distribution, the extent of particle agglomeration, porosity, and powder morphology are usually established during the decomposition and any subsequent high-temperature reactions. Manipulation of the calcination then offers some degree of control over these factors. Certainly, several characteristics of the precursor are also variables in this process. Often the decomposition may have topochemical aspects which produce agglomerates having the crystallographic orientation and shape of the initial particle. A comminution stage may be added to alter the properties from the final thermal treatment; however, one of the goals of chemical synthetic methods is to eliminate, or at least minimize, this requirement.

By lowering the temperature necessary to achieve the desired product, it is generally possible to produce the material in a more finely divided state. This increases the range of particle size which can be achieved, and the time and temperature of calcination can be used to attain some measure of control over the final powder characteristics. At the other extreme, it is possible to prepare amorphous particles or glass ceramics by preventing or controlling nucleation and growth during cooling from a high-temperature homogeneous melt.

The surface area of the product will be at a maximum immediately after each stage in the decomposition, as would be expected. The particles of the product powder grow and the porosity tends to close as the temperature is raised further. These changes are measured by a decrease in surface area and can also be confirmed by X-ray diffraction. Often, one assumes spherical particles and a particular density in order to calculate an effective average particle size from the surface area according to

$$ED = \frac{6}{\rho SA} \tag{8.5}$$

where ED is the effective diameter in μm, ρ is the density in $g \cdot cm^{-3}$, and SA is the surface area in $m^2 g^{-1}$.

The rate of heating can also be a factor. Fisher[26] has shown that the density and pore structure of calcium oxide formed from the decomposition of calcium carbonate

depend not only on the maximum temperature but also on the heating rate. High heating rates tend to heal over the surfaces, inhibiting diffusion and trapping gases. Large disruptive pores and fissures form under these conditions. Slower heating rates yield a denser product having smaller pores more suitable for subsequent densification. There may be instances, particularly for highly exothermic reactions, where the heating rate is impossible to control, such as in the decomposition of oxalates in air or in the decomposition of materials with internal oxidizing agents such as nitrates.[27]

The use of large deep trays or crucibles, probably covered, for calcination accentuates these problems, and different sections of the sample will react at different temperatures and times. Shallow trays in a flowing atmosphere are an improvement, but tumbling and rotating tube furnaces or fluid bed calciners are obviously superior. For some reversible reactions it may be beneficial to perform a vacuum calcination for the ultimate removal of the product gases.

The preceding discussion of precursor decomposition has dealt with simple decompositions, such as occurs in alkaline earth carbonates in the production of reactive, finely divided, alkaline earth oxides. Many of the most useful precursors, however, are complex compounds or solid solutions, for example, $BaTiO(C_2O_4)_2{\cdot}4H_2O$, $LaFe(CN)_6{\cdot}5H_2O$, and $(Fe,Mn,Zn)C_2O_4{\cdot}2H_2O$. These compounds, produced by coprecipitation, yield $BaTiO_3$, $LaCoO_3$, and $(Fe,Mn,Zn)_3O_4$, respectively, after calcination in air. Such materials are formed at lower temperatures with greater flexibility and control of the particle size and purity than when traditional ceramic methods are used. Other precursors result from sol–gel synthetic routes, freeze-dried or spray-dried mixtures of salts, decomposition of a variety of organometallic materials, etc.

The subsequent thermal decompositions of these precursors generally involve a number a competing and consecutive reactions. At some stage, a mixture of intermediates may form that correspond to the starting materials used in the traditional synthesis. These intimately mixed and highly reactive powders, however, react much more readily than the conventionally mixed, bulk reactants. The complex oxalate mentioned earlier decomposes to yield a mixture of $BaCO_3$ and TiO_2 at one point, but these react near 600 °C to form the product, compared with about 1000 °C for the conventionally mixed material.

Solid–Solid Reactions

Much of what has been discussed in the preceding section applies to solid–solid reactions as well. These reactions are generally exothermic in contrast to thermal decompositions and phase transformations. The latter are usually driven by a positive change in entropy, whereas the former are primarily driven by a negative enthalpy. Hence, in principle, the solid–solid reactions have a measurable rate at room temperature, but in reality they must reach temperatures at which the necessary mass transport will occur within a reasonable time. The exothermicity can lead to a runaway reaction, however, once the kinetics become favorable. This effect is the

basis for the synthetic technique referred to as self-propagating high-temperature synthesis (SHS).

A particularly informative and authoritative text on solid-state reactions has been written by Schmalzried.[28] Such reactions are classified as (1) single-phase homogeneous, (2) single-phase inhomogeneous with miscibility, or (3) heterogeneous with a product barrier. An example of the first category is the atomic rearrangement or order-disorder taking place within a spinel, such as $NiFe_2O_4$, as the distribution of nickel and iron ions shifts between the tetrahedral and octahedral sites with changing temperature.

The second category is represented by the reaction

$$xAO + (1 - x)\ BO = (A_xB_{1\ -\ x})\ O \tag{8.6}$$

where the product is a simple solid solution. The third category does not form a miscible solid solution but rather a series of one or more distinct compounds:

$$AO + BO_2 = ABO_3 \tag{8.7}$$

The reaction can only progress via mass transport across or around the layer of product.

The third category also may involve the formation of more than one product. If ion *A* diffuses more rapidly than ion *B*, then a phase of A_2BO_4 might form as an intermediate species. This is frequently the case where coarse powders are used and the diffusion paths are longer. Examples of multiple product formation have occurred in the synthesis of $BaSnO_3$ and $BaTiO_3$. Given stoichiometric amounts of *A*O and BO_2, the equilibrium composition of pure single-phase ABO_3 will ultimately predominate.

The rate laws for solid-state reactions are included in Table 8.4. The diffusion equations are particularly interesting for these reactions, as they were derived assuming that one reactant is entirely surrounded by the other. However, these equations are frequently followed even with one-to-one ratios of the reactants and only point contacts between the particles. An example of this is the reaction of α-Fe_2O_3 with Li_2CO_3 to form $LiFeO_2$.[29]

The explanation for this agreement lies in the relatively rapid surface diffusion of one of the components, in the above case Li_2CO_3. As a consequence, one reactant is quickly coated with a layer of the other so that the conditions corresponding to the rate law are achieved. Under these conditions, it was shown that the rate constant is proportional to the square of the surface area of the least mobile component. Again, this result demonstrates the need to verify the apparent mechanism inferred from the kinetics using other experimental methods.

Since reducing the particle size and increasing the particle-to-particle contacts enhance the rate of reaction, prolonged milling of the mixture improves reactivity. Care must be taken, however, not to leach out one of the reactants preferentially or to significantly contaminate the sample with grinding media. The milling may also

influence the rate of subsequent reactions by introducing strain, defects, and nonstoichiometry into the powder particles.

Controlling the partial pressure of oxygen over the reacting mixture can also have a profound effect on the rate of reaction in cases where the number of defects and even the particular phases involved can be changed. The current interest in high-temperature superconductors provides an excellent example. Because the range of oxygen nonstoichiometry can be relatively large in these materials, the number of anion vacancies can vary widely. The vacancy content of the product layer, in this example, will determine the diffusion rates within the barrier phase and thereby control the rate of reaction.

The Hedvall effect was mentioned previously as another potential influence on reactivity. Since changes in rate have been noted during magnetic transitions, it may seem reasonable to conclude that the internal magnetic field set up by the reactants and products alters the rate of the reaction during that time. That raises the question of whether or not the imposition of an external magnetic field will affect the course of a reaction involving magnetic materials. Studies of this topic have not always agreed—see, for example, Reference 30 and references therein.

It is less controversial that an external electrical field will affect reactions, since there is frequently a flux of electrons involved in the particular overall reaction. The nature of the electrical contacts is important in such reactions; for example, is there a closed-circuit conduction path or is there only a field applied without contacts? Even the provision for a short circuit without the application of an external field will facilitate many reactions. The buildup of charge barriers at interfaces such as grain boundaries becomes an important consideration in these cases.

The experimental methods used to study solid–solid reactions are the same as those described earlier. X-ray diffraction and thermal analysis provide average or integrated information about the extent of the reaction without directly observing the mechanism or morphology. The use of TG depends on the correlation of weight loss, such as in carbonate or hydroxide decomposition, with the course of the reaction. Integration of the partial area under the DTA or DSC peak as a function of time and temperature will yield useful information on the rate. Correlations based on volume changes are more difficult because of porosity and shrinkage as well as other volume changes due directly to the reaction.

Microscopy and EDX microprobe studies are most useful for detailed analysis of mechanisms. If massive sintered samples or single crystals are used as reactants, then an inert marker can be placed at the initial interface and the position of the product phase relative to the marker will indicate which species are diffusing. A microprobe scan across a polished cross section will reveal any concentration gradients. These gradients will indicate the stoichiometry and number of intermediate and final products that occur, along with any solid solubility within the phases. Figure 8.10 presents the results of such a compositional scan for the system CoO–TiO_2.[28] Clearly, there are three intermediate phases and there seems to be some

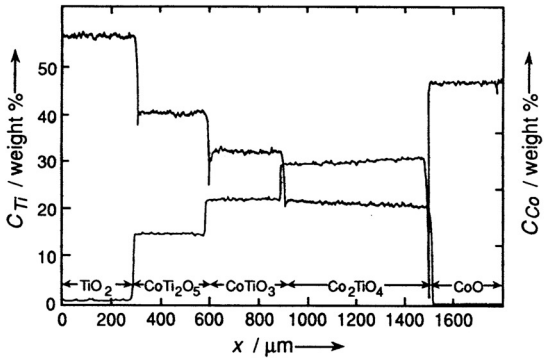

Figure 8.10 Microprobe trace of the reaction product after a reaction between TiO_2 and CaO at 1420 °C for 93 h in air.

slight range of composition possible for $Co_2\,TiO_4$. The other four phases show little tendency to form solid solutions of variable composition.

With the advent of solid electrolytes, such as the stabilized forms of zirconia, the field of solid-state electrochemistry has grown. Galvanic cells utilizing this material as an electrolyte for anionic (O^{2-}) conduction have been used in conjunction with the Nernst equation to measure within various ceramic systems (1) the Gibbs free energy of formation, (2) the activity of O^{2-}, and (3) the kinetics of solid-state reactions. Electrolytic cells can be used to drive reactions in the non-equilibrium direction by the application of an electrical current. The reader is again referred to Schmalzried.[28]

Solid–Liquid Reactions

The presence of a liquid phase has marked influence on both diffusion rates and the area of contact between phases. The latter aspect depends upon the wetting properties of the respective phases. Due to improved mass transport, equilibrium is generally established more rapidly in the liquid phase at the same temperature. Consequently, fluxing agents are frequently added to facilitate reactions, sintering, or crystal growth. Local liquid zones will often lead to whisker growth from the vapor phase. Increased reaction and solubility at that point deposits fresh solid underneath the small liquid pool, and anisotropic growth or precipitation results.

The formation of a liquid phase by melting or eutectic reactions is readily determined by DTA or DSC. Microscopic observation of a quenched sample will generally indicate the presence and amount of a liquid phase at the higher temperature.

Many texts and monographs have been written on the subject of solution-precipitation phenomena. The formation of colloid phases and the rheological properties of suspensions are outside the scope of this chapter. The electrical properties of the solid surface and the associated layer of electrolyte or solvent phase play major roles in the transport and flocculation of the solid phase.

Applications to the field of ceramics are in the areas of crystal growth, precursor precipitation, and corrosion. A distinguishing aspect of solid–liquid reactions, in contrast to solid–gas reactions, is the ability of the liquid phase to allow electrolytic conduction. This conductive path frequently leads to increase corrosion rates by providing connections between local cathodic and anodic zones. The scanning tunneling microscope and atomic force microscope can be used from within the liquid phase to examine the surface topography of a rigid solid surface, such as an electrode, ceramic, or metal.

Solid–Gas Reactions

Some of the major forms of gas–solid chemical interactions are (1) catalytic reactions, (2) simple chemisorption, chemical vapor deposition (CVD), or crystal growth, (3) oxidation or reduction reactions, and (4) addition reactions, such as carbonate or sulfate formation. Each of these classes presents unique experimental challenges. The first two categories involve reactions at the surface and do not require bulk diffusion. The latter two types, however, need material transport through the product layer in order to continue. There are numerous examples where the film of product initially produced is essentially impervious and thus becomes protective, forming a barrier to further reaction.

The variety of specific surface analytical tools described elsewhere in this volume are the primary methods of characterizing the changing surface chemistry during catalytic and CVD processes. Microscopy, particularly ESEM, described in Section 8.3, provides morphological and structural information. X-ray diffraction will reveal the crystal structure, or lack thereof, for the thicker films as they are deposited or formed. Frequently, one can detect and use for calibration purposes the pattern of the underlying substrate, especially when working at other than room temperature. The texture or orientation of the surface is determined by both the topochemical factors of any reactions and the properties and structure of the underlying substrate.

Thermoanalytical methods are also useful. TG is often used to detect weight gains from the adsorption of gases onto the surface. This analysis can be nonselective, such as the use of nitrogen at low temperature to measure the surface area and porosity (BET), or it can be done selectively through chemisorption on specially active sites, such as acidic gases on basic sites and vice versa or hydrogen onto metallic sites in supported catalysts. If the surface reaction has a reasonable density of reactive sites and favorable kinetics, it can be detected and followed using DSC or DTA. The aspects involving desorption or exchange of gases with the surface are directly detectable through EGA techniques. The appearance of water vapor in the gas phase during the reduction of oxides by hydrogen or the formation of product gases over a catalyst are typical examples.

A number of gas–solid reactions involve substantial changes in weight. The rates of such processes as crystal growth, the oxidation of metals, and the removal of

sulfur dioxide from flue gases are readily determined by TG or EGA invoking the rate law expressions presented in Table 8.4. If a gas is consumed or evolved, it is even possible to use the total pressure of a closed system to follow the course of the reaction.

Gas–solid reactions may require mass transport through the product film. Markers similar to those described earlier for solid–solid reactions can be used to determine the primary direction of mass transport. If the transport is from the underlying reacting solid to the product/gas interface, then the marker will remain at the solid reactant/product interface and substantial void space will also be observed underneath the product layer.

8.5 Summary

Some fundamental aspects of equilibrium and non-equilibrium phase equilibria have been discussed, along with the major factors that influence reactivity in the solid state. These topics are of crucial importance in ceramic technology and must be addressed in spite of their complexity and the considerable time, effort, and expense required to perform meaningful experiments. They impact on the entire range or relevant science and engineering from synthesis to sintering and final determination of the material's properties.

Many of the current products so vital to our technologically based society—window glass, spinel ferrites, and some composites—are based upon metastable phases. An appreciation of the associated phase equilibria is essential in preparing and optimizing such materials. Control of the solid-state reactivity is also necessary to provide equilibrium materials having the optimum morphology, composition, and atomic order.

Microscopic, diffraction-based, and thermoanalytical techniques are the three most important classes used to study these phenomena. Examples of each of these have been described in some detail.

References

1 P. K. Gallagher, D. W. Johnson, F. Schrey, and D. J. Nitti. *Am Ceram. Soc. Bull.* **52**, 842, 1973.

2 T. A. Hardt. Electroscan Co., Wilmington, MA, 1992. Personal communication.

3 J. Moser, M. Aindow, W. A. T. Clark, and H. Fraser. In press.

4 P. K. Gallagher. In *Advances in Analytical Geochemistry*. (M. W. Rowe and M. Hyman, Eds.) JAI Press, Greenwich, CN, in press.

5 M. I. Pope and M. D. Judd. *Differential Thermal Analysis*. Heyden & Sons, London, 1977.

6 J. R. Carruthers, G. E. Peterson, M. Grasso, and P. M. Bridenbaugh. *J. Appl. Phys*. **42**, 1846, 1971.

7 P. K. Gallagher, H. M. O'Bryan, and D. Brandle. *Thermochim. Acta*. **133**, 1, 1988.

8 R. L. Holman. In *Materials Science Research*, Vol. 2. Plenum Press, New York, 1979.

9 U. R. Evans. *The Corrosian and Oxidation of Metals*. St. Martin's Press, New York, 1960.

10 O. T. Sørenson. *Nonstoichiometric Oxides*. Academic Press, New York, 1981.

11 P. K. Gallagher. *Thermochim. Acta*. **174**, 85, 1991.

12 P. Bracconi and P. K. Gallagher. *J. Am. Ceram. Soc*. **62**, 171, 1979.

13 T. J. Quinn. *Temperature*. 2nd ed., Academic Press, New York, 1990.

14 S. Dushman. *Scientific Foundations of Vacuum Technique*. 2nd ed., Academic Press, New York, 1962.

15 R. H. Wentorf and R. C. DeVries. In *Encyclopedia of Physical Sciences and Technology*. (R. A. Meyers, Ed.) Academic Press, New York, 1987, p. 492.

16 J. A. Hedvall. *Chem. Rev*. **15**, 139, 1934.

17 P. D. Garn and T. S. Habash. *J. Phys. Chem*. **83**, 229, 1979.

18 P. K. Gallagher and D. W. Johnson. *J. Phys. Chem*. **86**, 295, 1982.

19 H. A. Sauer and J. R. Fisher. *J. Am. Ceram. Soc*. **43**, 297, 1960.

20 M. E. Brown, D. Dollimore, and A. K. Galwey. *Reactions in the Solid State*. Elsevier, Amsterdam, 1980.

21 J. Rouquerol. *Thermochim. Acta*. **144**, 209, 1989.

22 M. L. Huckabee and H. Palmour. *Am. Ceram. Soc. Bull*. **51**, 574, 1972.

23 F. Paulik and J. Paulik. *Thermochim. Acta*. **100**, 23, 1986.

24 P. K. Gallagher and D. W. Johnson. *Thermochim. Acta*. **6**, 67, 1973.

25 W. H. Gitzen. *Alumina as a Ceramic Material*. American Ceramic Society, Columbus, 1970, p. 14–20.

26 H. C. Fisher. *J. Am. Ceram. Soc*. **38**, 245, 1955.

27 K. Kourtakis, M. Robbins, and P. K. Gallagher. *J. Solid State Chem*. **83**, 230, 1989.

28 H. Schmalzried. *Solid State Reactions*. Verlag Chemie, Basel, 1981.

29 D. W. Johnson and P. K. Gallagher. In *Reaction Kinetics in Heterogeneous Chemical Systems*. (P. Barret, Ed.) Elsevier, Amsterdam, 1975.

30 M. W. Rowe, P. K. Gallagher, and E. M. Gyorgy. *J. Chem. Phys*. **79**, 3534, 1983.

9

Mechanical Properties and Fracture

EDWIN K. BEAUCHAMP

Contents

9.1 Introduction

The mechanical strength of ceramics, more than any other factor, limits their performance in applications. The key to successful use of ceramics, therefore, is a detailed understanding of how they respond to mechanical stress and, ultimately, how they fail. It is also essential to be able to optimize the design of structures that employ ceramics so that mechanical stress in the ceramic is minimized.

The intent of this chapter is to provide a perspective on the mechanical behavior of ceramics and glasses and an introduction to procedures that will assist in optimizing the engineering application of these materials. The chapter begins with a description of the fracture process and methods of measuring and analyzing brittle failure. In addition, because fracture surface analysis is such a valuable tool, not only in developing an understanding of failure processes in ceramics, but also in assessing design inadequacies, the chapter includes a discussion of how fracture surface features are generated and how they are employed in analysis.

9.2 The Fracture Process

Mechanical Strength of Brittle Materials

In most applications, ceramics and glasses behave as brittle materials; that is, they display a linear stress/strain curve up to the failure stress and then an abrupt failure

as a crack propagates through the part.[1] In many typical applications, such as the glass in automobile windows, failure occurs at a low value of stress (1000–10 000 psi). These low-strength failures have led to the view that glass is a weak material. In fact, the *theoretical strength* of glasses and ceramics is very high (about 3 million psi or 20 GPa for silicate glasses and even higher in oxide ceramics). Moreover, with proper care in production and handling, glass with strengths approaching theoretical can be achieved in practice. For example, in fiber-optics applications, the fibers have strengths that are one-tenth to one-third of the theoretical value.

Calculated values for the theoretical strength of a material are obtained by assuming that the applied stress has stretched every bond, in a plane perpendicular to the applied stress, to the point at which all the bonds break simultaneously. One of the common assumptions in such analyses is that the bonds must be stretched one-tenth of their original length to produce failure.

The discrepancy between the theoretical strength of glasses and the values obtained in many practical applications exists because materials contain flaws that lower their strength. Operationally, a flaw is any structural feature in the part that raises the local stress at the feature above the applied stress in the part. The amplification of stress, or the *stress concentration factor*, varies with the character of the flaw. For a cylindrical hole in a sheet of an isotropic material such as glass, the amplification is a factor of three at the edge of the hole. For cracks, which can be considered ellipsoids with a minimum radius of curvature of atomic dimensions, the stress concentration at the crack tip can be a factor of hundreds or thousands. Thus, with an applied stress of, say, 1000 psi, the stress at the crack tip can be raised to the theoretical value.

For all flaws, the local stress is a maximum adjacent to the flaw and decreases rapidly away from the flaw. Irwin[2] obtained an expression for the stresses in the vicinity of a crack tip that exemplifies how these local stresses vary (Figure 9.1). In these equations, K_1 is the stress intensity factor and a function of the applied stress and the flaw severity. One of the features of these equations that is important in understanding how cracks propagate is that the stress is a maximum in the plane in front of the crack tip. As a consequence, for an isotropic material, the bonds directly in front of the crack tip are the ones that will fail; that is, the crack grows in the plane perpendicular to the applied stress. Moreover, in a uniform, planar, applied stress field (where $\sigma_x = \sigma_y$ = constant), once the crack has started to grow in a given plane, it will continue to propagate in that same plane.

Although the description above invokes the idea of bond failure at a specific local stress value at the crack tip, it is often more useful to describe the failure process as one in which sufficient energy is supplied to each bond at the crack tip to rupture that bond. One of the more important equations of fracture mechanics, the Griffith equation, was obtained by using this approach.[3] Griffith noted that, in a purely mechanical failure (in which no other energy was supplied to rupture the bond), the energy required to break the bonds and create new surface during some incremental extension must have been supplied from the strain energy released during

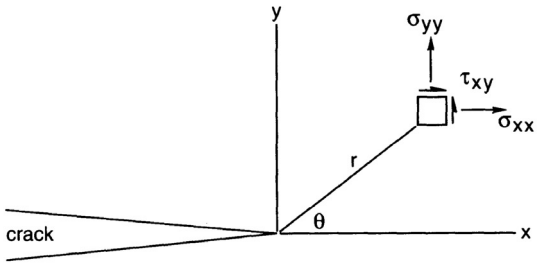

$$\lim_{r\to 0} \sigma_x = \frac{K}{\sqrt{2\pi r}} \cos\frac{\theta}{2}\left(1 - \sin\frac{\theta}{2}\sin\frac{3\theta}{2}\right)$$

$$\lim_{r\to 0} \sigma_y = \frac{K}{\sqrt{2\pi r}} \cos\frac{\theta}{2}\left(1 + \sin\frac{\theta}{2}\sin\frac{3\theta}{2}\right)$$

$$\lim_{r\to 0} \tau_{xy} = \frac{K}{\sqrt{2\pi r}} \cos\frac{\theta}{2}\sin\frac{\theta}{2}\sin\frac{3\theta}{2}$$

Figure 9.1 **Stress distribution near the crack tip from the Irwin analysis. (From Reference 2.)**

that extension. A necessary condition for the onset of fracture is, then, that the strain energy release is equal to the energy used in breaking the bond.

The original equation derived by Griffith has been modified to include the contributions of Inglis,[4] Orowan,[5] and the Irwin formulation. The most commonly used form of the equation relating the failure stress, σ_f, to the crack size, c, is

$$\sigma_f = \frac{YK_{1c}}{c^{1/2}} \tag{9.1}$$

where K_{1c} is the *critical stress intensity* factor for the material and Y is a factor which is related to the geometry of the flaw. K_{1c}, also commonly referred to as the *fracture toughness*, is a measure of the resistance to crack growth in the material.

More generally, Equation 9.1 can be written to describe the stress intensity for a crack of length c and an arbitrary applied stress σ:

$$K_1 = \frac{\sigma c^{1/2}}{Y} \tag{9.2}$$

It should be obvious from Equation 9.1 that the criterion for failure is that $K_1 \geq K_{1c}$.

Flaws, Statistics of Fracture, and Measurement Techniques

In general, the flaws that determine the practical strength of a ceramic or glass are introduced in the fabrication of the material or in subsequent machining or handling. Flaws produced in ceramic fabrication are often a consequence of imperfect packing of the starting powder and appear as large voids or poorly sintered zones. Contaminants, particularly those in the form of inclusions with a different thermal

expansion or a different elastic response than that of the matrix, can lead to locally high stress concentrations.

For alumina and other ceramics with anisotropic thermal expansion, differential contraction between adjacent grains with different crystal orientation produces residual stresses that can promote crack propagation and lower the strength of the ceramic. Elastic modulus anisotropies also create local stresses during loading. The effects of anisotropy are exacerbated in large grains. As a result, exaggerated grain growth during sintering can lead to low-strength failures. Large grains can be particularly effective flaws when the grains contain easy cleavage planes. As an example, the effective fracture toughness for the easy cleavage plane in β″-alumina is 0.2 MPa·m$^{1/2}$, whereas the toughness perpendicular to that plane is 2.0 MPa·m$^{1/2}$. Fine-grained β″-alumina has K_{1c} = 1.8 MPa·m$^{1/2}$. To obtain reasonable strength, it is absolutely essential to limit grain size in this material.

Flaws produced in glass fabrication are usually a result of incomplete melting of the batch constituents or of attachment of contaminant particles to the surface of the glass during forming. Rapid quenching at contact with a mold can produce *chill marks* that result in high stress concentrations.

Most of the flaws produced during machining and handling have the character of Hertzian cracks, that is, cracks generated by the very high stresses in the zone of contact of a hard, sharp particle with the glass or ceramic surface.[6] The size of these cracks depends on the area of the zone of contact (the size of the particle) and the magnitude of the contact load. Where high strength is critical in a part that must be machined, it is common practice to machine in steps beginning with large-grained abrasive and reducing the grit size in successive steps. The intent is to remove the machining damage of each preceding step so that the final product has only the flaws introduced in the final machining step.

Practical ceramics contain numerous flaws of varying severity and usually of various types. If the ceramic part is uniformly stressed to the point of failure, the origin for that failure will be the worst flaw in the part, that is, the one with the highest stress intensity. In the more usual case of a varying stress field in the part, failure will still be produced by the flaw whose stress intensity first reaches the critical value; however, that may not be the largest flaw in the part.

In most instances, a group of ceramic or glass samples produced under nominally identical conditions will have worst flaws that vary in severity and location. As a consequence, strength values for those samples will vary, often over a rather wide range. The distribution of failure stresses is usually analyzed in terms of the *extreme value statistics* developed by Weibull.[7] The most common functional form used in these statistical treatments is

$$F(\sigma) = 1 - \exp[-(\sigma/\sigma_0)^m] \tag{9.3}$$

where F is the probability that a part will fail at stress σ, σ_0 is the modal value for failure stresses in the set of samples, and m is the Weibull coefficient. Obviously, it

is desirable to have a high value of the modal, σ_0. For high reliability, it is also important to have a narrow range of failure stresses, that is, a high value for m.

A variety of sample geometries and loading schemes have been used to obtain strength data on ceramic materials. Most data in current literature were obtained using one of the ASTM standard tests described in Reference 8. In general, the brittle character of ceramic failure makes it difficult to use a simple tension test. The most convenient geometry, from the standpoint of ease of fabrication and loading, is a bend specimen. Quinn and Morrell[9] have given an excellent review of the use of bend tests for characterizing brittle materials behavior. In all testing, it is essential to remember that, in general, the process used to fabricate the test specimen will introduce a flaw population with a different character than that produced in the component application. Therefore, the test results must be used with caution in predicting the behavior of the component.

Because of the importance of K_{1c} in the mechanical performance of ceramics, a variety of techniques have been developed to measure this parameter. Reference 10 is an excellent source of information on these techniques and on their use in characterization of ceramics.

Subcritical Crack Growth

In the preceding description of the fracture process, it was assumed that the only source of energy to break the structural bonds was the strain energy provided by the loading system. It was also assumed that no crack growth was possible unless the stress intensity at the crack tip exceeded K_{1c}. That assumption implies that, for a crack of a given size, no crack growth should occur until the stress reaches the critical value and, once that critical value is obtained, fracture should be immediate.

That assumption is not appropriate for sustained loading of most ceramics and glasses. It has long been observed that, under sustained loading, delayed failure can occur at stresses substantially lower than the value necessary to produce immediate failure. This *static fatigue* behavior is enhanced by high relative humidity in the air surrounding the stressed part. Wiederhorn[11] showed that static fatigue in silicate glasses and certain oxide ceramics resulted from slow crack growth at stress intensities less than K_{1c}. He concluded that final, catastrophic failure occurred when slow growth extended the crack to the point that the Griffith criterion was satisfied, that is, when K increased to K_{1c}.

Michalske and Freiman[12] introduced a model for subcritical crack growth in silicate glasses in which an originally unreactive Si–O bond becomes more reactive as it is deformed in the stress field at the crack tip. At some level of stress intensity, a water molecule adjacent to the bond is able to react with it and produce two silanols; that is, it breaks the bond. At low K_1, the reactivity of the bond is low but it increases approximately logarithmically as K_1 increases. The higher the reactivity, the more rapidly bonds break and the faster the crack grows.

Michalske and Freiman pointed out that the water molecule is particularly suited to react with the Si–O bond because it has a labile proton and a lone electron pair

whose separation is about the same as the Si–O bond length. They argued that other molecules with similar bond structures should also react with the Si–O bond and produce subcritical crack growth in silicate glasses. Subsequent experiments showed that ammonia, hydrazine, and other reagents with the proper acid/base character produced subcritical crack growth with essentially the same logarithmic dependence—the same slope for log V versus K_1 plots—as that obtained with water.

In ceramics such as 94% alumina, which has a substantial quantity of glass phase at the grain boundaries, subcritical crack growth is usually through the glass phase. On the other hand, subcritical crack growth in Al_2O_3 single crystals involves a slightly different process than that described above for silicate glasses.[13] Experimentally, the subcritical crack growth curves obtained for Al_2O_3 with water, ammonia, and pyridine have different slopes. Al–O bonds can be broken relatively easily by adsorbing molecules of these reagents even when the Al–O bonds are unstrained. Apparently it is the mechanical response of the activated complex, including the adsorbed molecule, that determines the kinetics of bond breakage. The character of that activated complex depends on the specifics of the adsorbed molecule; therefore, the K_1 dependence—the slope of the log V versus K_1 plots—varies with the reagent.

9.3 Generation of Fracture Surface Features

The fracture surface features used in failure analysis are all a consequence of the interaction of the advancing crack with the microstructure of the material, with the applied stress fields, and with stress pulses produced by the advancing crack and reflected back to it. The fracture surface contains a detailed record of those interactions. The interpretation of those features requires an understanding of the interactions. An excellent description of how those features are used to deduce the failure event is presented in Reference 14.

Features Produced by Crack Interactions

One of the major factors in the generation of fracture surface features as well as in determining the macroscopic trajectory of a crack through a body is that, in an isotropic body, the crack will grow so that the fracture surface is perpendicular to the direction of the maximum tensile stress at the crack tip. For a uniform stress in a homogeneous, isotropic brittle material, the result, at low crack velocities, is a smooth, *mirror* fracture surface. However, in a varying stress field, the growing crack responds to a change in the direction of the applied stress by changing its direction of growth.

An example of the response of a crack to a changing stress field is shown schematically in Figure 9.2. In this example, the crack is moving from left to right with the crack plane perpendicular to the plane of the figure. Initially, the crack is driven by a constant stress (σ_y) in the y-direction. However, during its transit from Point

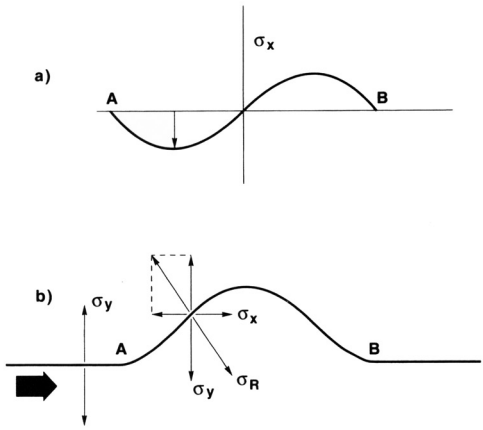

Figure 9.2 **Schematic of Wallner line formation. A sinusoidally varying stress in the *x*-direction (part *a*) is superimposed on a constant stress in the *y*-direction. Prior to that, the crack (moving from left to right) was planar (and perpendicular to the plane of the figure).**

A to Point B, it encounters a sinusoidally varying tensile stress (σ_x) in the *x*-direction. Figure 9.2*a* shows how the *x*-stress varies during that transit. The resultant stress, σ_R, changes direction as a consequence. Figure 9.2*b* shows the change in the trajectory of the crack as it responds to the change in direction of σ_R. The crack curves out of the initial crack plane, then back into that plane, leaving a smooth undulation on the fracture surface.

This type of smooth undulating feature on the fracture surface is exemplified in *Wallner lines*. In Figure 9.3, the Wallner lines are the curved features on the fracture surface. Wallner lines are often created by stress pulses generated as the crack interacts with inclusions in the body or with surface imperfections. (Those stress pulses usually consist of a compression followed by a dilatation so that the general wave form approximates the σ_x stress in Figure 9.2*a*.)

Figure 9.4 shows schematically how the interaction of the stress pulse with the crack front produces Wallner lines. In this instance, the crack is moving away from the origin at a constant velocity of 0.5 the speed of sound in the material so that the crack front at any instant is circular in shape. The pulse is generated at Point P and moves at the speed of sound, that is, twice the velocity of the crack. At the instant the pulse is generated, the crack front lies on the dashed line extending from Point P. By the time the crack moves out a distance *r*, the stress pulse will have moved a distance 2*r*. The locus of intersection of the moving stress pulse and the propagating crack will, therefore, be the heavy line passing through P and P′.

The example is for a rapidly moving crack. For a slow moving crack—one moving at only a small fraction of the velocity of sound in the material—the Wallner lines correspond well with the position of the crack front at the moment the stress

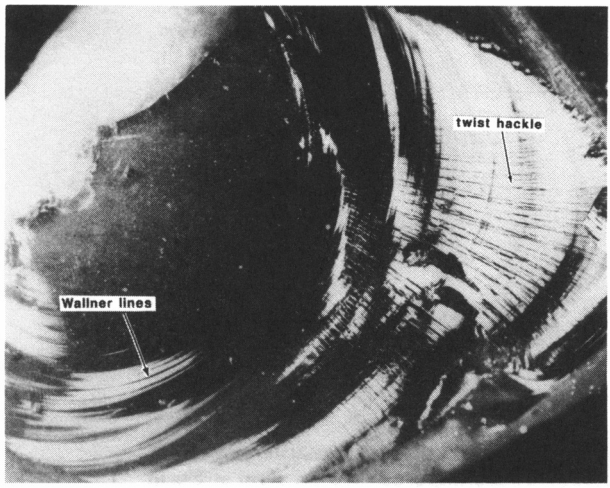

Figure 9.3 **Fracture surface in glass showing Wallner lines (curved features) and twist hackle (linear features perpendicular to the Wallner lines). The fracture origin (not shown) was in the upper left corner of the figure.**

pulse was created. In a uniform stress field, the crack front is concave toward the fracture origin. Consequently, in that instance, Wallner lines will be concave toward the origin of fracture and can be used to locate the origin. However, in a nonuniform stress field in which the velocity of the crack varies with position, the Wallner lines could even be convex toward the origin and mislead the observer.

In some instances, a crack will stop growing and will then be restarted under a different stress system. The result is an abrupt change in direction of crack growth that produces a feature like the Wallner line. This feature is termed an *arrest line*.

Another very common feature on fracture surfaces is *twist hackle*. In Figure 9.3, the twist hackle features are the nearly straight-line features lying roughly perpendicular to the curved Wallner lines. Like Wallner lines, twist hackle is produced by a change in orientation of the stress. However, unlike the situation depicted in Figure 9.2, the change that produces hackle is a rotation of the stress vector about an axis lying along the direction of propagation of the crack. In Figure 9.2, that would be equivalent to adding a component of stress in the z-direction to the one in the y-direction. Torsional loading of a rod produces this type of stress generation but it is common in many other loading situations.

The final result of a rotation of the stress vector will be a rotation of the fracture surface so that it remains perpendicular to the new stress direction. However, for a rapidly varying stress, the crack does not change direction smoothly as a unit to produce a ribbon-like surface. Instead, as illustrated in Figure 9.5, the crack advances in segments, each perpendicular to the new stress direction but separated from other segments by an initially unfractured ligament. At this point, the fracture

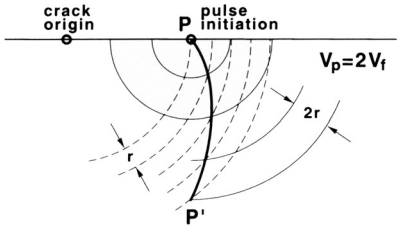

Figure 9.4 **Schematic of Wallner line formation. A crack moving out from the origin at constant velocity initiates a stress pulse at Point P. That stress pulse, traveling at twice the velocity of the crack, interacts with the crack front along the path P–P′, creating the Wallner line.**

surface would have had the appearance of a venetian blind. The final step in the fracture process is lateral growth of the fracture segments to produce an intersection with the adjacent segments. It is these lateral growths that constitute the visible features called hackle. The density of hackle features increases with the magnitude of the rotation of the stress.

Hackle is very useful in fracture analysis because it is always oriented parallel to the direction of crack propagation (perpendicular to the crack front). Moreover, fine hackle features tend to coalesce into coarser features and then eventually disappear as the fracture segments converge into a common plane. That coalescence gives an array of hackle features the appearance of tributaries flowing into a river. Because of this appearance, hackle is often referred to as *river lines*. As the analogy implies, the direction of crack propagation corresponds to the direction of flow of the river.

Hackle features are also generated by the interaction of the crack front with pores and inclusions in the material. The features are produced when the crack interacts

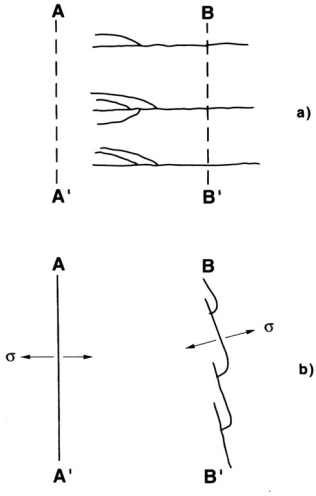

Figure 9.5 **Schematic of twist hackle formation. (*a*) The fracture surface is generated by a crack moving from left to right. (*b*) Cross sections through the fracture surface are generated along the lines indicated. A change in stress orientation, when the crack front is at CC′, produces noncoplanar crack growth in segments. Initially, those segments are unconnected. Subsequent lateral growth (the curved features in (*b*) produces intersection of those segments.**

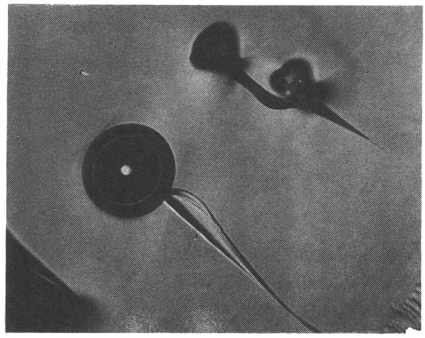

Figure 9.6 **Micrograph of wake hackle in glass fracture. The upper, large circular feature is a spherical pore. The lower two features are crystalline inclusions. The wake hackle, extending diagonally from those features, shows that the crack moved from upper left to lower right.**

with the stress field surrounding the pore or inclusion so that the crack splits into two noncoplanar segments. The stress field is created either because of the difference in elastic modulus of the inclusion relative to the bulk material or by residual stress generated by differential contraction of the particle and the matrix. The intersection of the two noncoplanar segments on the opposite side of the inclusion produces the feature known as *wake hackle*. An example of wake hackle on a glass fracture surface is shown in Figure 9.6. The larger circular feature is a void (bubble), and the smaller features to the right are crystalline inclusions.

Mist and Velocity Hackle

The features described above can be generated by either a slowly or a rapidly moving crack. There is, however, a class of features called *mist* and *velocity hackle* that are produced only when the crack velocity approaches that of acoustic waves in the material. Figure 9.7 is a micrograph of a fracture surface in glass with examples of mist and velocity hackle. This fracture initiated at the point marked "O" and grew

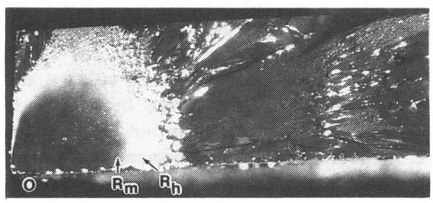

Figure 9.7 **Micrograph of fracture surface in glass showing the mirror region surrounded by mist and hackle. The location of the fracture origin is marked "O" and the boundaries of the mist and hackle regions are indicated, respectively, by R_m and R_h.**

initially with a very smooth surface, the so-called "mirror" region. The interior boundary of the mist region is at R_m and the interior boundary of the hackle region at R_h.

One of the factors that contribute to the generation of mist and hackle has to do with the rate of release of strain energy as the crack propagates. As noted earlier, when the stress intensity is K_{1c}, the strain energy released when a bond breaks and the neighboring bonds relax is just equal to the energy necessary to break the bond. For $K_1 > K_{1c}$, the neighbor bonds are strained to a higher level so that more energy is released as they relax. That extra energy is available to accelerate the crack to higher velocity. Figure 9.8 shows, schematically, that the velocity of propagation of the crack increases rapidly for K_1 values above K_{1c}. Ultimately the crack velocity is limited to about 0.6 of the sonic shear velocity.

The extra energy released from the strained bonds is also available to produce the additional fracture surface associated with the mist and velocity fractures. However, there is a second factor that leads to instability at the crack front that initiates the formation of those features. That factor is the change in the stress distribution near the crack tip as the crack velocity approaches the sonic velocity. Earlier, it was noted that, in the Irwin analysis, the maximum stress at the crack tip is perpendicular to the crack plane so that there is an inherent stability in crack growth. Unless the direction of the applied stress changes, the crack continues to run in a single plane. That situation applies to relatively slow moving cracks. For a rapidly moving crack, Yoffe[15] showed that the maximum tensile stress is no longer directly in front of the crack tip and oriented perpendicular to the crack plane. Instead, that maximum is at an angle to the crack plane, and that angle increases with velocity. As a consequence, the rapidly moving crack has a tendency to veer out of the primary plane.

As indicated in Figure 9.8, mist, hackle, and, finally, branching occur at successively higher values of K_1 (and higher velocity). In the usual case of a constant or

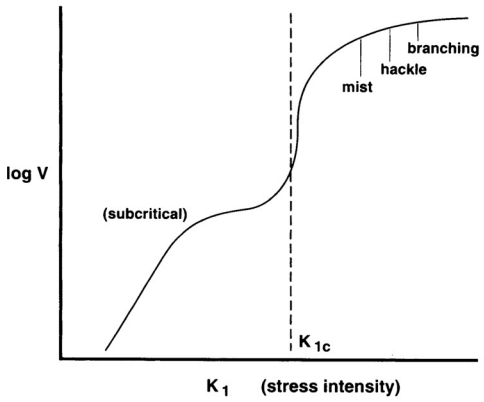

Figure 9.8 **Schematic showing dependence of crack velocity, *V*, on stress intensity, *K*.**

slowly varying applied stress field in which K_1 increases as the crack length increases, that sequence provides a valuable clue to the direction of crack propagation.

Experimentally, it has been observed that, for a crack that grows in a uniform stress field, the boundaries of the mist and hackle regions are semicircular. Furthermore, if the origin is a well-defined semicircular flaw, the radii of those boundaries bear fixed relationships to the radius of the flaw.[16] Equivalently, the applied stress at failure and the boundary radius are related by equations with the form

$$\sigma_f = \frac{A_i}{R_i^{1/2}} \tag{9.4}$$

where A_i is a constant (for a given material) corresponding to a given boundary and R_i is the radius of that boundary. These equations have the same form as the Griffith equation and imply that, at a particular value of K_1, mist begins to form and, at other particular values of K_1, hackle and branching occur. For hackle and branching, this seems to be true. The hackle boundary appears to be discrete and to reflect the onset of a new process for fracture surface alteration. Similarly, branching occurs at a particular value of K_1 indicating some special condition at the crack front. In contrast, although optical observations would suggest a discrete onset for mist formation, examination with the scanning electron microscope reveals mist-like features well within the mirror region. The features are simply smaller than those found at the mirror boundary. Apparently, mist-like features are already forming at much smaller values of K_1 than that corresponding to the mist boundary and grow in size as K_1 increases. The mirror/mist boundary simply corresponds to the point at which they have grown large enough to scatter visible light so that they can be observed in the optical microscope.

There is no consistent explanation for the generation of these features at particular values of K_1. Nevertheless, the fact that a value of K_1 can be inferred from a measurement of R_i is useful in analyzing failure. Mecholsky and Freiman[16] have shown how to use these features to quantify the stress state in the part, including localized residual stresses, to determine whether subcritical crack growth occurred, and to quantify the severity of the flaw.

The examples of fracture surface features shown in the micrographs above are all of glass fractures. These examples were used because the features in isotropic, homogeneous materials such as glass are easier to see than those in polycrystalline ceramics. In polycrystalline anisotropic materials in which substantial residual stresses can be generated by differential contraction of grains, the direction of crack growth may be strongly influenced by those residual stresses. Even when the crystal structure of the ceramic is cubic so that no residual stresses are generated at grain boundaries, variability of resistance to crack growth on different crystallographic planes within the crystal or differences in K_{1c} on the grain boundary and within the grain affect the direction of crack growth. As a consequence, in a polycrystalline ceramic, the more subtle features such as Wallner lines may not be visible.

In spite of the interference by internal residual stresses and crystalline anisotropy, the features described above can often be found on crack surfaces in polycrystalline and single-crystal ceramics. For very fine-grained ceramics, where grain size is smaller than the wavelength of visible light, the additional perturbations produced by grain boundary interactions may not even be visible in optical examination and the fracture surface will resemble that in glass. An excellent collection of micrographs of fracture surfaces in ceramics is given in Reference 17.

9.4 Procedures and Equipment Used in Fractography

From the preceding description of how fracture surface features are formed, it should be apparent that the presence and orientation of those features on a fracture surface can be used to infer crack direction, crack velocity, and other details of the fracture event at the moment the features were created. With that kind of information available, one can deduce a complete history of the failure process, including magnitude and direction of local stresses. In fact, the wealth of information available on the fracture surface makes fractographic examination a very powerful tool in determining how failure occurred.

Most of the procedures and equipment used in fractography have been developed to obtain the maximum amount of information from the fracture surface. Much of the examination is optical and begins with low-power observation of macroscopic features such as the general fracture pattern, including intersections and branching of cracks. It is often useful in macroscopic examination to reassemble fragments so that the fracture pattern can be discerned; however, it is essential that the fracture surfaces are not obscured by damage introduced during this reassembly. Macroscopic examination is also useful in determining how other elements of an assembly contributed to the failure of the ceramic or glass part. Often, this preliminary examination at low-power magnification will lead the observer to the general area where failure initiated, so that only a small area of the fracture surface needs to be examined in detail.

One of the keys to successful optical examination at any level of magnification is lighting the surface so that the fracture surface details are easily visible. At lowpower magnification, the best lighting is usually obtained with oblique illumination from a diffuse source. Shadows highlight hackle and other features. At higher magnification, in a metallurgical microscope, dark field illumination is useful for highlighting these same features. More subtle features, such as faint Wallner lines, can be enhanced by using interference microscopy.

Often, the problem in optical examination of polycrystalline ceramics such as alumina is that light reflected from interior grain surfaces can interfere with observation of fracture surface features. One can suppress these internal reflections by coating the fracture surface with carbon or other opaque material. Alternatively, the surface can be replicated and analysis conducted on the replica. Replicas using a

transparent material such as silicone rubber have the additional advantage of permitting examination with transmitted light so that additional contrast can be obtained. Replicas are also usually easier to archive than the fractured part itself and, for a large part or a fracture surface which is curved or very irregular macroscopically, may provide the only means for examining the surface at high magnification.

Because of its large depth of field and high magnification, the scanning electron microscope (SEM) is a powerful tool for obtaining detailed information about the fracture origin, particularly for rough fracture surfaces such as those in a polycrystalline ceramic. Chemical inhomogeneities in the vicinity of the site, including those associated with different phases as well as impurities or inclusions, can be detected through compositional backscattered electron imaging or using X-ray fluorescent spectrometry in the SEM.

9.5 Applications of Fractography

Failure Analysis Using Fractography

From the preceding discussion, it should be obvious that ceramic failure in any practical application implies the existence of a flaw that degrades the strength below the theoretical value and a stress sufficiently high to propagate that flaw. The intent of the failure analysis is, usually, to determine the nature of the flaw and, if possible, to ascertain how it was introduced. It is also desirable to determine the magnitude of the stress and how the stress was generated.

The fracture surface features described previously permit subtle details of the fracture process to be inferred. However, failure analysis usually requires the integration of information from many sources, including interviews with those who observed the failure. The examination of the failed part usually begins at a low level of magnification where the general trajectories of the cracks can be followed. Those trajectories not only lead the analyst to the origin of the fracture, but they can also provide detailed information about the nature of the stress distribution in the part at the moment of failure. For example, it is possible to determine in this examination whether failure of a bottle of carbonated beverage occurred from internal pressure or from impact with another bottle. For a complex fracture that fragments the ceramic, it may be useful to reconstruct the part to aid in this examination.

The Use of Fractography in Design Development

In this section, the use of fractographic analysis in the development of component design and assembly processing is illustrated with an example. The example is a metal/ceramic assembly, shown in Figure 9.9, in which a manganese zinc ceramic ferrite element was metallized, then solder-bonded into a stainless-steel header. The header was then welded into a housing and the entire assembly was machined in a surface grinder to bring the ferrite flush with the header and the face of the housing.

In the fabrication of prototypes of this assembly, cracks were discovered in the ferrite part after welding and additional cracking was observed after the grinding

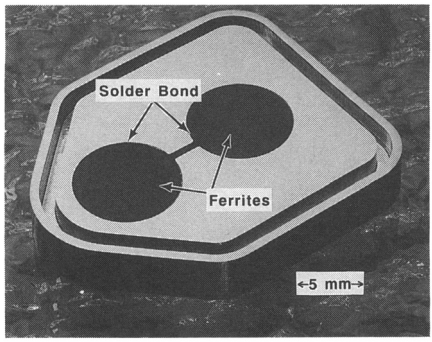

Figure 9.9 **Header assembly with ferrites solder bonded into stainless-steel header.**

was completed. The appearance of cracks at this stage of processing led the design engineers to assume that welding created stresses that cracked the ferrite and that grinding extended the cracks or, perhaps, simply rendered them visible. On that assumption, an intensive study of six months' duration was undertaken to try to improve the welding and grinding processes. That assumption was incorrect and the effort produced essentially no improvement in the cracking problem. The answer to the problem came from a subsequent, careful fractographic examination.

Figure 9.10 is a set of micrographs of one of the cracked parts with a sketch (in Figure 9.10*a*) showing dotted lines where the cracks intersected the machined surfaces of the ferrite element. Only the smaller diameter cylindrical surface of the part was soldered to the header (after that surface had been metallized by sputter coating). During grinding of the assembly, only the top surface of the ferrite part (Figure 9.10*b*) was accessible for optical examination.

The first step in any fractographic examination is to look at the intersections of multiple cracks. In this example, that preliminary examination was fruitful. The intersections on the flat T-shaped surface (sketched in Figure 9.10*a*) showed that there were two sets of cracks. One of these was approximately in the diametral plane bisecting the T and the other orthogonal to that and running along the plane that separated the large-diameter section of the part from the small-diameter section. On closer examination, as sketched in Figure 9.10*a*, it was observed that the cracking in the diametral plane was actually made up of two segments which were not quite coplanar. The conclusion from that observation was that the crack pattern on the T-shaped surface could only have been created if the crack segments in the diametral plane were formed after the crack in the orthogonal plane was formed.

When the part was removed from the header assembly, it separated into three fragments (marked B, C, and D in Figure 9.10*a*) along the fracture surfaces that had existed prior to disassembly. Two of those fracture surfaces are shown in Figures 9.10*c* and 9.10*d*. (Actually, these are silicone rubber replicas of the original fracture surfaces. The two fringed areas at the top and the right side of Figure 9.10*d* are areas where the rubber was trimmed away. Only the portion of the micrograph within the straight edges shows the fracture surface of the ferrite part.)

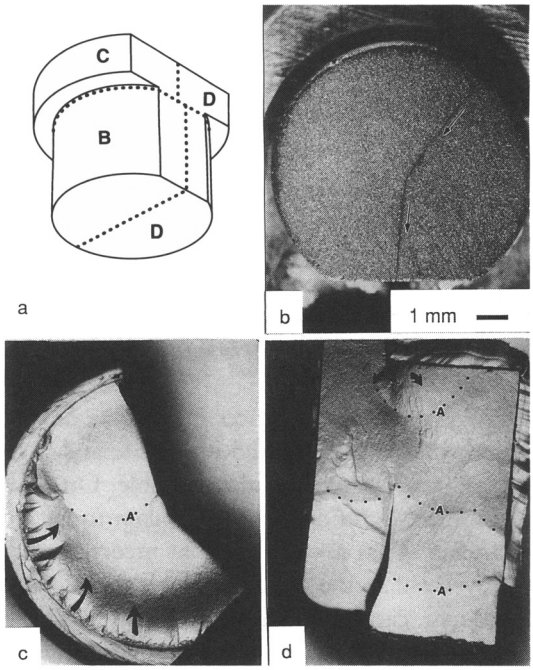

Figure 9.10 **Fracture of a ferrite part: (*a*) trajectories of the cracks along the surface of the part, (*b*) the part in the assembly with the visible cracks, and (*c*) and (*d*) fracture surfaces.**

Figure 9.10*d* is the fracture surface in the diametral plane. The flat T-shaped surface of the part is at the bottom of the micrograph. The apparent offset in the bottom portion of the micrograph is a consequence of the fact that the two portions of the fracture surface in this region are not coplanar and the view of that surface is at an angle to the T-surface. The dark vertical feature is a shadow produced by illuminating the surface at a slight angle away from normal to the surface. (As had been remarked in the previous section, oblique lighting is often used to enhance the fracture features.)

Most of the important aspects of this fracture can be inferred from the twist hackle features and the arrest lines on the surface of Figure 9.10*d*. The arrest lines are the dotted lines marked "A." Some hackle features can be seen crossing the arrest lines approximately at right angles. As noted earlier, arrest lines delineate the position at which the crack stopped and then restarted under a different stress system. The implication from the multiplicity of arrest lines in Figure 9.10*d* is that crack growth occurred at several stages of processing.

The conclusion from examination of these features is that the fracture originated at the top of the micrograph and ran initially as indicated by the two curved arrows. It then stopped at the semicircular arc about 1.5 mm from the origin. In the next stage of fracture, the crack ran to the approximate center of the part and again

stopped. In the final stages of fracture, the crack split. In the portion to the left of center in the micrograph, the hackle lines running diagonally indicate that the crack ran initially along the left edge of the fracture surface then toward the right and stopped at the vertical feature. The portion to the right of center propagated in two stages. In the first stage, it ran to the curved feature (another arrest line) approximately 1.5 mm from the T-surface then, finally, to the T-surface.

Part of the fracture surface that was orthogonal to the diametral plane in the sketch is shown in Figure 9.10*c*. In the sketch in Figure 9.10*a*, it is the fracture surface that runs from the intersection of the segment of the ferrite marked "C" and that marked "B" to the intersection of segments "C" and "D." (In Figure 9.10*b*, it is the fracture surface exposed by removing the segment of the large diameter section to the left of the crack from the rest of the part.)

Examination showed that the fracture in Figure 9.10*c* started at multiple origins along the circular edge. The curved arrows in the figure were placed so that their bases were located at some of those origins. The hackle lines that extend from the edge of the fracture surface are intersections of the various fracture surfaces that initiated at those different origins. Those hackle lines terminate where the multiple cracks coalesced into a single smooth crack. An arrest line (marked "A") shows where the crack stopped. A second growth step completed the fracture.

When the two fracture surfaces are compared, it becomes apparent that the arrest line running horizontally across the center of Figure 9.10*d* crossed the fracture surface in Figure 9.10*c* at the point at which the circular arrest line meets the diagonal edge. The two cracks started at opposite sides of the part in nearly orthogonal planes and stopped when they intersected.

The interpretation of these observations provides insight into how processing of the ferrite might have created the cracks. First, the fact that the fracture surface in Figure 9.10*c* had started at *multiple* origins at the ground surface of the part, then coalesced into a *smooth* surface and then *stopped* before fracture was completed is strong evidence that the stress that initially drove the crack was very high at the surface of the part but decreased rapidly away from the surface. It is precisely the type of stress field produced by thermal down-shock, in which a hot part is quenched in a cold fluid. The fact that the initial fracture planes were perpendicular to the surfaces of the part is consistent with thermal shock of the isolated part, that is, without the constraint of adjacent structures. Therefore, the thermal shock probably occurred before the ferrite part was soldered into the header. The fact that those fractures initiate in diametral planes as well as in planes orthogonal to those is also consistent with the stress system generated by quenching a part.

The development of the fracture surface can be understood in terms of the processing sequence that the ferrite part saw. The scenario that was developed begins with an initial down-shock in which the hot ferrite was dropped into a cold liquid. Probably, the crack in the diametral plane extended only to the first arrest line in that down-shock, but the crack in the orthogonal plane may have run all the way to the circular arrest line. The next step in the growth of the cracks may

have occurred on cooling after the ferrite was soldered into the header. Tensile stress would have been generated in the radial and circumferential directions in the ferrite because of the differential contraction relative to the header. Those stresses would have propagated the diametral crack, but not the orthogonal one. Some information about the sequence of fracture was obtained when it was noted that there was solder flux on the upper area of the surface in Figure 9.10*d* and on all of the surface up to the circular arrest line in Figure 9.10*c*. Since the part saw no heating after the soldering operation that would have melted the flux, it seems safe to conclude that the portions of the fractures in the lower half of Figure 9.10*d* and within the shiny circular zone of Figure 9.10*c* were produced after the soldering operation.

Stress analysis showed that additional tensile stress in the radial and circumferential directions was generated in the ferrite during welding. That probably extended the crack on the left side of Figure 9.10*c* to the T-surface and on the right side to the lower arrest line. The constraint of the header on the ferrite part prevented the crack on the right side from extending to the machined surface of the part. That last portion of the fracture surface was produced in removing the ferrite from the header during disassembly.

With this information, it was clear that the welding and subsequent grinding operations were not the primary cause of the cracking and that the probable cause was an earlier process step that would have resulted in down-quenching of the part. That step was identified and modified to prevent the down-shock. Also, examination of the fracture origins at high magnification showed that they were very severe flaws and had been introduced by machining. To increase the strength of the ferrite, investigators recommended altering the machining process to increase the radius at the junction between the large and small radius portions of the part and to reduce the size of the flaws.

Fractography in Materials Development

One of the keys to optimizing the strength in a ceramic material is to understand how the failures are being produced. To a large extent, this means knowing what the strength-limiting flaws are. Are they, for example, flaws introduced in machining of the part and therefore amenable to removal by modifying the machining operation, or are they inherent in the material? If they are inherent in the material, can they be removed or at least modified by changing the processes used in synthesizing the material?

Understanding how failures are produced also requires knowledge of the true state of stress at the flaw. In a bend specimen, for example, where was the flaw located relative to the neutral plane? Was there any prestressing of the flaw because of residual thermal stresses or because of anisotropy of the material system?

These are the kinds of questions that can be answered through fractographic analyis. Not only does the analysis permit the location of the critical flaw, but it permits a description of the severity of the flaw in terms of a penny-shaped flaw of equivalent size. Furthermore, as noted above, an examination of the shape of the

mirror and mist boundaries permits the detection and quantification of internal stresses.

As noted earlier, the characterization of the mechanical behavior of a ceramic requires measurement of the failure stresses for a number of nominally identical samples and a statistical treatment of the resultant data. Quinn et al.[18] argued that fractography is an absolutely essential part of any mechanical characterization of a ceramic. In particular, they recommend that Weibull plots or any other graphical presentation of collections of data include information on the type of defect responsible for every failure. They further recommend that, in any archiving of ceramic mechanical strength data, micrographs of the failure surfaces be included as an integral part of the archived data.

Quinn et al. also point out that fractographic analysis is highly interpretive and requires considerable judgment. In Reference 15, they propose a standard procedure for optimizing the use of fractography as an adjunct to mechanical testing.

Fractography in Materials Research

The manner in which the crack interacts with the microstructure of a ceramic can affect both the fracture toughness and the strength. In composite ceramics such as those with SiC fibers in an Al_2O_3 matrix, for example, the highest toughness is obtained when the bond between the fibers and the matrix is weak enough that the fibers pull out of the matrix rather than fail when the crack front intersects them. It should be obvious that examination of the fracture surface can provide information on the failure mode and, thus, aid in the optimization of the toughness.

Even for single-phase polycrystalline ceramics or two-phase ceramics where the second phase is a thin grain boundary layer separating the grains of the primary phase, details of the path of the fracture determine how tough and strong the ceramic will be. Often, the part of the microstructure most vulnerable to subcritical crack growth is the grain boundary phase. It is, therefore, invaluable in developing a material for optimum behavior to examine the fracture surface to determine whether the fracture path was through the grains or along the grain boundaries.

Examination of the fracture surface can also yield essential information in the study of the fundamentals of brittle fracture. As an example, it had been observed that the fracture of alumina and some other ceramic materials displayed R-curve behavior; that is, the effective fracture toughness increased as the crack length increased.[19] The explanation for this increase was obtained through a detailed examination of crack propagation through the ceramic and the observation that crack interface bridging was occurring.[20] The bridges effectively supported part of the applied stress and reduced the stress intensity at the crack tip.

References

1 B. R. Lawn and T. R. Wilshaw. *Fracture of Brittle Solids*. Cambridge University Press, Cambridge, 1975.

2 G. R. Irwin. *Hanbuch der Physik*. Vol. 6. Springer, Berlin, 1958.

3 A. A. Griffith. *Phil. Trans. Roy. Soc.* (Lon.). **221A**, 163, 1920.

4 C. E. Inglis. "Stresses in a Plate Due to the Presence of Cracks and Sharp Corners." *Trans. Inst. Navla Archit*. **55**, 219, 1913.

5 E. Orowan. "Energy Criteria of Fracture." *Weld. Res. Supp*. **34**, 157, 1958.

6 B. R. Lawn and D. B. Marshall. *Indentation Fracture and Strength Degradation in Ceramics*. Fracture Mechanics of Ceramics, Vol. 3. Plenum, 1978, p. 205.

7 W. Weibull. *J. Appl. Mech*. **18**, 293, 1951.

8 *Annual Book of ASTM Standards*, Vol. 15.02, American Society for Testing and Materials, Philadelphia, 1990.

9 G. D. Quinn and R. Morrell. "Design Data for Engineering Ceramics: A Review of the Flexure Test." *J. Am Ceram. Soc*. **74** (9), 2037–2066, 1991.

10 Fracture Mechanics of Ceramics, Vol. 6. Plenum, 1983, pp. 1–62.

11 S. M. Wiederhorn. *Subcritical Crack Growth in Ceramics*. Fracture Mechanics of Ceramics, Vol. 2. Plenum, 1974, p. 613.

12 T. A. Michalske and S. W. Freiman. *J. Am. Ceram. Soc*. **66** (44), 284, 1983.

13 T. A. Michalske and B. C. Bunker. *J. Appl. Phys*. **56**, 2686, 1984.

14 V. D. Frechette. *Failure Analysis of Brittle Materials*. Advances in Ceramics, Vol. 28. Am. Ceram. Soc., 1990.

15 E. Yoffe. "The Moving Crack." *Phil. Mag*. **42**, 739, 1951.

16 J. J. Mecholsky and S. W. Freiman. "Determination of Fracture Mechanics Parameters through Fractographic Analysis of Ceramics," *Fracture Mechanics Applied to Brittle Materials (11th Conference), ASTM STP 678*. American Society for Testing and Materials, Philadelphia, 1980, p. 136.

17 R. W. Rice. "Ceramic Fracture Features, Observations, Mechanisms and Uses," *Fractography of Ceramic and Metal Failures, ASTM STP 827*. American Society for Testing and Materials, Philadelphia, 1984, pp. 1–103.

18 G. D. Quinn, J. F. Swab, and M. J. Slavin. "A Proposed Standard Practice for Fractographic analysis of Monolithic Advanced Ceramics." MTL TR 90–57, Nov. 1990.

19 A. G. Evans. *J. Am. Cer. Soc*. **73**, 187–206, 1990.

20 P. L. Swanson, C. J. Fairbanks, B. R. Lawn, Y.-W. Mai, and B. J. Hockey. *J. Am. Ceram. Soc*. **70**, 279, 1987.

10

Ceramic Composites

S. JILL GLASS AND RAJAN TANDON

Contents

10.1 Introduction

Ceramic composites can be defined as materials in which one or more ceramic materials are deliberately added to another, in order to enhance or provide some property not possessed by the original materials. Although studies of ceramic composites for structural applications dominate the literature, composites for electronic and optical applications are also of interest. For example, electroceramic composites are being developed as smart materials.[1]

Ceramic composites include particulate-, whisker-, and fiber-reinforced ceramic and glass matrices. Particulate-reinforced ceramic composites include polycrystalline or glass matrices with particles such as zirconia and silicon carbide. In some cases the glass matrix is crystallized to produce a ceramic particulate-reinforced glass–ceramic composite. This approach overcomes some of the problems associated with consolidating dissimilar materials, because the materials are mixed when the matrix is a glass and easy to form. Whisker-reinforced ceramic composites usually consist of a polycrystalline or glass matrix to which single-crystal whiskers have been added. Whiskers have also been grown in situ in materials such as Si_3N_4. Fiber-reinforced ceramic composites consist of a polycrystalline or glass matrix with single-crystal, polycrystalline, or glass fibers. Fibers with a wide range of compositions and properties are available, but the most commonly used are carbon,

graphite, and SiC. Ceramic composites also include composites formed by mixing ceramics and metals, and ceramics and polymers.

Each of these combinations of materials can be considered composites on a microscale. Ceramic composites, which can be considered composites on a macroscopic scale, include laminated structures and composites that have been termed functionally gradient materials (FGMs). FGMs, which are designed to have smooth gradients in composition, have been fabricated by vapor deposition, plasma sputtering, and electrodeposition techniques. Lamination techniques are used for FGM applications in which more abrupt compositional changes are acceptable.

Although ceramic materials are often classified as either single-phase or composite, it is difficult to identify a ceramic that is not a composite on some scale. For example, many polycrystalline single-phase ceramics are made up of grains (small single crystals) of one composition and phase surrounded by an amorphous grain boundary of a different composition. The properties of the grain boundary can differ significantly from the properties of the grains, producing a material that has properties intermediate between the two compositions or completely different from either. Nickle zinc ferrites ($Ni_{0.4}Zn_{0.6}Fe_2O_4$), in which conducting grains are surrounded by grain boundaries of lower conductivity, are a classic example of this type of composite.[2]

In most applications of composites, interfacial properties are critical to the performance. For example, consider fiber-reinforced composites. If there is a reaction between the matrix and the fiber, the two materials are generally strongly bonded to each other. This produces a ceramic composite with a low toughness because, when the fibers remain firmly bonded to the matrix, no energy is consumed in pulling the fibers out of the matrix as a crack propagates. Under these conditions, the mechanical behavior of the composite is similar to that of the unreinforced matrix. Its stress-strain behavior is linearly elastic until the point of failure, that is, failure is catastrophic, as shown in Figure 10.1 for monolithic zircon.[3] On the other hand, if the fibers have a nonreactive coating, such as carbon or boron nitride, there is little or no bonding at the interface. As a crack propagates through the stressed material, energy is consumed as fibers pull or slide out of the matrix. The stress-strain curve for this type of composite, also shown in Figure 10.1 for composites containing both coated and uncoated SiC fibers, demonstrates that composite failure occurs noncatastrophically.

Although interfaces usually constitute a small fraction of the total volume of a composite, the effects of their properties on the bulk properties are large because of the large surface area of the interfaces. The properties of the interface depend on whether or not there has been a reaction at the interface, the type of bonding at the interface, and on the nature (crystalline or amorphous) and morphology of the interface material. The consequences of having a smooth versus a rough interface are far more important in structural applications where one phase, such as a fiber, must be able to slide out of the matrix to some extent, in order to achieve optimum mechanical behavior.

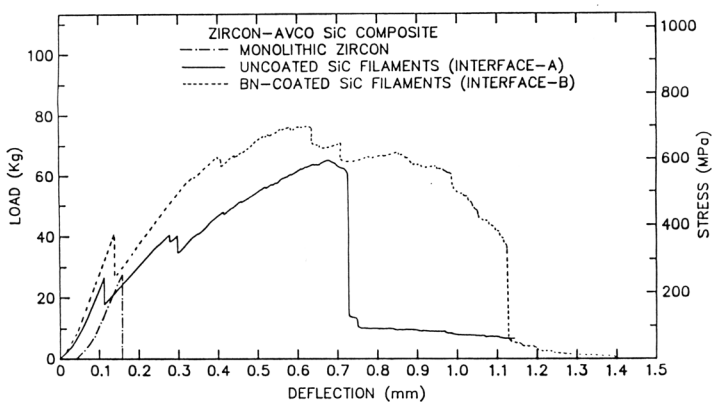

Figure 10.1 Stress–strain curves for an unreinforced zircon, a SiC fiber-reinforced zircon composite in which there is strong interfacial bonding (Interface-A), and for a SiC fiber-reinforced composite in which there is weaker interfacial bonding (Interface-B).[3]

The properties of the original constituents of a composite are often well known or easily measured; however, the properties of the interface are not. Some of the difficulties with obtaining interfacial properties arise because interfacial reactions often produce phases which do not exist in bulk. Because of the difficulty of obtaining interfacial properties, they are frequently inferred from correlations between bulk properties and information about the interfaces determined using surface and interfacial characterization techniques. The information usually sought is whether or not there has been mass transport across the interface and what reactions have occurred between the constituents. The surface and interfacial microcharacterization techniques which are most commonly used for obtaining the above information are described in the lead volume of this series, *Encyclopedia of Materials Characterization*.

The remainder of this chapter contains brief descriptions of some of the bulk properties of interest for ceramic composite applications and examples of how information obtained from surface and interfacial characterization techniques has been used to attempt to understand bulk behavior. Sometimes, in spite of differences in interfacial structure, no difference in the measured bulk behavior is observed.

10.2 Mechanical Properties of Ceramic Composites

R-Curve Behavior

A material is said to exhibit R-curve behavior if its resistance to crack propagation increases with increasing crack length. R-curve behavior is important in terms of the mechanical performance because it imparts a degree of flaw tolerance to the material. That is, the strength of a material becomes insensitive to the flaw size. This characteristic is demonstrated in Figure 10.2,[4] which shows the strength of two

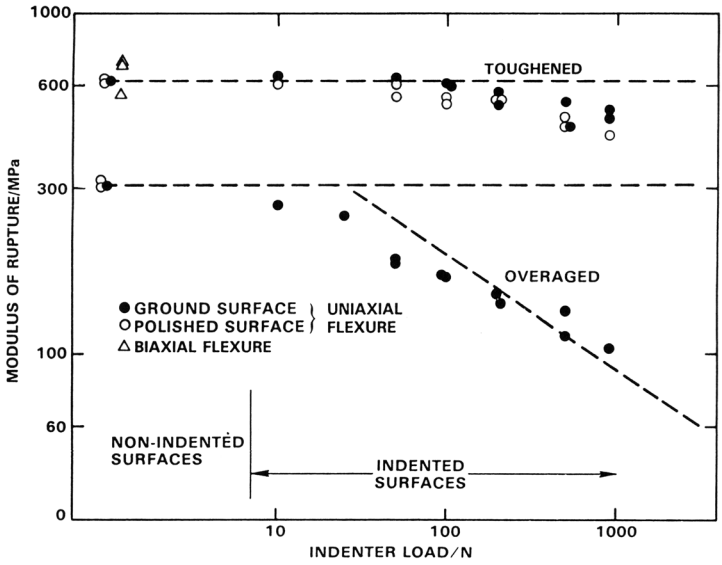

Figure 10.2 Strength of indented ceramics versus indentation load. Note the lack of a dependence of strength on indentation load for the toughened ceramic.[4]

zirconia ceramics (toughened and overaged) that had deliberate flaws introduced into the surface, as a function of the load used to generate the flaw. The toughened material showed pronounced R-curve, whereas the overaged material exhibited a sharp decrease in strength as a function of the indentation load.

Example Ceramic composites of alumina and 28 vol % glass were studied by Padture et al.[5] using transmission electron microscopy (TEM) to determine the effects of grain boundary crystallinity on R-curve behavior. Aluminas containing 28 vol % glass were subjected to several heat treatments to crystallize the glassy grain boundary in an effort to enhance grain boundary stresses and R-curve behavior. These heat treatments influenced both the grain boundary composition and the phases that were present. TEM was used to identify whether the grain boundaries were glassy or crystalline after the heat treatments. Figure 10.3 shows TEM micrographs of aluminas containing glass and crystalline grain boundaries. Further analyses of the materials containing glassy grain boundaries were conducted using energy-dispersive spectroscopy (EDS) to determine the glass composition. By comparing the compositions obtained from different regions of the same sample, Padture et al. also determined the uniformity of the glass composition throughout the body. In the aluminas heat-treated to produce a crystalline grain boundary phase, TEM identified the crystalline phase as anorthite. In spite of differences in grain boundary composition and crystallinity, no differences in the R-curve behavior were observed.

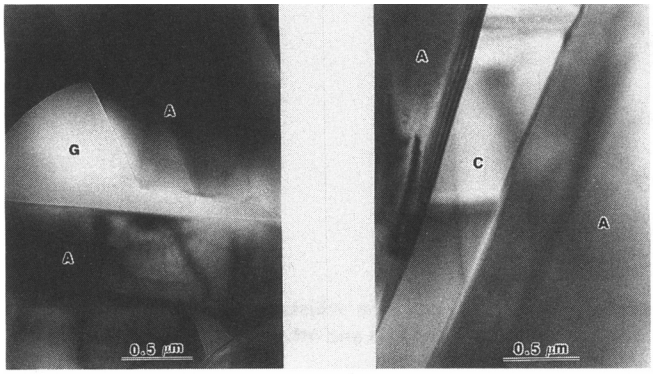

Figure 10.3 **TEM micrographs of aluminas (A) containing (*a*) glass (G) and (*b*) crystalline grain boundaries (C).[5]**

Creep

Creep is the process or processes by which permanent deformation occurs, usually at elevated temperatures. Elevated in the context of ceramics usually means temperatures exceeding half the melting point. For a given material, creep is a function of stress, time, and temperature; it occurs by diffusion, dislocation motion, grain boundary sliding, or softening of grain boundary phases. The presence of second phases can have a significant effect, either positive or negative, on the rate at which a material creeps. Many ceramic composites which contain glass have poor creep resistance because glass enhances grain boundary sliding. Many whisker-reinforced ceramic composites exhibit improved mechanical properties at low temperatures, and studies are being conducted to determine if creep resistance is also improved. Although there is much speculation as to what mechanisms are responsible for improved creep resistance in reinforced ceramic composites, electron microscopy can often provide definitive proof. For example, scanning electron microscopy (SEM) can reveal grain-boundary offsets and grain rotations, which are both indicative of grain boundary sliding. Another creep mechanism is intergranular cavity formation, leading to cavity coalescence to form microcracks. This mechanism is also easily identified with electron microscopy.

Example 1 Swan and O'Meara[6] compared the creep for Si_3N_4 with and without SiC whisker reinforcements. Creep mechanisms, phase content, whisker distribution, grain boundary crystallinity, and oxidation behavior were studied using TEM and X-ray diffraction (XRD). Figure 10.4 shows a TEM micrograph of an oxide scale on a whisker. The oxide scale contained Si_2N_2O and other crystalline phases in an amorphous layer. No improvement was found for the creep behavior of the composite over the unreinforced Si_3N_4.

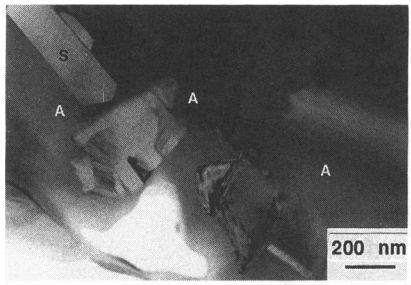

Figure 10.4 TEM micrograph showing oxide scale on whisker-reinforced Si_3N_4. The oxide scale contains Si_2N_2O (S) and other crystalline phases in an amorphous layer (A).[6]

Example 2 A study by Lin and Becher[7] included an evaluation of the effects of whiskers on the creep resistance of alumina–SiC–whisker composites. Whisker additions up to 20 vol % improved the creep resistance relative to alumina alone, but higher whisker loadings degraded the creep resistance. The creep rates of the higher whisker-loaded composites were one to two orders of magnitude higher than those for the 10 and 20 vol % composites. TEM observations showed that composites with higher whisker loadings (30 and 50 vol %) exhibited cavity number densities a factor of two higher than the 20 vol % composites. The TEM micrograph in Figure 10.5 shows a number of cavitation sites in a 20 vol % composite. The whiskers may have introduced additional cavity nucleation sites, and if so, the

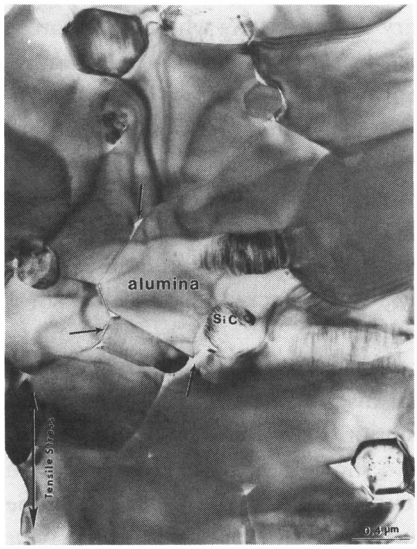

Figure 10.5 TEM micrograph of creep cavitation sites in the 20 vol % SiC whisker-reinforced composite.[7]

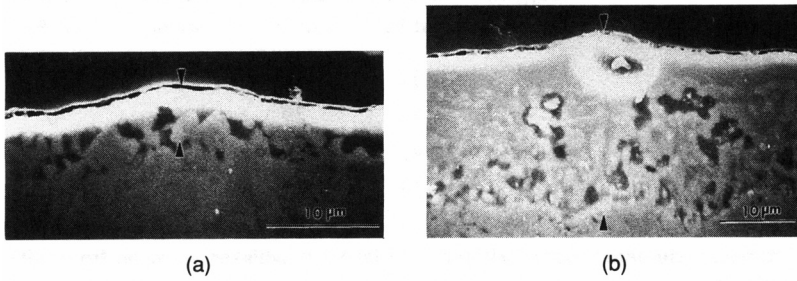

Figure 10.6 SEM micrographs used to measure oxidized layer thickness: (*a*) 20% SiC_W and (*b*) 30% SiC_W.[7]

increased creep deformation is likely to be directly related to the increased creep cavitation. Higher creep rates were also associated with increased oxidation rates in the composites containing higher whisker loadings. TEM also revealed the presence of greater amounts of intergranular glass phases in the composites showing enhanced oxidation. The presence of the glass appears to further degrade the creep resistance of the composite. SEM was used to determine the thickness of the oxidized layers shown in Figure 10.6.

Fracture Toughness

The fracture toughness of a material defines its resistance to crack propagation. Most ceramics have low fracture toughness values compared with other materials,

Material	Fracture Toughness, $MPam^{1/2}$
Ice	0.2
Pyrex glass	0.75
Common woods parallel to grains	0.5–1
Nylon	3
Alumina	2.7–4.2
Silicon Nitride	4–6
Partially stabilized ZrO_2	8–9
SiC whisker/Al_2O_3 matrix composites	9–10
Common woods perpendicular to grains	11–13
Cast iron	6–20
7075 T6 Al	32
4340 steel (tool steel)	46
High-strength steel	120–153

Table 10.1 Fracture toughness values for common materials.

Whisker	Oxygen, wt%	Silicon, wt%	Carbon, wt%	Nitrogen, wt%	Calcium, wt%
As-received	33	31	36	0	0
Air heat treatment	34	37	29	0	0
4% H_2 in N_2 heat treatment	20	42	29	9	0
10% H_2 in Ar heat treatment	27	33	34	5	2

Table 10.2 Estimated elemental compositions of Silar-SC-9 whisker surfaces from XPS analyses.

as given in Table 10.1. Ceramic composites often exhibit significantly higher toughness values than do monolithic ceramics. The fracture toughness of a composite ceramic is largely determined by the strength of the bonding between the reinforcement phase (fiber, whisker, or particle) and the matrix. Weak interfaces tend to give

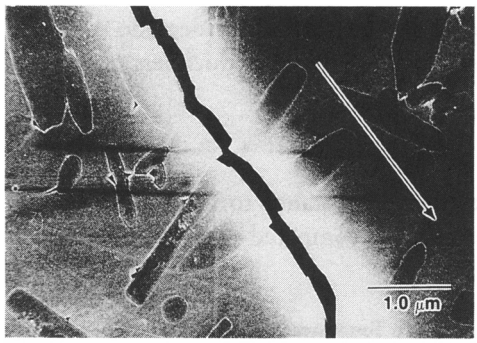

(a)

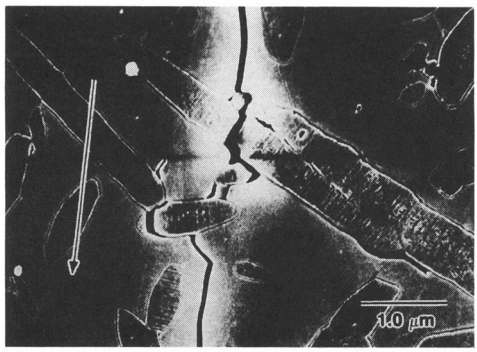

(b)

Figure 10.7 SEM micrographs highlighting the increased crack-whisker interactions for the composite which contains silicon oxycarbide species (*b*).[8]

the highest toughness values, and fracture surfaces which show fibers or whiskers that pulled out of the matrix are usually observed in conjunction with high toughness values. Interfacial strength is largely a function of the interfacial chemistry, and there are several microcharacterization techniques well-suited to identifying the reaction products.

Example 1 Homeny et al.[8] evaluated the fracture toughness of SiC whisker-reinforced (30 vol %) Al_2O_3 composites as a function of whisker surface chemistry, which was varied by heat-treating the composites in controlled atmospheres. X-ray photoelectron spectroscopy (XPS) was used to correlate the whisker surface chemistry with the fracture toughness. Table 10.2 gives the XPS estimated elemental compositions of the whisker surface as a function of treatment. Detailed spectra were analyzed to identify the specific chemical compounds present on the whisker surfaces. The highest toughness values were associated with the presence of silicon oxycarbide species, free carbon, hydrocarbon species, or a combination of these. Figures 10.7***a*** and ***b*** are SEM micrographs that exemplify the difference in crack microstructure interactions in composites with different whisker chemistries.

Example 2 Rawlins et al.[9] fabricated NICALON (Si-oxycarbide) fiber-reinforced SiC composites using a chemical vapor infiltration (CVI) process. SEM showed regions with good and poor fiber pullout within the same sample, as shown in Figure 10.8. A thick film was observed on the fibers in the regions of good pullout as shown in Figure 10.9. No film could be detected within the resolution of the SEM on fibers that exhibited poor pullout. Scanning Auger microscopy (SAM) and spectroscopy were used to determine that the fibers were primarily Si and C, whereas their surfaces were primarily Si and O (probably SiO_2). A typical Auger electron spectroscopy profile is shown in Figure 10.10. The left side of the profile is the fiber surface. To produce more reliable fiber behavior, Rawlins et al. deliberately coated the fibers by chemical vapor deposition techniques prior to

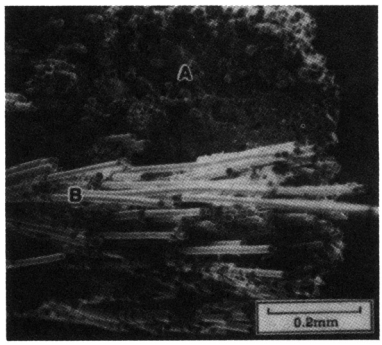

Figure 10.8 SEM micrograph showing regions of good fiber pullout and no fiber pullout within the same specimen.[9]

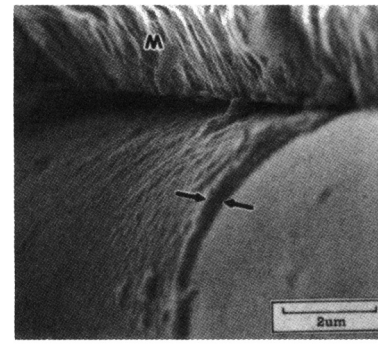

Figure 10.9 SEM micrograph showing film on fibers that pulled out easily.[9]

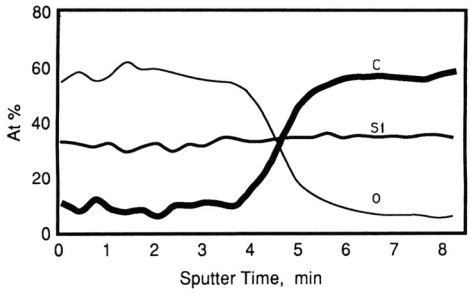

Figure 10.10 Auger electron spectroscopy profile of a fiber which reveals that the fiber surface (left side) is primarily Si and O.[9] (Sputter rate is about 10 nm/min.)

chemical vapor infiltration of the composite. Carbon and silicon coatings were tested. The carbon coating produced more uniform pullout in the composite as shown in Figure 10.11, where carbon-coated fibers can be seen pulled out of the matrix. The silicon coating drastically reduced the extent of pullout in the composite.

Flaws

Flaws reduce the strength of composites because they amplify applied stresses to the degree that the intrinsic material strength is exceeded in the vicinity of the flaw. Common flaws include pores, cracks, delaminations, large grains, agglomerates, and inclusions. Because of the difficulties of consolidating and densifying dissimilar materials, processing flaws are often more numerous and more severe in composites than in monolithic ceramics. As composite processing becomes more sophisticated and flaw sizes are reduced, it is becoming increasingly difficult to detect the flaws that remain. Microcharacterization techniques, especially those that are nondestructive, are playing increasingly important roles in finding and characterizing these flaws. For further information, see Chapter 13, "Nondestructive Evaluation."

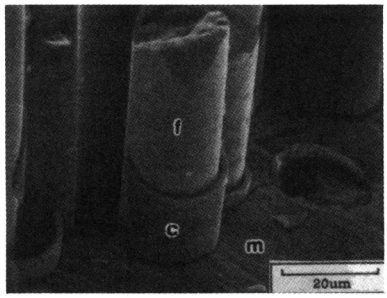

Figure 10.11 SEM micrograph of a carbon-coated fiber which has pulled out of the matrix.[9] (f = fiber, m = matrix, and c = carbon coating.)

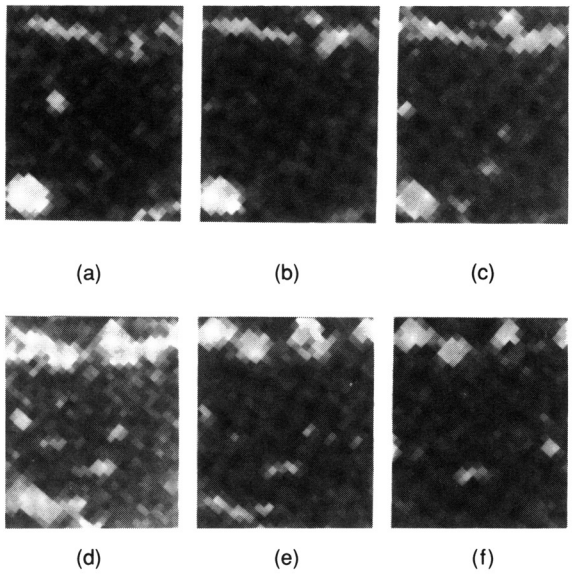

Figure 10.12 Microtomography images of porosity (*light contrast regions*) in a Si_3N_4/SiC composite which was not degassed during fabrication. All images were obtained from adjacent volumes of material.[10]

Example Stock et al.[10] used microtomography to study the effect of vacuum degassing on porosity in silicon carbide fiber-reinforced silicon nitride composites. Large pores (light contrast) and dense regions (dark contrast) are easily distinguished in the specimen that was not degassed, as shown in Figure 10.12. The 15-μm SiC fibers cannot be resolved because the pixel size is only slightly larger than the fiber diameter and because the X-ray absorptions of the fibers and matrix are similar. Microtomography can also be used to follow damage accumulation and cracking during mechanical testing of this type of composite.

Fatigue Crack Propagation Resistance

Crack propagation often occurs when a material is cyclically stressed, even when the magnitudes of the cyclic stresses are lower than those required to propagate a crack under static loading. Crack propagation can occur both under tension–tension and tension–compression cyclic loading. Cyclic stresses can be induced by heating and cooling, vibrations, and structural loading and unloading. Fatigue behavior in ceramic composites appears to be sensitive to crack tip shielding effects due to transformation zones or crack bridging in the wake of the crack tip. Thus, prior loading history influences subsequent crack propagation.

Example Tsai et al.[11] investigated fatigue behavior in zirconia–alumina composites after heat treatments designed to modify the zirconia transformation yield stresses. Raman spectroscopy was used to quantify the fractions of monoclinic

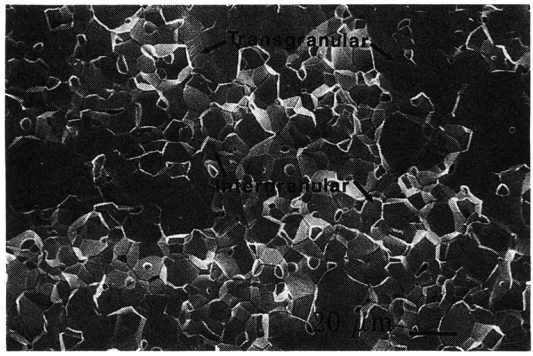

Figure 10.13 SEM micrograph of a fracture surface of a Mn–Zn ferrite exhibiting both intergranular and transgranular fracture.

zirconia in the transformation zone at the crack tip. These fractions were used to calculate the magnitude of the crack tip shielding due to the transformation zone. Calculated crack tip shielding was slightly higher in the cyclically loaded specimens than in the statically loaded specimens. Raman spectroscopy also showed that the amount of monoclinic zirconia in the transformation zone decreased as a function of distance away from the crack plane. This finding suggests that the calculated absolute values of shielding were overestimated. Raman measurements of the volume fraction of monoclinic zirconia in the transformation zone were also useful because they showed that reverse transformation due to load cycling did not play a role in the fatigue behavior of these composites.

Fracture Mode

Cracks propagate intergranularly (between grains), transgranularly (through grains), or with fractions of both fracture modes. The grain boundary toughness plays a large role in determining the fracture mode; however, the direction of crack propagation relative to the orientation of the grain boundary, the crack velocity, grain size, residual microstresses, and environmental factors also influence the fracture mode. Figure 10.13 shows a fracture surface of a Mn–Zn ferrite ceramic which exhibits both intergranular and transgranular fracture. Intergranular fracture often increases the degree of crack deflection, which can result in higher toughness values. Grain boundary impurity segregation is often associated with intergranular failure, and microcharacterization techniques can be used to detect and identify impurities. (See Chapter 9, "Mechanical Properties and Fracture.")

Example Powell-Dogan and Heuer[12] studied the fracture mode and mechanical properties of 96% pure alumina as a function of the grain boundary glass composition and crystallinity. Grain boundary crystallization was induced by annealing at 1100 °C for 100 h. TEM was used to identify six crystalline grain boundary phases, including anorthite, gehlenite, grossular garnet, spinel, calcium hexaluminate, and α-alumina. Residual glass was also observed after annealing.

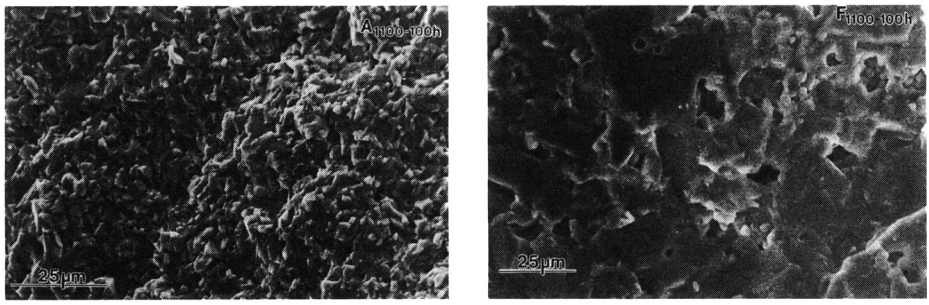

Figure 10.14 **SEM micrographs of heat-treated 96% alumina specimens showing (*a*) primarily intergranular fracture in alumina containing a CaO-rich glass and (*b*) primarily transgranular fracture in alumina containing a MgO-rich glass phase.[12]**

Because all of the observed second phases have higher or lower coefficients of thermal expansion than the α-Al_2O_3 (e.g., $\Delta\alpha = 7.6 \times 10^{-6}/°C$ for α-Al_2O_3 and gehlenite), residual stresses are produced in the second phases and the α-Al_2O_3. Strain contrast observed in the TEM confirmed the presence of these stresses. SEM micrographs in Figures 10.14***a*** and ***b*** show that fracture was primarily intergranular in the alumina containing a CaO-rich glass and primarily transgranular in the alumina containing a MgO-rich glass. Despite differences in grain boundary composition, crystallinity, and fracture mode, similar strength and toughness values were measured for the 18 materials tested.

Adhesion

Adhesion can broadly be defined as the strength of the interface between two regions of a material system.[13] Adhesion can be due to strong primary bonds such as ionic, covalent, and metallic bonds, due to secondary bonds such as van der Waals forces, or simply due to mechanical interlocking at the interface. Adhesion plays an important role in powder processing, coating technology, wear, friction, and joining. The work of adhesion is the amount of energy per unit area required to separate the two materials at the interface. For ceramics, work of adhesion can be measured by fracturing the interface or by adhesive pull-off at Hertz-like contacts.[14] In some applications a strong interface is desirable, such as in a structural application in which a high-strength composite is desired, whereas in processing or friction applications a very weak interface is desirable.

Example 1 Kurokawa et al.[15] used SEM and TEM to investigate the mechanism of adhesion between aluminum nitride (AlN) and tungsten (W) electrodes in a multilayer capacitor. Several investigators have reported the absence of a chemical reaction interlayer between W and AlN, but the mechanical strength of the interface is still considerable (>20 MPa). Electron microprobe analysis using an

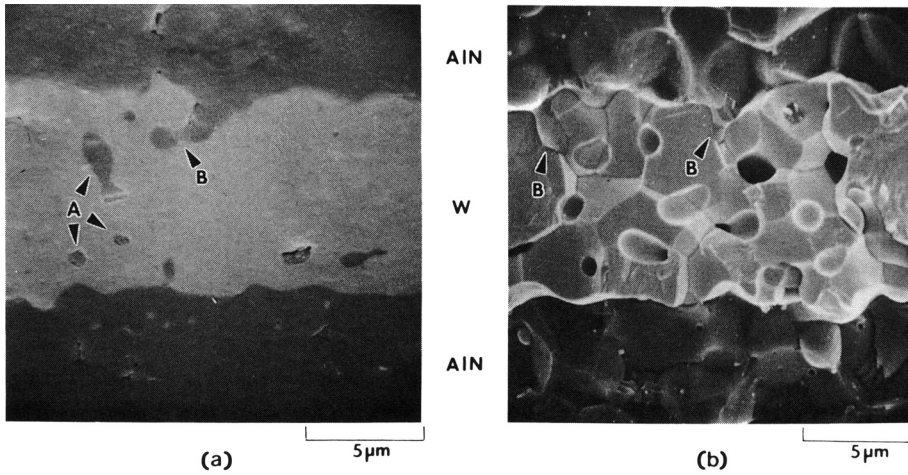

Figure 10.15 SEM micrographs of cross sections of AIN–W–AIN interface: (*a*) polished section and (*b*) fractured section (bars = 5 μm).[15]

SEM and selected area diffraction patterns on the TEM were used to confirm the absence of any chemical reaction between the two components. High-magnification SEM images of the composite revealed intricate interlocking structures at the interface, as shown in Figure 10.15. In the absence of a chemical reaction layer, the high adhesive strength of the system was attributed to this mechanical interlocking.

Example 2 Hollis et al.[16] used a pulse-reflection acoustic microscope to image glass fibers inside a polycarbonate matrix. The composites were optically opaque but transparent when viewed acoustically. Significant differences between the acoustic images of low- and high-strength composites were observed. For the low-strength composites, numerous fibers could be seen acoustically below the surface of the sample. This was not the case for the high-strength composite, as shown in Figure 10.16. More importantly, the subsurface images of the fibers in the low-strength composite appeared to have considerably larger diameter as compared with those in the high-strength composites. Thus, it appeared that the fibers in the low-strength composite were not well bonded to the matrix and had cylindrical voids surrounding them. These voids create a large acoustic impedance mismatch which generates contrast in the acoustic image. The presence of the voids was confirmed by examining fracture surfaces of samples in an SEM.

10.3 Oxidation Resistance of Ceramic Composites

Ceramic composites often consist of mixtures of oxide and nonoxide ceramics. Although oxides generally exhibit good oxidation resistance, most nonoxides do

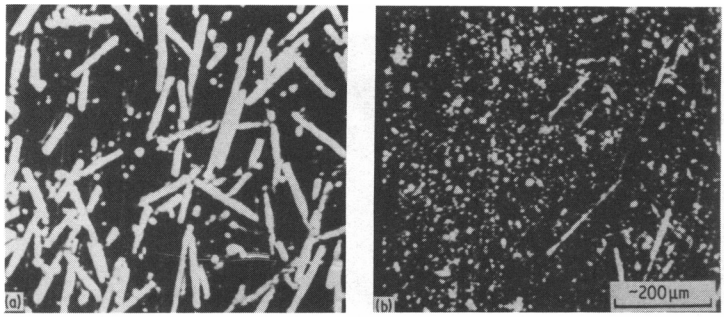

Figure 10.16 Comparison of specimens obtained with lens at Z = 15 µm to show subsurface fibers: (*a*) low-strength sample and (*b*) high-strength sample.[16]

not. Oxidation of the nonoxide often produces porosity and cracks, which can in turn lead to further oxidation and degradation. Although oxidation rates have been carefully measured for many ceramic composites and the thickness of the oxidized layer often follows a parabolic rate law, oxidation mechanisms are not well understood. Surface and interfacial microcharacterization techniques can provide valuable information.

Example Backhaus-Ricoult[17] used SEM, TEM, and XRD to follow the microstructural evolution of a silicon carbide-whisker–reinforced alumina–zirconia composite as oxidation of the SiC occurred and to measure the change in the thickness of the oxidized layer. XRD showed that the starting material contained only alumina (Al_2O_3), silicon carbide (SiC), and zirconia (ZrO_2). After the oxidation treatment, an oxidized scale was observed that macroscopically consisted of a black region, a white region, and a glassy surface layer. XRD showed that the major phases in the black sublayer were Al_2O_3, ZrO_2, zircon ($ZrSiO_4$), mullite ($3Al_2O_3{\cdot}2SiO_2$), and SiC. XRD also revealed that SiC was completely absent from the white sublayer and that the major phases were mullite, Al_2O_3, and ZrO_2. No $ZrSiO_4$ or carbon were detected, and this was confirmed with TEM and SEM using energy-dispersive analysis by X-ray (EDAX). SEM also revealed a substantial amount of porosity in the white sublayer. X-ray mapping using SEM EDAX also showed oxygen enrichment in the white region of the scale, as shown in Figure 10.17.

The growth of the white sublayer followed a parabolic rate law, consistent with previous studies, but the black sublayer did not. A model was proposed whereby oxygen, which diffuses into the microstructure via grain boundaries and dislocations, reacts with the SiC to form SiO_2, carbon and carbon monoxide. The SiO_2 then reacts with Al_2O_3 to form a low-viscosity aluminosilicate which penetrates the grains boundaries. Al_2O_3 and ZrO_2 in contact with this glass film react to form mullite and zircon. Zircon reacts with unreacted Al_2O_3 to form more mullite.

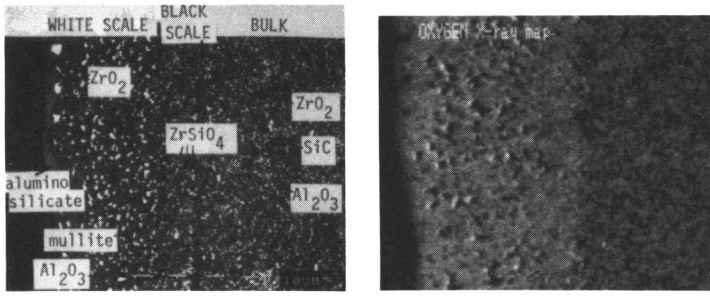

Figure 10.17 X-ray map of oxide scale showing oxygen enrichment in the white region.[17]

10.4 Electrical Properties of Ceramic Composites

Piezoelectricity

Piezoelectricity is a property whereby mechanical strain produces dielectric polarization and, conversely, an applied electric field produces mechanical strain.[18] Piezoelectricity is exhibited by piezoelectric crystals, polarized polymers, and composites, and is utilized in a variety of electromechanical transducers. To induce piezoelectricity in certain ceramic crystals, one must apply a high dc field to switch the polar axis of the crystals to the symmetry allowed directions nearest to the applied field. This process is called poling.

Example Waller et al.[19] studied poling of a piezoelectric ceramic polymer composite using a corona discharge technique being considered as an alternate to the high field dc technique traditionally used for poling. The piezoelectric ceramic was a 50–50 mixture of $PbTiO_3$ and $BiFeO_3$. The composites poled using both the corona discharge and the dc techniques had similar electrical properties. Waller et al. used X-ray diffraction (XRD) on the surface of the composite samples in order to investigate the extent of poling of the ceramic materials. Figure 10.18 shows the

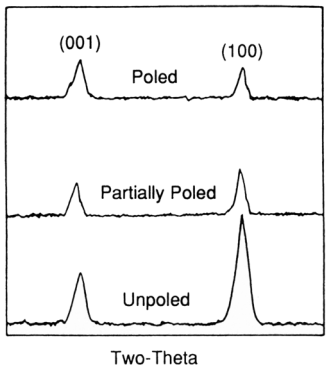

Figure 10.18 (001) and (100) X-ray diffraction peaks taken on the surface of the PT–BF–polymer composite before and after poling (PT–BF = $0.5PbTiO_2$ $0.5BiFeO_2$).[19]

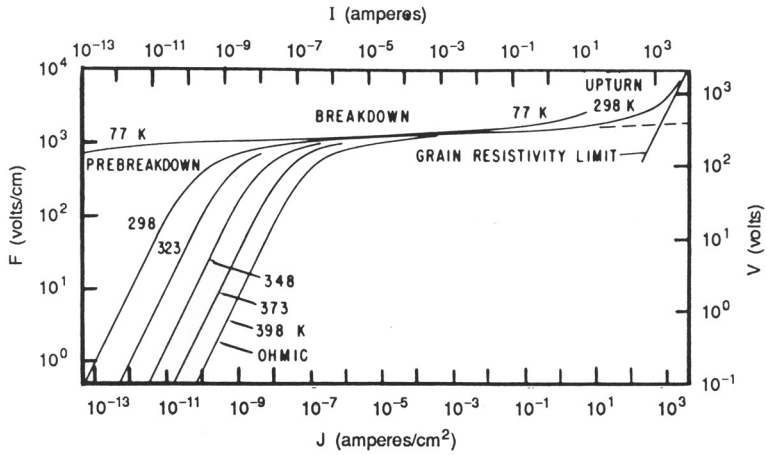

Figure 10.19 Current–voltage characteristics of a metal oxide varistor at 77 K and for a small range of temperatures near 300 K.[20]

X-ray diffraction peaks for unpoled, partially poled, and poled composites. The relative intensities of the (001) and (100) peaks are reversed in the unpoled and poled samples, which indicates near-saturation poling of the composites. Hence, a simple XRD technique can yield information about the electronic properties of composites.

Voltage-Dependent Conductivity

Conductivity is discussed in Chapter 12, "Electronic and Magnetic Ceramics," but voltage-dependent conductivity is included in this chapter because ceramic composites display this property. Figure 10.19[20] shows schematically the nonlinear current–voltage (I–V) characteristics for a ceramic composite varistor. Ceramic composite varistors are commonly made from ZnO (80 mol % or more) and additives such as Bi_2O_3, Sb_2O_3, Cr_2O_3, and Co_3O_4. The nonlinear I–V characteristics are due to the segregation of the metal oxide additives at the grain boundaries. The nonlinear I–V behavior depends on conducting grains being surrounded by a very thin insulating layer, as shown schematically in Figure 10.20.[21]

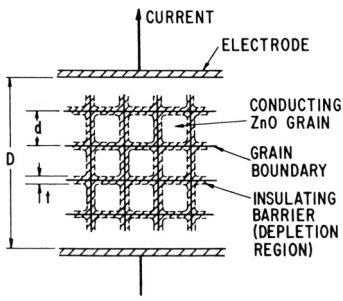

Figure 10.20 Block model of a ZnO varistor having grain size d (~20 μm) and intergranular depletion barrier thickness t (~1000 Å). D is the electrode separation.[21]

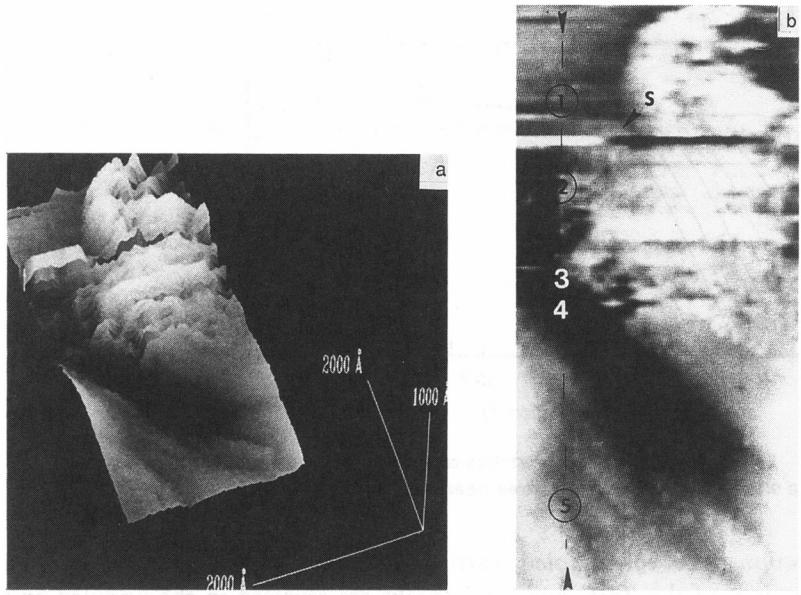

Figure 10.21 **(*a*) Three-dimensional rendering of a 200 × 400 nm image of a grain-boundary region; the total height of the image is 40 nm. (*b*) Gray-scale top-view rendering of the same image. Arrows at the top and bottom indicate the line along which the *I–V* curves were acquired. The feature labeled "S" is a spike due to a temporary tip instability and is not related to the sample surface.[22]**

Example Rohrer and Bonnell[22] used scanning tunneling microscopy (STM) and tunneling spectroscopy (TS) to investigate the correlation between the geometric structure and electrical properties in three different regions of a polycrystalline ZnO varistor material. More than 90% of the surface was observed to be a flat background area which had a tunneling spectrum similar to those obtained from single-crystal ZnO surfaces. These regions correspond to individual ZnO grains. The second type of region showed metallic spectral characteristics, which were attributed to carbon contamination on the surface. The third type of region showed low conductivity and appeared as topographic depressions in the image separating the large flat regions. This feature has the size, shape, and expected electronic properties of ZnO varistor grain boundaries. Figures 10.21 and 10.22 show how STM and TS can be used to image and detect electrical property variations across interfaces in electronic ceramic composites.

10.5 Summary

The examples in this chapter demonstrate the heavy reliance on electron microscopy (both SEM and TEM) for topographical characterizations, compositional

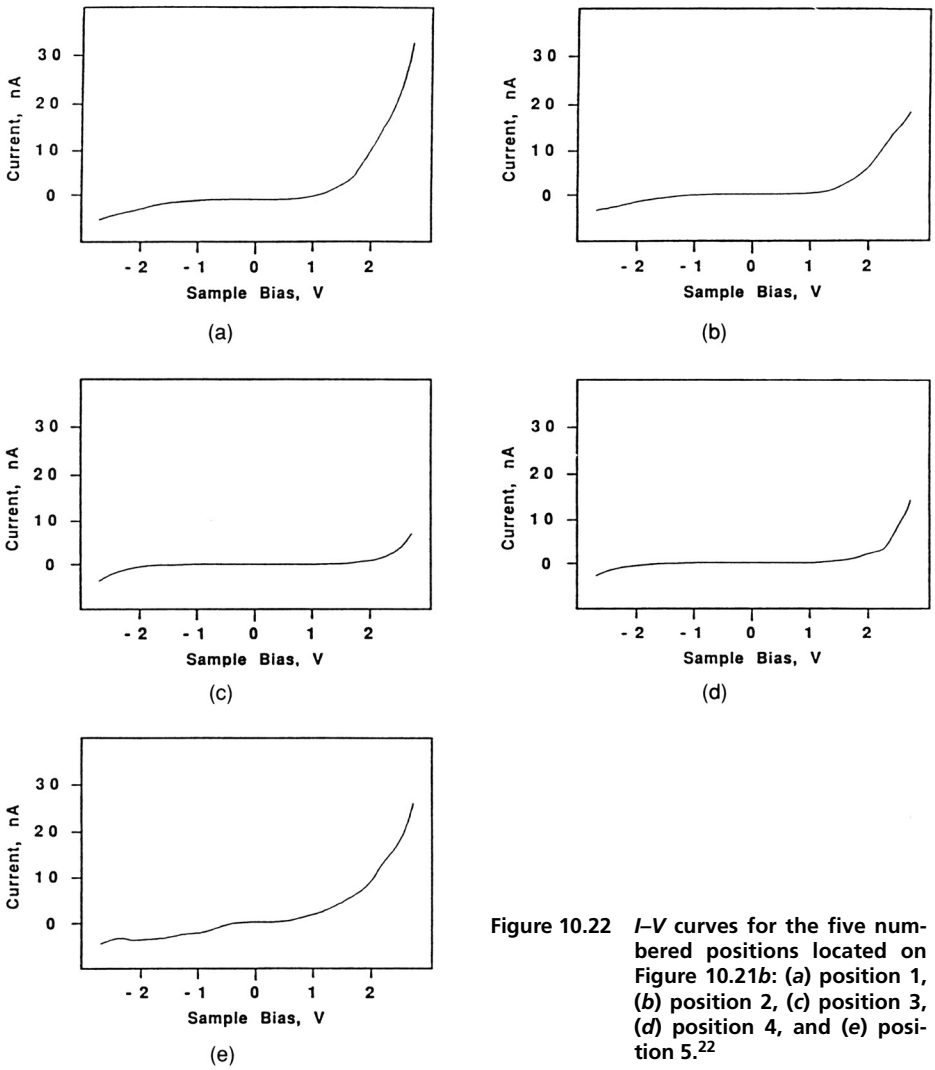

Figure 10.22 ***I–V*** **curves for the five numbered positions located on Figure 10.21*b*: (*a*) position 1, (*b*) position 2, (*c*) position 3, (*d*) position 4, and (*e*) position 5.[22]**

information, and phase identification of ceramic composites. Although other microcharacterization techniques can be used to obtain some of the same information, they are not as widely used because they do not provide as broad a range of information. The examples in this chapter also demonstrate that, although microchar-acterization techniques often indicate interfacial differences that are expected to lead to differences in bulk behavior, bulk properties sometimes remain unaffected.

References

1 R. E. Newnham and G. R. Ruschau. *J. Am. Ceram. Soc.* **74** (3), 463–480, 1991.

2 C. G. Koops. *Phys. Rev*. **83** (1), 121–124, 1951.

3 R. N. Singh. "Role of Fiber-Matrix Interfacial Shear Stress on the Toughness of Reinforced Oxide Matrix Composites." In *High Temperature/High Performance Composites*. Mat. Res. Soc. Symp. Proc., Vol. 120. (F. D. Lemkey, S. G. Fishman, A. G. Evans, and J. R. Strife, Eds.) Mater. Res. Soc., Pittsburgh, 1988, pp. 259–264.

4 D. B. Marshall. *J. Am. Ceram. Soc*. **69** (3), 173–180, 1986.

5 N. P. Padture, H. M. Chan, B. R. Lawn, and M. J. Readey. "The Role of Crystallization of an Intergranular Glassy Phase in Determining Grain Boundary Residual Stresses in Debased Aluminas." In *Interfaces in Composites*. Mat. Res. Soc. Symp. Proc., Vol. 170. (C. G. Pantano and E. J. H. Chen, Eds.) Mater. Res. Soc., Pittsburgh, 1990, p. 245.

6 H. K. Swan and C. O'Meara. "Creep Properties and Interfacial Microstructure of SiC Whisker Reinforced Si_3N_4." In *Interfaces in Composites*. Mat. Res. Soc. Symp. Proc., Vol. 170. (C. G. Pantano and E. J. H. Chen, Eds.) Mater. Res. Soc., Pittsburgh, 1990, p. 223.

7 H-T. Lin and P. F. Becher. *J. Am. Ceram. Soc*. **74** (8), 1886–1893, 1991.

8 J. Homeny, W. L. Vaughn, and M. K. Ferber. *J. Am. Ceram. Soc*. **73** (2), 394–402, 1990.

9 M. H. Rawlins, T. A. Nolan, D. P. Stinton, and R. A. Lowden. "Interfacial Characterization of Fiber-Reinforced SiC Composites Exhibiting Brittle and Toughened Fracture Behavior." In *Advanced Structural Ceramics*. Mat. Res. Soc. Symp. Proc., Vol. 78. (P. F. Becher, M. V. Swain, and S. Somiya, Eds.) Mater. Res. Soc., Pittsburgh, 1987, p. 223.

10 S. R. Stock, A. Guvenilir, T. L. Starr, J. C. Elliott, P. Anderson, S. D. Dover, and D. K. Bowen. "Microtomography of Silicon Nitride/Silicon Carbide Composites." In *Advanced Characterization Techniques for Ceramics*. Ceram. Trans., Vol. 5. (W. S. Young, G. L. McVay, and G. E. Pike, Eds.) The American Ceramic Society, Westerville, OH, 1988, p. 161.

11 J.-F. Tsai, C. S. Yu, and D. K. Shetty. *J. Am. Ceram. Soc*. **73** (10), 2992–3001, 1990.

12 C. A. Powell-Dogan and A. H. Heuer. *J. Am. Ceram. Soc*. **73** (12), 3684–3691, 1990.

13 J. A. Pask and A. P. Tomsia. "Wetting, Surface Energies, Adhesion, and Interface Reaction Thermodynamics." In *Ceramics and Glasses*. Engineered Materials Handbook, Vol. 4. ASM International, 1991, pp. 482–492.

14 K.-T. Wan, D. T. Smith, and B. R. Lawn. *J. Am. Ceram. Soc*. **75** (3), 667–676, 1992.

15 Y. Kurokawa, C. Toy, and W. D. Scott. *J. Am. Ceram. Soc*. **72** (4), 612–616, 1989.

16 R. L. Hollis, R. Hammer, and M. Y. Al-Jaroudi. *J. Mat. Sci*. **19**, 1897–1903, 1984.

17 M. Backhaus-Ricoult. *J. Am. Ceram. Soc*. **74** (8), 1793–1802, 1991.

18 L. Solymar and D. Walsh. *Lectures on the Electrical Properties of Materials*. 2nd ed., Oxford University Press, Bath, U.K., 1979, Section 10.11.

19 D. Waller, T. Iqbal, and A. Safari. *J. Am. Ceram. Soc*. **72** (2), 322–324, 1989.

20 F. D. Martzloff and L. M. Levinson. In *Surge Protective Devices in Electronic Ceramics—Properties, Devices, and Applications*. (L. M. Levinson, Ed.) Marcel Dekker, New York, 1987, Chapt. 5.

21 L. M. Levinson and H. R. Philipp. "Application and Characterization of ZnO Varistors." In *Ceramic Materials for Electronics—Processing, Properties, and Applications*. (R. C. Buchanan, Ed.) Marcel Dekker, New York, 1986, pp. 375–402.

22 G. S. Rohrer and D. A. Bonnell. *J. Am. Ceram. Soc*. **73** (10), 3026–3032, 1990.

11

Glass and Ceramic Joints

ANTONI P. TOMSIA AND RONALD E. LOEHMAN

Contents

11.1 Introduction

Successful application of ceramics in many devices and structures requires some type of ceramic–metal joining. Ceramic–metal seals are used extensively in a wide variety of applications. Examples include vacuum tubes, high-voltage feedthroughs, transistor packages, sapphire–metal windows, rocket ignitor bodies, and many others. Newer joining applications include engine components, such as the Si_3N_4 turbocharger rotor joined to a metal shaft now being produced commercially,[1] multilayer electronic devices that comprise both ceramics and electrodes, electroding and metallizing of hybrid microcurcuit substrates; and ceramic–metal composites. All applications require a high-strength metal–ceramic bond.

Two factors drive the need for the development of improved joining technologies. First, it is difficult to fabricate large ceramic structures with complex shapes. Although small individual pieces of complex shape, such as a turbine rotor, can be fabricated, the path of least technological resistance to developing larger structures will often entail joining assemblies of more easily fabricated small components. If the joints are sufficiently strong, this may also provide indirect benefits, since quality control and nondestructive testing of smaller components may be simpler. Second, although ceramics may possess a unique and desirable set of properties, there

will be applications in which these properties are needed and desirable, not for an entire structure, but only in one portion of a structure. For these applications, it will be necessary to join the ceramic to either another ceramic or to a metal. The development of viable joining techniques will facilitate the assimilation of advanced ceramics into complex multimaterial (often metal-dominated) structures.

11.2 Characterization of Interfaces

The usual approach in analyzing complex ceramic–metal interfaces is to characterize experimentally the specific properties of the ceramic–metal interfaces that one wishes to understand and control. In this chapter, brazing of AlN is used as an example. The objective is for one to learn as much as possible about the reactions that occur at the interface in order to control processing and to optimize properties. In turn, one must understand the mechanisms of adhesion and the development of microstructure, recognizing that the information may be particular to the system studied.

Complete characterization of a ceramic–metal interfaces may require knowledge of the energetics of wetting and interface reactions, the microstructure and composition of interface compounds, the stress state of the interface, and the structure of an interface at the atomic level. Knowledge of mechanical stresses at interfaces is important because a stressed interface may be weak mechanically even if there are strong chemical bonds. For example, a Cu–27Ag–2Ti (wt %) brazing alloy will react strongly with AlN at 900 °C and yield good chemical bonding. However, if the brazing alloy is too thick, the structure will fracture on cooling because of stresses generated by coefficient of thermal expansion (CTE) mismatch. Similarly, stresses can occur from cyclic mechanical loading of two joined materials if their elastic moduli are mismatched. Thus, knowledge of the mechanical properties of reaction products is necessary for a complete understanding of adhesion. However, the focus of this paper is the characterization of microstructural properties of the joints; mechanical properties will not be discussed further.

The interface characterization just described has been accomplished using a variety of experimental techniques. Sessile drop experiments[2] are used to determine the relative interfacial energies for a liquid drop on a solid surface. Such experiments provide a means of studying wetting and spreading of a liquid on a solid and of determining relative surface and interfacial energies. Proper interpretation reveals if a reaction is taking place at the interface and if there is contamination of the surfaces, and its effect. The technique also provides a convenient method of studying the reactions that occur at the interface by characterizing polished cross sections obtained by cutting the frozen sessile drop assembly perpendicular to the interface.

Scanning electron microscopy (SEM) is used with energy-dispersive spectroscopy (EDS) to obtain general microstructural and compositional information, usually on cross sections of the ceramic–metal interface or on fractured surfaces. Electron microprobe (EPMA) scans across the interface give compositional profiles

at a 1-μm spatial resolution, including light elements, such as O and N, not generally accessible to EDS. With proper standards, accuracies of ±0.1 wt % can be obtained.

Detailed understanding of reaction mechanisms requires knowledge of the valence state of the reaction products, which can be obtained with X-ray photoelectron spectroscopy (XPS). Because XPS is sensitive to a depth of only a few monolayers, there is the general problem of ensuring that the surface being analyzed is not an artifact of environmental contamination. Fracturing the specimen along the interface in the ultrahigh vacuum (UHV) chamber prior to analysis is one technique for minimizing surface contamination. Another is to make model interfaces by depositing a thin layer of the metal on the ceramic in the UHV chamber, heating it, and then analyzing it without ever exposing the specimen to the atmosphere. Transmission electron microscopy (TEM) can image interfacial microstructures at higher resolution than SEM; in addition, its electron diffraction capability gives crystal structure information. TEM at atomic resolution has been used to image the crystal lattice orientation of interfaces, such as Nb on sapphire.[3]

11.3 Methods of Joining

Many techniques are available for joining ceramics to other ceramics or to metals. The review of ceramic joining by Suganuma et al.[4] and an earlier review by Rice[5] provide a more detailed overview.

There are three general categories or types of joining processes. In the first, attachment is *mechanical* and is achieved through the use of mechanical interlocking of components. The second approach is *direct joining*, in which components are bonded either by a solid-state process or by fusion. The third approach could be referred to as *indirect joining* in the sense that an intermediate layer of material, such as an adhesive, cement, or braze, is used to bond two components.

Mechanical Joining

Mechanical joining has the advantage of being very simple and efficient. A common example of this type of attachment is provided by the carbon–carbon composite Space Shuttle leading edges, which are attached by fasteners to facilitate removal and replacement. Provided that the materials are refractory and chemically compatible, this approach should provide high strength at high temperatures. However, Rice points out that the lack of ductility in ceramics severely limits the temperature range over which this method is applicable because of the high local tensile stresses that can develop in systems with thermal expansion mismatches, causing failure in the ceramic.[5] Nicholas[6] adds that successful application of mechanical attachment in demanding environments is difficult to achieve, especially if leak-tight joints are required or if the joint will be subjected to thermal cycling. For these applications, joints with atomically bonded interfaces, as can be formed by direct and indirect joining methods, are preferred and necessary.

Direct Joining

Solid-state pressure bonding has been applied to joining of ceramics to ceramics and ceramics to metals.[7–14] Successful pressure bonding relies upon the achievement of adequate interfacial contact and subsequent diffusion or plastic flow to eliminate interfacial porosity. When both materials undergo limited plastic flow (e.g., ceramic–ceramic bonding) or when deformation of the workpiece must be avoided (e.g., the niobium–sapphire bond in high-pressure sodium lamps), special care must be taken to assure smooth mating surfaces.[6] When ceramic–metal bonds are being formed, and deformation of the metal is permissible, plastic flow generally occurs within the metal.

Increasing either the fabrication pressure or time generally improves the quality of the joint, as measured by the failure strength of the assembly. However, of the processing parameters that can be controlled, temperature appears to be the most important. Nicholas reports that an increase in the joining temperature of $T_m/10$ (where T_m is the melting temperature in kelvin) can make the difference between a low-strength and high-strength assembly.[15] Although increases in time and temperature can improve the joint quality, there are limits. Initially, chemical reactions at the interface often have a favorable effect. However, if the time and temperature are excessive, thick interfacial reaction product layers can form. These layers can generate volume mismatch strains and stresses at the interface that are of sufficient magnitude to degrade assembly strength.[16]

The advantages of solid-state pressure bonding include a simple fabrication procedure, a one-step process, and potentially very high joint strength. However, there are also several limitations and disadvantages: high cost; only flat specimens can be joined; a vacuum/inert atmosphere is required; and pressure must be applied. The need to apply pressure during diffusion bonding imposes restrictions on the joint geometry; most joints are of the face seal type and are not well-suited for accommodating thermal expansion mismatch. As a result, the bonded components must either be small, one component must be thin,[9, 11, 12] or the thermal expansion coefficients of the components must be well matched. The use of graded thermal expansion laminates for bonding materials with highly dissimilar thermal expansion coefficients is one method of overcoming this limitation.[7, 17]

Indirect Joining

The use of a liquid, a glass, or a solid foil that flows readily under low applied stress to join materials can have advantages. Flow of a wetting liquid or glass or of the ductile solid can fill irregularities in the surface and therefore imposes less stringent demands on surface preparation and the degree or extent of surface mating required. Ductile metal interlayers can undergo plastic flow and thus reduce the stress that builds up in the ceramic during thermal cycling.[12–15] The major categories of joining using an intermediate layer include joining with adhesives, cements, glasses, and brazes.

Joining with organic-based materials is simple and widely used. A broad range of materials can be joined by this method. Precise processing conditions have been specified for the preparation of aluminum and aluminum-alloy surfaces for adhesive bonding, a consequence of the importance of this joining approach in the aerospace industry. The Al surfaces can be characterized by XPS, Auger, electron spectroscopy, etc. In the context of joining ceramics, the low elastic modulus of organic materials allows large strains to be accommodated without the development of significant stress,[5] an attractive characteristic. However, the limited temperature capabilities of organics, and their susceptibility to chemical attack and degradation, limit their use.

Joining with cements or mortars has some of the same advantages as adhesive joining and provides a higher temperature capability. However, as the temperature range is increased, so too is the effect of thermal expansion mismatch. Rice indicates that the strengths that are obtained using this approach are often substantially lower than those of parts joined with an adhesive.[5] Chemical interactions between the cement and the ceramic, and decomposition of the cement, can limit the temperature range of application. Collectively, these characteristics diminish the appeal of this approach for joining materials for demanding high-temperature, high-stress structural applications.

Inorganic glasses and glass–ceramics generally wet (form an acute contact angle with) and bond to ceramics. As a result, they can be used to coat one or both mating surfaces, and in principle, can form strong joints. The thermal expansion coefficients of glasses can be varied to match, or at worst decrease the mismatch with, a particular material. Thermal expansion measurements are performed with various types of dilatometers. Thus, when two articles of the same material are to be joined, glasses or crystallized glasses provide an attractive joining route. However, in comparison to metals, glasses are less tolerant of thermal expansion mismatch. Thus, for applications in which materials with different thermal expansion characteristics are to be joined, glass–ceramics may be more desirable. For example, glass–ceramics can be made with expansion coefficients ranging from zero (β-eucryptite) to over 200×10^{-7}/°C (mixtures of cristobalite and tridymite match the CTEs of Cu and some stainless steels). The ability to fill reentrant angles and complex internal shapes by viscous flow of the molten glass and then to crystallize it with subsequent heat treatment to match the CTE of the metal makes glass–ceramics particularly suited to applications where high strength of the system is important. Glasses and glass–ceramics often provide good environmental compatibility, although it may not equal that of the components to be joined. Difficulties may also arise from excessive chemical reaction between the glass and the ceramic (or metal). In some cases, the metal may be dissolved by the glass.[17] Softening of the glass and decomposition of certain glasses are additional concerns, particularly for high-temperature applications. Glass softening can be characterized by differential thermal analysis (DTA) and dilatometry.

Brazing involves bonding using a metallic interlayer. Braze alloys are far more ductile than glasses and thus more forgiving. In cases where ceramics are being introduced into predominantly metal structures, brazes provide a more familiar joining material. The criteria for selection of brazing alloys are that they must wet or coat the ceramic, must form a chemical bond at the interfaces resulting in a strong joint, and they should cause minimal degradation of the base material or materials. Successful brazing alloys produce bonds that are (1) strong, (2) reliable, and (3) relatively inexpensive to manufacture. Brazing techniques are versatile and can produce vacuum-tight joints with high strength and substantial temperature capability. Brazes can often be developed to resist a variety of chemical environments. Brazing also lends itself more readily to mass production than solid-state pressure bonding.

Brazing of ceramics is not without difficulty. In contrast to glasses, many metals and alloys bead up on ceramic substrates, that is, the molten metal does not wet the ceramic. To promote wetting, the surface must either first be metallized, or a braze containing a chemically reactive or active metal, often titanium, must be used. Titanium reacts with the ceramic and generally facilitates wetting via the formation of a more metallically bonded reaction product at the interface.[18–20]

As is the case for any joining process, there are also some important constraints and concerns, many of which are the direct consequence of the presence and action of the reactive metal. The flow of some reactive metal alloys is reported to be sluggish, and as a result, preplacing foils is often necessary. The reactivity of the alloys generally demands that they be used in a vacuum or in an inert atmosphere containing sub-parts-per-million oxygen levels. As is often the case in diffusion bonding, an interfacial reaction product forms. If the brazing time or the brazing temperature is excessive, and if the reaction product is brittle or has a significant thermal expansion mismatch with the ceramic, weakening of the joint can result.

11.4 Fundamentals of Interfacial Bonding: Wetting and Spreading

The surface of any phase has an associated free energy. That energy, γ (J/m^2), is always positive and is equivalent to the energy required to create a unit area of new surface of the material. The adhesive energy or work of adhesion between two phases is given by $W_{AB} = \gamma_A + \gamma_A - \gamma_{AB}$, where the subscripts A and B indicate the free surfaces of phases A and B, and AB indicates their common interface. Two materials form a stable bond when the work of adhesion is negative, that is, when creating the AB interface gives a net decrease in the free energy of the system by eliminating the high positive free energy of the interface.[21]

When one of the phases is a liquid during the sealing process, for example, molten glass on metal or a braze alloy on a ceramic, the liquid phase generally must wet the solid for bonding to occur. There is general agreement that wetting is an essential prerequisite for making a good bond. It is understood, however, that

wetting alone is not sufficient to guarantee good adhesion. Chemical bonding is usually associated with a small acute contact angle in a sessile drop (wetting) experiment. Sessile drop experiments are important because they provide valuable information on the formation of true or intimate interfaces and the existence of reactions that normally may not be recognized and therefore might be overlooked. It is thus worthwhile to examine and understand the associated principles.

The sessile drop technique is used extensively in the study of glass–metal bonding and ceramic/metal brazing. Figure 11.1 is a schematic of cross sections of a wetting and a nonwetting sessile drop. Wetting occurs when the surface energy of the solid exposed to the atmosphere is greater than that of the liquid, that is, $\gamma_{sv} > \gamma_{sl} > \gamma_{lv}$, and the driving force for wetting is $(\gamma_{sv} - \gamma_{sl})$ (an example of such a system is an oxide liquid on a metal substrate). The resisting force is the energy required to increase the surface area of the liquid drop. A balance of these forces is represented by the Young-Dupre equation[21]:

$$\gamma_{sv} - \gamma_{sl} = \gamma_{lv} \cos \theta \tag{11.1}$$

The equation is valid at steady state in the absence of a reaction, that is, under either stable or metastable equilibrium. If a reaction takes place at the interface in which the solid is an active participant (i.e, its chemical composition changes), the ΔG_R (free energy of reaction) contributes to the driving force for wetting (Figure 11.1). The equality in the equation is lost and a dynamic situation arises wherein the driving force for wetting approaches γ_{lv}, with a decrease in contact angle θ. When the force exceeds γ_{lv}, θ becomes zero and the liquid continues to spread. If the solid is a passive participant in the reaction (its chemical composition does not change), then ΔG_R does not contribute to the driving force for wetting and spreading does not occur. Surface energies, however, change with composition adjustments that occur.

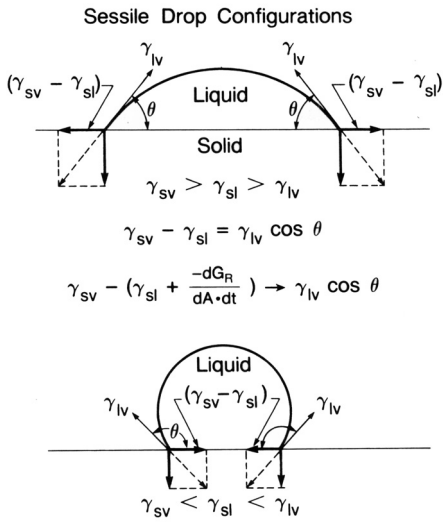

Figure 11.1 Sessile drop configurations for wetting and nonwetting.

If the solid is not wet by the liquid and no reaction occurs, then $\gamma_{sv} < \gamma_{sl} < \gamma_{lv}$ and there is no driving force for wetting (an example of a system is a metal liquid on a solid ceramic substrate). The equation is the same as given but the contact angle is now obtuse (Figure 11.1). In the case of a reaction where the solid is an active participant, ΔG_R develops a driving force for wetting. If this force is large enough, then with continued spreading the contact angle continues to decrease until it becomes acute and then zero.

The work of adhesion of a liquid on a solid may be calculated as the sum of work performed in generating one unit area of liquid surface and one unit area of solid surface minus the original solid–liquid interfacial energy. The result is expressed by Dupre's equation:

$$W_{ab} = \gamma_{sv} + \gamma_{lv} - \gamma_{sl} \tag{11.2}$$

Substituting the Young's equation into the expression for work of adhesion yields:

$$W_{ab} = \gamma_{lv}(1 + \cos\theta) \tag{11.3}$$

W_{ab} is the reversible work of adhesion, which is the work required to separate a unit area of the interface into two original surfaces. Direct measurement of W_{ab} is not possible.[22] Indirectly, the work of adhesion can be determined from a measurement of the contact angle if the surface energy (or surface tension) of the liquid in equilibrium with its vapor is known. The work of adhesion has been calculated from first principles for different metals on Al_2O_3[23, 24] Good agreement was found between the calculated and experimentally measured values for that particular study. However, adhesion is a complex phenomenon that is difficult to model theoretically for systems of practical interest.

The overall free energy at an interface is further decreased by any reaction between the two substances. Depending on the system, these can be reactions to form new phases or various (redox) and dissolution reactions.[25] Redox reactions during ceramic–metal bonding have been studied extensively, and that work has been used to formulate a theory of glass–metal and ceramic–metal bonding that has gained wide acceptance.[26] The theory states that the most stable interface is one where there is an intermediate layer saturated in a cationic species that is in equilibrium with the parent phases. At equilibrium the reaction layer contains cations with valence intermediate to the metal and the glass or ceramic. The theory cannot predict the thickness of the intermediate zone, but in principle it could be as thin as one monolayer. The layer may be created by oxidation of the metal and reduction of one or more cations in the glass. Alternatively, the equilibrium zone may be formed by preoxidizing the metal followed by dissolution of the oxide in the molten glass. Which redox reactions occur can be predicted from available thermodynamic data in many cases. For example, heating a Co-doped siliocate glass on a Fe substrate results in reduction of Co^{2+} to Co° and oxidation of Fe° to Fe^{2+} to form an interfacial layer saturated with FeO (Fe° + CoO(glass) = FeO(interface) + Co°,

ΔG_R^o (927 °C) = –44.21 kJ).[27] Existence of such zones can be determined by TEM and gross compositions by SEM/EDS and by EMPA. The nature of the chemical bonding can be determined by XPS on fractured surfaces.

11.5 Reactive Metal Brazing of Aluminum Nitride

The experimental techniques described above to analyze ceramic–metal interfaces will now be illustrated using an example of brazing AlN. Comparatively little work has been reported on brazing aluminum nitride ceramics.[28, 29] Since a primary application for aluminum nitride is as a substrate for electronic applications, the focus has been on low-temperature brazing, using a variety of commercially available alloys based on the copper–silver–titanium system.

Wetting Studies

Ti is widely used as the reactive element in active metal braze filler alloys that are increasingly being applied for ceramic joining. Other reactive elements, such as Nb, Al, Cr, V, Ta, and Zr also have been investigated in varying levels of detail.[30, 31] The example used here reports a comparative study of the reactions and resulting microstructures for Ti and Zr on AlN. The activities of the Ti and the Zr were varied by dissolving them at 1 and 5 wt % in the 72Ag–28Cu eutectic.

The results of the contact angle studies of the Cu–Ag brazes on AlN are presented in Figure 11.2. Several features are evident. First, the higher the Ti or Zr concentration, the lower the contact angle. Continuous decreases of contact angle with time and spreading are indicative of reactions in sessile drop experiments. Second, for all experimental conditions used, contact angles for the Ti-containing alloys are lower than for those with Zr. At 1000 °C, the Zr-containing alloys initially melted, but then they rapidly formed a partially solidified drop that was unable to spread significantly on the ceramic. At 1100 °C, the Zr alloys were liquid and conventional contact angles were observed. This temperature dependence is related to alloy phase behavior, as discussed below. Figure 11.3 shows a cross section of the interface between AlN and Cu–Ag–5Zr (wt %) brazing alloy heated at 1100 °C for 60 min at $P(O_2) = 10^{-16}$ atm. The dark area on the left is AlN. The thin (0.5 μm) compound at the interface is ZrN formed by reaction between Zr from the brazing alloy and AlN, the triangle close to the interface is a $AgZrCu^3$ phase precipitated on cooling, and on the right of the photo is a Ag–Cu eutectic microstructure.

Figure 11.2 also shows that Cu–Ag (Cusil) alloy did not wet AlN ceramic, as indicated by invariant obtuse contact angles. On cooling, the metal formed a near-spherical bead that rolled off the nitride substrates when they were tilted. The lack of wetting by Cusil is a consequence of the relatively large AlN–liquid metal interfacial energy (γ_{sl}) and the absence of reaction at the interface. Effectively, a true interface does not form.

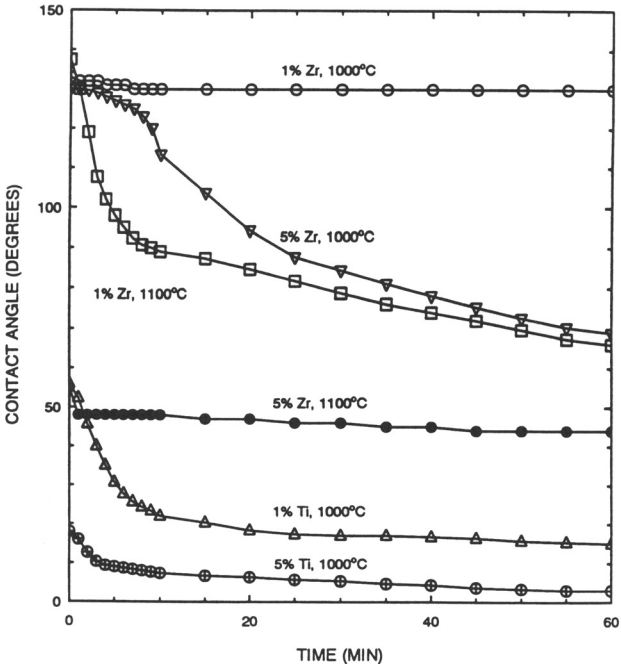

Figure 11.2 Wetting behavior or Zr–Ag–Cu and Ti–Ag–Cu alloys on AlN. Compositions indicated on curves are in weight percent.

Qualitatively similar results were obtained for the 76Cu·24Ti alloy, Pd/Si alloys, and Cu–Ni–Ti alloys; those that contain Ti or Zr wet and spread on the AlN substrates, whereas those that do not contain Ti or Zr (e.g., 94Pd·4Si·2Al) ball up and fall off the AlN after cooling.[32]

The segregation of an alloy element to the solid–liquid interface is usually an indication of the reduction of γ_{sl}. For example, Figure 11.4 shows a backscattered electron image and Ti, Al, Cu, Ag, and N X-ray maps of the cross section of a

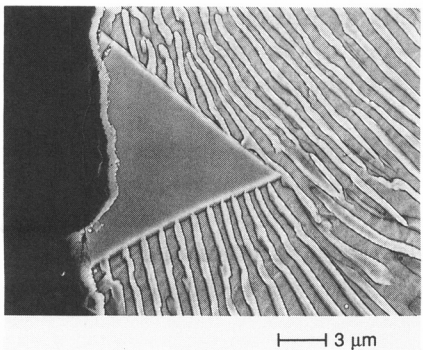

Figure 11.3 Microstructure of the Zr–Ag–Cu alloy close to the AlN interface. Dark phase has the composition of $ZrAgCu_4$.

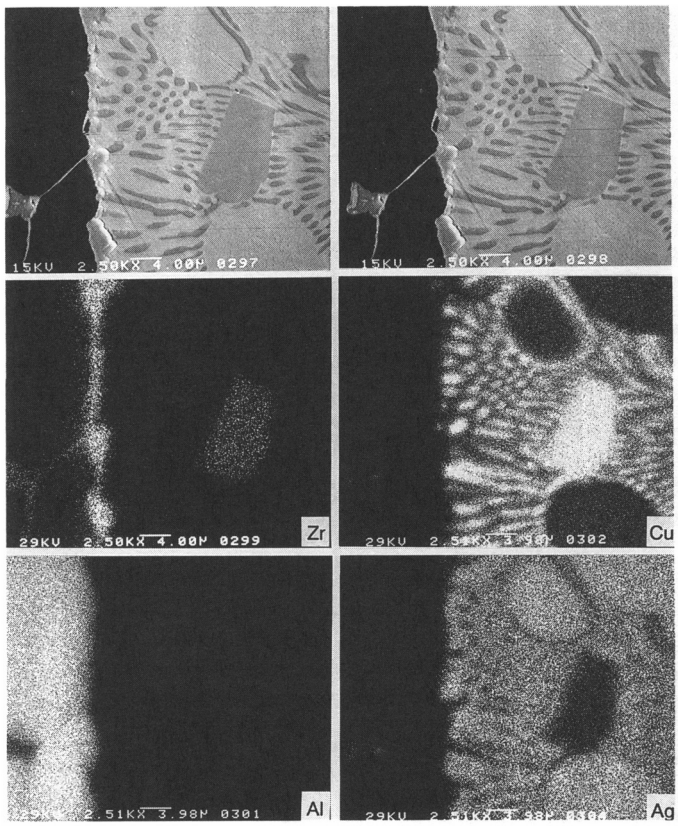

Figure 11.4 EDS compositional maps of interface between Zr–Ag–Cu and AlN. Reacted at 1000 °C for 60 min.

28Cu·72Ag–5Ti/AlN braze sample; titanium is clearly seen to segregate to the AlN-alloy interface. Figure 11.5 shows similar X-ray maps for 28Cu–72Ag–5Zr/AlN interface. While it is possible that segregation alone might sufficiently reduce γ_{sl} to produce adequate wetting, there is also clear evidence for the presence of interfacial reaction products not accounted for by the Young–Dupre equation. In fact, Yost and Romig[33] have shown that the free energy of formation of an interfacial reaction product (δG_r) will be an additional thermodynamic driving force for reducing θ; such an analysis yields a modified wetting equation[26]:

$$\gamma_{sv} - \left(\gamma_{sl} + \frac{\delta G_r}{\delta A \cdot \delta t}\right) \leq \gamma_{lv} \cos\theta \tag{11.4}$$

where the interfacial reaction free energy is normalized to the change in the interfacial area (δA) and the reaction time (δt). The dynamic nature of this relationship makes the use of the inequality sign necessary.[26] According to Equation 11.4,

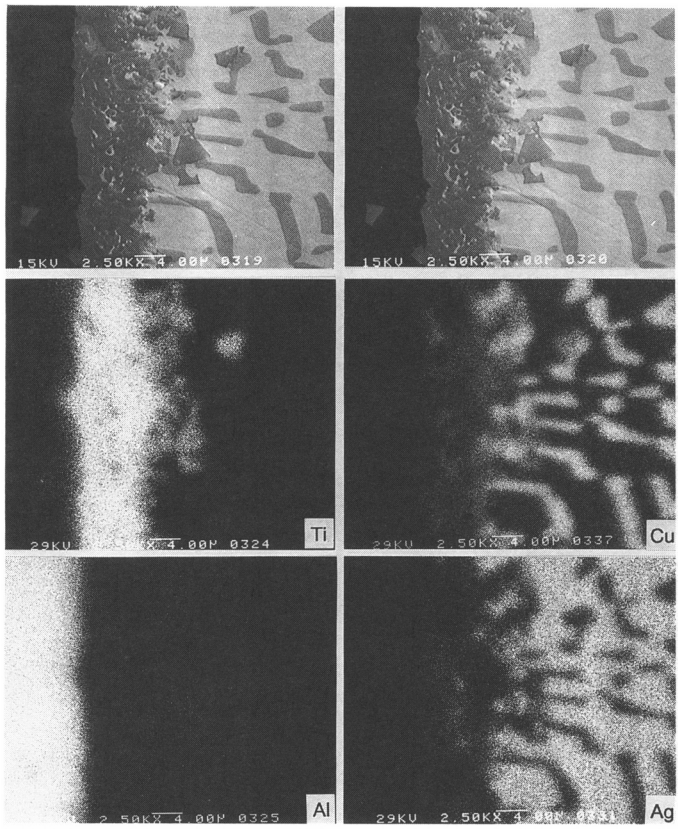

Figure 11.5 EDS compositional maps of interface between Ti–Ag–Cu and AIN. Reacted at 1000 °C for 60 min.

interfacial reactions with negative free energies will further reduce the influence of γ_{sv} and, if large enough, could promote wetting and spreading even in systems where $\gamma_{sv} < \gamma_{sl}$.

Interfacial Reactions

Microstructures and compositions of the reaction zones for reaction of both Ti–Ag–Cu alloys with AlN were very similar to those previously reported for commercial braze alloys on AlN.[28, 34, 35] The microprobe data presented in Figure 11.6 show a reaction zone adjacent to the alloy about 25 μm in thickness with the approximate composition $TiN_{0.7}$. Well away from the ceramic–metal interface, the alloy exhibits the Ag–Cu eutectic structure with no Ti; essentially all the Ti has segregated to the interface. Between the Ag–Cu eutectic and the TiN_x layer is the the region where previous TEM studies have shown the existence of a $(Ti,Al,Cu)_6N$ η-nitride.[35]

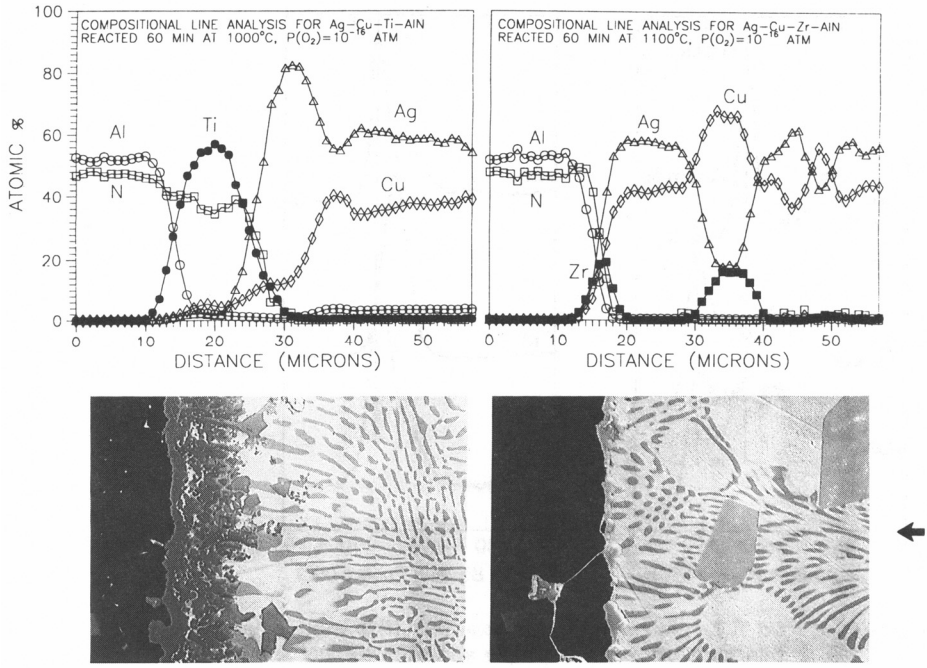

Figure 11.6 Microprobe compositional line analyses for Zr–Ag–Cu and Ti–Ag–Cu on AlN reacted for 60 min at 1000 °C.

The interface resulting from reaction between 4.7Zr–57.4Ag–37.9Cu (wt %) and AlN at 1100 °C is somewhat different from that of the comparable Ti alloy. One major difference is that the ZrN reaction zone is only about one-third the thickness of the Ti reaction zone. Another difference is that, within experimental error, the ZrN layer is stoichiometric. A third difference is that not all the Zr has segregated to the interface with the ceramic. Grains with the average composition $ZrAgCu_4$ are observed throughout the metal drop (see Figure 11.6).

XPS Characterization of Ti-AlN Interfaces

Additional studies were made of interfacial reactions that could further improve wetting, according to Equation 11.2, by using XPS to characterize the interfaces of heat-treated Ti-thin films deposited on AlN substrates. XPS is particularly useful for these studies because it is sensitive not only to different elements but also to their different chemical environments. Figure 11.7 summarizes some of the thin film results. The Ti 2*p* (Figure 11.7*a*) and Al 2*p* (Figure 11.7*b*) photoelectron spectra shown were obtained from a reaction couple (80 nm Ti on AlN) heated to 900 °C for 30 min in argon and from several reference samples. The Ti/AlN couple was sputter-cleaned by an Ar-ion gun to remove an oxidized surface layer and to reveal the reaction products that include TiN (Ti 2*p* binding energy ≈ 455.0 eV)[36, 37] and a metallic Al-phase (Al2*p* binding energy ≈ 72.3 eV).[37]

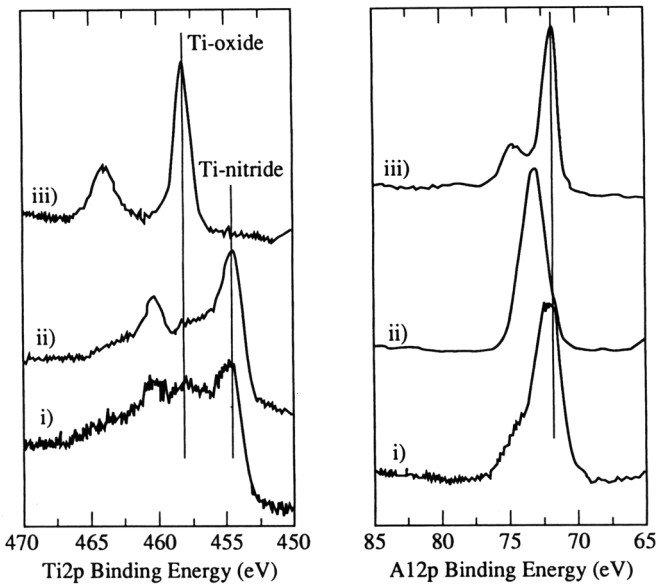

Figure 11.7 **(*a*) Ti 2*p* photoelectron spectra from (*i*) a sputter-cleaned Ti-thin film/AlN reaction couple and from (*ii*) TiN and (*iii*) TiO_2 reference samples; (*b*) Al 2*p* photoelectron spectra from (*i*) the same Ti/AlN reaction couple and from (*ii*) AlN and (*iii*) Al-metal reference samples.**

The simplest reaction consistent with these XPS results is

$$Ti + AlN = TiN + Al \tag{11.5}$$

If one uses tabulated free-energy data,[38] this reaction has a δG_r, of –8.8 kcal/mol at 1200 K and thus would provide the additional thermodynamic driving force for wetting given by Equation 11.2.

In reality, the reaction products that form at Ti/AlN interfaces are more complex than those suggested by the reaction in Equation 11.3. Beyers et al.[39] proposed a Ti–Al–N phase diagram predicting that $TiAl_3$ and TiN form when Ti reacts with AlN at 600 °C. Norton et al.[40] reacted TiH_2 films with AlN at 850 °C and found Ti_2N and Ti_3Al at those interfaces. Because the Al 2*p* binding energies of these different Ti/Al intermetallics are virtually indistinguishable from that of Al and because the Ti 2*p* binding energies of the different TiN phases are also quite similar, the XPS analyses could not adequately distinguish between those reaction products. However, the development of stable interfacial compounds, whatever their stoichiometrics, still supports the suggestion that the addition of reactive components to a conventional braze improves wetting as well as strengthens the interfacial bonding.

TEM Characterization of Ti–AlN Interfaces

The presence of additional alloying elements, particularly Cu, further complicates the interfacial reactions. TEM analysis of Ag–Cu–Ti/AlN interfaces[35] confirmed

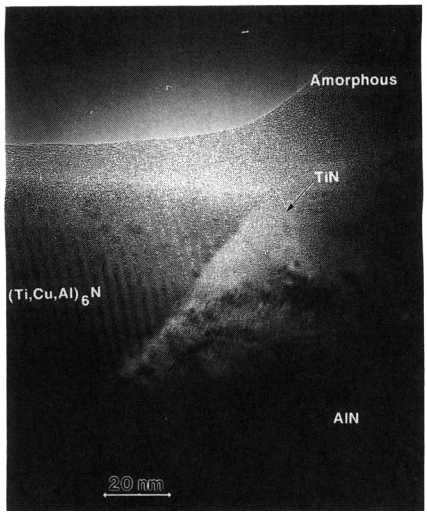

Figure 11.8 Transmission electron micrograph showing the reaction products that form at AlN/Ti–Ag–Cu interface after 5 min at 900 °C; both TiN and the η-nitride phase can be detected.[35]

that TiN is a reaction product that forms during conventional brazing operations. In addition, a second phase, identified as an η-nitride with a stoichiometry of $(Ti,Cu,Al)_6N$, forms between the TiN layer and the remaining Cu/Ag alloy (Figure 11.8). High-resolution electron microscopy demonstrated that the AlN/TiN and TiN/η-nitride interfaces are abrupt, with no other crystalline or amorphous intervening phases.[35] These results are consistent with a gradual decrease in the Al- and N-activities, and a gradual increase in the Ti-activity as one moves from AlN across the reaction interface and into the braze alloy; such a gradual change in elemental activity produces the electronic and chemical gradients necessary for the formation of a strong metal–ceramic bond.[26]

11.6 Summary

This example illustrates the range of analytical techniques that can be used to study the formation of metal–ceramic joints. Sessile drop experiments are used to determine the relative interfacial energies for a liquid drop on a solid surface and provide a means of studying wetting and spreading of a liquid on a solid. Proper interpretation reveals if a reaction is taking place at the interface and the effect of surface contamination. The technique also provides a convenient method of studying the reactions that occur at the interface by characterizing polished cross sections obtained by cutting the frozen sessile drop assembly perpendicular to the interface. The cross sections can then be analyzed by scanning electron microscopy (SEM) with energy-dispersive spectroscopy (EDS) to obtain general microstructural and compositional information and by electron microprobe (EPMA) to generate

compositional profiles across the interface. Transmission electron microscopy (TEM) can image interfacial microstructures at higher resolution than SEM, and, in addition, its electron diffraction capability gives crystal structure information. The valence state of the reaction products can be obtained with X-ray photoelectron spectroscopy (XPS) on fractured surfaces.

References

1 M. Ito, N. Ishida, and N. Kato. "Development of Brazing Technology for Ceramic Turbocharger Rotors." In *Proceedings*. Automotive Ceramics—Recent Developments, International Congress and Exposition, Detroit, 29 Feb.—4 March, 1988, SAE Technical Paper Series 880704. Society of Automotive Engineers, Warrendale, PA, 1988, p. 207.

2 A. P. Tomsia, F. Zhang, and J. A. Pask. *Acta Metall.* **30** (6), 1203–1208, 1982.

3 M. Ruhle, K. Burger, and W. Mader. *J. Microsc. Spectrosc. Electron*. 163–167, 1986 (11).

4 K. Suganuma, Y. Miyamoto, and M. Koizumi. *Ann. Rev. Mater. Sci*. **18**, 47–73, 1988.

5 R. W. Rice. In *Advances in Joining Technology*. (J. J. Burke, A. E. Gorum, and A. Tarpinian, Eds.) Brook Hill Publishing, Chestnut Hill, MA, 1976.

6 M. G. Nicholas. "Joining Structural Ceramics." In *Designing Interfaces for Technological Applications*. (S. D. Peteves, Ed.) Elsevier Appl. Science, Amsterdam, 1989, pp. 49–76.

7 K. Suganuma, T. Okamoto, M. Shimada, and M. Koizumi. *J. Am. Ceram. Soc*. **66** (7), C117–118, 1983.

8 M. Koizumi, T. Okamoto, M. Shimada, and K. Suganuma. *Am. Ceram. Soc. Bull*. **63** (9), 1173, 1984.

9 K. Suganuma, T. Okamoto, M. Koizumi, and M. Shimada. *J. Am. Ceram. Soc*. **67** (12), C256–257, 1984.

10 K. Suganuma, T. Okamoto, and M. Shimada. *High Temperatures—High Pressures*. **16** (6), 627–635, 1985.

11 K. Suganuma, T. Okamoto, M. Koizumi, and M. Shimada. *J. Am. Ceram. Soc*. **68** (12), C334–335, 1985.

12 K. Suganuma, T. Okamoto, Y. Miyamoto, M. Shimada, and M. Koizumi. *Materials Science and Technology*. **2**, 1156–1161, 1986.

13 M. Koizumi, M. Takagi, K. Suganuma, Y. Miyamoto, and T. Okamoto. In *High Tech Ceramics*. (P. Vincenzini, Ed.) Elsevier, Amsterdam, 1987, pp. 1033–1042.

14 K. Suganuma, T. Okamoto, M. Koizumi, and M. Shimada. *J. Mater. Sci*. **22** (4), 1359–1364, 1987.

15 W. G. Nicholas and D. A. Mortimer. *Materials Science and Technology*. **1**, 657–665, 1985.

16 R. M. Crispin and M. G. Nicholas. *J. Mater. Sci*. **11** (1), 17–21, 1976.

17 J. E. Kelley, D. H. Sumner, and H. J. Kelley. In *Advances in Joining Technology*. (J. J. Burke, A. E. Gorum, and A. Tarpinian, Eds.) Brook Hill Publishing, Chestnut Hill, MA, 1976, pp. 155–83.

18 M. G. Nicholas. "Reactive Brazing of Ceramics." *Proceedings*. MRS Conference on Advanced Ceramics, Tokyo, 1988.

19 W. Rostoker. *Trans*. AIME. **194**, 981–982, 1952.

20 R. E. Loehman, A. P. Tomsia, J. A. Pask, and S. M. Johnson. *J. Am. Ceram. Soc*. **73** (3), 552–558, 1990.

21 A. Adamson. *Physical Chemistry of Surfaces*. 4th ed. John Wiley, New York, 1982.

22 B. V. Derjaguim. *Recent Advances in Adhesion*. Gordon and Breach, New York, 1971, p. 513.

23 K. H. Johnson and S. V. Pepper. *J. Appl. Phys*. **53**, 6634, 1982.

24 J. E. McDonald and J. G. Eberhart. *Trans. Met. Soc., AIME*. **512** (233), 515–217, 1965.

25 J. T. Klomp. In *Ceramic Microstructures '86*. (J. A. Pask and A. G. Evans, Eds.) Plenum Press, New York, 1987.

26 J. A. Pask. *Am. Ceram. Soc. Bull*. **66** (11), 1587–1592, 1987.

27 J. A. Pask and A. P. Tomsia. In *Surfaces and Interfaces in Ceramic-Metal Systems*. (J. A. Pask and A. G. Evans, Eds.) Plenum Press, New York, 1987, pp. 411–419.

28 R. K. Brow, R. E. Loehman, A. P. Tomsia, and J. A. Pask. "Interface Interactions During Brazing of AlN." In *Advances in Ceramics*. Vol. 26, 189–196, 1989.

29 M. G. Nicholas, D. A. Mortimer, L. M. Jones, and R. M. Crispin. "Some Observations on the Wetting and Bonding of Nitride Ceramics." *J. Mater. Sci*. Harwell AERE Report 12940.

30 G. Elssner and G. Petzow. *ISIJ Intl*. **30** (12), 1011–1032, 1990.

31 T. Okamoto. *ISIJ Intl*. **30** (12), 1033–1040, 1990.

32 R. E. Loehman and A. P. Tomsia. "The Chemistry and Microstructures of Ceramic-Metal Interfaces." Presented at the International Symposium on Metal/Ceramic Interfaces organized by Max-Planck-Institut für

Metallforshung on 1–4 July 1991 at Irsee, Germany. In press, *Acta Metall & Material*.

33 F. G. Yost and A. D. Romig, Jr. *MRS Proc*. **108**, 385–390, 1988.

34 R. K. Brow, R. E. Loehman, and A. P. Tomsia. "Reactive Metal Brazing of AlN." *Proceedings*. TMS Symp. on Metal Ceramic Joining, TMS Meeting, 7–11 Oct. 1990, Detroit.

35 A. H. Karim and R. E. Loehman. *J. Mater. Res*. **5** (7), 1520–1529, 1990.

36 C. Ernsberger, J. Nickerson, A. E. Miller, and J. Moulder. *J. Vac. Sci. Technol*. **A3** (6), 2415–2418, 1985.

37 C. D. Wagner et al. "Handbook of X-ray Photoelectron Spectroscopy." Perkin-Elmer Corp., Eden Praire, MN, 1979.

38 I. Barin and O. Knacke. *Thermochemical Properties of Inorganic Substances*. Springer-Verlag, Berlin, 1977.

39 R. Beyers, R. Sinclair, and M. E. Thomas. *J. Vac. Sci. Technol*. **B2** (4), 781–784, 1984.

40 M. G. Norton, J. M. Kajda, and B. C. H. Steele. *J. Mater. Sci*. **5** (10), 2172–2176, 1990.

12

Electronic and Magnetic Ceramics

ROBERT W. SCHWARTZ

Contents

12.1 Introduction

Inorganic nonmetallic materials, electronic ceramics are used in applications ranging from capacitors to chemical sensors and varistors. Because of their high resistivity and chemical inertness, electronic ceramics originally were used only as electrical insulators. However, depending on their composition and the fabrication cycle used, current electronic ceramics exhibit a wider range of properties (that is, their polarization, mechanical, and optical responses to an applied electric field). This variety of electric field responses, which may be controlled through compositional control, chemical substitution, doping, and fabrication conditions, results in the use of ceramics in a diverse range of electronic applications that far surpasses the original use of ceramics as simple electrical insulators.

To understand the behavior of electronic ceramics, we need to understand the relationship between the observed material properties and the underlying physical phenomena responsible for those properties. For example, the presence of oxygen vacancy point defects in ZrO_2 ceramics leads to their use as oxygen sensors in

automotive and other applications. We may generalize this example by stating that the different applications of ceramics depend on material structural features from the atomic to the macrostructural level. Features such as atomic arrangement (crystal structure), point defects, domain structure, and microstructure all define the observed electronic properties of the material. Examples of the interrelationships between electrical properties and material structure are given below.

Although glasses and single-crystal ceramics are used in numerous electronic applications, in general, most electronic ceramic materials are polycrystalline in nature. Thus, the observed electronic properties are frequently dependent on either phase assemblage or controlled chemical heterogeneities within the ceramic polycrystalline body (for example, the controlled segregation of a particular dopant at the grain boundaries).

The focus of this chapter is therefore two-fold. First, the defining characteristics of electronic ceramics used for various applications are discussed and related to the underlying physical, chemical, and structural features of the material. Second, this chapter selectively describes the use of various analytical techniques for characterizing the properties of electronic ceramics that make them suitable for a given application. Since a growing area of research is the development of ceramic thin film devices, particular emphasis is placed on the applicability of various characterization techniques for analysis of electronic ceramic thin films.

12.2 Insulators and Capacitor Materials

Insulator and capacitor applications depend on the dielectric properties of ceramics, that is, on their polarization response to an applied electric field. The four polarization mechanisms which describe the displacement of charged species in ceramics are (1) electronic polarization—the shift of the valence electron cloud with respect to the nucleus; (2) ionic or atomic polarization—movement of cation and anion species; (3) dipolar polarization—perturbation of the thermal motion of ionic or molecular dipoles; and (4) interfacial polarization—inhibition of charge migration by a physical barrier. Further discussion of polarization phenomena may be found in Reference 1.

Ceramic Insulators

Ceramic insulators are used to support electrical conductors and prevent the flow of electrical charge between them. As discussed by Buchanan,[2] for insulation applications, the important dielectric properties include (1) dielectric constant (k'): a measure of the ability of a material to store electrical charge; (2) electrical resistivity (ρ): a measure of the resistance to current flow exhibited by a unit volume of the material; (3) dissipation factor ($\tan \delta$): a measure of the energy loss per cycle (in an ac field); and (4) dielectric breakdown strength (DS): the maximum voltage gradient that can be impressed across a dielectric without destroying its insulating characteristics. Materials with low dielectric constants ($k' < 30$) and low dissipation

factors (tan $\delta < 0.001$) are used as insulators, so that dielectric loss ($k' \times \tan \delta$) may be minimized.

Early insulator applications (high-voltage insulation) were most frequently based on the use of triaxial porcelains, which are prepared by a liquid-phase sintering process.[2] The raw materials that are used to fabricate these insulators include kaolin and ball clay (primarily $Al_2O_3 \cdot 2SiO_2 \cdot 2H_2O$), feldspar ($(K,Na)_2O \cdot Al_2O_3 \cdot 6SiO_2$), and flint ($SiO_2$). The relative amounts of the phases present in the triaxial body (mullite, alkali-silica glass, and silica) are determined by the starting composition and the processing cycle. In general, compositions that lead to large amounts of the residual glassy phase display greater dielectric loss and poorer insulation characteristics, due to the high mobile ion content of this phase. Larger amounts of this phase are desirable for material processing, however, because it facilitates fabrication at lower temperatures.

Due to the long history of the use of these materials in insulation applications, the interrelationships among composition, processing, microstructure, and dielectric and insulating properties are well understood. Therefore, the present need for modern analytical characterization techniques is somewhat limited. The dielectric properties (k' and $\tan \delta$) of these materials may be determined through the use of instruments such as an impedance analyzer. (Actually, with this instrumentation, capacitance, and not k' is measured. The dielectric constant is subsequently calculated from the measured capacitance through knowledge of electrode areas, sample geometry, and the electrode separation, i.e., the thickness of the dielectric.) Dielectric property characterization with this type of equipment is limited to an upper frequency of ~10 MHz. The accurate characterization of dielectric properties of ceramics intended for high-frequency applications—applications with operational frequencies from 500 MHz to 12 GHz, such as microwave dielectrics used in satellite and cellular communication systems—is typically much more involved, but may be accomplished by using a resonance cavity apparatus.[3] Of particular importance for these applications is the measurement of Q, the quality factor, which is equal to $1/\tan \delta$. Further discussion of this class of ceramic dielectrics is beyond the scope of this chapter. However, a brief review of these materials may be found in Reference 4.

In addition to simply measuring the dielectric constant and loss at a single frequency at room temperature, measurement of these properties as a function of both of these parameters can lead to a more detailed understanding of the operative polarization mechanisms. For most insulation applications, characterization of the resistivity and dielectric breakdown strength of the dielectric is also important. These properties are characterized by measurement of the current–voltage (I–V) behavior of the dielectric.[5] Finally, the interrelationships between dielectric properties and microstructure are determined through the use of microscopy (optical and electron).[6] As will be seen in the section on thin film devices, it is difficult to overemphasize the importance of using multiple characterization techniques to understand the reasons a given set of electrical properties is observed for a particular ceramic.

Other, more recent higher technology insulation applications are based on the use of materials other than triaxial porcelains. One of the largest of these applications is the packaging of very large-scale integration (VLSI) circuits. VLSI or multilayer ceramic (MLC) technology involves co-firing of conductor and insulator layers to build up multilayer electronic modules, thus increasing overall circuit density.[7] The ceramic used most frequently for these applications is 99% alumina (Al_2O_3). Since this material is prepared by a solid-state sintering process, ionic conduction processes associated with the mobile ion content of the glassy phase of triaxial porcelain insulators are not a consideration. Lower dielectric losses are therefore observed.[8] Other materials that have been employed for packaging applications include beryllia (BeO)—useful because of its high thermal conductivity—and, more recently, aluminum nitride and glass-ceramics such as cordierite and cordierite/mullite composites.[9, 10]

For packaging applications, characterization of the electrical properties of substrate materials, and determination of their suitability for a particular application, is similar to that discussed above.[9, 10] Impedance analyzers are again typically used. Characterization of other material properties, such as thermal conductivity (for heat dissipation), is also important. The characterization of these other properties is addressed in other chapters in this volume.

Ceramic Capacitor Materials

Ceramic materials suitable for capacitor applications (i.e., charge storage) are also dependent on the dielectric properties of the material. For these applications, however, since the primary goal is to maximize charge storage, materials with high dielectric constants are typically desired. Capacitance is defined as

$$C = k' \varepsilon_0 \frac{A}{d} \tag{12.1}$$

where k' is the dielectric constant, ε_0 is the permittivity of free space, A is the electrode area, and d the thickness of the dielectric. Although the dielectric constant is considered to be a fundamental material property, it is also dependent on factors such as measurement or use frequency, electric field strength, stress, and temperature. Physical features of the ceramic, such as porosity and grain size, may also affect the observed dielectric constant.

There are a number of approaches, both mechanical and material related, for increasing absolute capacitance and capacitance volumetric efficiency. These include

- preparing thin dielectric layers (see Equation 12.1)[11]
- using a multilayer approach—as with multilayer capacitors—to prepare structures with alternating electrode/dielectric layers, thus increasing the storage ability of the capacitor[12]
- using relaxor ferroelectrics—nonlinear dielectrics with high dielectric constants

- preparing materials with large effective dielectric constants ($k \approx 10\,000$ to $60\,000$) by controlling the electric susceptibilities and resistivities of grain and grain boundary phases (for example, internal boundary layer capacitors—ILBCs)[13]
- using some combination of these approaches.

Since the 1940s, ceramic capacitors have typically been fabricated from doped barium titanate compositions, since these materials display dielectric constants greater than 2000. To achieve the desired room temperature dielectric constant and dielectric constant versus temperature characteristics, analysts add various substituents $BaTiO_3$. For example, additions of strontium titanate to barium titanate shift the Curie point (that is, the temperature at which the ferroelectric to para-electric phase transition occurs, and the maximum dielectric constant is typically observed) to lower temperatures. Typical results are shown in Figure 12.1 for various $SrTiO_3$–$BaTiO_3$ compositions.[14] Barium titanate-based materials have also been used in multilayer configurations to achieve still greater capacitance efficiencies.

More recently, because of their high dielectric constants ($k' > 20\,000$), lead-based relaxor ferroelectrics have been used as capacitor materials. These ceramics have the general chemical formula $Pb(B_1,B_2)O_3$, where B_1 is typically a low-valence cation and B_2 is a high-valence cation. Compositions used in capacitor applications are frequently based on lead magnesium niobate, $Pb(Mg_{1/3},Nb_{2/3})O_3$, and lead zinc niobate, $Pb(Zn_{1/3},Nb_{2/3})O_3$. Other substituents and modifiers are added so that dielectric layers of these materials can be densified at relatively low temperatures (~900 °C). The low firing temperatures permit the use of relatively inexpensive co-fired electrode materials, such as silver. Typically, tape casting is used in the preparation of the dielectric layers.

The observed dielectric properties of the relaxor ferroelectrics are due to the compositional disorder of the B-site (B_1, B_2) cation distribution and the associated

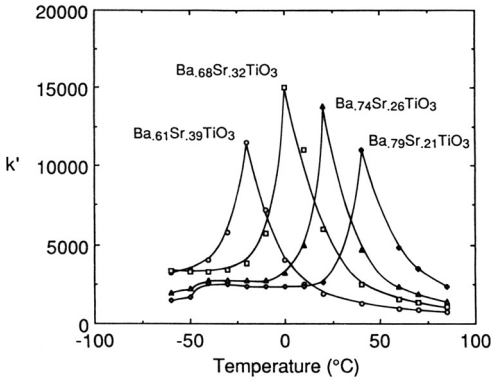

Figure 12.1 Effect of the barium titanate to strontium titanate ratio on the dielectric properties of barium titanate–strontium titanate composites. (After Reference 14.)

dipolar and ferroelectric polarization mechanisms.[4] Again, the dielectric properties of these materials are typically measured using an impedance analyzer. Of particular interest for these materials are the frequency dispersion of the dielectric properties and the dependence of the Curie transition temperature on frequency.

Other ceramic capacitors are based on the preparation of polycrystalline ceramics that possess grain and grain boundary phases with different resistivities and dielectric constants. These internal boundary layer capacitor (IBLC) materials may be fabricated with effective dielectric constants ranging from 20 000 to 60 000. The observed dielectric properties are the result of electric field splitting between the grain and grain boundary phases, due to their different electrical properties.[13] One technique that has been useful in characterizing the relationship between the dielectric properties of these materials and the underlying ceramic microstructure is electron probe microanalysis (EPMA). This technique has been used to determine the compositional variations across grain and grain boundary phases in these materials. Representative results for a bismuth-doped $SrTiO_3$ capacitor material are shown in Figure 12.2*a*.[13] The figure shows that bismuth is preferentially located at the grain boundaries and extends slightly into the grains, which in this case were 20–60 μm in size. While bismuth gives rise to insulating characteristics at the grain boundaries, the incorporation of other dopants, which do not segregate to the grain boundaries, as well as the use of controlled processing conditions, produces grains that are semiconducting in nature. These features of the two phases, together with their relative thicknesses, result in the high dielectric constants observed for these compositions.

Using microscale electrical property measurements, it is possible to directly determine the effects of the compositional variations within the ceramic on the electrical properties of the grain and grain boundary phases.[13] Results are shown in Figure 12.2*b* for the *I–V* characteristics of the grain and grain boundary phases and for the bulk ceramic.[13] As discussed, the resistivity of the grain boundary phase is several orders of magnitude greater than that of the grains. These results fit the models that have been developed to explain the behavior of IBLC devices.[15]

12.3 Piezoelectrics

Under the application of an electric field, all materials display a strain, that is, a slight change in dimensions. When the induced strain is proportional to the square of the electric field intensity, it is known as the electrostrictive effect and is given by

$$S = \xi E^2 \tag{12.2}$$

where ξ is the electrostrictive coefficient (m^2/V^2) and E is the applied electric field (V/m). Materials that display the reverse effect, that is, an induced polarization resulting from an applied stress, are called piezoelectrics, and the phenomenon is referred to as the direct piezoelectric effect. Piezoelectricity is only observed in

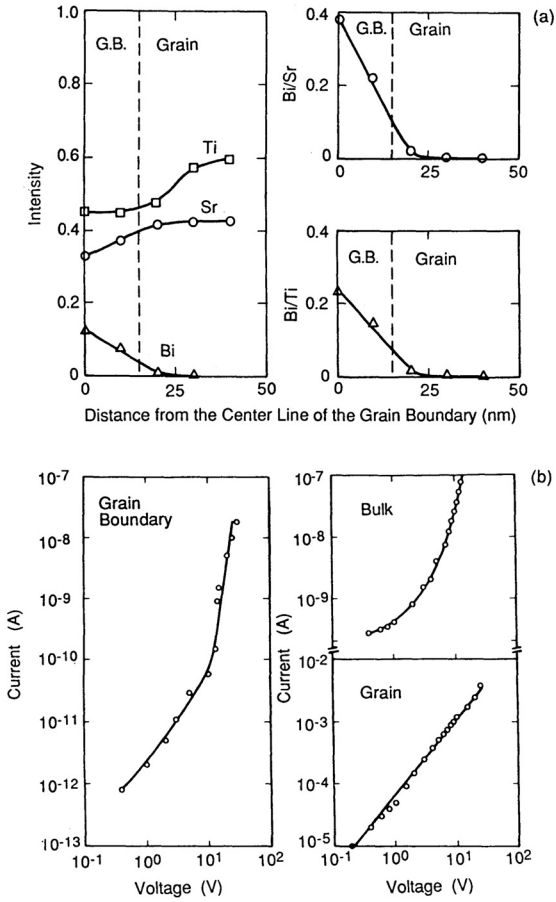

Figure 12.2 **(*a*) Chemical composition across grain and grain boundary phases of bismuth doped $SrTiO_3$ IBLC material. Bismuth is preferentially located in the grain boundary region. (*b*) Results of microscale electrical property measurements of the current–voltage behavior of bulk, grain, and grain boundary regions of a $SrTiO_3$ internal boundary layer capacitor. (After Reference 13.)**

materials which possess crystal structures that lack a center of symmetry and have one or more polar axes. Of the 32 crystal classes of materials, 20 display the piezoelectric effect. The piezoelectric response of a material may be described in terms of T, the applied stress, d, the piezoelectric coupling coefficient expressed in C/N, and D, the dielectric displacement, according to

$$D = dT \tag{12.3}$$

which describes the direct piezoelectric effect. Piezoelectrics also display the reverse effect, that is, the development of a strain, S, under the application of an electric field.

This effect, called the converse piezoelectric effect, is expressed by:

$$S = d^*E \tag{12.4}$$

where d^* is the converse piezoelectric coupling coefficient, expressed in m/V. Although not indicated, ξ, d, and d^* are all tensor properties and, thus, are directional in nature. Since piezoelectricity is a first-order effect and electrostriction is a second-order effect, the piezoelectric response of ceramics is typically much larger than their electrostrictive response.

Piezoelectric electromechanical coupling allows for the conversion of mechanical energy into electrical energy, or electrical into mechanical energy, and thus, defines two classes of transducer applications. Uses include, but by no means are limited to, hydrophones, microphones, and power transducers for ultrasonic cleaning baths.[16] The most widely employed class of piezoelectric ceramics crystallizes in the ABO_3 perovskite structure, where A is typically a low-valence cation and B is a high-valence cation. Materials used for transducer applications are typically based on compositions in the PZT ($PbZrO_3$–$PbTiO_3$) family. Since the materials are used in a polycrystalline form, the bulk ceramic must first be uniformly polarized to observe the piezoelectric effect. This is frequently accomplished through poling (placing the ceramic in a high dc field) after other processing is completed.[17]

Analysts typically determine the piezoelectric properties of materials by studying the resonance characteristics of an appropriately shaped specimen subjected to a varied electric field.[4] Details of the experimental setup are given in References 18 and 19. Investigations into the utility of PZT thin films for micromotors and other devices are also in progress. Fundamental properties of these films, such as piezoelectric coupling coefficients, have been measured by laser interferometry.[20]

12.4 Pyroelectric Ceramics

Pyroelectrics are materials that possess a unique polar axis and are spontaneously polarized in the absence of an electric field. Of the 20 crystal classes that display piezoelectricity, 10 exhibit pyroelectricity. Since pyroelectric ceramics are a subset of piezoelectric materials, they are also piezoelectric in nature. The polarization exhibited by pyroelectric materials is also a function of temperature, and the change in polarization with temperature may be expressed by

$$\Delta P_i = p_i \Delta T \tag{12.5}$$

where ΔP_i is the change in polarization, p_i is the pyroelectric coefficient ($Ccm^{-2}K^{-1}$) and is a vector quantity, and ΔT is the change in temperature. In ferroelectric materials, which are also frequently used because of their pyroelectric properties, since the polarization varies dramatically at temperatures just below the Curie point (T_c), the highest pyroelectric coefficients are typically observed in that temperature range. However, from a device design standpoint, more constant values of p_i are

desired, and therefore, materials are typically chosen so that the operating temperatures are well below T_c, where p_i varies less with changes in ambient temperature.[21]

Since pyroelectric ceramics are also piezoelectric, a temperature change also induces a change in the polarization due to the secondary pyroelectric effect, which is described by the product of the thermal expansion strain times the piezoelectric coupling coefficient. While this secondary effect can be large in polymers due to their large thermal expansion coefficients, in ceramics, it is typically small compared with the (first-order) pyroelectric effect.

The most common application that utilizes the pyroelectric behavior of ceramic materials is infrared detection, especially for long wavelengths ($\lambda > 2.5\ \mu m$).[21] A significant advantage to the use of pyroelectric ceramics in these applications is that these materials offer room-temperature device operation, unlike photon detector devices, which require cooling. The most frequently used ceramics for these applications are again the ABO_3 perovskite ferroelectrics. Lead-based perovskites (in polycrystalline form), such as PST (lead scandium tantalate) or PZFN (lead zirconate iron niobate), have been extensively investigated and the effects of various additives on pyroelectric device performance have been characterized.[22] Incorporation of these additives allows for optimization of properties such as dielectric constant and dielectric loss. Material processing for device fabrication is described in Reference 21.

The pyroelectric properties of ceramics may be measured using a current amplifier and a heating source to heat or cool the sample at a controlled rate.[4] With this approach, the measured current, I_M, is approximately equal to the pyroelectric current, expressed by

$$I_M \approx I_p = pA\frac{dT}{dt} \tag{12.6}$$

The pyroelectric coefficient may then be calculated from the measured current flow and the rate of temperature change.

From an applications standpoint, measurement of other properties, namely dielectric constant and dielectric loss, again measured using an impedance analyzer, and T_c, which may be determined from k versus T measurements or by temperature dependent X-ray diffraction, allows for calculation of material and device figures of merit. These parameters are important in determining the suitability of a material for a particular application. Recently, pyroelectric coefficients and device performance figure of merit have also been determined for solution-derived ferroelectric thin films.[23]

12.5 Ferroelectric Ceramics

From the standpoint of crystal structure, ferroelectric materials are a further subset of pyroelectric and piezoelectric materials. As with pyroelectrics, ferroelectrics also display a spontaneous polarization in the absence of an applied electric field. The

distinguishing feature of ferroelectrics, however, is that the spontaneous polarization must be reorientable under an applied electric field of lower magnitude than the material's dielectric breakdown strength. This behavior, the ferroelectric effect, is determined empirically.

The ferroelectric properties of materials are intimately related to their domain and crystal structures. In the most widely used class of ferroelectric ceramics, the ABO_3 perovskite materials, the spontaneous polarization that occurs on cooling below the Curie transition temperature results from a crystal structure change from a centrosymmetric to a noncentrosymmetric structure. For example, on cooling from temperatures greater than ~125 °C, $BaTiO_3$ transforms from a cubic paraelectric structure to a tetragonal ferroelectric structure in which the *B*-site titanium ions are displaced slightly off-center. In $BaTiO_3$, there are six equivalent directions in which the titanium may be displaced during this transformation. Since the displacement of the titanium species in one unit cell affects the displacement of the titanium species in neighboring cells, ferroelectricity is considered to be a cooperative ordering effect. This results in the formation of regions of homogeneous polarization in the material, referred to as domains, which typically encompass thousands of unit cells. Adjacent domains with different polarization directions are separated by domain walls that are typically a few unit cells thick. With cooling in the absence of an electric field, the domains are randomly oriented, and the net polarization of the material as a whole is thus zero. The domains may become oriented with the application of an electric field, however, as discussed below.

Another distinguishing feature of ferroelectric behavior is the polarization versus electric field (*P*–*E*) hysteresis loop. The hysteresis loop results from the domain reorientation which occurs as the electric field direction is varied. The size and shape of the loop is determined by the magnitude of the dipole moment of the unit cell and the domain-switching characteristics of the material. Hysteresis loop behavior is measured using either a Sawyer–Tower circuit or a Diamant–Pepinsky bridge. Details of the construction and operation of a Sawyer–Tower circuit are given in Reference 24. Thin film properties have also been measured with these two devices, and in addition, a commercially available measurement system has been widely used.[25]

Relatively few applications have utilized the ferroelectric effect in ceramics. Ferroelectric ceramics have been widely employed because of the other properties that they display, however. Their dielectric, piezoelectric, and pyroelectric properties have led to their use in capacitor, actuator and other piezoelectric applications, and infrared detection devices. Again, the most widely used materials are the lead-based ABO_3 perovskite compounds.

12.6 Ceramic Superconductors

Superconductors are materials that display two unique properties at temperatures below T_c, the superconducting transition temperature: (1) they must become

diamagnetic, that is, they must expel an externally applied magnetic field, and (2) the electrical resistivity must decrease to zero. Historically, superconductivity—the tendency of a material to display essentially no resistance to current flow below a given temperature—was observed in metallic elements and in metal alloys.[4] In 1986, however, Bednorz and Müller reported on their observations of superconductivity in $(La,Ba)_2CuO_4$, which displayed the transition to the superconducting state at ~35 K.[26] This discovery, which resulted in a Nobel prize, was extraordinary for two reasons. First, it demonstrated that in addition to metal alloys, ceramic materials were also capable of superconductivity at comparatively high temperatures. Second, the reported superconducting transition temperature, T_c, was the highest yet observed for any material.

Bednorz and Müller's report on superconductivity in $(La,Ba)_2CuO_4$ stimulated research on related ceramics in laboratories worldwide and quickly led to the discovery of other ceramic compounds with even higher transition temperatures, including $Bi_2CaSr_2Cu_2O_x$, $T_c \approx 80$ K; $YBa_2Cu_3O_{7-\delta}$, $T_c \approx 93$ K; and $Tl_2Ca_2Ba_2Cu_3O_y$, $T_c \approx 125$ K. Other bismuth and thallium-based superconductors have also been reported. The observed superconducting properties of these materials are related to their underlying crystallographic features and to the oxygen vacancy content. These material features impact the nature of the copper–oxygen layers, which largely define the electronic properties of the cuprate superconductors.[27]

Ceramic superconductors have been prepared in powder, thin film, and single-crystal form by a variety of approaches. Powders have been prepared both by traditional mixed oxide processing methods[28] and by chemical coprecipitation.[29] Bulk ceramics are then prepared from these powders by techniques such as pressing and extrusion. Single crystals have been prepared by flux growth,[30] and thin films have been prepared by laser ablation,[31] sputtering,[32] and chemical solution deposition.[33] Epitaxial growth of $YBa_2Cu_3O_{7-\delta}$ has been demonstrated and weak-link Josephson junction devices have been developed.[34] Other applications for these materials include superconducting quantum interference devices (SQUIDs) and magnetic resonance imaging (MRI) systems for the medical industry.

A variety of techniques has been used in the characterization of these materials. Superconducting transition temperatures and the magnetic susceptibility measurements (i.e., confirmation of the Meissner effect) are studied through the use of a SQUID magnetometer. Electric property characterization usually involves a simple measurement of the resistance of the sample. Finally, high-resolution transmission electron microscopy has also been widely employed in the characterization of these materials to aid in understanding their complex crystal structures.[35]

12.7 Ferrites

Magnetic ceramics may be divided into one of three different classes depending upon the type of crystal structure and magnetic properties that they display. The three classes of magnetic ceramics include the spinel ferrites, the hexagonal ferrites

and the rare earth ferrites, that is, the garnet materials. Because of the different magnetic properties that they display, the three classes of ferrite materials are used for a wide range of different applications.

Ferrimagnetic ceramics display a number of properties analogous to those displayed by ferroelectric ceramics. The most notable of these properties are hysteresis and Curie behavior. As for ferroelectrics, ferrimagnetic materials exhibit a Curie transition temperature—a temperature at which, on cooling, the material transforms from the paramagnetic to the ferrimagnetic state. At this temperature, as with ferroelectrics, regions of homogeneous magnetization called domains form within the material. One substantial difference between the domain structure of ferroelectric and ferrimagnetic materials is the domain wall thickness. In ferrimagnetic materials, the domain wall thickness is typically 10–100 nm, since the magnetization cannot change discontinuously at the boundary.[4]

The hysteresis loops observed for ferrites serve to describe the B (magnetic induction)–H (magnetizing field) behavior, as shown in Figure 12.3. The size and shape of the hysteresis loop observed for a particular compound results in a further description of ferrites as either hard or soft. Hard materials are difficult to demagnetize: a large magnetic field is required to switch the magnetic induction of the material. Because of this feature of these materials, they are successfully used in permanent magnet applications, such as motor and loudspeaker magnets, where demagnetization is undesirable. These materials usually possess coercive fields of greater than 150 kAm^{-1}, as well as large magnetizations. A general chemical formula for hard ferrite materials is $MeO{\cdot}6Fe_2O_3$, where MeO is a divalent oxide and Me is usually Sr or Ba. Because these materials crystallize in a hexagonal structure, they are frequently called hexagonal ferrites, or simply hexaferrites.

Other widely used magnetic ceramics, the soft ferrites, display quite different ferrimagnetic properties than the hard ferrite compounds. These materials show more square B–H hysteresis loops and display coercive fields that are typically below 500 Am^{-1}. They are therefore used in applications requiring switching. These applications include telecommunications, low-power transformers, recording heads, and magnetic recording media.[36] The soft ferrites crystallize in the spinel structure and possess the general formula, $MeFe_2O_4$, where Me is usually Ni, Co, Mn, or Zn. The observed magnetic properties are due to the magnetic properties of the cationic species and the antiferromagnetic coupling between the cations on the two different crystallographic sublattices.

As with a number of the other ceramics discussed, ferrites are most often prepared by traditional processing methods using oxide and carbonate precursors of the various cations. Doping and firing atmosphere control are also frequently used, depending on the particular application, to improve specific material properties, such as resistivity.[37]

The magnetization behavior (B versus H) of ferrite ceramics may be measured by an induction method. Other properties frequently measured are initial permeability,

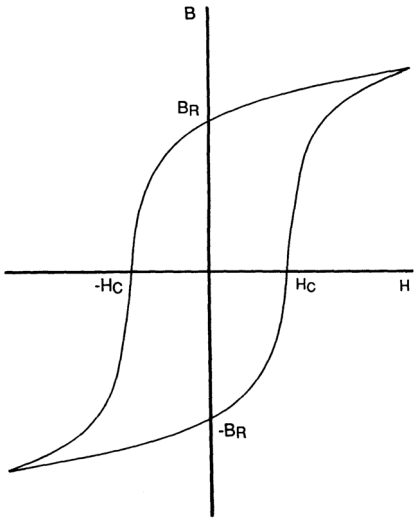

Figure 12.3 **Typical *B* (magnetic induction) versus *H* (magnetizing field) hysteresis loop behavior for a ferrite material.**

saturation flux density, core loss, magnetic loss factor, and electrical resistivity, since it determines eddy current loss in the material.[36]

12.8 Ceramic Sensors

Ceramic sensors are devices that provide environmental feedback by transforming a nonelectrical input into an electrical output. The applications for which these devices are used are widely varied. A brief list includes the use of sensors to determine the concentration of various gases, such as oxygen and carbon monoxide, temperature measurement devices, and pressure, radiation, and humidity sensors.[38] Sensors have also become widely used in automotive applications.[39] In manufacturing, because of the increasing need for waste minimization, process control, and environmentally conscious manufacturing, the increasing emphasis on sensor use and development is likely to continue to expand.[40] The use of feedback loops in conjunction with sensors for process control/optimization has also increased in recent years.

Sensor performance for different applications is defined by various features of the ceramic.[38] For example, the electrical output of most pressure sensors is dependent on the bulk piezoelectric properties of a PZT ceramic. Oxygen gas sensor performance is defined by the conductivity behavior of ZrO_2 ceramics, which is in turn dependent on the oxygen vacancy content of the material. The performance of still other sensors, for example, ceramic thermistors, is dependent on the grain boundary characteristics of doped $BaTiO_3$ ceramics. For humidity sensors based on NiO/ZnO, the *p–n* junction characteristics of the interface define sensor performance.

In general, it may be stated that the performance characteristics of a particular sensor are dependent on the bulk, grain boundary, interface, or surface properties

of the material.[38] Further, the relationship between the electrical output of the sensor and a given change in the environmental variable, that is, the nonelectrical input, exists because the change in pressure, temperature, gas concentration, etc., determines the charge generation and transport in the material.

To develop new sensors effectively requires an understanding of the underlying solid-state chemistry and physics of materials. It is also essential for the analyst to understand how processing conditions—namely, dopant incorporation and heat-treatment atmosphere—can be controlled to define material chemistry. For example, in the processing of thermistors, these two processing parameters are manipulated to produce a material with semiconducting grains and insulating grain boundaries. The result is a material that displays an increase in resistivity of several orders of magnitude at a particular temperature.

As expected from the above discussion, a variety of techniques is utilized in the characterization of sensor materials. One property frequently studied is the conductivity or resistivity of the material as a function of a second parameter, such as temperature, or the pressure or concentration of a particular gaseous species. In gas concentration-sensing applications, other properties of the material, such as gas transport, are also critical for device performance and must also be characterized.

12.9 Ceramic Thin Films

One rapidly growing area of materials development is ceramic thin films. Materials have been developed for a wide range of applications, including chemical sensors,[41] coatings,[42] membranes,[43] and a variety of electronic devices.[44] These later applications, which are perhaps less developed than the other applications mentioned, to date have focused on both ferroelectric and superconducting ceramics. The work on Josephson junction devices has been already discussed. A larger area of investigation has been the development of ferroelectric ceramic thin films for use as nonvolatile memory devices, decoupling capacitors, and optical storage media,[45] among others.

The successful development of these thin films for device applications requires that two goals be met: (1) the preparation of materials with device quality characteristics and (2) for certain applications, successful integration of the thin film with underlying silicon circuitry, without degradation of circuitry performance characteristics. A number of analytical characterization techniques have been employed to study film preparation and thin film–device integration issues. Some of these techniques and their applicability in characterizing ferroelectric thin film device preparation will be briefly discussed.

Ferroelectric thin films which are being developed for nonvolatile memory applications are most often based on the use of solution-deposited lead zirconate titanate (PZT).[44] Solution deposition generally involves the following steps: (1) preparation of the precursor solution from metal alkoxide and carboxylate compounds; (2) the tailoring of solution characteristics such as solids content, viscosity,

and concentration; (3) film deposition by spin-casting or dip-coating; (4) heat treatment of the deposited film for organic pyrolysis; and (5) heat treatment at higher temperatures to induce densification and crystallization into the desired perovskite structure.[46] The resulting dielectric and ferroelectric properties of films prepared by this process have been observed to depend on the parameters used during each phase of the fabrication process. For example, films prepared from solutions utilizing different precursors and different solvents have been noted to display dramatically different electrical properties.[46]

One technique that has been employed in an attempt to understand the reasons for these differences is nuclear magnetic resonance (NMR) spectroscopy.[47] Results are shown in Figure 12.4 for a ^{13}C NMR study of one solution preparation process. In this process, alkoxides of zirconium and titanium are combined with lead acetate in an acetic acid and methanol mixture. The resonances that are observed in the NMR spectrum allow for an understanding of the reactions occurring during solution preparation. First, the presence of ester resonances indicates that an esterification reaction has occurred. In this reaction, the free alcohols that are present have reacted with acetic acid to form methyl-, isopropyl-, and *n*-butyl-acetate. Another byproduct of this reaction is water, which can subsequently initiate hydrolysis and condensation reactions of the alkoxide precursors. Other NMR studies have shown that, in addition to the esterification reaction, acetic acid also acts as a chemical modifier, chelating the metal alkoxides and replacing the alkoxy ligands initially present.[47] This result is important because the metal oxo-acetate species formed in this reaction is expected to exhibit different solubility characteristics than the starting alkoxide compounds. By using NMR spectroscopy, it has thus been possible to determine the role of different reactants involved in the solution preparation process, study the nature of the by-products formed, and speculate on the nature of the PZT solution species formed.[47]

In addition to studying the initial solution preparation phase of the film fabrication process, researchers have used other techniques to investigate the structural evolution of the thin film, from the amorphous phase through the metastable pyrochlore phase into the stable ABO_3 perovskite crystal structure.[48] One such technique, which has been developed to study the phase constitution of the PZT thin films, is glancing angle X-ray diffraction. Results are shown in Figure 12.5. By using this technique, analysts have found it possible to determine that a residual pyrochlore phase, which does not transform to the stable perovskite phase, is present under certain preparation conditions. Further, by using multiple incidence angles, analysts found it possible to develop a phase constitution versus depth profile for the film, which showed that, in addition to the residual pyrochlore phase that was present in the surface region of the film, a minor perovskite phase was present in this region.[48]

Analysis of these specimens by transmission electron microscopy (TEM) yielded identical results to glancing angle X-ray diffraction, which are shown in Figure 12.6*a*.

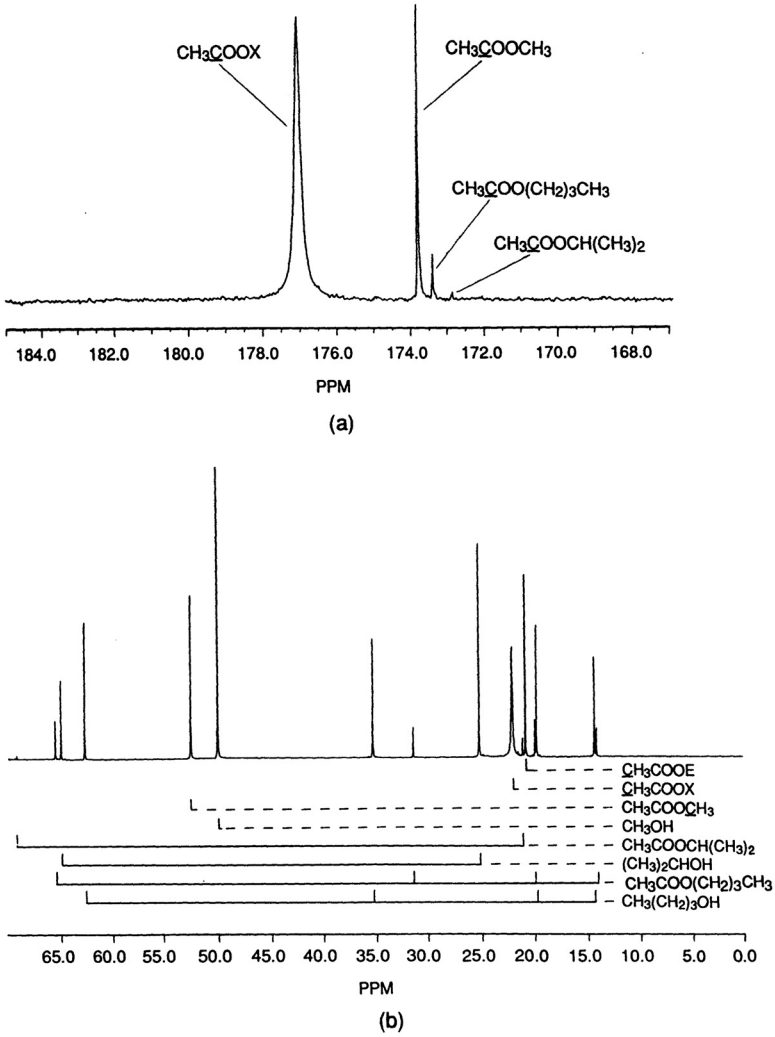

Figure 12.4 **^{13}C NMR spectrum of a PZT 53:47 sol–gel precursor solution: (*a*) carboxylic region and (*b*) aliphatic and proton region (E = methyl, *i*-propyl, or *n*-butyl; X = H or metal).[47]**

In this cross-sectional specimen, it can be seen that the residual pyrochlore phase extends across the entire surface of the film.[47] The presence of this layer results in a degradation of the electric properties of the film due to a series dilution effect; that is, the pyrochlore phase has a low dielectric constant compared to the perovskite phase, and in addition, is nonferroelectric. In a planar specimen, prepared by thinning from the backside, it is possible to use selected area electron diffraction (SAED) to identify the two phases. Results are shown in Figure 12.6*b* and *c*.

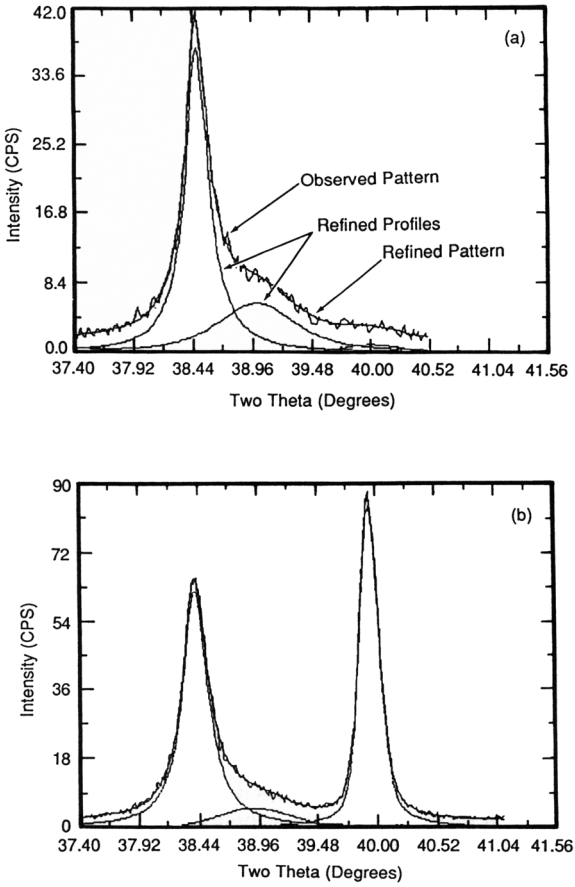

Figure 12.5 Phase distribution versus depth in sol–gel derived PZT 53:47 thin films as determined by glancing angle X-ray diffraction. (*a*) Diffraction trace of the (111) perovskite peak from ~350 Å; an obvious shoulder due to a minor perovskite phase with slightly different chemistry than the main phase is evident. (*b*) Diffraction trace of the (111) perovskite peak from ~2320 Å; the minor phase peak is diminished compared to the main peak. A peak to due the underlying Pt electrode (~40.0°) is also evident. (After Reference 48.)

Pyrochlore compounds are, in general, lead deficient compared to the desired ABO_3 perovskite phase. To enhance formation of the perovskite phase, excess lead is typically incorporated in the precursor solution to compensate for the lead loss which occurs during heat treatment, due to its high volatility.[46] The lead loss that occurs for different firing temperatures has been studied by electron probe microanalysis (EPMA). Results are presented in Figure 12.7.[49] As would be predicted, higher lead losses are observed for the higher firing temperatures. Because of this

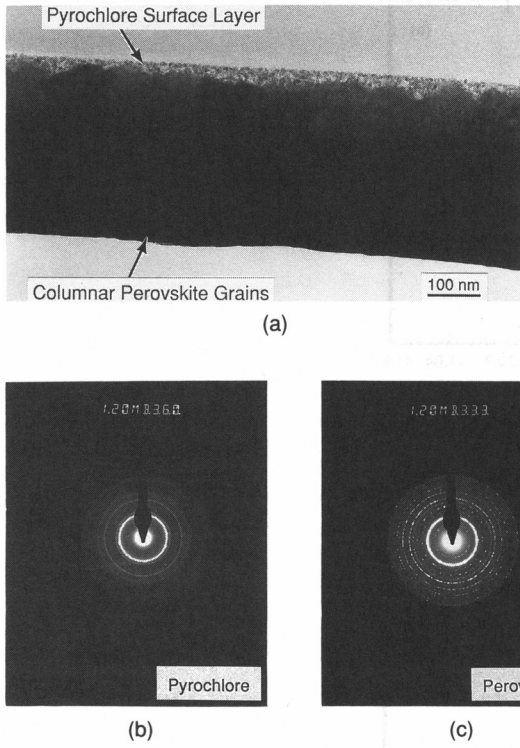

Figure 12.6 **(*a*) Bright field TEM photomicrograph[47] and corresponding electron diffraction patterns for (*b*) pyrochlore and (*c*) perovskite phases in a diphasic PZT 53:47 thin film.**

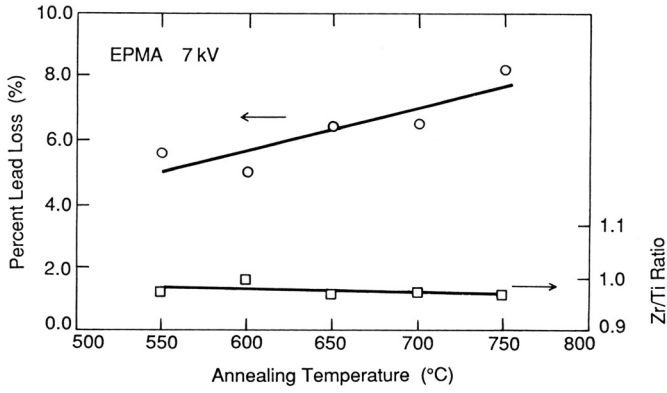

Figure 12.7 **Electron beam microprobe analysis of Pb, Zr, and Ti stoichiometry as a function of heat-treatment temperature for sintered PZT thin films (2 h anneals). Lead loss is enhanced at higher annealing temperatures. (After Reference 49.)**

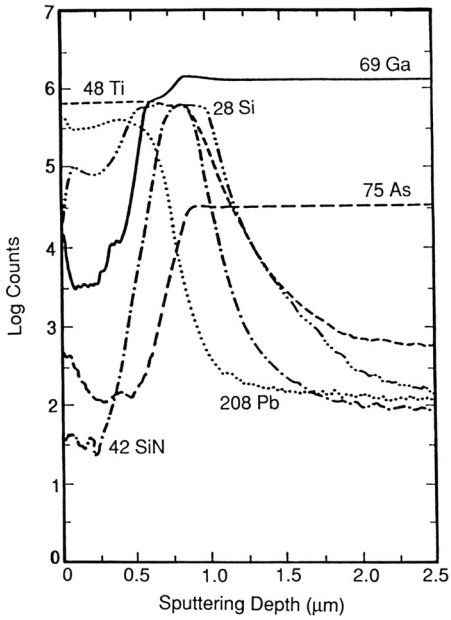

Figure 12.8 SIMS analysis of a $PbTiO_3$ thin film on encapsulated GaAs. (After Reference 50.)

behavior, frequently, in the processing of PZT films for ferroelectric applications, a compromise is required in the choice of the firing temperature used for film crystallization. A temperature high enough to promote grain growth and thus improve the ferroelectric properties, yet low enough to minimize lead volatility, is selected. Also along these lines, solution chemistry may be manipulated to impact perovskite crystallization behavior, development of ferroelectric properties, and lead loss. This may simply involve the incorporation of an excess of the lead precursor, or a tailoring of the solution chemistry to yield films with lower densification and perovskite crystallization temperatures.

The second important aspect of device preparation involves integration of the ferroelectric thin film with underlying silicon or gallium arsenide circuitry. Two common problems that must be solved for successful integration of the film onto a semiconductor device are the interdiffusion which occurs between the substrate and the ferroelectric thin film, and the degradation of the initial as-deposited electrode stack, which may occur with subsequent heat treatment of the PZT thin film. Several techniques, including SIMS (secondary ion mass spectrometry) and RBS (Rutherford backscattering) have been used to study these aspects of the fabrication process. Results are illustrated in Figure 12.8 for the SIMS analysis of a sol–gel deposited lead titanate layer on GaAs.[50] Even though this film was crystallized using a rapid thermal processing (RTP) approach and an encapsulant layer, it is evident

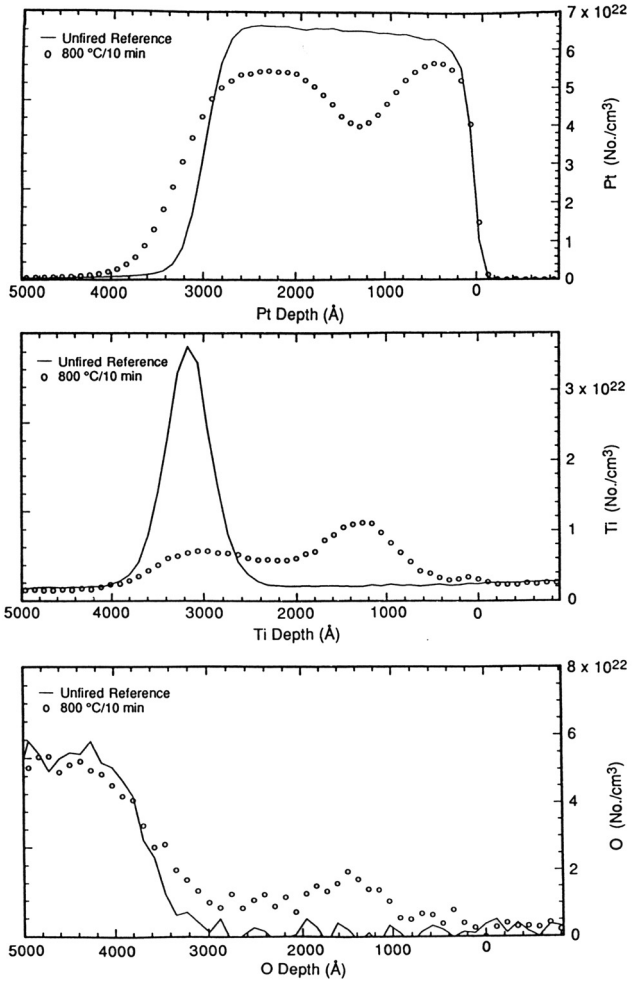

Figure 12.9 RBS spectra of a typical electrode stack in a substrate used for a thin film ferroelectric capacitor device. Results are shown for the effects of annealing the substrate at 800 °C for 10 min on the Pt, Ti, and O profiles.[51]

that there is still some interdiffusion of the substrate and film species. This may result in a degradation of both the film and semiconductor properties.

Degradation of commonly used electrode stack configurations during PZT film heat treatment have also been observed by RBS, as presented in Figure 12.9.[51] The results indicate that there is formation of a titania phase within the platinum top layer due to diffusion of titanium from the titanium adhesion layer and diffusion of oxygen from the surface of the film. If the formation of this phase becomes extensive, the conductivity of the platinum electrode can be substantially diminished. The use of several of these analytical techniques in conjunction with one another can

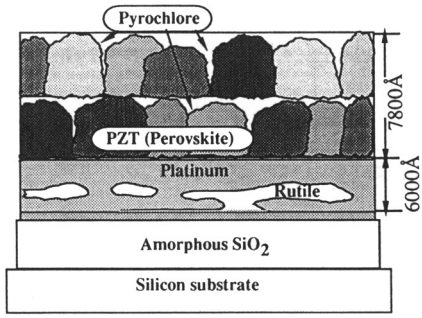

Figure 12.10 **Schematic showing summary of XRD, TEM, and RBS results for PZT thin film capacitor on electroded Si substrate. Pyrochlore is still present in the surface region of the film and at the interface of two coatings which were heat treated in separate processing steps. Also, rutile has formed within the platinum layer. (After Reference 48.)**

be used to prepare a picture of the integrated PZT thin film. Such a picture, shown in Figure 12.10, can be used to understand thin film-semiconductor integration problems and modify processing conditions to improve device performance.[48]

References

1 L. L. Hench and J. K. West. *Principles of Electronic Ceramics*. John Wiley & Sons, New York, 1990.

2 R. C. Buchanan. "Properties of Ceramic Insulators." In *Ceramic Materials for Electronics*. (R. C. Buchanan, Ed.) Marcel Dekker, New York, 1986.

3 B. W. Hakka and P. D. Coleman. *IRE Trans., Microwave Theory Tech*. **8**, 402–410, 1960.

4 A. J. Molson and J. M. Herbert. *Electroceramics*. Chapman & Hall, New York, 1990.

5 P. J. Harrop. *Dielectrics*. John Wiley & Sons, New York, 1972.

6 D. R. Clarke. In *Grain Boundary Phenomena in Electronic Ceramics*. Advances in Ceramics, Vol. 1. (L. M. Levinson, Ed.) The American Ceramic Society, Columbus, OH, 1981, pp. 67–90.

7 B. Schwartz. *Am. Ceram. Soc. Bull*. **63** (4), 577–581, 1984.

8 R. R. Tummala. *Am. Ceram. Soc. Bull*. **67** (4), 752–758, 1988.

9 A. H. Kumar and R. R. Tummala. *Intl. J. Hybrid Microelectronics*. **14** (4), 137–150, 1991.

10 N. Kuramoto, H. Taniguchi, and I. Aso. *Am. Ceram. Soc. Bull*. **68** (4), 883–887, 1989.

11 L. F. Francis. "Sol-Gel Processing, Perovskite Phase Development and Properties of Relaxor-Based Thin-Layer Ferroelectrics." Ph.D. dissertation, University of Illinois, 1991.

12 G. Goodman. "Ceramic Capacitor Materials." In *Ceramic Materials for Electronics*. (R. C. Buchanan, Ed.) Marcel Dekker, New York, 1986.

13 H. D. Park and D. A. Payne. In *Grain Boundary Phenomena in Electronic Ceramics*. Advances in Ceramics, Vol. 1. (L. M. Levinson, Ed.) The American Ceramic Society, Columbus, OH, 1981, pp. 242–253.

14 E. N. Bunting, G. R. Shelton, and A. S. Creamer. *J. Res. Natl. Bur. Std*. **38**, 337–349, 1947.

15 D. A. Payne and L. E. Cross. In *Microstructure and Properties of Ceramic Materials*. (T. S. Yen and J. A. Pask, Eds.) Science Press, Beijing, 1984, pp. 380–390.

16 L. E. Cross. *Am. Ceram. Soc. Bull*. **63** (4), 586–590, 1984.

17 G. H. Haertling. "Piezoelectric and Electrooptic Ceramics." In *Ceramic Materials for Electronics*. (R. C. Buchanan, Ed.) Marcel Dekker, New York, 1986.

18 "IRE Standards on Piezoelectric Crystals: Determination of the Elastic, Piezoelectric, and Dielectric Constants—the Electromechanical Coupling Factor, 1958." *Proc. IRE*. **46**, 764–778, April 1958.

19 W. P. Mason and H. Jaffe. *Proc. IRE*. **42**, 921–930, June 1954.

20 K. G. Brooks, J. Chen, K. R. Udayakumar, and L. E. Cross. "Lead Zirconate Titanate Stanate Thin Films for Large Strain Microactuator Applications." In *Ferroelectric Thin Films II*. (A. I. Kingon, E. R. Myers, and B. A. Tuttle, Eds.) Mater. Res. Soc. Symp. Proc., Vol. 243, Pittsburgh, 1992, pp. 443–449.

21 R. W. Whatmore, A. Patel, N. M. Shorrocks, and F. W. Ainger. *Ferroelectrics*. **104**, 269–283, 1990.

22 R. W. Whatmore. *Ferroelectrics*. **49**, 201–210, 1983.

23 C.-P. Ye, T. Tamagawa, Y.-Y. Lin, and D. L. Polla. "Pyroelectric Microsensors by Sol–Gel Derived $PbTiO_3$ and La-$PbTiO_3$ Thin Films." In *Ferroelectric Thin Films II*. (A. I. Kingon, E. R. Myers, and B. A. Tuttle, Eds.) Mater. Res. Soc. Symp. Proc., Vol. 243, Pittsburgh, 1992, pp. 61–66.

24 J. C. Burfoot and G. W. Taylor. *Polar Dielectrics*. University of California, Berkeley, 1979.

25 "RT66A Ferroelectric Test System." Radiant Technologies, Inc., Albuquerque, NM.

26 J. G. Bednorz and K. A. Müller. *Zietschrift für Physik*. **64**, 189–193, 1986.

27 K. Kitazawa. *Am. Ceram. Soc. Bull*. **68** (4), 880–882, 1989.

28 M. K. Wu, J. R. Ashburn, C. J. Thong, P. H. Hor, R. L. Meng, L. Gao, Z. L. Huang, Q. Wang, and C. W. Chu. *Phys. Rev. Lett*. **58** (9), 908–910, 1987.

29 B. C. Bunker, D. L. Lamppa, and J. A. Voigt. "Superconductor Precursor Mixtures Made by Precipitation Method." U.S. Patent 4,839,339, 1989.

30 A. B. Bykov, L. N. Demianets, I. P. Zibrov, G. V. Kanunnikov, O. K. Melnikov, and S. M. Stishov. *J. Crystal Growth*. **91**, 302–307, 1988.

31 L. Lynds, B. R. Weinberger, G. G. Peterson, and H. A. Krasinski. *Appl. Phys. Lett*. **52** (4), 320–322, 1988.

32 K. Char, A. D. Kent, A. Kapitulnik, M. R. Beasley, and T. H. Geballe. *Appl. Phys. Lett*. **51** (3), 2164–2166, 1987.

33 A. H. Hamdi, J. V. Mantese, A. L. Micheli, R. A. Waldo, Y. L. Chen, and C. A. Wong. *Appl. Phys. Lett*. **53** (5), 435–437, 1988.

34 K. Char, M. S. Colclough, S. M. Garrison, N. Newman, and G. Zaharchuk. *Appl. Phys. Lett*. **59** (6), 733–735, 1991.

35 J. P. Zhang, D. J. Li, H. Shibahara, and L. D. Marks. *Supercond. Sci. Technol*. **1**, 132–136, 1988.

36 A. Goldman. "Magnetic Ceramics." In *Electronic Ceramics*. (L. M. Levinson, Ed.) Marcel Dekker, New York, 1988.

37 A. Goldman. *Am. Ceram. Soc. Bull*. **63** (4), 582–585, 590, 1984.

38 L. Ketron. *Am. Ceram. Soc. Bull*. **68** (4), 860–865, 1989.

39 M. Naito. *Ceram. Eng. Sci. Proc*. **8** (9/10), 1106–1119, 1987.

40 L. M. Sheppard. *Advanced Materials & Processes*. 19–25, Sept. 1986.

41 C. J. Brinker and G. W. Scherer. *Sol–Gel Science, The Physics and Chemistry of Sol–Gel Processing*. Academic Press, Boston, 1990, p. 867.

42 R. B. Pettit, C. J. Brinker, and C. S. Ashley. *Solar Cells*. **15**, 267–278, 1985.

43 J. Haggin. *Chem. Eng. News*. **66**, 25–32, 11 July 1988.

44 *Proceedings*. The Third International Symposium on Integrated Ferroelectrics, Colorado Springs, April 1991.

45 D. B. Dimos and R. W. Schwartz. "Electrooptic Properties of PZT Films for Image Storage Applications." In *Ferroelectric Thin Films II*. (A. I. Kingon, E. R. Myers, and B. A. Tuttle, Eds.) Mater. Res. Soc. Symp. Proc., Vol. 243, Pittsburgh, 1992, pp. 73–78.

46 R. W. Schwartz, B. C. Bunker, D. B. Dimos, R. A. Assink, B. A. Tuttle, D. R. Tallant, and I. A. Weinstock. *Proceedings*. The Third International Symposium on Integrated Ferroelectrics, Colorado Springs, 1991, pp. 535–546.

47 R. W. Schwartz, R. A. Assink, and T. J. Headley. "Spectroscopic and Microstructural Characterization of Solution Chemistry Effects in PZT Thin Film Processing." In *Ferroelectric Thin Films II*. (A. I. Kingon, E. R. Myers, and B. A. Tuttle, Eds.) Mater. Res. Soc. Symp. Proc., Vol. 243, Pittsburgh, 1992, pp. 245–254.

48 R. P. Goehner, M. O. Eatough, B. A. Tuttle, and T. J. Headley. "Characterization of PZT Thin Films—Crystallographic Phases." In *Advances in X-ray Analysis*. Plenum Press, New York, 1992.

49 C. K. Kwok, S. B. Desu, and L. Kammerdiner. In *Ferroelectric Thin Films*. (E. R. Myers and A. I. Kingon, Eds.) Mater. Res. Soc. Symp. Proc., Vol. 200, Pittsburgh, 1990, pp. 83–89.

50 R. W. Schwartz, Z. Xu, D. A. Payne, T. A. DeTemple, and M. A. Bradley. In *Ferroelectric Thin Films*. (E. R. Myers and A. I. Kingon, Eds.) Mater. Res. Soc. Symp. Proc., Vol. 200, Pittsburgh, 1990, pp. 167–172.

51 G. W. Arnold, Jr., Sandia National Laboratories, 1990. Unpublished results.

13

Nondestructive Evaluation

LYNN NEERGAARD

Contents

13.1 Introduction

"Those who break a thing to find out what it is made of have left the path of wisdom."—J. R. R. Tolkien.

In metallurgical practice, it is possible to evaluate nondestructively the size and severity of defects. This allows prediction of lifetimes and removal of severely flawed parts from the product stream. Metal parts for which reliability is a critical issue are routinely evaluated. Nondestructive evaluation (NDE) consists of the prediction of properties based on a series of disciplines (see Table 13.1). First, the size, position, and orientation of defects are measured. Then, theoretical models relating defect characteristics to property degradation are used to predict material properties.

For the past 20 years it has been a goal in the ceramics community to use NDE techniques to predict lifetimes and to remove severely flawed ceramic parts. Several advantages will accrue from successful routine NDE of ceramics. It is difficult to sell products that have been broken, so destructive testing reduces production yields. With NDE, on the other hand, each component manufactured can be tested. It is also useful for a manufacturer to be able to guarantee his product for a given lifetime. NDE allows components that are likely to fail (i.e., components with large flaws) to be removed from the product stream. In research and development

Technique	Speed	Resolution	Sample Limitations	Enhancement Techniques	Information Available
X-ray transmission	Very fast	25 μm for high density, 100 μm for low density	Rough surfaces and thick samples limit resolution	Penetrant dyes, low frequency X-rays	Presence of internal flaws, especially high-density inclusions
X-ray tomography	Very slow	0.02 × 0.02 × 2.0 mm	Speed inversely proportional to size	Penetrant dyes, low frequency X-rays	Position of dense inclusions and surzface connected features
Time-of-flight ultrasonics	Fast	100 μm at 100 MHz	Parallel reflecting surface preferred[a]	Laser ultrasonics	Position of density fluctuations
Ultrasonic spectroscopy	Fast	100 μm	—[a]	Laser ultrasonics	Presence of small, uniformly distributed flaws
Scanning laser acoustic microscopy	Slow	25 μm	—[a,b]	Quadrature synchronization	Position of delaminations, undensified regions
Acoustic microscopy	Very slow	25 μm	Must be immersible	Computer data analysis and display	Position of internal porosity
Ultrasonic birefringence	Slow	60 MPa	Minimum thickness required	Various	Residual stress
Optical birefringence	Very fast	55 MPa	Must be transparent	Shorter wavelengths for optically opaque specimens	Average residual stress through the volume
Photo acoustic microscopy	Fast	1 μm	Only polls the surface	Mirage effect	Position of coating delaminations, and surface-connected cracks
Infrared microscopy	Very fast	> 25 μm[c]	—[b]	—	Presence of delaminations, undensified regions, and inhomogeneities
Acoustic emission	Slow	One event	Minimal	—	Presence of irreversible, destructive processes
Shearography	Fast	> 10 μm[c]	Most useful for laminar composites	—	Delaminations
X-ray diffraction	Slow	40 MPa	Only polls the surface	Position-sensitive detector	Residual stress near the surface

[a]Surface–transducer contact necessary.

[b]Complex shapes present data analysis difficulties.

[c]Dependent on distance below the surface.

Table 13.1 Nondestructive evaluation techniques.

work, NDE allows one to repeat a test on the same specimen to ascertain the efficacy of a sequence of processing treatments (hot isostatic pressing, for example), or to predict loss of strength resulting from mechanical abuse. In-service damage can also be monitored to predict failure of critical components.

Attainment of the preceding goals requires the development of reliable, high-resolution NDE techniques. Because of the brittle nature of ceramics, flaws leading to crack propagation within design load limits (critical flaws) are extremely small. For example, the critical size for an atomically sharp Griffith flaw in an alumina ceramic subjected to a 500 MPa stress is 65×10^{-6} m or 65 μm. In most cases, equipment used for the NDE of metals does not have sufficient resolution to image these flaws in ceramics.

There are a number of quantities which may be easily measured without destroying the sample. Examples include color, mass, and temperature. NDE, however only refers to those nondestructive techniques which are alternatives to destructive techniques—specifically, measurement of mechanical strength and residual stress. Standard strength tests generally consist of fabricating mechanical testing coupons and loading them to failure. In destructive residual stress techniques, material is removed and strain is measured using surface strain gages. Examples are hole drilling, ring core drilling, and sectioning. Residual stress is calculated using Hooke's law and a knowledge of the elastic moduli. The high stiffness of ceramics reduces the sensitivity of destructive and nondestructive residual stress measurements.

NDE of components to predict strength and useful lifetime requires that flaws be detected and characterized. Flaws in ceramics fall into three categories: pores, inclusions, and cracks. Any of these flaws may be interior or surface. Smooth pores cause little stress concentration, but cracks in the interior surface of pores cause great stress concentration. It is important, therefore, to be able to characterize the surface texture of pores, as well as their size. At present, there are no techniques that can do this. It is therefore most conservative to assume that the interior surfaces of all pores are covered with atomically sharp cracks. Inclusions can cause hoop or radial stresses upon cooling, depending on the relative thermal expansion coefficient. If these stresses are sufficiently high, cracks may be associated with inclusions. Cracks are always effective stress concentrators; as such they are relatively easy to characterize, once detected.

13.2 X-ray Techniques

Radiography

Radiography refers to the production of an image of a part and its internal defects by passing penetrating radiation (X, gamma, beta, neutron) through the part and exposing a photographic film. The advantages of radiography are that it detects internal defects, it can be used with complex shaped objects, and it gives real-time images. Radiographs must be taken from multiple angles to ascertain flaw positions,

geometries, and orientations. X-ray radiography is the most popular type of radiography because it is relatively portable and because the equipment does not produce radiation when not energized. Although the comments in this section are specific to X-ray radiography, they apply to all kinds of radiography.

X-ray radiography is similar to a chest X-ray because it measures X-ray absorption, which is a function of density and composition. Pores, cracks, inclusions, and undensified regions cause variations in density. The X-ray absorption of fully dense ceramics is significantly less than that of metals. Metallic inclusions in ceramics can therefore be seen easily, but the contrast of pores and cracks is low. As a result, X-radiography can image metallic inclusions in ceramics down to 25 μm and cracks and pores down to 100 μm.

Resolution of cracks and pores exposed to the surface can be enhanced using radiation opaque penetrant dies. Opaque dies can also be used to differentiate between low-density inclusions and surface-connected pores. Suppose a surface-connected feature is observed that has lower X-ray absorption than the rest of the material. After it is soaked in dye, a pore will have a higher X-ray absorption than the background, while the absorption of a low-density inclusion will not change.

Enhanced resolution (on the order of tens of microns) may be had by using microradiography. Microradiography requires low-energy X-rays, thin samples, and high-resolution film. Resolution may also be enhanced by digitizing the radiographs for image processing.

Tomography

Computed tomography (CT) gives a three-dimensional map of X-ray absorption as a function of position. This map is displayed slice by slice, as digitized two-dimensional sections through the volume. Resolution of tomography is often reported as the size of the picture element, or pixel. The slice thickness is also important, so the resolution should be reported as the size of the volume element, or voxel. Each voxel represents the average linear X-ray absorption in a volume of material. Low absorption indicates an undensified region, a pore, a low-density inclusion, or a crack. For advanced ceramics, uniform density is a necessary but not sufficient condition for quality. Although it is slower than radiography, tomography is more reliable in thick, rough, or variable cross-sectional specimens, where radiography may not resolve small or low-contrast features. Tomography is reliable only for detecting large defects (e.g., a 50-μm-wide crack in a 1-cm-thick specimen), but not critical flaws. Voxel resolution is limited by the ability to collimate the X-ray beam. For well-collimated beams, voxel resolutions of 0.02 × 0.02 × 2.0 mm have been reported,[1] implying that resolutions of 0.02 × 0.02 × 0.02 mm are possible. The disadvantage of this microtomographic technique is that collection time for a single slice with area 1 × 1 mm is 8 h. Computed tomography is extremely slow and cannot be used for routine testing in most production settings, but it is useful for measuring the internal morphology of complex structures.[2] Co-fired multilayer

ceramic packages, multilayer capacitors, laminated ceramic matrix composites, and co-fired fuel cells are examples of complex ceramic structures.

Analog tomography consists of moving the film and source in opposite directions to blur all but one plane of the specimen. Analog tomography is as inexpensive as radiography, but the image is blurred and has low contrast because a digital filter cannot be used. This difficulty can be avoided by digitizing the resulting image and using post filtering. The resolution of analog tomography is 0.2 × 0.2 × 1 mm.

13.3 Ultrasonic Techniques

Background

The power of ultrasonic NDE is that ultrasonic waves are mechanical vibrations. As such, they are influenced by the same microstructural features that influence mechanical properties. In ultrasonic NDE, a very high-frequency wave is introduced into a medium. This wave is reflected by flaws larger than or approximately the same dimension as the wavelength. Either the reflected wave or the transmitted wave is detected and analyzed. For reflected waves, a transducer emits a pulse into the material, which is detected on the same side of the sample. Detection is accomplished by either the same transducer (pulse echo) or another transducer on the same side (pitch–catch). This mode is useful for time-of-flight measurements of flaw size and position. For transmitted waves, the receiving and transmitting transducers are on opposite sides of the sample. This mode is useful for absorption measurements. The sensitivity of both modes can be changed by adjusting frequency.

The speed of sound in an elastic medium is a function of elastic modulus and density as follows: $v = (E/\rho)^{1/2}$, where v is velocity, E is modulus, and ρ is density. Because ceramics are stiffer and less dense than metals, the speed of sound in ceramics is greater than in metals. For example, the speed of sound in iron is 5.13 mm/μs, compared to 9.78 mm/μs in alumina. This means that, at the same frequency, the wavelength is greater in a ceramic and the resolution essentially halved. This difficulty and the fact that critical flaws in ceramics are much smaller than those in metals mean that frequencies between 10 and 100 MHz are required for ultrasonic evaluation of ceramics.

There are three different methods of displaying ultrasonic data: A-scan, B-scan, and C-scan. Because the received signal is displayed as a function of time, A-scan display is essentially one-dimensional. The transducers do not move, and only material which is in the ultrasonic beam is polled. This type of display is useful for measuring absorption as a function of frequency, density, and elastic moduli.

B-scan display is essentially two-dimensional. The pulse–echo elapsed time is converted to distance beneath the surface. As the transducer is scanned across the surface, internal defects reflect the wave, as does the opposite surface. From these reflections, an image is generated of a slice of the material. Note that the depth resolution is on the order of tens of microns, but the resolution parallel to the surface is equal to the transducer size. Thus, if the precise position of defects in the plane parallel to the

surface is important, transducer size must be minimized. B-scan is useful for detection and characterization of flaws.

C-scan ultrasonics, or ultrasonic microscopy, is essentially a three-dimensional technique. The transducer is rastered across the sample surface in the same pattern as the electron beam in a television. Information on the depth of flaws beneath each position on the sample surface is recorded and stored in a computer. The computer then allows projection of the three-dimensional network of flaws onto the screen. The image is usually rotatable to take advantage of the dimensionality of the data. C-scan may be used to characterize and display the complete flaw distribution in a sample.

Ultrasonic Time of Flight

Time of flight may be used to measure local density fluctuations. In a chemically homogeneous ceramic, changes in velocity result from differences in density and modulus caused by undensified regions. For dry-pressed bodies, sound velocity has been found to relate to density by the equation[3]: $\rho = \alpha v^{1/3}$, where ρ is density, v is velocity, and α is a function of the material and the amount of interparticle contact. Furthermore, as a powder is dry-pressed, sound velocity increases with pressure. Thus time-of-flight ultrasonics can be used to monitor the dry-pressing process.

Another use of time-of-flight ultrasonics is measurement of flaw size and position. The ultrasonic wave will be reflected by any feature which has a significant impedance mismatch with the host material. This includes the sample surface, internal pores, cracks, and inclusions. If a pulse–echo transducer is scanned along a line on the surface of the specimen, the output may be displayed as a B-scan. The effect is similar to sectioning the material mechanically and observing it under a microscope. Flaw-detection sensitivity is on the order of the wavelength of the ultrasonic signal. For Si_3N_4, a typical ceramic, the frequency must be at least 100 MHz to detect flaws of 100 μm.

A material absorbs ultrasonic energy at a different rate for different frequencies. A constructive use of this phenomenon is ultrasonic spectroscopy, covered in the next section. Another consequence is that a single spike pulsed into the sample for time-of-flight measurements is distorted during transmission. This makes it difficult to time the interval between echoes precisely. A continuous sine wave is a single frequency, but it interferes with itself upon reflection. A compromise is found in a tone burst, a sine wave applied for a short time.

For interference to be avoided, the duration of the tone burst must be less than the echo transit time. This means that flaws within a distance equal to one half of the tone burst duration of the surface cannot be resolved. In some applications (in torsion and flexure) the surface stresses are greater than the interior stresses, so surface flaws are of interest. Near-surface defects can be detected using a surface ultrasonic wave. One geometry for the generation of surface ultrasonic waves is shown in Figure 13.1. Surface waves reflect from surface-exposed defects in exactly

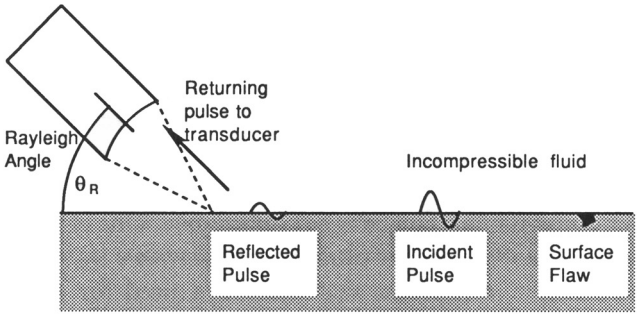

Figure 13.1 Schematic of ultrasonic setup for the generation and detection of surface waves. (From Roberts et al.[4])

the same way that volume waves interact with interior defects. Any defect within one wavelength of the surface may be detected and characterized using surface waves.

Ultrasonic Spectroscopy

All materials absorb sound to a certain extent. Those flaws which are significantly smaller than the ultrasonic wavelength will not reflect the incoming energy. Flaws larger or approximately the same size as the wavelength will reflect the energy, leading to reduced transmission. The principle is similar to the observed opacity of a foam such as meringue. Neither component of meringue (egg whites or air) is opaque, but there are enough reflecting surfaces in the meringue to cause it to appear opaque. Similarly, those samples or sections of sample that have more reflectors will reflect the ultrasonic signal away from the receiving transducer. As a result, attenuation in a given material is greater for larger defects and shorter wavelengths.

In ultrasonic spectroscopy, a single pulse (consisting of a broad spectrum of frequencies) is input, and a Fourier transform is performed on the received pulse. Losses due to spreading and sample/transducer impedance mismatch must be either calculated or compared to a standard and corrected for. One method of correcting for these sample-independent absorptions is to compare attenuation as a function of frequency in the test piece (α) to that in a standard, such as SiO_2 glass (α_0). High relative attenuation at high frequencies indicates many inhomogeneities the same scale as the wavelength. This indicates either course grain size or high porosity. If one assumes small grain size and either a spherical or cylindrical pore geometry, pore volume and average pore size can be estimated from the frequency versus attenuation plot.[4] Using this method, one can map the porous and large grain areas of a sample. These microstructural flaws may not be critical if they are in areas of low design stress. Although specific flaws cannot be imaged using ultrasonic spectroscopy, it is useful to check and to improve a production process. Ultrasonic spectroscopy can be used on green ceramics, but because they have high porosity they will exhibit high absorption. High attenuation also makes this technique unattractive for thick green samples. For go/no-go inspection, the frequency may

be tuned to pick up critical flaws, then only the received amplitude need be measured. Small (subcritical) flaws will not reflect the wave.[5]

Ultrasonic analyses are generally performed using a piezoelectric transducer to generate and detect the ultrasonic wave. Recently, techniques have been developed to generate and detect ultrasonic waves without contacting the sample. These techniques allow elastic constants to be measured at elevated temperatures, densification to be monitored, and microcracking due to thermal fatigue to be characterized. One of these noncontact methods is to generate and detect the ultrasonic wave with a laser.[6]

From the foregoing discussion it is apparent that there is a need for small transducers and short excitation lengths. Laser techniques also have the advantage of better spatial resolution. A short laser pulse impinging on the sample surface produces, in a small area, a single ultrasonic spike of picosecond duration. This picosecond pulse provides high resolution and enables analysts to study films of submicron thickness. At low power, the laser produces transient surface heating, which results in a tangential stress, generating a shear wave in the material. At higher power, some ablation takes place, a normal stress is produced, and a compression wave is generated.[7] A laser interferometer may be used to measure surface deflection caused by the return of the wave. One disadvantage of this technique is that the acoustic characteristics of laser sources and receivers are not well understood. This makes some standard ultrasonic effects, such as diffraction, difficult to evaluate. Another disadvantage is that laser ultrasonic equipment is not yet commercially available.

Scanning Laser Acoustic Microscopy (SLAM)

In scanning laser acoustic microscopy, a continuous sine wave is generated with a piezoelectric transducer. This wave is diffracted, refracted, and absorbed by the microstructure of the sample. When it reaches the opposite side, it is detected using scanning laser interferometry. Large flaws and flaw concentrations can be imaged using only the amplitude output of the system. The technique can be enhanced using a quadrature detector synchronized with the output of the transducer.[8] This system allows the generation of phase and amplitude signals. From the phase and amplitude signals, the back-propagated wave can be calculated at any desired plane in the material. This greatly increases the resolution of the technique and allows flaw shape and position to be found.

Acoustic Microscopy

Ultrasonic microscopes consist of a spherically focused transducer submerged in an incompressible medium (water, for example) and attached to precision positioners. Resolution is limited by spherical aberration caused by diffraction at the medium/sample interface and by the precision of the positioners. Standard resolution is on the order of 100 μm. Finer focus enhances resolution, but drastically increases the time required to get data. Fine-focus acoustic microscopy may be used to find critical flaws in high-stress portions of a device, but even reducing the volume of

material polled does not make this a rapid method. Acoustic microscopy is most useful during process optimization to reduce the size of processing flaws.

Ultrasonic Birefringence

The speed of sound through a medium is a function of applied strain. The relationship is governed by the acoustoelastic coefficient. Stress states with unequal principle stresses (i.e., nonhydrostatic) have the effect of introducing anisotropic acoustic behavior to otherwise isotropic materials. This effect is similar to strain-induced optical birefringence (covered in the next section). The advantage is that ultrasonic birefringence can be measured in optically opaque materials.

There are three ways of measuring ultrasonic birefringence. To measure stress in an entire specimen, one may measure the time of flight of ultrasonic waves as a function of propagation direction. For smaller sections of sample, shear wave velocities are measured as a function of the orientation of the plane of oscillation of the shear wave. Surface stress can be ultrasonically measured using the velocity of Rayleigh waves as a function of direction. Any of these methods will yield the direction of principle stress and relative stress intensities between samples of identical materials. To find actual values of stress, one must know the value of the acoustoelastic coefficient of the material. An experimental setup for measuring bulk acoustoelastic coefficients has been reported by Koshti.[9]

13.4 Other Techniques

Strain-Induced Optical Birefringence

Strain-induced optical birefringence can be used to measure residual stress in a specimen. When an optically isotropic material (such as glass) is subjected to a mechanical stress, it becomes optically anisotropic. Optical anisotropy can be easily observed by placing the material between polarized plates oriented such that the polarization planes are perpendicular. Light passing through the first polarizer is polarized one direction and is not admitted through the other polarizer. A birefringent material will rotate the polarization plane of the light. Thus, the stressed areas of an isotropic material will appear illuminated.

Strain-induced optical birefringence is a rapid and powerful technique for transparent isotropic materials. Not only is it possible for one to see residual strains introduced as a result of processing, but inclusions that are invisible to the naked eye can be seen by their associated strain fields. This technique is extremely fast. The product can be conveyed between two crossed polarizers, allowing a single inspector to inspect the output of a small factory. This technique is capable of resolving stresses of as little as 55 MPa (8 kpsi) in Pyrex glass.

Penetrant Techniques

Penetrant techniques can be used to highlight surface flaws such as open porosity and surface-breaking cracks for optical or radiographic inspection. The usefulness

of opaque dies in radiography is discussed in the section on radiography. Dies used are either fluorescent or a high-contrast color when compared with the ceramic.

Photoacoustic Microscopy

Photoacoustic microscopy (PAM) allows measurement of heat dissipation, a function of thermal properties near the surface.[10] A pulsed laser is scanned across the surface, generating localized heating. The sample's response is measured one of three ways. The first is to seal the sample into a chamber with a microphone. As the surface heats, the gas in the chamber heats and expands, creating pressure, which is converted into an electrical signal by the microphone. The second method is to use the mirage effect. A second laser is directed over the specimen near the impact point of the heating laser. As the gas above the specimen is heated, its index of refraction is reduced, resulting in a deflection of the reading laser. A third method is to measure the thermal expansion of near surface material using laser inter-ferometry. From the thermal expansion, the local temperature may be calculated.

Both phase and amplitude signals are useful for imaging surface flaws. PAM is rapid enough to be used in a production setting and is sensitive to changes in the thermal properties near the surface. It is especially useful for plasma spray coatings (e.g., SiC on graphite). The resolution of PAM is 1 μm, but because it is sensitive to thermal properties it can image tight vertical cracks with widths significantly less than 1 μm.

Infrared Microscopy

Infrared (IR) microscopy is similar to photoacoustic microscopy because it consists of a rastering laser beam and it measures the material's thermal properties. IR microscopy is, however, a transmission technique. An IR image of the side of the sample opposite the rastering laser is taken using an IR camera. Flaws in the body of the specimen interfere with the transmission of heat and are thus detected. IR microscopy is especially powerful for detecting undensified regions, inhomogeneities, and delaminations in laminar composites.

Acoustic Emission

Acoustic emission is the microscopic equivalent of seismography. When an earthquake occurs, the sounds generated are picked up and recorded on seismographs. The location of the source is calculated by comparing the time the sound was received by seismographic receivers in different places and triangulating. Each time a deformation mechanism is activated in a material, it emits a characteristic sound: an acoustic emission. Since ceramics are brittle in nature, the predominant mechanism of deformation is microcracking, although stress-induced crystalline transformations also emit acoustic waves. The source of the emission may be pinpointed by using three or more receiving transducers to triangulate.

Strictly speaking, acoustic emission is not NDE because sound is emitted only by irreversible, destructive processes. Acoustic emission is helpful if used during

proof tests because it can detect damage caused by the proof test, even in those samples that survive. Another application is detection of impending failure by continuous monitoring of critical components. In the laboratory, acoustic emission can be used to monitor the accumulation of fatigue damage.

Shearography

Shearography is a NDE technique in which the dimensions of a component in the stressed and unstressed state are compared using speckle-shearing interferometry (hence the name). The graphical output of shearography is a fringe pattern produced by interference between the images of the stressed and unstressed component. Each fringe is a locus of points of constant surface deformation. The difference in deformation between fringes is one laser wavelength. In an unflawed specimen, the contour lines are evenly spaced and gradually curving. Since flaws introduce local changes in the stiffness of a material, fringes near a flaw exhibit anomalous kinks. This is a powerful method for detecting interlaminar delaminations in composites.

Lattice Distortion

Residual stresses near the surface can be measured using X-ray diffraction (XRD). Because the beam penetrates only the first millimeter of material, XRD is a surface-sensitive residual stress technique. The principle of the method is that individual grains of a polycrystalline ceramic will deform elastically under the influence of residual stress. The amount of elastic deformation is found by measuring the interplanar spacing of grains just beneath the surface and comparing those interplanar spacings to their stress-free values. Thus, the grains of the material act as strain gages referenced to zero strain.

There are several X-ray techniques for finding the strain in a material surface.[11] In general, interplanar spacings are measured as a function of orientation with respect to the surface, and the stress is calculated using the equation

$$\sigma_\phi = \frac{E}{(1-\nu)\sin 2\psi}\,\frac{d_i - d_n}{d_n}$$

where σ_ϕ is the stress in the direction of the plane of measurement, d_i is the lattice spacing of a plane inclined an angle ψ with respect to the surface, d_n is the lattice spacing of a plane normal to the surface, E is Young's modulus, ν is Poisson's ratio, and ψ is the angle between the sample surface perpendicular and the plane normal. Stress parallel to the surface is found by tilting the sample to some angle ψ to find d_i. Stress at some angle to the first stress may be found by repeating this experiment after rotating the sample to a new position, ϕ. The geometry is shown in Figure 13.2. There are three experimental methods whereby the governing equation may be solved.

In the two-exposure method, interplanar distances are measured for two planes, one perpendicular and one at an angle to the surface. This method is rapid but does

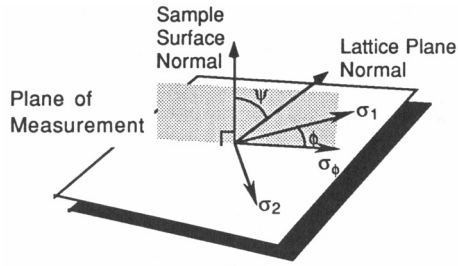

Figure 13.2 Geometry of the measured stress σ_ϕ and direction of X-ray incidence with respect to principle stresses σ_1 and σ_2. (From Cullity.[12])

not allow for correction of artifacts such as microstructural texturing and sample misalignment.

In the sine-squared-ψ method, lattice spacings are measured at five or more ψ angles. The governing equation is then least-squares fit to find the best value of σ_ϕ. Observation of the behavior of the quantity $(d_i - d_n)/d_n$ as a function of $\sin^2 \psi$ allows instrument misalignment and preferred orientation to be detected. This method is slower than the two-exposure method, but is more statistically significant.

A third method is the position-sensitive detector system. This method is actually a modification of detector design, which allows more rapid determination of the peak position at each value of ϕ and ψ. In standard X-ray diffraction, a single detector is scanned through a set of diffraction angles to find the angle at which the radiation is most intense (i.e., the peak position). The difference for a position sensitive detector system is that an array of detectors is used, allowing accumulation of data from several diffraction angles simultaneously.

13.5 Summary

Most techniques for the nondestructive evaluation of ceramic materials fall into two categories: high-energy penetrating radiation (for example, X-ray) and high-frequency elastic waves (ultrasonics). Some NDE techniques have been developed for specialized applications, such as optical birefringence for transparent specimens and shearography for laminar composites.

Nondestructive evaluation of ceramics is currently useful for process development and improvement, failure analysis, and detection of gross defects. At this time, there is no NDE technique to find critical volume flaws quickly in arbitrarily shaped technical ceramics.

References

1 S. T. Stock, A. Guvenilir, T. L. Starr, J. C. Elliot, P. Anderson, S. D. Dover, and D. K. Brown. *Advanced Characterization Techniques for Ceramics*. Ceramic

Transactions, Vol. 5. The American Ceramic Society, Westerville, OH, 1988, pp. 161–170.

2 B. D. Swicka, W. A. Ellingson, and C. McPheeters. *Ceram. Eng. and Sci. Proc*. **8** (7–8), 1987.

3 M. C. Bhardwaj. *Metal and Ceramic Composites: Processing, Modelling, and Mechanical Behavior*. 1990, pp. 509–522.

4 S. M. Nair, D. K. Hsu, and J. H. Rose. *J. of Nondestructive. Eval*. **8**, 1, 1989.

5 T. Derkacs. *Nondestructive Testing of High Performance Ceramics*. The American Ceramic Society, Westerville, OH, 1987, pp. 52–58.

6 J. P. Monchalin, J. D. Aussel, R. Héon, J. F. Bussiére, and P. Bouchard. "Nondestructive Monitoring of Materials Properties." *Materials Research Society Symposium Proceedings, Vol. 142*. 1989.

7 H.-N. Lin, R. J. Stoner, and H. J. Maris. *J. of Nondestructive. Eval*. **9** (4), 1990.

8 A. C. Way and L. W. Kessler. *Ceram. Eng. and Sci. Proc*. **10** (7–8), 1989.

9 A. M. Koshti. M.S. thesis. University of Oklahoma, Norman, 1985.

10 D. N. Rose, D. C. Bryk, W. Jackson, M. Chaika, G. Sohram, G. Quay, R. L. Thomas, L. D. Farro, and P. K. Kuo. *Ceram. Eng. and Sci. Proc*. **8** (7–8), 1987.

11 C. A. Peck. *Residual Stress in Design Process and Materials Selection*. ASM International, Cincinnati, 1987.

12 B. D. Cullity. *Elements of X-ray Diffraction*. 2nd ed., Addison Wesley, Reading, MA, 1978, p. 454.

Appendix: Technique Summaries

The technique summaries in the following pages are fully described in the *Encyclopedia of Materials Characterization* by C. Richard Brundle, Charles A. Evans, Jr., and Shaun Wilson.

Auger Electron Spectroscopy (AES) 1

In Auger Electron Spectroscopy (AES), a focused beam of electrons (typically a few keV to a few 10's of keV in energy) strikes the sample, causing electrons to be ejected. Some of these (the Auger electrons, named after Pierre Auger who first observed them) have kinetic energies characteristic of the atoms from which they came and so identification of the elements present in the sample can be made directly from the measurement of these energies. On a finer scale, it is sometimes also possible to determine the chemical state of the element from small shifts in the Auger energies caused by the chemical bonding of the element (chemical shift). For a solid, AES probes 2–20 atomic layers deep, depending primarily on the kinetic energy of the ejected Auger electron concerned, and somewhat on the material. With appropriate standards the relative concentration of the elements present within the probing depth can be estimated from the relative intensities of the Auger peaks in the spectrum. The great strength of AES is the high spatial resolution achievable through use of a focused beam (down to 10's of nm), and the ability to combine measurement with ion sputtering material removal, to obtain a three-dimensional elemental profile. The main use is with metals and conducting or semiconducting inorganic materials, since beam damage and charging can be issues with non-conducting and organic materials. Many Auger spectrometers are designed to maximize sensitivity (typically down to 100 ppm of element concentration) and speed of analysis, and do not have the spectral resolution to use chemical shifts for chemical state identification. Auger is capable of identifying all elements, except hydrogen and helium.

Electron Energy-loss Spectroscopy in the Transmission Electron Microscope (EELS) 2

If an energy analyzer is added to a Transmission Electron Microscope (TEM) or Scanning Transmission Electron Microscope (STEM) after the image plane, the energy losses suffered by the incident electron beam as it passes through the thin TEM/STEM sample can be measured. The losses are caused by plasmon excitation (a few 10's eV energy) and atomic core level excitation. Atomic core binding energies are characteristic of the atom concerned, so the threshold energy for core level excitation provides a direct atomic identification (cf. XPS). Relative concentrations of elements present in the sample can be determined from the relative intensities of the energy loss threshold. Near-edge structure on the energy loss features can also provide bonding information (cf. XPS). The sample must be very thin (100 Å to 2000 Å, depending on beam energy) to avoid multiple inelastic scattering, resulting in peak broadening, and loss of intensity. A consequence of avoiding multiple scattering is a lack of beam spreading as the electrons pass through the sample, which results in the lateral resolution being determined largely by the width of the incident beam. In STEM mode a lateral resolution of a few Å is therefore possible. The main use of EELS is for elemental and chemical composition analysis at ultra-high spatial resolution (at grain boundaries, for instance).

Electron Microprobe X-Ray Microanalysis (EPMA) 3

In Electron Microprobe X-Ray Microanalysis (EPMA) a beam of electrons (5–30keV) is focused onto a solid sample and the X rays emitted (fluorescence) are analyzed for their energies and intensities. The energies are characteristic of the atoms undergoing the emission, providing an atomic identification (Be to the actinides), and the intensities can be related to the concentrations present, providing a quantitative analysis. The X rays are detected and measured using either an Energy Dispersive X-Ray Spectrometer (EDS), or a Wavelength Dispersive X-Ray Spectrometer (WDS). EPMA systems usually have both methods available (EDS is experimentally simpler and faster; WDS is more accurate and can reach lower detection levels), together with SEM capability. For smooth, flat samples, detailed correction procedures for matrix effects (backscattering which varies with atomic number; secondary X-ray absorption and fluorescence occurring during emission), together with elemental standards, allow quantification typically to about +/– 4%. For rough surfaces, or particles, analysis is usually only semi-quantitative. The detection limit for EDS is about 1000ppm and about 100ppm for WDS. Probing depths, and spatial resolution, depend on the incident beam energy, ranging from about 0.1μm at the lowest energy to 5μm at high energy. Quantitative mapping on flat surfaces is common. The major use of EPMA is nondestructive quantitative elemental analysis of major and minor constituents in the top few um of inorganic materials.

Energy-Dispersive X-Ray Spectroscopy (EDS) 4

Energy-Dispersive X-Ray Spectroscopy, EDS, is a specific technique for the detection and energy distribution determination of X-Ray Fluorescence, XRF. XRF is the phenomena where X rays are emitted from a material when bombarded by high energy radiation (electrons, ions, X rays, neutrons, gamma rays). Some of the X-ray energies emitted are characteristic of the atoms present, allowing atomic identification in the material of interest.

In EDS a solid state X-ray detector, usually lithium drifted Si, and pulse counting electronics are used. The detector converts an incoming X-ray photon into an electronic pulse of amplitude proportional to the energy of the X ray. The signal processing electronics counts the number of pulses of each different amplitude, resulting in a histogram of X-ray energy versus intensity. The X-ray energies allow atom identification, and the relative peak intensities can be related to relative atomic concentrations by comparision to standards, or by theoretical calculations.

All elements with an atomic number higher than Li are, in principle detectable, though effectively dealing with low Z elements requires some care and correctly set up instrumentation. In practise, EDS is primarily used in conjunction with e-beam columns (SEMs, TEMs, STEMs, Auger instruments) as the excitation source.The depth probed is dependant primarily on the energy of the electron beam, and on the material being probed. It can vary from as little as 20 nm (high Z material, low beam energy) to as much as 5000 nm (low Z material, high beam energy). The lateral resolution is similar to the depth probed but is not determined by the primary beam diameter. It is determined by the beam energy and the sample material, because the beam spreads by scattering as it penetrates into the material, creating X rays in this enlarged volume.

The particular strength of EDS is the simultaneous (or parallel) detection of elements rapidly and cheaply, by placing the physically small detector inside the SEM, or other electron beam system. As such it adds an elemental analytical capability to imaging electron beam columns. Its drawback is that the typical solid state detector has very poor energy resolution, which means that there are significant peak overlaps, sometimes making it difficult to distinguish elements. This is particularly true in the low energy region.

Fourier Transform Infrared Spectroscopy (FTIR) 5

In Infrared Spectroscopy (IR), a beam of light (electromagnetic radiation) in the infrared wavelength region impinges on the sample and the wavelength/frequency is scanned. Whenever there is a match of the light frequency to the vibrational frequency of a vibrational mode within the sample (i.e., vibration of atomic positions) it is possible that the radiation at that frequency will be absorbed and the vibration excited (selection rules apply and not all vibrations can be excited). The absorption occurring, as a function of IR wavelength, is monitored by comparing the input intensity of the radiation to the output intensity, thus revealing the vibrational frequencies existing in the sample. Since a vibrational frequency value is dependant on the bonding between the atoms involved in that vibration, vibrational frequencies of materials are characteristic of the chemical groups existing in the material (e.g., OH, CN, CH_2, COOH, etc.), so determination of the vibrational frequencies present allows determination of which chemical groups are present. With standards the concentrations of the groups present can also be determined from the strength of the absorptions.

Fourier Transform IR simply describes the most common modern technique for scanning the wavelength of the impinging IR beam. It is based on the Michelson interferometer, where constructive and destructive interferences between the two halves of a split light beam are controlled by changing the path length of one of the beams with respect to the other by moving reflecting mirrors. Since the path length difference for destructive/constructive interference depends on wavelength, the oscillation of the mirrors provides a way of scanning the wavelengths from a polychromatic light source.

For solids, IR spectroscopy can be performed either in reflection or in transmission if the sample is thin enough to pass the radiation. This varies enormously with material because absorption coefficients vary enormously (some materials are transparent to IR, some highly absorbing). In reflection, coupling the radiation to an optical microscope allows a lateral resolution down to 20 μm, with the depth probed depending on absorption coefficient, but usually being many μm. Another reflection mode is Attenuated Total Reflection, ATR, where light enters at grazing angle and probes only the surface region (10's of nm). IR of solids does not require a vacuum, but the path length of the radiation through ambient atmosphere must be purged using dry nitrogen, to avoid gas phase absorption from strong absorbers such as water vapor.

The strength of IR is the qualitative and sometimes quantitative (with standards) identification of the presence of chemical species, or functional groups, sometimes down to trace levels in liquids and solids. For solids stress, strain, crystallinity/amorphousity, and inhomogeneities can be detected from absorption peak broadenings and shifts.

Light Microscopy 6

The visible light microscope dates back over 300 years for the study of natural materials (plants, animals). At its simplest level the method involves visible observation using white light, with useful magnification of up to 1400X. This allows observation resolving features down to around 0.2 μm, as opposed to about 200 μm by the naked eye. Resolving power can be increased by using UV radiation (doubled) or by immersing optics in oil, but both procedures greatly increase the compexity of instrumentation. For biomedical samples and many other materials (e.g., fibres, wood, hairs, pollens), the morphology revealed in the image is the main information, and materials identification can usually be made through use of extensive atlases of every conceivable structure observed. For materials science, simple morphology alone is often insufficient for identification, and it is necessary to investigate a number of other parameters such as opacity, color, refractive index, crystal system, fluorescence, and many others. These can be quickly determined using a variety of procedures and attachments to a microscope or several microscopes.

The main role of the light microscope is to image structures, either natural or man made, which are not observable to the naked eye, but have features greater than 0.1 μm. It is extensively used during the preparation of samples for observation by other analytical techniques, such as SEM or AFM, and should always be the first step in a materials analysis.

Neutron Diffraction 7

Neutron Diffraction uses thermal neutrons of wavelength, λ, 1–2 Å to determine the atomic structure in crystalline phases in an essentially similar manner to X-Ray Diffraction. Neutrons are diffracted according to Bragg's Law ($\lambda = 2d \sin\theta$, where d is the spacing between atomic planes). The intensity of the diffracted beams is measured as a function of either the diffraction angle, 2θ, or by scanning λ for a fixed θ. The former is done using neutrons of a fixed, known wavelength from a nuclear reactor. The later involves using a high energy beam of photons impinging on a heavy metal, which produces pulses of neutrons (a spallation source). The major difference between Neutron Diffraction and X-Ray diffraction is (a) the neutrons penetrate solids much deeper, so that the analysis is always of the bulk material; (b) diffraction is from nuclei, not the electrons surrounding it, so the positional accuracy is much better (10–13 m); and (c) all elements are detected with roughly equally sensitivity, since there is no Z^2 dependence for scattering of neutrons. The major uses of Neutron Diffraction are for structural refinement of atomic positions, particularly where light atoms are present with heavy atoms (e.g., O atom positions in superconductors), residual stress measurement (from diffraction line broadening), and determination of magnetic ordering. The major disadvantage of the technique is that it must be performed at a large government facility.

Physical and Chemical Adsorption for the Measurement of Solid Surface Areas 8

Physical adsorption isotherms involve measuring the volume of an inert gas adsorbed on a material's surface as a function of pressure at a constant temperature (an isotherm). Using nitrogen as the inert gas, at a temperature close to its boiling point (near 77K), such isotherms are used to determine the amount of the inert gas needed to form a physisorbed monolayer on a chemically unreactive surface, through use of the Brunauer, Emmett, and Teller equation (BET). If the area occupied by each physisorbed N_2 molecule is known ($16.2A^2$), the surface area can then be determined. For reactive clean metals, the area can be determined using chemisorption of H_2 at room temperature. Most clean metals adsorb one H atom per surface metal atom at room temperature (except Pd, which forms a bulk hydride), so if the volume of H_2 required for chemisorption is measured, the surface area of the metal can be determined if the atomic spacings for the metal is known. The main use of physical adsorption surface area measurement is to determine the surface areas of finely divided solids, such as oxide catalyst supports or carbon black. The main use of chemisorption surface area measurement is to determine the particle sizes of metal powders and supported metals in catalysts.

Raman Spectroscopy 9

In Raman spectroscopy, a light beam of fixed wavelength (usually in the visible range) from a laser undergoes inelastic scattering as it interacts with the sample material. The photons can suffer energy loss if they excite vibrations in the sample. The energy losses, and therefore the vibrational frequencies involved, are determined by measuring the wavelengths of the scattered light. The value of an excited frequency is sensitive to the bonding between the atoms involved in that particular vibration.

Raman spectroscopy is closely related to infrared spectroscopy, which also determines the values of vibrational frequencies (see the FTIR summary), but it differs in the physics in that it involves a photon scattering process with energy loss, where as IR involves varying the photon energy and observing absorption occurring at the vibrational frequencies. Raman spectroscopy is better suited to optical microscopes, because of the single laser wavelength involved, and spatial resolution down to the one μm range is possible (cf. approximately a 10 μm limit for IR).

The depth probed depends very strongly on the optical properties of the material involved and the laser wavelength used. Moving into the UV range greatly reduces the probing depths, and allows a depth profiling capabilities if several wavelengths are used.

The major area of application for solids and liquids is chemical fingerprinting and the identification of unknown compounds. For solids, Raman is also used for phase identification, following amorphous/crystalline transitions, measurement of stress and strain, and, in the microscope mode, the detection and analysis of defects, including particles during wafer processing.

Rutherford Backscattering Spectrometry (RBS) 10

In Rutherford Backscattering Spectrometry (RBS), a solid is bombarded with a monoenergetic beam of ions (typically He or H) in the one to several MeV energy range. As the beam penetrates into the solid, the ions undergo continuous small angle forward scattering through interactions with the electron density between the atomic nuclei, continuously losing small amounts of energy as a function of depth penetrated. In addition, a small fraction of the ion beam undergoes head on collision with the nuclei of the atoms present in the solid (the target atoms) and is consequently back scattered. The back scattering results in a major loss of energy (transferred to the atoms struck, which moves forward like in billiard ball collisions) from the probe ion beam, the amount of which is characteristic of the mass of the target atoms. Determination of the energy losses suffered by the back scattered ion beam after exit from the solid thus allows, in principle, identification of the atoms present, their depth distribution, and, from intensities, the atomic concentrations. The depth probed can vary from 1–20 μm depending on ion species used, ion energy, and instrumental set-up. At these high energies, the ion/material interactions are well described by classical kinematic equations, and quantification can be achieved without standards. The depth resolution also varies strongly, depending on the material, ion energy, and instrumental set-up, plus the depth probed (poorer at greater depth) ranging from a best of about 2 nm to 30 nm. Element sensitivity is a strong function of the position in the periodic table, varying as Z squared. It can be as poor as 10 atomic percent at the low Z end and as good as 10 ppm range at very high Z. In principle all Z values above that of the probe ion can be detected (so not H), but the poor energy resolution of the solid state detector used means that some elements cannot be distinguished from adjacent elements in the periodic table. Lateral resolution is limited to the beam diameter, usually 1 to 4 mm, but a few specialized microbeam systems do exist.

The main use of RBS is nondestructive element depth profiling of thin films in the few μm depth range. If the target is crystalline, specialized modes involving beam alignment with crystallographic axes can give structural information, such as the degree of lattice damage.

Scanning Electron Microscopy (SEM) 11

In Scanning Electron Microscopy (SEM), a probe electron beam (typically a few hundred eV to a few 10's keV energy) is finely focused (down to 10 Å capability in some instruments) and scanned over a solid surface. The interaction of the beam with the sample material generates a variety of responses, including fluorescence emission, which can be used for elemental analysis (see the EDS summary).

One of the major responses is a copious emission of low energy secondary electrons (0 to 50 eV range), which escape from the top few 10's Å of the material. The secondary electron yield strongly depends on the angle of impact between the probe beam and the local surface topography, so rastering the beam across the surface produces a changing intensity with changing topography. These changes in secondary electron emission intensity are used to modulate the brightness of a synchronously rastered cathode ray tube, creating an image. The image can be highly magnified up to 500KX, with a lateral resolution determined by the diameter of the probe beam, and have the look of an optical image (though the depth of focus is much greater).

In addition to the secondary electrons, a much smaller quantity of backscattered primary electrons are produced. Their intensity depends strongly on material (high for high Z elements), so the image also contains some Z contrast. Filtering out the low energy secondaries enhances this contrast (backscatter mode), producing an average Z dependant image instead of topography image.

The SEM is often the first or second (after an optical microscope) technique used to provide a magnified image of an area of the sample to be examined. It is often used in conjunction with an ancillary analytical technique, such as EDS, to provide elemental analysis capability to go with the imaging.

Scanning Transmission Electron Microscopy (STEM) 12

Scanning Transmission Microscopy (STEM) is a specialized form of TEM (see TEM summary) where the high energy electron beam (100 to 300 keV) is focused to a small spot (down to a minimum of about 3 Å) and scanned across a sample which is usually a material which has been sectioned to a very thin film (5 to 500 nm thick). After interaction with the material of the film, the transmitted beam can be subjected to various treatments, as in TEM (bright and dark field imaging; convergent beam electron diffraction, CBED; and electron energy loss spectroscopy, EELS). Also, the emitted X-ray fluorescence can be analyzed by EDS (see EDS summary). Keeping the sample to a very thin section stops the lateral spread of the primary beam as it passes through, allowing the spatial resolution to be determined by the diameter of the focus beam, down to almost atomic dimensions.

The major use of STEM is for imaging and compositional analysis (sometimes also chemical state analysis, from EELS) at very high spatial resolution across thin film material interfaces, such as found in semi-conductor and other high technology devices. Single atom imaging is possible for heavy atoms. The disadvantage is that a very thin interface cross-section must be first prepared. Also, at very high resolution, the electron beam is focused into such a small area that the local electron density becomes extremely high and can anneal, damage, or even burn through the film if the dwell time is too long.

Scanning Tunneling Microscopy and Scanning Force Microscopy (STM and SFM) 13

In Scanning Tunneling Microscopy (STM), a sharp tip is brought to within a few Å of a conducting surface in ultra high vacuum and held at a positive or negative potential with respect to the tip. At this distance a quantum mechanical electron tunneling current flows between an individual atom on the surface and an atom on the tip (or vice versa, depending on the polarity). The magnitude of the current is an exponential function between the two atoms involved. So scanning the tip across the surface therefore produces a strongly varying current as the topography and distance between tip and surface atoms changes. This allows mapping of the topography (actually the surface electron density) with a resolution of 0.01 Å in the Z direction, and atomic resolution in the XY direction.

In the related technique, Scanning Force Microscopy (SFM; also known as atomic force microscopy, AFM), the tip is mounted on a cantilever and the Van De Waals forces between the surface and the tip deflects the cantilever. The deflection is also a strong function of the separating distance, allowing topography mapping, as in STM. The resolution in SFM is about ten fold poorer than STM, but the technique has the great practical advantages of being operated in air and not requiring a conducting sample.

The major use of STM is in the research area of imaging atomic structures on clean conducting and semi-conducting surfaces, under UHV conditions. SFM, on the other hand, is widely used throughout industry as a very high resolution surface profilometer to monitor surface roughness, defects, and man-made micro or nano structures.

Solid State Nuclear Magnetic Resonance (NMR) 14

In Solid State Nuclear Magnetic Resonance (NMR), a solid specimen is subjected to a strong magnetic field (typically 1 to 14 Tesla). If the nuclei present have unpaired spins, the magnetic field interacts with the magnetic dipole (spin), splitting the otherwise degenerate spin states into an upper (excited) state and a lower (ground) state. The energy of the splitting, for a given magnetic field, is characteristic of the nuclei concerned and is in the radio frequency range. If the sample is subjected to a pulsed radio frequency band covering this energy splitting, excitation from ground to excited state will occur. As the nucleus relaxes back to the ground state, it re-emits a radio signal at the frequency of the splitting (the NMR signal). Detection of the NMR frequency identifies the presence of the nucleus, and the intensity is proportional to the concentration. Small variations and splittings of the NMR frequency are related to bonding interactions with neighboring nuclei. While hydrogen nuclei NMR is by far the best known area of study and use (organic chemistry and MRI), about half the elements in the periodic table have unpaired nuclear spins suitable for NMR. The major use of solid state NMR is for element-selective phase identification and quantification, and for structural characterization of disordered phases which cannot be done by diffraction methods. A disadvantage of the technique is the very strong magnetic fields required, and that several different magnets might be required for different nuclei to get the NMR frequencies in the working range of the radio electronics. For this reason laboratories tend to concentrate on studies involving one particular element.

Surface Roughness: Measurement, Formation by Sputtering, Impact on Depth Profiling 15

Surface roughness can be measured by a variety of scanning profilometer methods, which monitor individual features, or by methods which give averaged information. For the profilometers there is a wide variety of methods possible: mechanical, optical, scanning electron microscope (see the SEM summary), and the scanning force microscope and scanning tunneling microscope (see the STM and SFM summaries). These instruments have a large range of capability in terms of depth resolution, maximum depths measurable, and lateral resolution (roughness frequency range). The mechanical profilometers obviously contact the surface, and may damage it. The depth resolution can be down to 5 nm, and the lateral resolution 100 nm (depends on tip radius), for the most sophisticated (and expensive). Optical profilometers can measure down to 0.1 nm depth and 300 nm lateral resolution (depends on wavelength).

SEM is useful for observing very short range roughness (i.e., sharp spikes or dips) but ineffective for long range small amplitude roughness. SFM has depth resolution down to 0.01 nm and a normal lateral resolution of about 0.5 nm, which is more than needed in most practical applications. STM can do an order of magnitude better, but only for conductors under ideal conditions in UHV environments. It is basically a research tool.

Optical scatterometry (see the summary for this technique) gives averaged, not individual, information. The depth resolution achievable is 0.1 nm RMS, and long and short range roughness can be separated (i.e., measurement provides information as a function of roughness frequency range).

Transmission Electron Microscopy (TEM) 16

In Transmission Electron Microscopy (TEM), a very high energy monoenergetic electron beam (100 to 400 keV) passes through a thin specimen (less than 1000 nm) of diameter less than 3 mm (necessary to fit in the electron optics column). A series of post specimen lenses transmits the emerging electrons, with spatial magnification up to 1,000,000, to a detector (fluorescent screen or video camera) viewed in real time.

Any regions of the sample under the incident beam (usually a few μm diameter) exhibiting crystallinity, will diffract electrons away from the central spot, forming a diffraction pattern observable at the back focal plane of the objective lens. Like X-ray diffraction, this can provide identification of crystalline phase, orientation, and lattice parameters. In micro-diffraction, the incident beam is focused down to sub-micron areas, but this focusing degrades the diffraction pattern.

The above mode of operation is termed *Diffraction Mode*. Another mode is *Imaging Mode*. In this mode the reconstructed, highly magnified image (up to 1,000,000) is observed at the image plane of the objective lens. By placing an aperture in the diffraction plane, either the electrons in the undeflected beam (the center spot) can be imaged (Bright Field Mode), or those in a deflected beam (the diffracted or scattered electrons) can be imaged (Dark Field Mode). An amorphous sample of uniform thickness can undergo only Z contrast scattering (higher Z, more scattering), so regions of higher Z show up as dark areas on a bright background in Bright Field Mode. Any crystalline region will also show up as a dark area. In dark field, regions of crystallinity, or higher Z, will show up as bright spots on a dark background.

Yet another mode of use is High Resolution TEM (HRTEM), in which atom positions can be established by collecting electrons from both the undeflected and diffracted beams and comparing the observed phase interference patters to a simulation.

TEM, with its many modes, and often involving ancillary materials analysis capabilities such as EDS (see EDS summary), is the mainstay of material science and analysis of small volume (areas and thickness). A fully equipped TEM laboratory will have several microscopes with differing capabilities, plus all the necessary sample preparation techniques. See also Scanning TEM (STEM), where the incident beam is focused down to almost atomic dimensions and scanned across the sample.

Variable-Angle Spectroscopic Ellipsometry (VASE) 17

In ellipsometry, a collimated polarized single wavelength light beam (UV, visible, or IR) is directed at the material under study, at an oblique angle, and the relative light intensity of the reflected beam is measured as a function of its polarization angle. In Variable-Angle Spectroscopic Ellipsometry (VASE), these measurements are made as a function of varying both the wavelength and the angle of incidence. For a thin film with a surface parallel to the substrate (i.e., a constant thickness) and inhomogeneities of less than about 1/10 of the wavelength being used, Maxwell's equations plus the Fresnel equations for calculating reflection coefficients at interfaces can be used to model the experimental data. The variable parameters in the modeling are layer thickness and the optical constants for the material in the layer. Surface and interface roughness and/or mixing and interface reaction can, in principle, be handled by treating the interfaces as additional layers with their own optical properties and thickness. The parameter values in the model are itterated until a best fit with the data is obtained. Though data is easy to obtain, this model-dependent aspect of ellipsometry analysis, with many floating parameters, can make it a difficult technique to use correctly (it can never give a unique fit), unless some of the parameters (such as the optical constant) are already well known, and can therefore be constrained.

VASE, and also single wavelength ellipsometry (less reliable) are extensively used in the wafer processing and other thin film industries, primarily to monitor thickness of single or bi-layers of dielectrics, optical coatings, semi-conductors, and magneto-optic and magnetic disk material. Depending on the optical constants, film thickness from 1 to a few 100 nm can be handled (or even microns for transparent material). Because the instrumentation is operated in air and the light can penetrate liquids, ellipsometry can also be used for in situ electrochemistry and biological interfaces.

X-Ray Diffraction (XRD) 18

In X-Ray Diffraction (XRD), a collimated beam of mono-chromatic X rays between 0.5 Å and 2 Å wavelength strike a sample and are diffracted by crystal planes present. Bragg's law,

$$\lambda = 2d \sin\theta$$

relates the spacing between planes, d, to the diffraction angle, 2θ, which is scanned to pick up diffraction from the different crystal planes present. The azimuthal orientation of the different beams also reveals the crystalline orientation. If the material is poly-crystalline, then diffraction rings, instead of a spot pattern, are formed (powder diffraction). Distortions or broadenings of the diffraction beams carry information on crystal strain and grain size.

Because X rays penetrate deeply (strongly Z dependent; at λ = 1.54 Å the absorption length is 1 mm for carbon, 66 μm for Si, and 4 μm for iron), XRD is intrinsically a bulk technique. Typically, however, large areas are used (several mm diameter), and there is sufficient intensity and spectral resolution using modern standard equipment to study films of thickness down to the 100's nm range for high Z material. If specialized instrumentation and geometries are used (Grazing Angle XRD, Double Crystal Diffraction XRD, synchrotron radiation source), sensitivities down to 10's nm are easily achieved, and mono-layer sensitivity is possible. Small area capabilities also exist (micro-beam XRD), but then thicker samples are required to compensate for intensity loss of the smaller areas.

The major uses of XRD are identification of crystalline phases, determination of strain, crystalline orientation and size, epitaxial relationship, and the accurate determination of atomic positions (better then in electron diffraction). Because of the strong Z dependence of X-ray scattering, light elements are difficult to deal with, particularly in the presence of heavy elements.

X-Ray Fluorescence (XRF) 19

In X-Ray Fluorescence (XRF), the mono-energetic X-ray beam from a vacuum X-ray tube (W, Mo, Cr, and other targets are used to provide a range of energies) irradiates the sample, in air, causing excitations of core electrons of the atoms present. As these excited atoms decay back to their electronic ground states, light is emitted in the X-ray region. The specific wavelengths emitted are characteristic of the energy levels involved, and therefore of the atoms concerned. The X-ray fluorescent wavelengths are determined using a crystal diffractometer.

The depth probed is Z dependent, but, since X rays are involved both in the excitation and the emission, it is many μm, making XRF a bulk technique. A specialized grazing incidence (total reflection) adaptation exists, however, for analyzing material at the surfaces of semi-conductor wafers (see TXRF summary). Also, there is sufficient total intensity such that thin films (μm level or lower, depending on instrumentation and Z) can be analyzed provided there are no interfering elements in the substrate. Standard instruments have no significant spatial resolution (few mm), but micro-beam systems down to 10 μm do exist. The technique is applicable to all elements except H, He and Li. Energy dispersive X-ray analysis (see EDS summary) is a closely related technique.

The major uses of classical XRF, in air, are the identification of elements and the determination of composition for bulk materials. For thin films intensity/composition/thickness equations are used to determine the composition and thickness of individual layers in single or multi-layered stacks, such as used in the disk drive and semi-conductor industry.

X-Ray Photoelectron Spectroscopy (XPS) 20

In X-Ray Photoelectron Spectroscopy (XPS), also known as Electron Spectroscopy for Chemical Analysis (ESCA), mono-energetic soft X rays (usually Al K alpha at 1489 eV or Mg K alpha at 1256 eV) bombard a solid sample in ultra high vacuum. One of the interaction processes occurring is the ejection of photoelectrons, according to the Einstein Photoelectric Law:

$$KE = h\nu - BE$$

where $h\nu$ is the incident X-ray energy, KE is the kinetic energy of the photoelectron, and BE is the binding energy of the electron in the particular energy level of the atom concerned. Measurements of the KE's of the ejected photoelectrons directly determines the BE's, which, for core levels of atomic orbitals, are characteristic of the atoms concerned and therefore identify their presence. On a finer energy scale, small "chemical shifts" in the BE's provide chemical state identification (such as the oxidation state for a metal). The technique is applicable to all elements, except H and He, since they do not have characteristic atomic core levels.

For a solid, XPS probes 2 to 20 atomic layers deep, depending of the KE of the ejected electron, the angle w.r.t., the solid surface of detection, and the material. XPS is therefore a true surface technique. If measurement is made as a function of angle, depth distribution information is available over the depth probed. XPS is also used with sputter depth profiling to go beyond these depths. Modern laboratory XPS instruments can provide *practical* lateral resolution capability down to the 10 to 20 μm range. Specialized systems can go lower, but acquisition time becomes very long.

The particular strengths of XPS are semi-quantitative elemental analysis at surfaces without standards, quantitative analysis with standards, and chemical state determination for materials as diverse as biological to metallurgical.

Index

CHARACTERIZATION OF

CERAMICS

Ronald E. Loehman

Engineers and scientists who frequently deal with ceramics are unlikely to be aware of the full range of characterization techniques applicable for finding surface and microanalytical information on their materials. *Characterization of Ceramics* discusses areas of ceramics where surface and analytical information are important to processing and determination of properties. This unique reference presents material through case histories to illustrate the applicability of different analytical techniques to ceramics. Different techniques are compared and contrasted to give the reader sufficient basis for selecting one over another. Each chapter begins with brief background information on the topic, followed by a more extensive discussion of applications and benefits of the techniques.

This volume is one of a series originally issued under another imprint. The other volumes in this series are as follows:

Characterization of Catalytic Materials
Israel E. Wachs

Characterization of Metals and Alloys
Paul H. Holloway and P. N Vaidyanathan

Characterization of Polymers
Ned J. Chou, Stephen P. Kowalczyk, Ravi Saraf, and Ho-Ming Tong

Characterization in Silicon Processing
Yale Strausser

Characterization in Compound Semiconductor Processing
Gary McGuire and Yale Strausser

Characterization of Integrated Circuit Packaging Materials
Thomas M. Moore and Robert G. McKenna

Characterization of Composite Materials
Hatsuo Ishida

Characterization of Tribological Materials
William A. Glaeser

Characterization of Optical Materials
Gregory J. Exarhos

Characterization of Organic Thin Films
Abraham Ulman

MOMENTUM PRESS
www.momentumpress.net

ISBN: 978-1-60650-194-8
90000
9 781606 501948